UiT
NORGES
ARKTISKE
UNIVERSITET

FACULTY OF SCIENCE AND TECHNOLOGY
DEPARTMENT OF GEOLOGY

Post-glacial sedimentary processes and slope instabilities off Nordnesfjellet, Lyngenfjorden, northern Norway

Sigrun Maret Kvendbø Hegstad

GEO-3900 Master's Thesis in Geology
November 2014

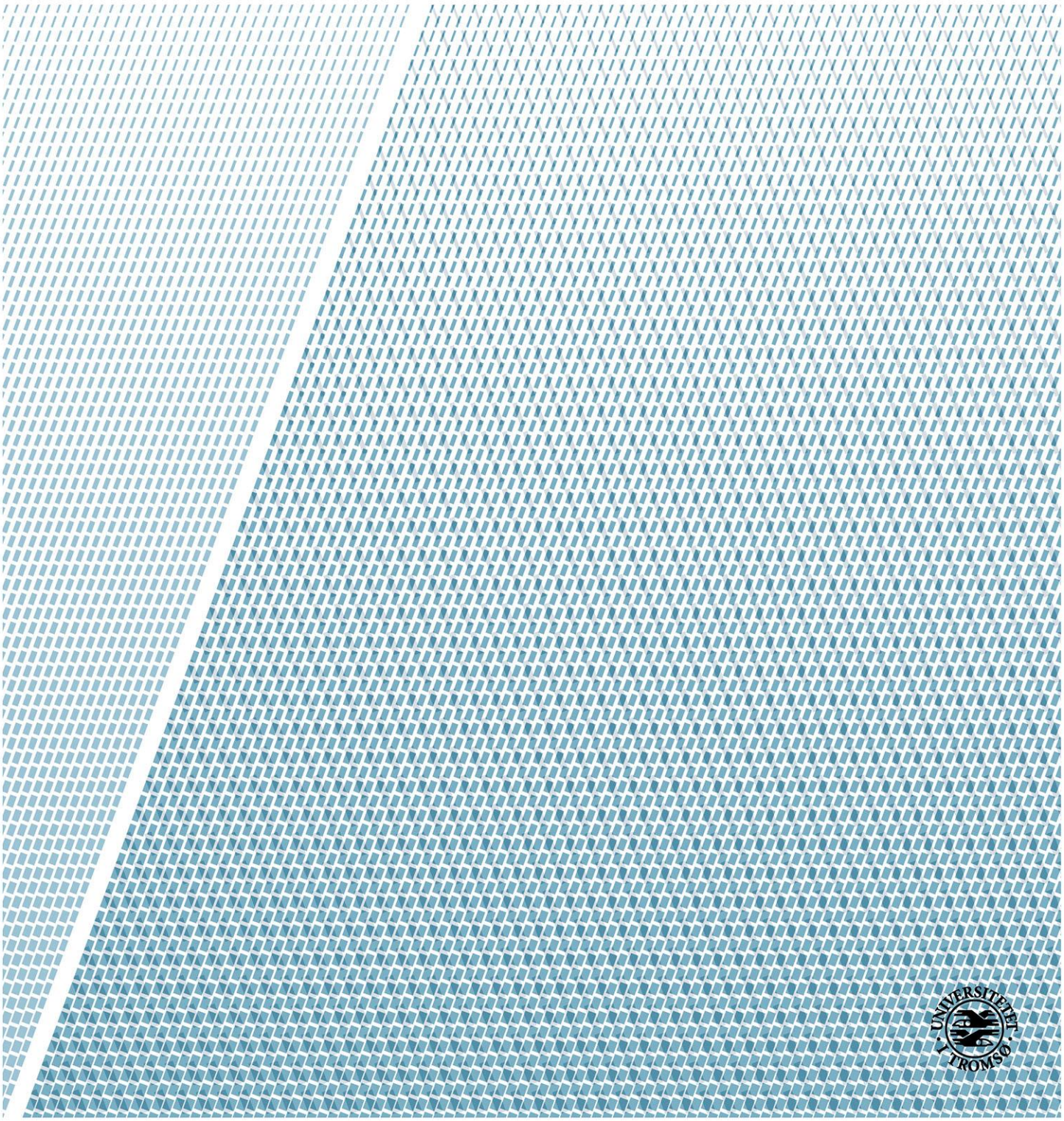

Abstract

The Lyngen- and Storfjorden system, Troms County, northern Norway, is surrounded by an alpine landscape, partly with steep mountain sides. Parts of the ~700 m high mountain Nordnesfjellet, on the eastern side of the fjord, are currently moving downslope, and could in the event of sudden failure generate tsunami waves which would affect low-lying areas within a larger region.

The main objective of this study is to integrate multi-proxy analyses of five sediment cores, swath bathymetry and high-resolution seismic data from one NNE-SSW oriented basin of Lyngenfjorden, off Nordnesfjellet, with the purpose of reconstructing mass-wasting activity in the past.

The fjord sides in the study area are up to >30^{o} steep and irregular with depressions, escarpments and furrows of various sizes and 'freshness'. These features are interpreted to be slide scars and gullies, respectively, related to slope failures. The central parts of the up to 270 m deep basin are generally smooth. However, an up to 8 m high step, crossing almost the entire fjord width, defines the northern limit of a relatively irregular seafloor in the southern part of the study area. Furthermore, sediment-lobe areas are visible as undulating seafloor on the western and eastern sides of the basin.

The high-resolution seismic data reveal that the uppermost <12 ms two-way-travel time (~9 m) are composed of acoustically transparent sediments with few, discontinuous reflections. Deposits causing a chaotic reflection pattern underlie this package within the areas of irregular and undulating seafloor, where also several acoustically well stratified sediment blocks (up to ~300 x 300 x 10 m^3) are identified. The acoustically chaotic deposits are e.g. debris flows or turbidites, whereas the blocks are either run-out blocks embedded in the debris flows or slide blocks. The mass-transport deposits are stacked together in several complexes which cover and partly erode into glaciomarine sediments. It is assumed that these complexes were deposited during a relatively short period of frequent mass-wasting directly following the last deglaciation of the study area (~10,800 cal. years BP).

Multiple acoustically transparent wedges thinning from the fjord sides towards the fjord axis are identified. These are most probably debris flows or turbidites. One prominent high-amplitude reflection can be traced over an area of > 7.4 x 1.3 km^2. It has varying thickness, on-laps the eastern fjord flank, while it thins towards west.

The cored sediment is mostly massive, olive grey mud. However, coarser, partly well sorted, intervals (up to 13 cm) with sharp and partly erosive lower boundaries occur. Well-sorted intervals are suggested to be turbidites. One turbidite was deposited from a high-density turbidity flow between 3026 and 2930 cal. years BP. It correlates with the strongest reflection within the acoustically transparent interval, thus, indicating that it extends over more than 7.4 x 1.3 km^2 of the fjord floor. Wood fragments and moss found within the turbidite suggest that the origin of the failure was onshore.

Mass-transport activity was high shortly after the deglaciation, decreased during the mid-Holocene and increased again during the late Holocene. The late Holocene increase in mass wasting might be related to a climatic deterioration.

Forord

Jeg vil gjerne rette en stor takk til mine veiledere Matthias Forwick og Jan Sverre Laberg. Tusen takk for at dere har delt deres kunnskap med meg, og for all inspirasjon det har gitt meg. Dere har vært til uvurderlig hjelp. En spesiell takk til Matthias, din tålmodighet når ingen grenser.

Takk til Edel Ellingsen, Ingvild Hald, Trine Dahl og Julia Sen for all hjelp i min periode på labben. Og takk til Jan P. Holm som har vært behjelpelig med mitt arbeid med figurer.

Jeg vil gjerne takke alle flotte folk jeg har vært så heldig å bli kjent med i løpet av disse 7 årene som student – ingen nevnt, ingen glemt.

Tusen takk til Silje og Kine, dere er alltid der!

Mamma og pappa, dere er best! Takk for at dere er som dere er; for at jeg er blitt den jeg er.. Og takk til «min lillebror, som har blitt så stor».

Kjære Anders, ord blir overflødige… Team SIGDERS (∞)

Sigrun Maret Kvendbø Hegstad, 15. november 2014

Table of Contents

1. Introduction

1.1 Objectives

The main objective of this study is to investigate the seafloor in the Lyngenfjord off the mountain Nordnesfjellet, northern Norway, with the purpose of reconstructing past mass-wasting activity. It will be achieved through multi-proxy analyses of five sediment cores, swath bathymetry data and high-resolution seismic data. The results of these analyses are used to:

- establish seismo- and lithostratigraphies for the study area, based on this
- investigate sedimentary processes with particular focus on
- submarine mass movements, their processes and chronologies and triggering mechanisms

1.2 Background

Rock avalanches and related tsunamis are among the largest threats to society in Norway (Blikra *et al*., 2006a). Fjords surrounded with steep mountains are characteristic features of the Norwegian landscape. The high and steep topographic relief of the Norwegian fjords makes them prone to rock avalanches generating waves of considerable height (Blikra *et al.*, 2006a). Due to the possibility of rock avalanches generating tsunamis, such events will not only affect the areas in direct reach of the avalanche, but the whole fjord system (Blikra *et al.*, 2006a; Hermanns *et al.*, 2013).

The approximately 80 km long Lyngen- and Storfjorden system is located in Troms County, northern Norway. The fjord is surrounded by an alpine landscape, where some of the mountains exceed 1500 m in altitude. Nordnesfjellet, which is an approximately 700 m high mountain located on the eastern shore of Lyngenfjorden, shows indications of unstable rock masses (Blikra & Bunkholt, 2012). Rock avalanches from Nordnesfjellet are predicted to generate tsunami waves in the fjord below. In the case of such a scenario, most of the low-lying areas in the municipalities of Storfjorden, Lyngen, Kåfjord, and maybe even Nordreisa, would be affected (NNFO, 2014). In a report from the Norwegian Geological Institute (NGI), by Glimsdal and Harbitz (2008), diverse tsunami outcomes are presented based on different scenarios of rock avalanches from Nordnesfjellet. The results are given with some uncertainty due to the complexity of rock avalanches and the subsequent waves, as well is the likelihood for the different scenarios not quantified.

Unstable rock masses have been documented several places along the mountainside, where the largest movements are located within the northern part of the mountain, in Jettan (Blikra & Bunkholt, 2012). Movement measurements from Jettan show that 5-9 m^3 of rock move as much as 5 cm/year, and it is suggested that movement in this area affects up to a total of 12- 22 x 10^6 m^3 of rock. The upper part of the area consists of 1-10 m wide and 1-10 m deep open fractures (Christiansen & Blikra, 2010), where some cracks clearly indicate that there has been movement during the past few years (NNFO, 2014).

Actually, observations suggest a weak acceleration in the degree of movement during the last few years in some parts of the unstable rock masses (Blikra *et al*., 2009). In the inner part of Nordnes (Indre Nordnes) the annual rock movement is measured to be substantially less, only a few mm per year (Blikra *et al.,* 2009), affecting an area of 3.5 – 6 x 10^6 m^3 (Blikra & Bunkholt, 2012). Unstable areas along this eastern side of the fjord have also been mapped by the Norwegian Geological Survey (NGU) to occur along the inner part of the fjord, Storfjorden (Blikra &Bunkholt, 2012).

The dramatic prospects for an eventual rock avalanche in this area claim extensive displacement measurements of the unstable rock masses in order to predict these events. Therefore, the areas of Inner Nordnes and Jettan, the last in a larger extent, are sites of intense investigations (NNFO, 2014). Monitoring is carried out by GPS surveys, crackmeters, tiltmeter and lasers (Christiansen & Blikra, 2010). Several thermal measurements, conducted during the International Polar Year 2007 to 2009, suggest that frost and permafrost also affect the stability of the rock masses (Christiansen & Blikra, 2010). The link between the recorded deformations and freezing and/or permafrost is believed to explain the documented seasonal variations of the displacements (Nordvik *et al.*, 2010)

Rock avalanches into fjords represent an indubitably hazard to humans in Norway. Given those perspectives it is important to be able to evaluate the background hazard levels. During the last years a selection of fjords has been mapped by swath bathymetry and reflection-seismic net in order to identify rock avalanche deposits (Blikra *et al.,* 2006a). A wide variety of features mirror rock avalanches plunging into fjords. Characteristic for the proximal parts are bouldery fans, lobes and ridges, while thin debris-flow deposits often occur far beyond that zone. A common effect of the rock masses is great deformation of the fjord sediments (Blikra *et al.,* 2006a). Preliminary results of acoustic and core data reveal mass-transport deposits on the seafloor and in the sub-seafloor off Nordnesfjellet. A large number of rock avalanches has been recorded in Troms County, but most of these have been dated back to a short period around the Younger Dryas period (13,000 – 11,500 calendar years BP) (Blikra *et al.,* 2006a).

In Lyngen, only one historical event has been documented: a rock avalanche in 1810 from Pollfjellet, a mountain located on the western shore of Lyngenfjorden, which reached the fjord (Blikra *et al.,* 2006a; Blikra *et al.,* 2006b). From historical reports it is known that the rock masses generated a tsunami when they plunged into the fjord. The wave tore away three farms and killed 14 people in Lyngsdalen, and is described to have reached places with great distance beyond the landslide (Blikra *et al.,* 2006b).

In this thesis, particular focus has been given to the investigation of mass-transported deposits on the seafloor and in the sub-seafloor off Nordnesfjellet in order to identify processes of sediment reworking, source areas and triggering mechanisms. The main focus has been to establish a chronology of mass wasting in the area. These results will complement ongoing investigations at the Nordnesfjellet and help to evaluate the risk of landslides in the future.

2 Study Area

2.1 Physiographic Setting

The study area is located in the Lyngen- and Storfjorden system in the northern part of Troms County, northern Norway (Fig. 2.1). The approximately 80 km long fjord system has a NNE-SSW orientation and is located between 69°16' – 70°00' N and 19°55' – 20°30 E. Storfjorden, a southern NE-SW oriented branch, merges into Lyngenfjorden just south for the Skibotndalen outlet. Further north a SE-NW fjord arm, Kåfjorden, branches off Lyngenfjorden. The three islands, Arnøy, Uløy and Vorterøya, define the eastern side of Lyngenfjorden in the outermost areas. An alpine landscape with steep mountains and valleys surrounds the fjord system (Fig. 2.1b).

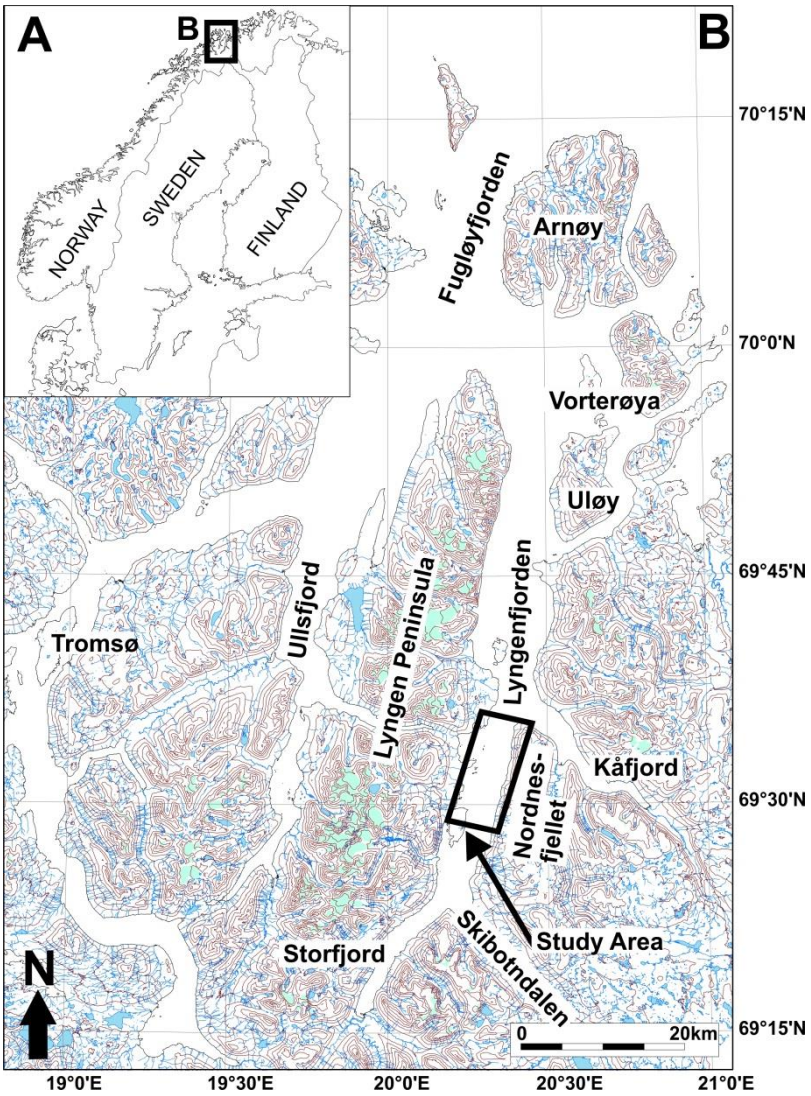

Figure 2.1:
a) *Overview map of Scandinavia and location of map B.*

b) *Map showing Lyngenfjorden and adjacent areas. The box shows the location of the study area.*

The area of focus in this thesis is the central part of the fjord system, the southernmost area of Lyngenfjorden, just south for the Kåfjorden branch. This part of the fjord is located directly off Nordnesfjellet (Fig. 2.1).

2.2 Bedrock Geology and Tectonics

The bedrock in Troms County comprises Precambrian rocks, Caledonian rocks, Post-Caledonian elements and postglacial elements.

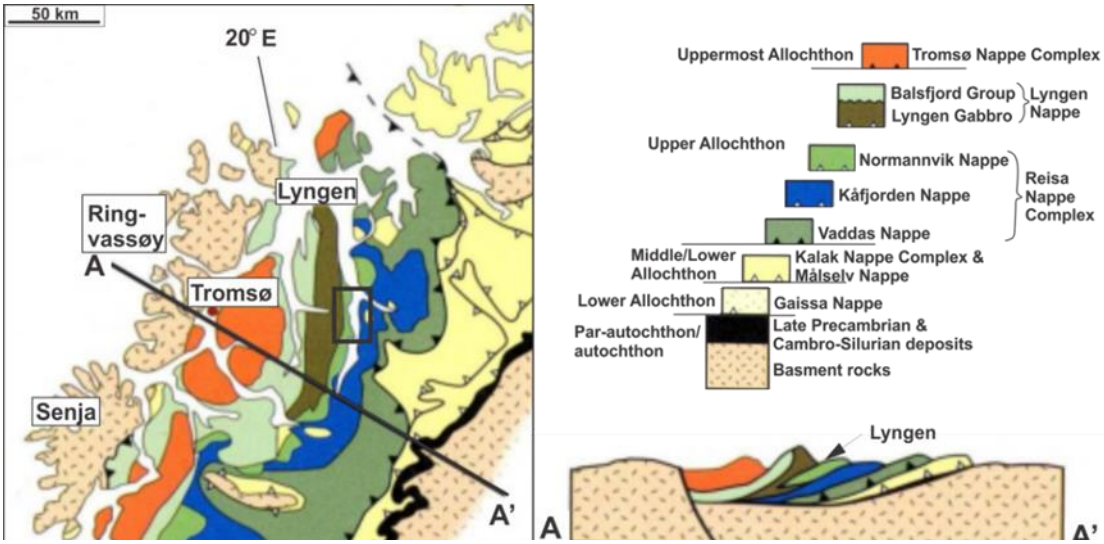

Figure 2.2: *Map of the bedrock geology of Troms County, where colour codes indicate the different sequences. The line AA' shows the position of the profile view of the bedrock sequences. The black box gives an approximately location of the study area. (Modified from Fossen et al., 2007)*

2.2.1 Precambrian Rocks

Precambrian rocks are today only exposed on the coast of western Troms County, and in the Sørkjosen- and Kvænangen-Alta tectonic window (Fig. 2.2). These areas are composed of Archean gneiss, and volcanic and sedimentary supracrustal rocks of Archean to Early-Proterozoic age (Zwaan, 1988).

2.2.2 Caledonian Rocks

Caledonian nappes characterise the majority of bedrock geology in Troms County. These were emplaced upon the Precambrian basement in Early- to Mid-Palaeozoic time as a result of the closure of the Iapetus Ocean. During the Caledonian orogeny, series of flat-lying NE-SW striking nappes were pushed upon the Baltoscandian platform from NE (Andresen, 1988; Zwaan, 1988; Fossen *et al.*, 2007). The different nappes represent different degrees of displacement and metamorphism, and are categorized into four main groups (from east to west): Lower, Middle, Upper and Uppermost Allochthons, characterised by an upward increase in degree of metamorphism (e.g. Roberts & Gee, 1985; Roberts, 2002; Fossen *et al.*, 2006; Rey *et al.*, 1997). The Caledonian nappes have a high diversity in origins. The Lower and Middle Allochthons are indigenous to the Baltoscandian margin, and constitute shelf and continental rise successions. The rocks of the Upper Allochthon are more diverse in composition, but mainly comprise oceanic crust (ophiolitic) and island arc sequences from the Iapetus Ocean. The Uppermost Allochthon has the most exotic character as it is interpreted to be

derived from the eastern margin of the Laurentian Plate or possible micro-continents (e.g. Roberts, 2002; Fossen *et al.,* 2007).

The Caledonian nappes are represented by three different units in the northern part of Troms County: the Kalak Nappe Complex (Middle Allochthon), the Reisa Nappe Complex (Upper Allochthon) and the Lyngen Nappe (Upper Allochthon) (Andresen, 1988; Zwaan, 1988) (Fig. 2.2).

The Kalak Nappe Complex is exposed on the eastern side of the Lyngen- and Storfjorden system (Fig. 2.2). The nappe complex comprises 8 nappes or thrust sheets, which all mainly consist of deformed arkoses and basement rocks (Andresen, 1988; Zwaan, 1988).

The Reisa Nappe Complex is exposed on both sides of the Lyngen- and Storfjorden system (Fig. 2.2). The complex comprises the Vaddas Terrane, the Kåfjord Nappe and the Nordmannvik Nappe (Andresen, 1988; Zwaan, 1988). The Vaddas Terrane consists of layered volcanic and sedimentary rocks (Zwaan, 1988). The Kåfjorden Nappe can be divided into two units, which both show a higher metamorphic grade than the Vaddas Terrane. The lowermost 400 m represents a zone consisting of blastomylonites, while calcite marbles and hornblende schist, as well as garnet mica schist, are found within the upper part of the nappe (Zwaan, 1988). The Nordmannvik Nappe lies above the Kåfjorden Nappe, and their boundary is represented by mica schist with blastomylonitic structure. The Nordmannvik Nappe consists of magmatic mica schist layered with thick layers of calcite marble and dolomite. The upper boundary of the unit is characterized by cataclastic deformed blastomylonites (Zwaan, 1988)

The Lyngen Nappe is suggested to represent a composite terrane (Fig. 2.2). It is usually divided into the Balsfjord Group and the Lyngen Gabbro, where the latter is the most eastern unit and makes up most of the Lyngen peninsula (Andresen, 1988). The Balsfjord Group consist of sediments once deposited on land and in shallow seas. The Lyngen Gabbro consists of greenstone, green schist, gabbro, ultramafic rocks and younger tonalitic rocks, which is assumed to be derived from oceanic crust (Zwaan, 1988)

2.2.3 Post-Caledonian Elements

An era of extensional tectonics followed the Caledonian orogeny, and caused the opening of the Atlantic Ocean and development of the Norwegian passive continental margin (Fossen *et al.,* 2007). Studies from the Lofoten-Vesterålen Margin suggest that several phases of extension forces have resulted in different fault systems which can be tracked both onshore and offshore (Bergh *et al.,* 2007; Hansen, 2009). Mapping of the Post-Caledonian structures in this region suggests that Mesozoic-Cenozoic rifting occurred in the Early Triassic, Mid/Late Jurassic and Early Cretaceous as a result of WNW-ESE oriented extension tectonics. While later rifting, in latest Cretaceous to Paleogene, occurred due to NNW-SSE oriented extension forces (Hansen, 2009). The correlated onshore

structures are found to have an N-S to NNE-SSW and NE-SW to E-W orientation, with subordinated NW-SE striking faults (Hansen, 2009).

The Lyngen- and Storfjorden system follows a graben structure. The graben is bounded on the eastern side of the fjord to a NNE-SSW oriented active normal fault with a WNW dip, and on the western side to an active normal fault with the same orientation but with an ESE dip (Hansen, 2009; Osmundsen *et al.*, 2009) (Fig. 2.3). The unique landscape of the Lyngen peninsula, compared to the surrounding areas, is suggested to be due to a tectonic uplift of the area. The Lyngen peninsula has a characteristic landscape which is densely incised and where only remnants of the paleosurface are preserved on the highest peaks. On the eastern side, the geomorphic contrast is clear. Here, the landscape is much gentler with more widely spaced glacial valleys (Hansen, 2009; Osmundsen *et al.*, 2009). Osmundsen *et al.* (2009) suggests that active normal faults control both the distribution of landscape and rock-slope failures in the Lyngen area. Work performed by Randall (1961) concludes that also the valleys of the region are structurally controlled. Several of the valleys entering the Lyngen- and Storfjorden system, e.g. Skibotndalen, Kitdalen, Signaldalen, as well as Kåfjorden, show a NW-SE to N-S orientation (Hansen, 2009) (Fig. 2.3).

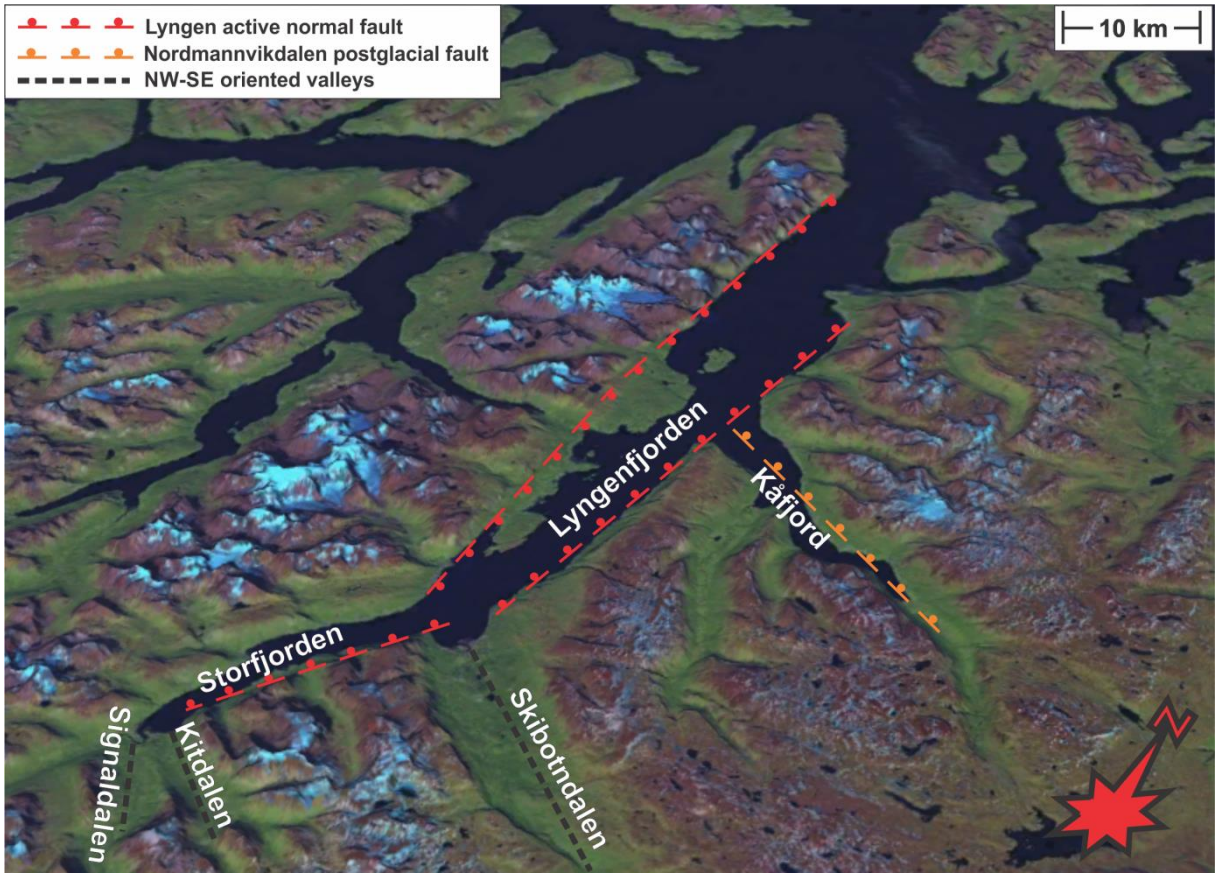

Figure 2.3: *Map displaying both post-Caledonian and postglacial elements found adjacent to the study area. The red stippled line represents the NNE-SSW oriented Lyngen active normal faults. The orange stippled line gives the position of the NW-SE striking Nordmannvikdalen postglacial fault. The dots on the stippled lines indicate the dip of the faults. The black stippled lines show the location of some of the NW-SE oriented, structurally controlled, valleys in the region.*

2.2.4 Postglacial Elements

Two postglacial faults have been documented in northern Norway; the NE-SW oriented, reverse Stuoragurra Fault in western Finnmark and the NW-SE striking, normal Nordmannvikdalen fault in the northern part of Troms County (Olesen *et al.*, 2004). The Nordmannvikdalen fault is located in the northern part of the Lyngen- and Storfjorden system, on the eastern side of the fjord, where it runs parallel to Kåfjorden with a NE dip (Fig. 2.3). The fault is suggested to be perpendicular to an extensive system of NE-SW trending reverse faults in northern Fennoscandia (Dehls *et al.*, 2000). On the NW slope of Nordmannvikdalen it is possible to observe that the fault offsets till, thus it is evident that this fault has been active during postglacial times (Dehls *et al.*, 2000).

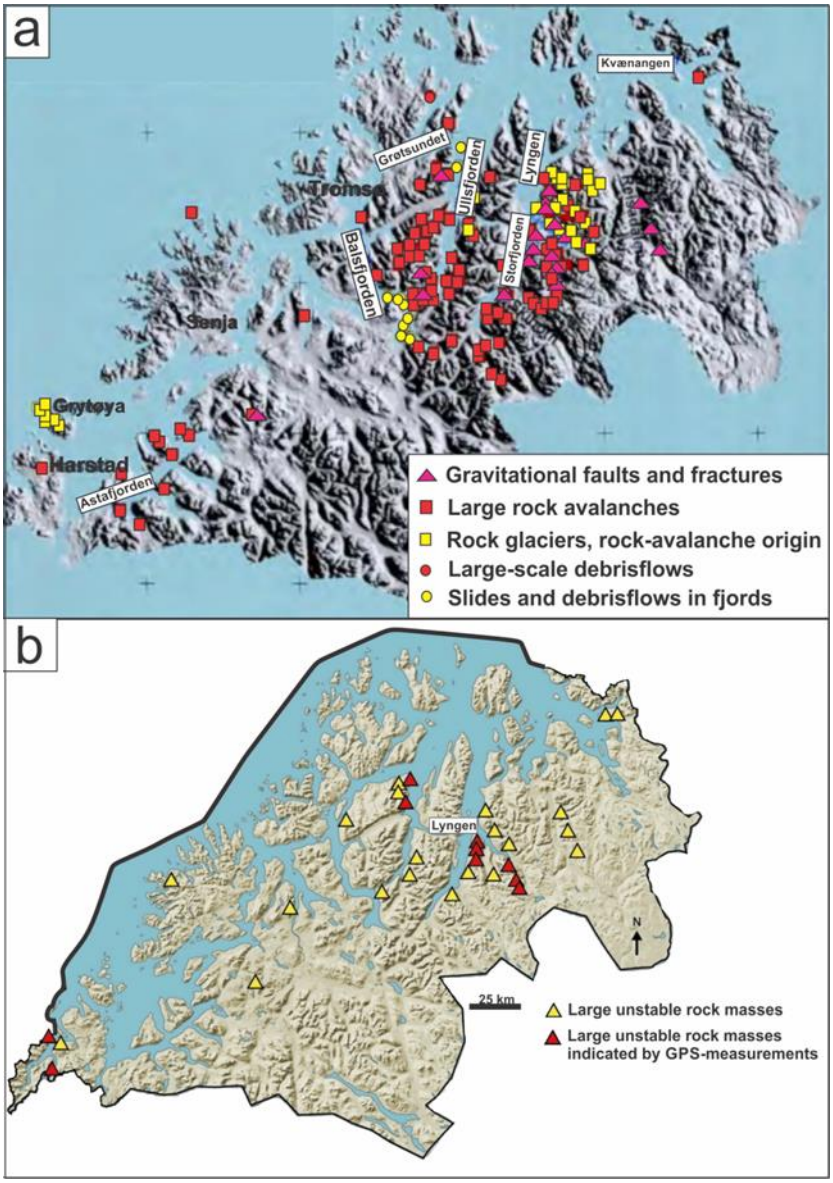

Figure 2.4: **a)** *Distribution of gravitational-slope failures in Troms County (Modified from Blikra&Longva, 2000).* **b)** *Distribution of unstable rock masses in Troms County today (Modified from Vorren et al., 2007)*

The faulting in northern Fennoscandia is closely related to the stress caused by post-glacial isostatic uplift. A high number of rock avalanche events have been documented in the Kåfjorden and Storfjorden areas (Fig. 2.4a), where large faults and crevasses indicate several large-scale gravitational features (Dehls *et al.,* 2000). The gravitational features mapped on Nordnesfjellet cover a larger area. Here, faults or crevasses are located on a relatively flat plateau, and parts of the gravitational faulting are interpreted to have started before 11,000 ^{14}C yr BP. The size and the large horizontal displacement of the area indicate that the trigger mechanism most likely was a large-scale earthquake (Dehls *et al.,* 2000). Rock-avalanche events in the region show a consistency in age indicating a palaeoseismic controller. Two periods of major earthquakes (order of $\geq$ 6.0) due to the stresses following the postglacial uplift have been suggested: one before 11,000 ^{14}C years BP and one between 10,000 and 9500 years BP. The Nordmannvikdalen postglacial fault is believed to have been active during the latter period. The seismic events probably explain the high number of rock avalanches in the region (Dehls *et al.,* 2000; Vorren *et al.,* 2007). Unstable rock masses found in this region today indicate that the area still is subjected to gravitational failures (Fig. 2.4b)

2.3 Glaciation- and Deglaciation History

2.3.1 Glaciation

The Norwegian landscape as we know it today is a product of repeated glaciations. The main morphologies are a result of hundreds of million years of geological evolution, but the glaciers of the latest period have modified these landforms. As glaciers move over an area, they scour the landscape and carve out the landforms. Pre-existing river channels, bedrock boundaries, fault zones, and general weakness within rocks, have been especially prone to erosion, whereas harder rocks, e.g. the gabbro of the high mountains of Lyngen, have been more resistant (Sveian, 2004).

A fjord is defined by Syvitski *et al.,* 1987, as a deep, high latitude estuary, which has been (or presently being) excavated or modified by land-based ice. The landscape of the Lyngen peninsula is also a typical glacial landform. Here, protracted glacial erosion, mainly from local cirque glaciers, has formed characteristic horns, cirques and arêtes (e.g. Corner, 2005b). It is believed that the formation of local glaciers started prior to Quaternary time, and that these glaciers were permanent in the highest areas throughout the period (Sveian, 2004; Vorren & Mangerud, 2007). This was probably the case in Lyngen as well, where remaining glaciers today still erode and modify the landscape. The cirque glaciers accumulated in the colder periods, and during the greater glaciations, merged with the continental ice-sheet which expanded to this area from the east. The sharp mountain peaks of this region have been preserved as they were exposed as nunatakes, reaching higher than the ice-sheets (Sveian, 2004).

Glacial ice is an active agent of erosion. During each new glaciation glacier products from former glaciations, as well as post-glacial deposits, are modified or totally removed both in terrestrial and marine settings. The last glaciation, Weichselian c. 118,000 to 11,500 years ago, is therefore particularly important for the morphology of the study area today (Sveian, 2004; Nesje, 2012). The Last Glacial Maximum (LGM) reached between c. 25,000 to 18,000 years ago (Vorren & Mangerud, 2007). During this time, the ice shield covered almost all of Scandinavia, and reached the shelf edge where it deposited great amounts of sediments (Jørgensen *et al.*, 1997; Vorren & Mangerud, 2007) (Fig. 2.5). Fjords in Troms County, e.g. Lyngenfjorden, served as main drainage pathways for the continental ice shield when they were covered by fast-flowing ice streams that extended to the shelf edge (Sveian & Corner, 2004).

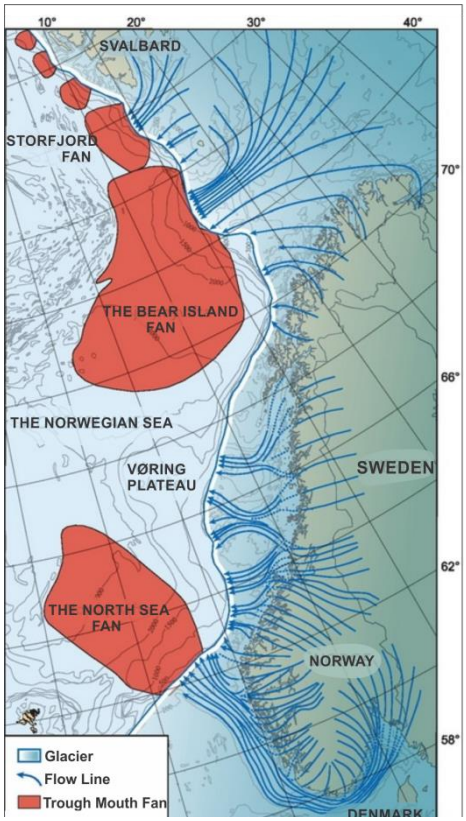

Figure 2.5: *Ice extent during the LGM. Note the large trough mouth fans deposited in front of ice streams, these have probably accumulated through several glaciations (Modified from Vorren & Mangerud, 2007)*

2.3.2 Deglaciation

A climatic warming caused the retreat of the ice shield from the shelf edge. However, ice ablation was not a continuous process, and repeated glacier re-advances led to the deposition of prominent moraines (e.g. Vorren & Plassen, 2002). Several marginal moraines revealing the retreat pattern during the last deglaciation were identified in the study area (Corner, 1980; Sveian & Corner, 2004; Donner, 1995) (Fig. 2.6)

During the first period of the glacial retreat, the ice shield withdrew from the shelf edge to the outer coast areas, and later in to the fjords. Moraines from two major glacial re-advances have been described regionally in Troms County. The Skarpnes event, which is probably due to two glacial advances (Jørgensen *et al.,* 1997), occurred during a colder period in the Older Dryas for approx. 14,000 years ago (Lysså & Vorren, 1997; Sveian & Corner, 2004). The following glacial re-advance in the early Younger Dryas resulted in the largest and best developed moraines, which can be observed in every fjord district (Andersen *et al.,* 1995). In Troms County these moraines represent the Tromsø-Lyngen event which occurred for about 12,800 – 11,500 years ago (Lysså & Vorren, 1997; Sveian & Corner, 2004). The marginal moraines originating from these two re-advances are closely spaced, some places both can be observed within a few kilometres (Vorren & Mangerud, 2007). The marginal moraines from both the Skarpnes event and the Tromsø – Lyngen event can be observed in Lyngen (Lysså & Vorren, 1997; Sveian & Corner, 2004) (Fig. 2.6). From Spåkneset, located in the outer part of Lyngenfjorden, a spit of land extends far out in the eastern part of the fjord and represents the glacial maximum 12,500 years ago (Sveian & Corner, 2004). Observations of lateral moraines along the eastern side of the fjord indicate that the glacier reached even further out into the fjord for a shorter period, which probably could be correlated to a smaller ridge located approximately 1 km beyond the main moraine in the fjord (Sveian & Corner, 2004). Moraine material also builds up a smaller cape to the south of Spåkneset, and a SW oriented ridge can be followed out into the fjord where it follows a distinct threshold on the fjord bottom (Sveian & Corner, 2004). Three to four major and several small, or uncertain, ice-front accumulations can be observed proximal to the Tromsø – Lyngen moraine in the area of Storfjord, Kåfjord and Lyngen. Corner (1980) correlated the moraines on the basis of marine limits and glaciogeological evidence, and suggests that they represent local glacial re-advances which occurred during Preboreal time. The moraines indicate two major, and probably one minor event; the Ørnes event, c. 9800 - 9900 ± 150 ^{14}C years BP, the Skibotn event, c.9500 – 9600 ± 150 ^{14}C years BP, and the later event, c. 9400 ± 250 ^{14}C years BP (Corner, 1980).

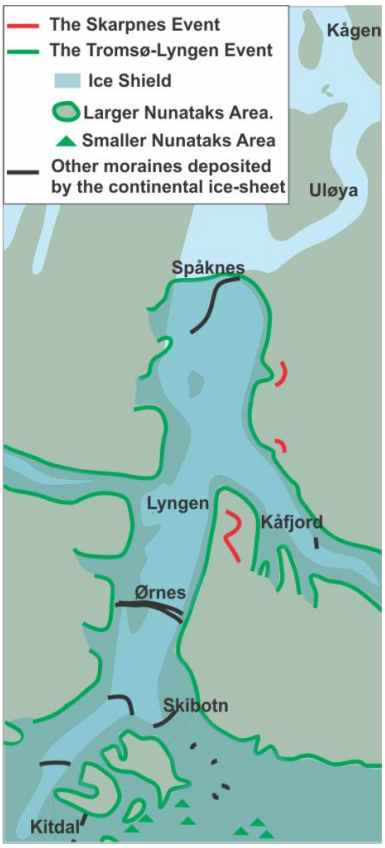

Figure 2.6: *Map showing marginal moraines indicating the extent of the ice sheet during the Skarpnes and Tromsø-Lyngen event in the region of the study area. Other registered marginal moraines, as well as nunatakes areas, are indicated (After Sveian & Corner, 2004)*

After the retreat of the continental ice-sheet from the Lyngen area, about 10,000 years ago, the local, smaller glaciers also responded to the increasingly warmer climate. Hardly any of the glaciers in Lyngen survived the climatic conditions in the period 9000 – 3000 years ago (Sveian & Corner, 2004). In response to a climatic change about 3000 years ago, local glaciers started to build up again in the highest areas. Most of these new glaciers reached their maximum extent during the cold period referred to as the Little Ice Age (1750 – 1920). Large moraine ridges, up to several hundreds of meters in front of today's glaciers, were deposited as a result to this glacial advance (Karlén, 1988; Jørgensen *et al.*, 1997; Bakke *et al.*, 2005; Sveian & Corner, 2004; Vorren *et al.*, 2007; Nesje, 2012). In Lyngen the most prominent ridges originate from the years 1750, 1850 and 1920 (Sveian & Corner, 2004). From the end of Little Ice Age maximum and until today, the Norwegian glaciers have been retreating. At present approximately 140 minor and smaller glaciers covers an area of about 100 km^2 in the Lyngenalps (Sveian & Corner, 2004).

The landscape exposed after the last glaciation was in an unstable or metastable phase, and thus particularly exposed to modification at high denudation rates (Ballantyne, 2002). Glacially steepened rock walls and slopes were sites of mass reworking. Glacier forelands would be exposed to wind erosion and frost action, and rivers redistributed large amounts of the unconsolidated glaciogenic sediments into terrestrial, lacustrine and marine sediment sinks (Ballantyne, 2002).

2.3.3 Postglacial uplift

The postglacial uplift in Fennoscandia is a direct response to the deglaciation after the LGM. The additional weight added from the massive ice-sheets during the last glaciation caused depression in the Earth's elastic crust. The rate of glacial isostatic uplift is a factor of the thickness of the ice, meaning that areas once covered with greatest ice masses experienced the largest rate of uplift (Vorren *et al.*, 2007). In Norway, this resulted in an uneven uplift, where the rate of uplift successively increased from the coast towards the inland (Jørgensen *et al.*, 1997) (Fig. 2.7).

Isostatic rebound is still an active process in Fennoscandia. The region shows much higher seismicity than what is expected for an interior plate region, e.g. today's uplift rate of the coast of northern Norway is within the order 1.0 mm/yr (Fjeldskaar *et al.*, 2000). One suggested explanation is that these areas, in addition to the glacial isostatic uplift, have a weak tectonic uplift component (Fjeldskaar *et al.*, 2000). The pattern of the seismicity in Scandinavia does not correlate with the current uplift rates, but can be seen as the result of a tilting of Norway and Sweden due to ridge push (Dehls *et al.*, 2000). Fjeldskaar *et al.* (2000) conclude that the stresses in western Scandinavia are controlled by both postglacial uplift and ridge push. See Chapter 2.2.4 for details on the postglacial seismicity and structures connected to the area studied in this thesis.

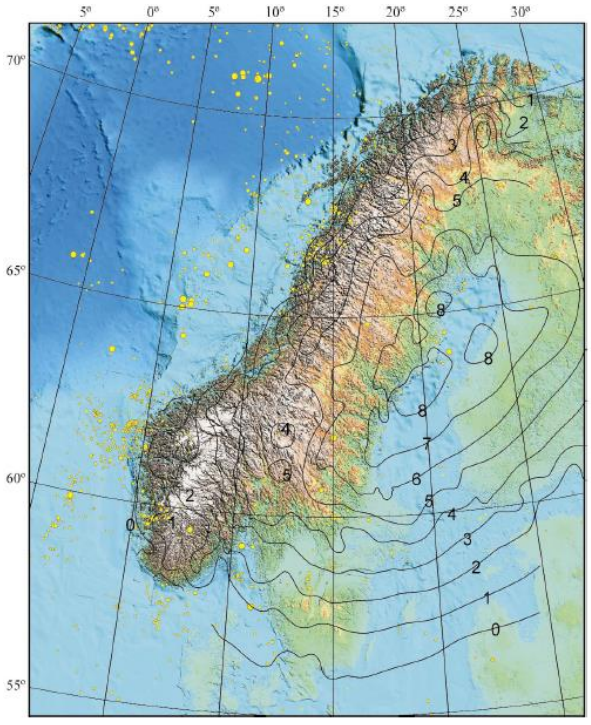

Figure 2.7: *Map showing the current apparent uplift (in mm/yr). The yellow circles represents locations of earthquakes with magnitude greater than 3.0 since 1965 (Dehls et al., 2000).*

2.3.4 Sea Level Fluctuations and Shore Lines

When the ice shield started its retreat after the last glacial maximum, sea level started to rise and reached a much higher elevation than observed today. The marine limit (ML) refers to the maximum sea level after the LGM at a given site, and is a product of both eustatic and isostatic changes. At the end of the last glacial the land areas were still compressed due to the heavy weight of the ice-cover, and a transgression was caused by release of melt water to the oceans from the melting glaciers. In the following period the isostatic changes transcended the eustatic changes, even though the global sea level increased by 120 m, and the coast of Norway experienced a regression (Jørgensen *et al.*, 1997; Sveian *et al.,* 2004). The elevation of the ML varies depending on the rate of isostatic uplift. In the inner parts of Troms County it is about 8 metres above sea level (m a.s.l) compared to about 30 m a.s.l. in the outer coastal areas (Sveian *et al.*, 2004). Marine erosion terraces, notches and ice-front deltas are useful morphological features for locating earlier MLs in Troms County. The ML in the study area is approximately 80 m a.s.l. (Corner, 1980).

There are two distinct shorelines in Troms County; the Main and the Tapes shoreline. The Main shoreline was formed during a relatively stable sea-level in the early Younger Dryas, and is correlated to the Tromsø – Lyngen event (e.g. Andersen, 1968; Jørgensen *et al.*, 1997; Sveian *et al.*, 2004; Bergstrøm *et al.*, 2005; Vorren *et al.*, 2007). The Main shoreline is often represented by broad bedrock terraces, supporting the theory of minimal sea-level fluctuations during its time of formation (Andersen, 1968). The Tapes shoreline originates from the postglacial warm period (about 9500 - 6500 years ago), Tapes time (e.g. Andersen, 1968; Jørgensen *et al.,* 1997; Sveian *et al.,* 2004; Vorren *et al.*, 2007). It is found as a complex of shorelines (Andersen, 1968), and represents a transgression due to equalization of the isostatic uplift from the eustatic sea-level (Jørgensen *et al.*, 1997; Sveian *et al.*, 2004; Vorren *et al.*, 2007). Moreover it is possible to observe shorelines that correspond to the Skarpnes event, which lie approximately 7 – 10 m above the Main shoreline at the Skarpnes moraines. However, no distinct shorelines exist between the Main shoreline and the shoreline representing the Skarpnes moraines (Andersen, 1968).

2.4 Geomorphology of fjords

2.4.1 General view

The origin of fjords can be faults, lithology-controlled or fluvial eroded troughs, which have been further excavated by glaciers (Howe *et al.*, 2010). The geomorphology of a given fjord is the result of local geological conditions, climate, glacial and postglacial history (Syvitski *et al.*, 1987).

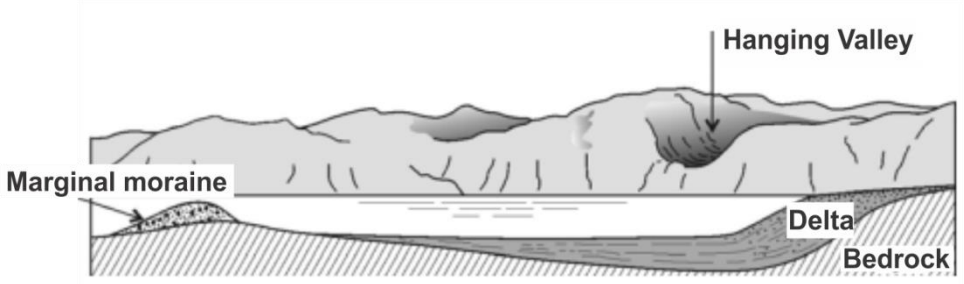

Figure 2.8: *Schematic profile along fjord (Dahl, 1989).*

Fjords are typically found as long, narrow, deep and steep sided inlets penetrating mountainous land areas (Fig. 2.8). The direction and shape of a fjord, as well as possible branches, is often determined by geological structures such as fault zones, igneous dykes, sills, plutons and variations in the composition of the bedrock. E.g. if the ice follows major fault zones, the resulting fjord can be observed as remarkably straight, either in whole or in parts (Syvitski *et al.*, 1987). Fjords can often be regarded as semi-enclosed inlets as they commonly comprise a relatively shallow threshold at their mouths (Fig. 2.8). In addition to the sill located at the fjord mouth, which defines its outer limit, additional submarine sills are typically observed separating overdeepened basins (Syvitski *et al.*, 1987; Corner, 2006). The head of the fjord often terminates into a delta formed by a river running through a U-shaped valley. These valleys must be seen as a synonymous feature to the fjord, where the only difference being that the fjord would be submerged. Fjords can also end more abrupt in a relatively steep headwall (Syvitski *et al.*, 1987; Corner, 2005a). The inner part of a fjord is typically narrower compared to its outer reaches, where it broadens and commonly separates into different fjord-arms. Additionally, fjords typically deepen outwards as they are joined by fjord branches (Corner, 2005a).

2.4.2 Lyngenfjorden

Four main thresholds are found within the Lyngen- and Storfjorden system, separating the fjord into four main basins (Jenssen, 2006). The thresholds are composed of both bedrock and glaciogenic material, where the latter represent marginal moraine deposits (Corner, 1980; Mellem, 1991; Lyså & Vorren; 1997). The basins are found to be shallowest proximal to the thresholds with a depth increasing distally, which is probably due to the glacier margin being the main sediment source (Jenssen, 2006). Today the main sediment input is from rivers, which can explain the why the fjord is shallower in

The greatest depth of 340 m occurs in the northernmost basin (Basin I, Fig. 2.9). The shallowest areas only have a water depth of ~20 m, this applies to the area between the two northernmost basins (threshold T2) and the inner part of the southernmost basin (basin IV) (Jenssen, 2006). In the two central basins (Basin II & III) it is possible to correlate the widest parts with the valley outlets, which was the areas where the Storfjord glacier merged with the Skibotndalen and Kåfjord glaciers (Jenssen, 2006).

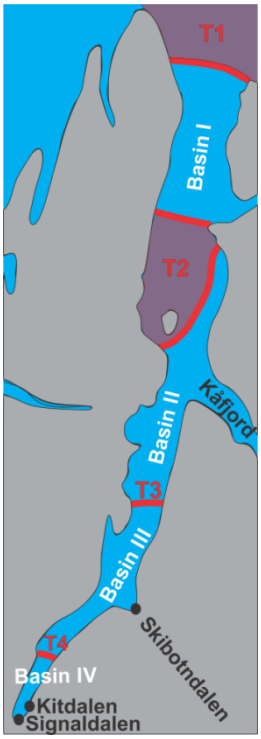

Figure 2.9: *The main thresholds (T) and basins found within the Lyngen- and Storfjorden system.*

2.5 Sedimentary processes and products within fjords

2.5.1 General view

Aarseth (1997) describes fjords as large depocentres, where large amounts of sediments accumulate during interglacials and are redistribuated during glacials. Corner (2006) divides the sediment infilling into two successive stages. During deglaciation the glacier and melt water deposit sediment at and beyond the retreating glacier margin. During halts of tidewater-glacier the deposition of till, glaciofluvial sand and gravel occurs at, or close to, the calving or the grounding line. Finer sediments are kept in suspension and deposited at greater distance to this margin (Corner, 2006). As the glacier retreats into the valley, glacier-fed rivers deposit sand and gravel at the head of the fjord, while finer sediments are transported away in suspension (Corner, 2006). During the following postglacial stage, river transported and remobilized glacigenic sediments, as well as terrace sediments, account for the main sediment supply (Fig. 2.10). The supply at this stage is typically lower than during the deglaciation, but it can be efficient in the case of high sediment-filled valleys where uplift causes

incision (Corner, 2006). The result is a fjord morphology which typically comprises steep sided walls terminating into a relatively broad floor (Corner, 2006).

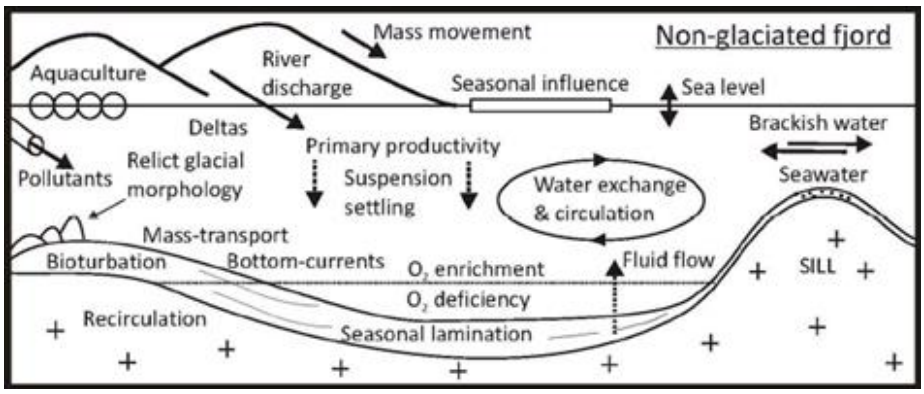

Figure 2.10: *Principle sketch of a non-glaciated fjord showing the sediment processes and deposits (Howe et al., 2010).*

As a direct consequence of their steep slopes and high sedimentation rates, fjords frequently experiences slope failures/landslide events. The occurrence of gravitational reworking, fluid flow and external triggers (e.g. earthquake) contribute to the high amount of different sediment deformations found within the fjord environments. Evidence of sediment slides, slumps and extensional/compressional deformation structures has been found in fjords worldwide (e.g. Stoker et al., 2010)

Lyngenfjorden is classified as a temperate fjord, i.e. a fjord were the formation of sea ice during winter is generally absent, but where some ice may occur e.g. off river mouths. Here, the main sediment supply is terrestrially derived material and mass wasting (Syvitski & Shaw, 1995) (Fig. 2.10). Deposition will occur at the outlet of rivers and streams, features such as deltas and river-derived fans can be produced at the slopes. From the delta-fronts and fans, channels can act as pathways for transporting sediments to the basins. The steep slopes will become areas of increased instability due to the large amount of sediment accumulation. As a result they are often the site of e.g. sediment creep, slides, debris flows and turbidity flows (Howe *et al.*, 2010).

The sediment distribution may reflect whether the fjord is located in the northern or southern hemisphere due to the Coriolis force, which deflects flows to the right in the northern and to the left in the southern hemisphere (e.g. Howe *et al.*, 2010).

2.5.2 Lyngenfjorden

Seismic data indicate that the sediments deposited within the fjord system mainly originate from glaciomarine sedimentary processes, and where the main part is interpreted to be ice proximal sediments deposited during the latest part of the deglaciation (Jenssen, 2006). However, the upper parts of the fjord basins is suggested to comprise postglacial deposition from suspension fall-out, as

well as reworked sediments derived both from the sides of the fjord and from the thresholds (Jenssen, 2006).

Jenssen (2006) describes an asymmetric fjord floor for the Lyngen- and Storfjorden system, where some areas along the fjord are found to be shallower on the eastern side than the western. This has been observed at the three thresholds within the fjord, at the outlet of Skibotn River and Kåfjorden, as well as in the innermost part of the fjord. All these areas are parts of the fjord where the sediment accumulation was/ is great. Jensen interprets the asymmetric accumulation within the fjord to be caused by the Coriolis Effect.

2.6 Climate

Climate has a large influence on fjord environments. The amount and type of precipitation, runoff and water temperature are directly derived from the climate conditions, which in turn will influence the estuarine circulation (Howe *et al.,* 2010). Weathering of rocks will increase the quantity of sediment input, while prevalence of vegetation in the catchment area will stabilize the sediments and lower the input (Howe *et al.,* 2010). Wind may have the capacity to transport large amounts of sediments, as well as affecting the water circulation (Syvitski *et al.,* 1987; Howe et al., 2010).

The Lyngen- and Storfjorden system is located in a region which exhibits arctic and periglacial conditions (Nordvik *et al.,* 2009). The arctic winters are commonly long and the summers are short, both with a low mean temperature. The mean annual precipitation in the coastal areas of Troms varies from 750 mm in the outer areas, to maximum 1000-1500 mm in the mountainous areas and minimum 300-600 mm in the sheltered valleys (Dannevig, 2009).

The climatic impact on the frost and permafrost conditions is sufficient for the stability of the rock masses in Nordnesfjellet (Nordvik *et al.,* 2009). The permafrost thermal state for the region has been documented through borehole data. These data show that the lower limit for the permafrost in the outer coastal areas is 800-900 m a.s.l, and 200 m less in the inner coastal areas of Troms County (Christiansen *et al.,* 2010)

2.7 Oceanography - Hydrography

2.7.1 Oceanography on the shelf off Troms County

There are two northward flowing currents along the western coast of Norway; The Norwegian Atlantic Current (NAC) and the Norwegian Coastal Current (NCC) (e.g. Johannessen, 1986; Hopkins, 1991, Ersdal, 2001) (Fig. 2.11a). These are both surface waters.

The NAC is one of the branches of the Gulf Stream and consists of Atlantic Water which enters through the Faroe-Shetland Channel (Fig. 2.11a) (e.g. Johannessen, 1986; Hopkins, 1991; Ersdal, 2001) (Fig. 2.11a). The temperature of the Norwegian Atlantic Water (NAW) is at least 2°C (Hopkins, 1991) and its salinity is >35‰, regardless of its temperature (Johannessen, 1986; Hopkins, 1991).

The NCC consists of Norwegian Coastal Water (NCW) extending as a wedge out from the shore and onto the NAW (Fig. 2.11b). The source of the NCW is the brackish outflow from the Baltic Sea, together with runoff from the Norwegian fjords and water along the western coast of Europe (Mork, 1981; Johannessen, 1986; Ersdal, 2001) (Fig. 2.11a). The salinity of the NCW is less than 35‰, and it decreases during summer (32‰) due to increased runoff from the fjords. The temperature of the water masses lies in the range 2-13°C (Hopkins, 1991).

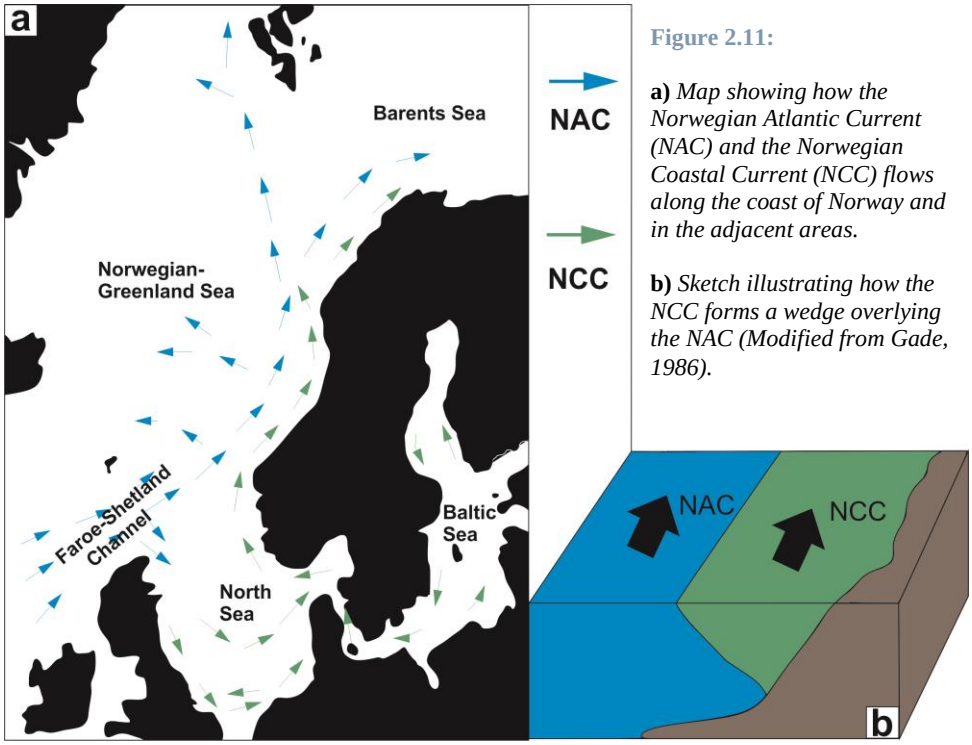

Figure 2.11:

a) *Map showing how the Norwegian Atlantic Current (NAC) and the Norwegian Coastal Current (NCC) flows along the coast of Norway and in the adjacent areas.*

b) *Sketch illustrating how the NCC forms a wedge overlying the NAC (Modified from Gade, 1986).*

The boundary between the NAW and NAC is the Norwegian Shelf Front (NSF), characterized by the salinity difference between the two water masses (Hopkins, 1991). The prevalence of the NCC wedge varies during the course of the year, where meteorological effects and fresh water fluxes seem to be the dominant controlling features (Sundby, 1976; Mork, 1981). The topography of the continental shelf, dominated by numerous, relatively small banks separated by troughs, influences the circulation of the NCC (Sundby, 1984; Bøe *et al.*, 2009).

2.7.2 Hydrography in fjords

2.7.2.1 A general view

The hydrography in fjords is influenced by both internal and external factors. Hydrodynamics are very variable, not only between different fjords, but also seasonally within a given fjord. The hydrodynamics strongly influence sediment settling and are essential for the accumulation of sediments derived from biogenic material (Howe *et al.*, 2010).

Fjords have been described as miniature oceans (e.g. Skei, 1983; Howe *et al.*, 2010), or as Gade (1986) describes them: "… large containers in which seawater remains for extended times." The water masses in a fjord are derived from both the ocean and from the land areas surrounding it. Fjords are semi-enclosed systems, often with a narrow connection to the open sea due to the occurrence of a sill at mouth. This affects the exchange of coastal and basin water between the ocean and the fjord (Skei, 1983; Howe *et al.*, 2010). Fjords can be compared with estuaries, also semi-enclosed, less saline miniature oceans, but they are generally much deeper than the normal tidal estuaries (Gade, 1986).

Fjords are often found to be well stratified, where the water masses can be considered to consist of three main layers; an estuarine, an intermediate and one bottom water layer (Fig. 2.12a). The stratification is the result of buoyancy forces of the fresh water input, and the degree of water exchange with coastal waters (Gade, 1986; Howe *et al.*, 2010). Gade (1986) gives the following description of the stratification; the estuarine layer (the brackish layer) is restricted to the uppermost 50 m of the water column, but often much shallower. Its thickness is dependent on the freshwater supply and the degree of mixture due to wind-stresses. The intermediate water masses are located below the estuarine layer. These water masses circulate with the ocean or shelf waters, and have a maximum depth controlled by the height of the sill at the fjord mouth. The basin water is located below the sill crest, and therefore remains mostly stagnant. However, exchanges with the shelf water occur occasionally.

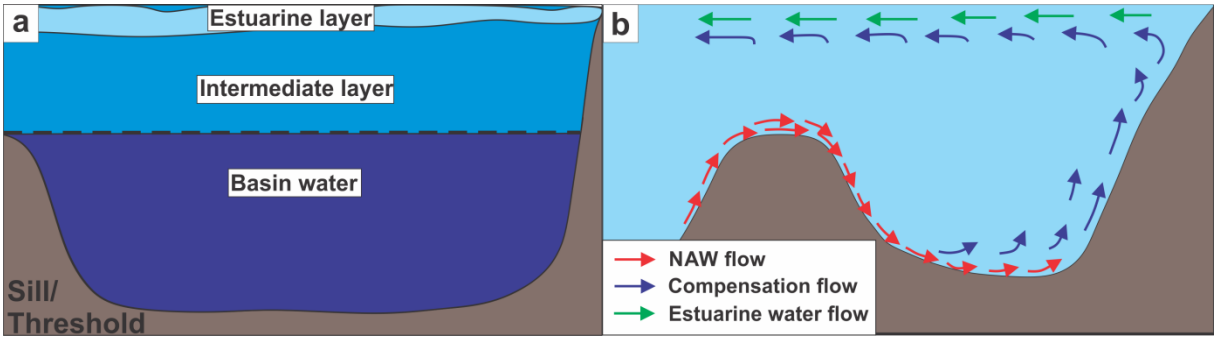

Figure 2.12: **a)** *Sketch illustrating the stratification of the water masses in a well stratified fjord (Modified from Gade, 1986)* **b)** *Sketch illustrating the circulation in a fjord basin. This figure exemplifies the circulation during spring and early summer, when the Norwegian Coastal Water flow across the sill (Modified from Gade, 1986).*

The stagnant basin water is typically oxygen and nutrient poor, and is mortal for biological and geochemical processes (Howe *et al.*, 2010). The degree of water flow between fjord basins and the coastal waters has fluctuated during time with changing sea level. In a smaller perspective water exchange can occur periodically or sporadically due to e.g. tides, the freshwater input, weather and season (Gade, 1986; Howe *et al.*, 2010).

2.7.2.2 Northern Norway in general, and in the Lyngen- and Storfjord system

The fjords in northern Norway are characterized by relatively high water temperatures. They are not significantly influenced by rivers and glaciers, and the amount of sea-ice during winter and spring is limited. However, they are influenced by the input of turbulent energy by tidal exchange and advection, and by coastal currents (Wassmann *et al*., 1995). The northern Norwegian fjords may show a rapid exchange of water masses between the coastal currents and the innermost fjords. Compared to other fjord systems, they are in a larger extent a part of the coastal currents (the NCC) (Syvitski *et al.*, 1987; Wassmann *et al.*, 1995).

The increased capability of water exchange between the fjords and the NCC and NAC in northern Norway could be explained by multiple influencing factors:

- The sill depths at the fjord mouths facilitate the connection between the fjords and the coastal waters (Wassmann *et al.*, 1995). The depth of the threshold at the mouth of the Lyngen- and Storfjorden system is approx. 200 – 300 m (Jenssen, 2006), which is adequate enough for a significant input of coastal water.
- Both the NAC and the NCC are narrow, deep and strong off the Lofoten islands, from where they follow the bathymetry of the north Norwegian coastal zone (Sundby, 1984). Pathways for the water masses into the fjords are found in troughs as extensions of the major fjords, along the shelf (Sundby, 1984). The coastal NAC and NCC enter the Lyngen- and Storfjorden system through a through separating the Nordvest and Fugløy banks, via Fugløyfjorden (Mareano, 2014; NGU, 2014).
- During summertime, from May until September, the NCW is concentrated in the uppermost 50-100m of the water column, and extends further out from the coast than during winter. In wintertime, the NCW can reach a depth of 200m (Sundby, 1976; Wassmann *et al.*, 1995). Seasonal north-westerly winds cause upwelling along the coast, which again changes the pressure field, with a result that the upper layer get flushed out of the main fjords (Sætre *et al.*, 1988; Svendsen, 1995). These seasonal lateral oscillations govern the differences in water exchange between the fjord basins and the coastal waters (Wassmann *et al.*, 1995). The upper boundary of the NAW will be highest during spring and early summer, an effect of the buoyancy differences and the upwelling, making it possible for the Atlantic water to flow into the fjords across their sills (Fig. 2.12b). The dense NAW will flow along the bottom of the

fjord, forcing the resident water up to the upperpart of the water column where it eventually will be flushed out (Gade, 1986). Aure (1983) suggests that coastal water flow through the inlet between Arnøy and Helgøy (Fig. 2.1b) all year round. In which case means that these water masses could be found at the mouth of the Lyngen- and Storfjorden system at all time.

The main freshwater source for all the north Norwegian fjords is rivers, where the amount of runoff changes seasonally. The maximum freshwater discharge takes place in early summer during snow melt, but could also be high in the autumn due to heavy rain (Wassmann *et al.*, 1995). As a result, the temperature and the salinity of the fjord and coastal waters show distinct seasonal variations, affecting the stratification and circulation pattern (Svendsen, 1995; Wassmann *et al.*, 1995). The maximum amount of stratification is in the period reaching from May/June to September. The largest freshwater discharge in most northern fjords occurs in their inner parts; this is reflected in the stratification of the upper layers which show an increasing tendency up-fjord (Wassmann *et al.*, 1995). Furthermore, the climate will vary along the longitudinal extension of the fjords, including the air temperature, wind and precipitation (Svendsen, 1995; Wassmann *et al.*, 1995).

The freshwater runoff into the Lyngen- and Storfjorden system, as for other north Norwegian fjords, is limited compared to fjord systems elsewhere. The main freshwater input sources are the Signaldalen and Skibotn rivers, whose outlets are located at the head of the fjord and in basin III respectively (Fig. 2.13). Skibotn River is the largest river entering the fjord, but the average annual water flow is only 19.88m^3/s (NVE, 2014). In addition, the fjord receives freshwater from several minor rivers located along the fjord, e.g. Kildal, Elsnes, Steindalen, Lyngsdalen and Strupbreen River, where the last three are glacially fed. The majority of the rivers have their output in the two innermost basins, while minimum freshwater runoff occurs in the outer basin.

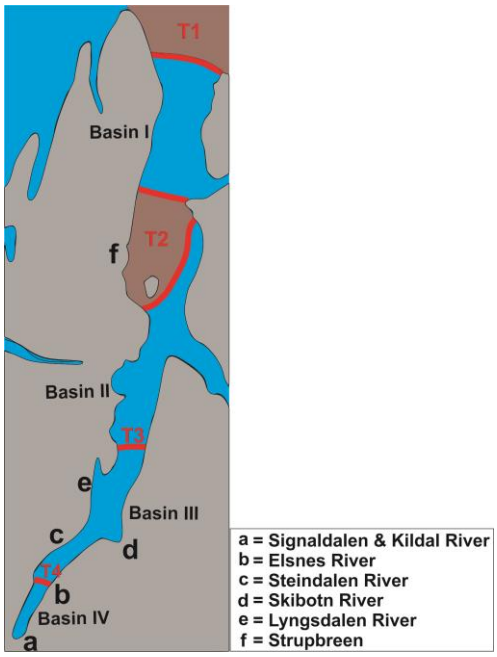

Figure 2.13: *The main rivers entering the Lyngen- and Storfjorden system. The main basins and thresholds (T) are also indicated.*

3 Materials and Methods

3.1 Swath bathymetry

The swath bathymetry data used in this study were collected on the 15th and 16th of October 2012, during an educational cruise arranged by the Department of Geology, University of Tromsø, on R/V Helmer Hanssen (Forwick & Rasmussen, 2012). The data were acquired using a hull-mounted Kongsberg Maritime Simrad EM 300 Multibeam echo sounder. Mulitbeam echo sounders are effective instruments used in order to investigate features on the seafloor, e.g. seabed shape, slope angles, type and distribution of sediment and rock (Carter, 2009). The instrument on R/V Helmer Hanssen has a nominal operational frequency of 30 kHz. It has a depth range from 10 to 5000 m, and its 135 beams have an angular coverage sector of 150°. In order to maximize the use of the beams, are the angular coverage sector and beam pointing angles variable with depth (Kongsberg Maritime, 2003).

The equipment was calibrated prior to the surveys using sound-velocity profiles of the water column recorded from CTD (Conductivity Temperature Depth) measurements. The data collected during the survey are considered to be of good quality (Forwick & Rasmussen, 2012). The Fledermaus software has been used to visualize the data in this thesis, with a resolution of 10 m.

To avoid mis-interpretetion of the data, possible noise within the dataset should be kept in mind. Multibeam swath bathymetry data often present sound refraction artefacts, where they in 3D topographical mapping appear as ridges reflecting the tracks of the vessel (Yang *et al.*, 2007). Refraction artefacts are often a problem in shallow water multibeam surveys (Kammerer, 2000)

3.2 Chirp sonar

The chirp sonar data used in this study were collected simultaneously with the swath-bathymetry data using an EdgeTech 3300-HM hull-mounted sub-bottom profiler (Chirp; 4x4), with a pulse frequency of 1.5 – 9.0 kHz and a 40 ms pulse length. The ship travelled at a speed between 5 and 8 knots, and the shot rate was 1 Hz (Forwick & Rasmussen, 2012).

Acoustic Chirp sonar systems provide high-resolution, real-time and artefact-free measurements of acoustic attenuation in marine sediments (Schock *et al.*, 1989). The sonar sends out a computer-generated, amplitude- and phase-compensated sweep of frequencies between 400 Hz and 20 kHz. Which correct for the sonar system response and reduce correlation noise and source-ringing influencing the vertical resolution (Schock *et al.*, 1989; Quinn *et al.*, 1998).

The figures presented in this thesis have been visualized using the Kingdom 8.8 software.

3.3 Sediment cores

Five sediment cores were recovered on the 17th of April 2013 using R/V Helmer Hanssen. Two of the cores were collected with a piston corer, while the three others are gravity cores. The exact position of the cores is shown in Figure 3.1, and further details are provided in Table 3.1.

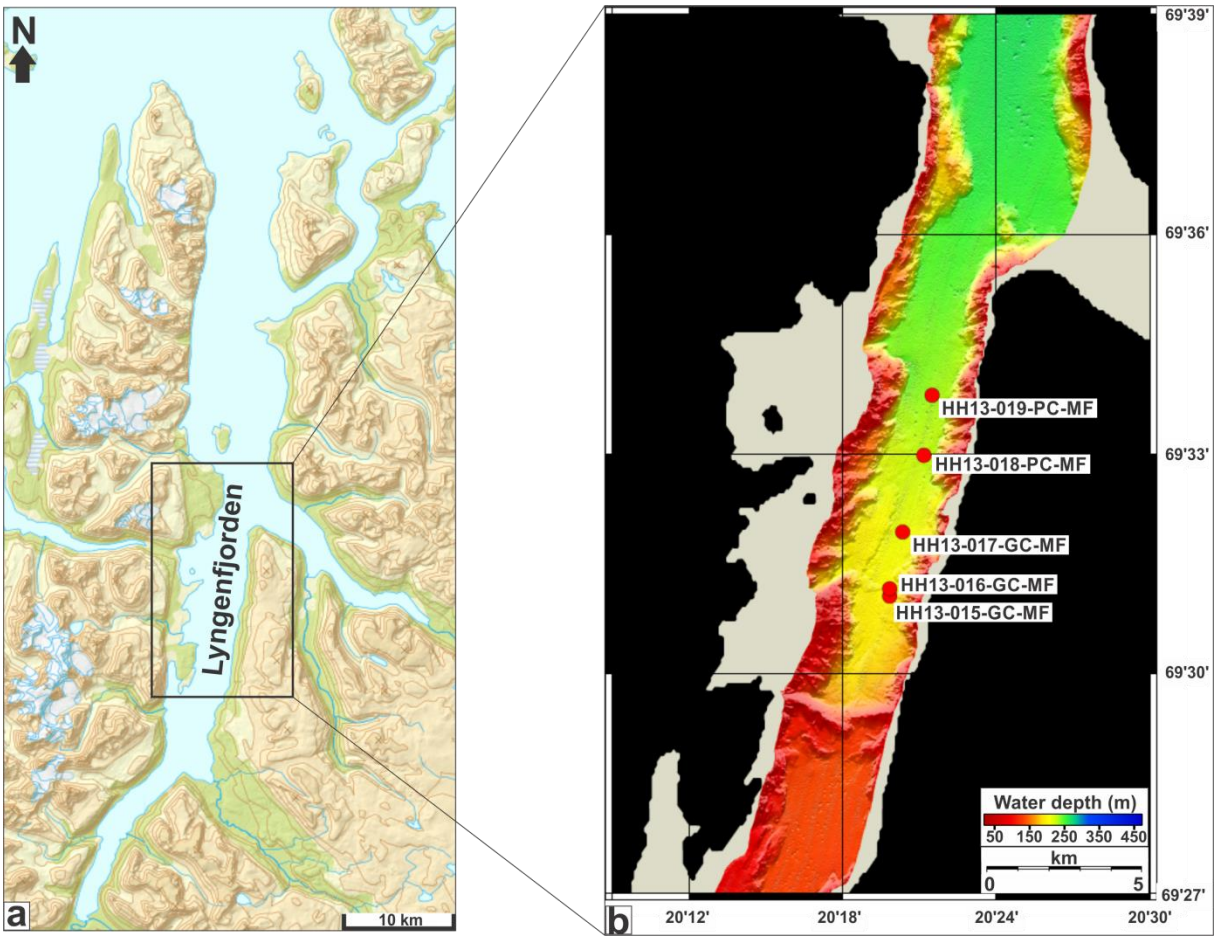

Figure 3.1: *The core locations.*

The gravity corer consisted of a 6 m long steel barrel with an inner diameter of ~11 cm. A 6 m long plastic liner with outer and inner diameters of 11 cm and 10.2 cm, respectively, was placed inside the steel barrel (Forwick *et al.*, 2013). A weight was attached to the top of corer to enable it to penetrate the seafloor; in this case the corer had a total weight of ~1900 kg (Forwick *et al.*, 2013). Attached to the bottom of the corer were a core cutter and a core catcher. The core cutter cuts the sediments and makes way for the gravity corer as it hits the seafloor. When the corer penetrates the sub seafloor the plastic liner is filled up with sediment, which is secured in the liner by the core catcher (e.g. NOC, 2014).

The piston corer consisted of a 12 m long steel barrel with an inner diameter of ~11 cm. A 12 m long plastic liner, with the same diameter as for the gravity corer, was placed inside the steel barrel. The total weight of the corer was ~2200 kg, including the lead bomb placed on top of the barrel (Forwick

et al., 2013). A trigger arm is placed on the top of the corer, and holds a trigger device by a wire. The trigger device on R/V "Helmer Hanssen" consists of a trigger bomb. The wire is of such a length that the trigger bomb is hanging lower than the barrel as the piston corer is lowered through the water, and thus hits the seafloor before the piston corer. As the trigger bomb hits the seafloor the pull is released from the trigger arm, leading to the free-fall release of the 12-m barrel and lead bomb some meters above the seafloor. The piston, which is fixed inside the liner close to the core catcher, secures the sediments in place by suction and inverted metal teeth (e.g. NOC, 2014).

After retrieving the cores, the plastic liner was removed from the steel barrel and cut into sections of approximately 1 m. All the sections were then labelled, and sealed with plastic caps and tape. The cores have been stored at approximately 4°C until they were opened in January 2014.

Station	Date	Time (UTC)	Lat. (N)	Long. (E)	Water depth (m)	Penetration (m)	Recovery (m)	No. of sections
HH13-015-GC-MF	13.04.17	0801	69° 31.068'	020° 19.829'	195	~6	3.98	4
HH13-016-GC-MF	13.04.17	0828	69° 31.164'	020° 19.833'	202	~6	5.87	4
HH13-017-GC-MF	13.04.17	0959	69° 31.943'	020° 20.342'	212	~6	4.30	5
HH13-018-PC-MF	13.04.17	1135	69° 32.992'	020° 21.174'	225	>8	5.74	6
HH13-019-PC-MF	13.04.17	1406	69° 33.812'	020° 21.498'	235	~12	4.69	5

Table 3.1: Coring sites, times of sampling, locations, water depths, penetrations, recovery and numbers of sections.

3.4 Laboratory analysis of the cores

The laboratory work was carried out in January, February and May 2014 at the laboratory of the Department of Geology at the University of Tromsø – The Arctic University of Norway.

3.4.1 Multi-Sensor Core Logger

Prior to opening, the cores were logged with the GEOTEK Multi-Sensor Core Logger (MSCL) in order to measure the physical properties of the sediment (Fig. 3.2). The measured parameters were gamma-ray attenuation, P-wave velocity and amplitude, magnetic susceptibility, temperature and thickness.

When logging the cores, sections of them are pushed past different sensors, a process driven by a stepper motor which can position a core to an accuracy of better than 0.5 mm. For this study the measuring interval was set to be 1 cm and the measuring time was set to 10 seconds.

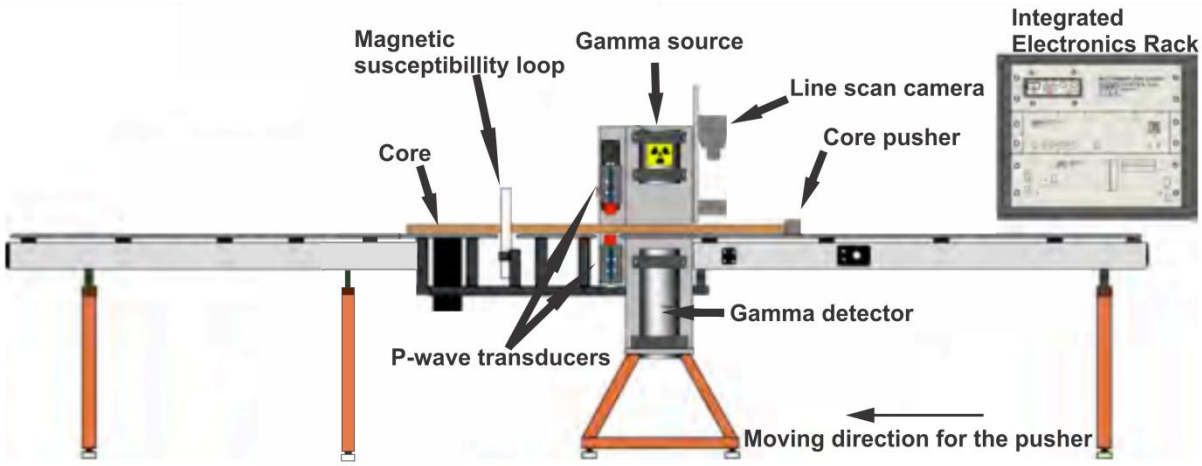

Figure 3.2: *Sketch showing the main features of the GEOTEK Multi-Sensor Core Logger (Modified after GEOTEK, 2000).*

3.4.1.1 Wet-bulk density

Bulk density is defined as the ratio of the mass of any particles of the material over the total volume they occupy (see formula below), and for soils and sediments this is a result of mineral composition and compaction.

$$\rho = \frac{M_t}{V_t}$$

Where: $\boldsymbol{\rho}$ *= bulk density,* $\boldsymbol{M_t}$ *= total mass of particles in the material and* $\boldsymbol{V_t}$ *= total volume (GEOTEK, 2014).*

When collecting bulk density measurements a narrow beam of collimated gamma rays, which are sent from a Caesium-137 source, travels through the centre of the core and are detected on the other side

(Fig. 3.2). As the photons travel through the core they are scattered by electrons contributing to a partial loss of energy. Since the density of electrons is related to the density of the material, the density of the sediments in the core can be determined by measuring the number of transmitted photons which passes through the core unattenuated (GEOTEK, 2014). As the sediments measured in this study were wet the obtained density is the wet bulk density.

As it is necessary to separate between scattered and transmitted rays, a counting window is set ensuring that only photons which have the same energy as the source are counted. The intensity of the Caesium-137 source will decay over time, and it is therefore necessary to calibrate the gamma count before the measurements are performed. The best method for calibrating is to use the liner, in which the core is contained, and the fluid contained in the sediments. This could be accomplished by sending a sealed liner containing a cylindrical piece of aluminium of varying thickness surrounded by water through the core logger. The calibration sample piece is then exposed to gamma rays adjusted with a high count time of 50 seconds, at the different aluminium thicknesses. The processed data from these measurements will be transferred into the gamma density processing panel, making it possible to make all the necessary empirical adjustments (GEOTEK, 2014). For collimating the gamma beam the 5 mm diameter collimator was used.

3.4.1.2 P-wave Velocity

P-waves are longitudinal or compressional waves, and their ray path will be a result of the physical properties of the material they travel through. The P-wave velocity within the sediments inside a core is found as the ratio between the sediment thickness and the travel time for the pulse through the sediment (GEOTEK, 2004):

$$V_p = \frac{d}{t}$$

Where: $\boldsymbol{V_p}$ *= P-wave velocity,* $\boldsymbol{d}$ *= distance travelled and* $\boldsymbol{t}$ *= time taken to travel distance d (GEOTEK, 2014).*

In order to measure the velocity two PWTs (P-wave transducers) are placed directly opposite each other, where one operates as a transmitter and the other as a receiver (Fig. 3.2). As the core passes the PWTs, a short P-wave pulse is produced at the transmitter and propagates through the core before it is detected by the receiver. The travel time of the pulse is measured with pulse timing software at a resolution of 50 ns, and the distance travelled is measured with an accuracy of 0.1 mm. The P-wave velocity can then, after necessary calibration, be calculated with a resolution of about 1.5 m/s depending on the thickness of the liner walls. The correctness of the data depends on the quality of the acoustic coupling, that is, both between the PWTs and the liner, as well as between the liner and the sediments. This implies that optimal results can only be achieved from cores where the liner is

completely filled with sediments. Inferior acoustic coupling will result in a decreased P-wave signal amplitude, and hence a decrease of the signal strength. In order to measure the strength of the received signal, the root mean square value of the signal is taken within a defined time window. The amplitude measurement window is specified by the starting and ending point of the amplitude seen relative to the total travel time measured (GEOTEK, 2014).
The distance between the active faces of the two PWTs defines the core thickness (GEOTEK, 2014).

Since velocities fluctuate with changes in temperature it is of great importance for these measurements that the temperature is known (Weber *et al.*,1997; GEOTEK, 2014). The room temperature, where the logging took place, was measured by a thermometer. The same temperature is assumed for the cores as they were stored in the room for one day prior to the measurements.

3.4.1.3 Magnetic Susceptibility

The magnetic susceptibility of a particular material type is a result of its capacity to get magnetized in response to an applied magnetic field. The range of magnetic susceptibility measurements is given in both positive and negative numbers. In the case of positive magnetic susceptibility the material will strengthen the magnetic field, while the opposite is the case of negative magnetic susceptibility. Changes in magnetic susceptibility correlate with changes in sedimentary origin and/or diagenetic environment (GEOTEK, 2014).

For the magnetic susceptibility measurements the sections are pushed through a loop sensor mounted at the end of the core logger (Fig. 3.2). Here, a low intensity non-saturating, alternating magnetic field is produced by an oscillator circuit. The magnetic susceptibility of any material close to the sensor will change the frequencies of the oscillator, which are converted into magnetic susceptibility values. In order to obtain maximum resolution of magnetic susceptibility it is important that the ratio between the loop-diameter and the core-diameter is as small as possible (GEOTEK, 2014).

The data initially provided from the magnetic susceptibility system is volume specific magnetic susceptibility data, which does not account for the density of the sample being measured. By using the gamma density measured at each point, it is possible to take into account the density of the sample. This type of data is referred to as mass specific magnetic susceptibility (GEOTEK, 2014). In this study both volume and mass specific magnetic susceptibility was calculated, however, only mass specific magnetic susceptibility is presented (*see Chapter 6*)

3.4.1.4 Fractional porosity and acoustic impedance

The gamma density measurements reveal the wet bulk density of the core. From these measurements it is possible to calculate the fractional porosity and impedance of the material, the last being the product of the wet bulk density and the P-wave velocity:

$$Z = V_p \times \rho$$

*Where: **Z** = impedance, $\boldsymbol{V_p}$ = P-wave velocity and **ρ** = wet bulk density (GEOTEK, 2014)*

3.4.2 Opening of the cores

All the core sections were opened in January 2014, using a core liner saw with vibrating blades and an osmotic knife. One half of the core was marked with work and the other half with archive, where the last was meant only for storage. Both section parts were wrapped in plastic and stored in a cold storage room at ~+4 °C. Due to circumstances around the equipment used in the further study of the cores, as well as need for extra dating material, both halves were used in the lab work.

3.4.3 Colour imaging

Prior to imaging the core surfaces were cleaned and smoothened, because irregularities at the sediments surface might decrease the quality of the pictures. It is also important that the core surface is dry before imaging since the presence of water could cause reflections in the picture. The sections were photographed in the Avaatech XRF core scanner with a Color Line scan camera (Jai L-107CC 3 CCD RGB), with ~70 μm resolution.

3.4.4 X-ray photography

X-ray photographs were taken of the half-core sections using the GEOTEK X-ray core imaging system (MSCL-XCT). The system provides digital pictures, imaging the differences in density as lighter or darker areas. The X-ray photos presented in this thesis display the high density material dark, and the low density material light/bright. This imaging of density of the core material makes it possible to identify internal structures not possible to observe at the sediment surface. Features such as clasts, fossils, bioturbation and sedimentary structures have been described from the X-ray photos to complement the lithological logs.

3.4.5 Element geochemistry

Qualitative element-geochemical measurements of half-core sections of the cores were performed with an Avaatech XRF Core Scanner. This method is non-destructive and does not require comprehensive sample preparation. The XRF core scanner performs qualitative measurements of all elements from Mg to U in the periodic system, given that they are above the detection limit of the instrument (Richter *et al.*, 2006; Avaatech, 2014).

The principle behind the XRF core scanning method is based on secondary radiation generated from the collision between X-rays and matter. The XRF scanner is equipped with incoming radiation from a Rhodium (Rh) target X-ray tube, from where primary radiation is shot at the core surface. When the X-rays collide with the atoms of the sediment surface, electrons are ejected from their inner atomic shell. This leaves the atom unstable, and the generated vacancy is consequently filled with electrons from an adjacent, outer shell. Since the replacing electron is from a higher shell, it holds higher energy than needed for the vacancy, and hence excess energy/radiation is generated and released. This secondary electromagnetic radiation (fluorescence) is characteristic for each element, making it possible for the detector in the XRF scanner to identify the chemical composition of the core (Fig. 3.3) (Richter *et al.*, 2006; Avaatech, 2014).

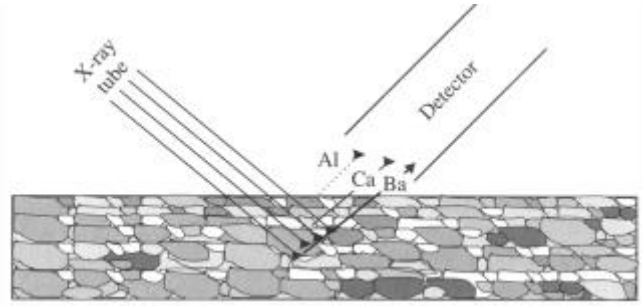

Figure 3.3: *Sketch illustrating the principle of XRF logging on split sediment cores and the response depth of selected elements to incoming X-ray radiation. The figure is not to scale (From Richter et al., 2006)*

During data acquisition, a helium-flushed chamber/measuring triangle is lowered onto the sediment surface at each measurement point. The incoming radiation enters at an angle of 45^{o} and the detector for the outgoing radiation is installed at the same angle. The area of measurement can be adjusted in a down-core and cross-core direction by adjusting slits between the X-ray source, the sediment surface and the detector. For this study the slits were set to 10 mm down-core and 12 mm cross-core. The purpose of the helium-flushed measurement system is to prevent partial or complete absorption of the secondary radiation by air, and thereby a better detection capacity (especially for the lighter elements) (Richter *et al.*, 2006; Avaatech, 2014). To prevent contamination of the measuring system the sediment surface was covered with a 4 μm ultralene foil. The cores were wrapped carefully to ensure that no air bubbles got stuck in between the foil and the sediment surface. Prior to the wrapping, the core surfaces were cleaned and smoothened. It is also important that the cores are left in room temperature for some time before the foil is placed on the sediment surface. This is to prevent the accumulation of water underneath the foil (see Tjallingii *et al.*, 2007).

The large weight range of elements analyzed using the Avaatech XRF Core Scanner is made possible due to option of defining variable measurement setting. E.g. can the tube voltage of the system be varied to obtain the optimal settings for specific elements or sets thereof (Fig. 3.3) (Richter *et al.*, 2006). The measurements are therefore typically performed in multiple runs. The data acquisition for this study was performed at 10 mm steps during two separate runs with the following settings:

1) 10kV, 1000 μA, 10 seconds counting time, no filter. This setting enables the measuring of light elements (from Mg to Co in the periodic system). In this study, only elements with count rates >10 000 during the 10kV run are seen as reliable, others were not included in the results.
2) 30kV, 2000 μA, 10 seconds counting time, Pd-thick filter. This setting is used to measure medium-heavy elements (from Ni to approx. Mo). In this study, only elements with count rates >5 000 during the 30kV run are seen as reliable, others were not included in the results.

The XRF scanner can also measure heavier elements (from Mo to U periodic system) with a 50kV run, but these elements were not seen as relevant for this study.

Ideally the material should be homogenous, dry and the surface should be flat and smooth for X-ray fluorescence analysis. However, these requirements are impossible to achieve for split sediment cores, and the XRF data are therefore only semi-qualitatively (Richter *et al.*, 2006). The issues of uneven surface, porosity and water content are referred to as matrix effects. Elements like Al, Ca, K, Si, Ti and Mn are more easily disturbed and may therefore record false concentrations (Tjallingii *et al*., 2007). For example, XRF scanning of wet sediment cores show largely reduced intensities of light elements, such as Si and Al, compared to dry samples (Tjallingii *et al*., 2007; Weltje & Tjallingii, 2008). These errors can be minimized by using element ratios rather than single element intensities, as element ratios would be less sensitive to small disturbances (Weltje & Tjallingii, 2008).

The use of XRF data within fjords are generally new research and little is known about element interpretation within these environments. In other geological settings have XRF data been used in sediment core studies to indicate the sediments provenance. Results and interpretations found in these studies are generally not applicable to fjord research, since fjords are sites of high and highly diverse sediment input. However, some already stated indicator properties have been found reliable for this study. The chemistry of the sediments is strongly controlled by the grain-size of the dominant mineral host, as well as the particle size sorting (e.g. Koinig *et al.*, 2003; Kylander *et al.*, 2010). The ratio between Zr and Rb can be used to provide information of the grain size and the composition of the sediment. Rubidium is a part of many common minerals, including mica and clay. Zirconium is associated with heavy minerals like zircon, and is often enriched in medium to coarse silt. Low Zr/Rb values represent fine-grained material, while high values represent coarse-grained material (Dypvik & Harris, 2001; Kylander *et al.*, 2010). K is often associated with clay minerals (Rothwell *et al.*, 2006; Kylander *et al.*, 2010), which can also be applied to Ti (Kylander *et al.*, 2010). However, Ti can also

be high in highly resistant materials and can therefore be enhanced in turbidite bases (Rothwell *et al.,* 2006). From research of deep ocean basins, and NE Atlantic sediment cores, have the Fe/Ca ratio been established as a good proxy for reflecting variations in the relative abundance of terrigenous material and biogenic carbonate (e.g. Croudace *et al.,* 2006; Richter *et al.,* 2006). However, the correlation is not transferable to this study. Rothwell *et al.* 2006 uses XRF data for turbidite detection, and suggest e.g. that the Fe/Ca profile within turbidite units shows less fluctuations than hemipelagic sediments due to the lack of bioturbation. Further observations indicate a good correlation between Fe/Ca and sedimentary units. Ca peaks can correspond to foraminifer- or shell-rich sediments (e.g. Rothwell *et al.,* 2006). Excess concentrations of strontium can be correlated to carbonate rich sediments (e.g. Dean *et al.,* 1997; Dypvik & Harris, 2001), this is due to its ability to merge into the crystal (Dean *et al.,* 1997). Si is also an important productivity indicator (e.g. Rothwell *et al.,* 2006; Heimbürger *et al.,* 2012).

3.4.6 Visual description and logging

The cores were studied and described based on their visible characteristics of grain-size, clast and fossil content, bioturbation and sediment structure. The Munsell Soil Color Chart was used for the colour determination. Lithological logs of the cores were created based on these observations.

3.4.7 Undrained shear strength

The undrained shear strength of the sediments was determined with the fall cone test using the Fall Cone apparatus, first introduced in 1915 (GEONOR, 2014). The apparatus is equipped with four cones of different weight and apex angle, thus can the apparatus be adjusted to suit the different properties of the sediments. The test is carried out in the following way; the cone is attached to the instrument by a magnet and is lowered so that the tip is just in contact with the surface of the sediments. Then, when the cone is placed in the correct position, a switch allows the connection between the cone and the magnet to be manually removed, and, as the connection is lost the cone penetrates the sediments due to gravity. The penetration depth (in mm) is instantaneously read from a scale on the side of the instrument and converted into values for undrained shear strength (KPa). The values are converted using a table calibrated by (Hansbo, 1957)

The undrained shear strength of the sediments was mainly measured every 10 cm of the cores. But for the non-uniform units the measurements were carried out with a closer and more varying spacing given by the visible changes in the sediment conditions. At least three measurements were done at each measuring depth, and it was their average penetration depth that was converted into values for the undrained shear strength (kPa).

3.4.8 Sediment sampling

A spatula was used to take samples of approximately 5 cm^3 every 10 cm down the length of the cores. Samples were in addition obtained on both sides of unit boundaries, and with smaller and varying spacing in the inhomogeneous units, in order to collect data from the different lithofacies. These samples provide the material needed for the calculation of the water content and grain-size distribution.

The samples were weighed immediately after they were collected and then stored in a freezer room before they were freeze dried.

3.4.8.1 Freeze drying

The process of freeze drying the samples was performed with a Christ Alpha 1-4 freeze dryer, connected to the Leybold Trivac B vacuum pump.

The freeze drying process is based on direct conversion from solid to gaseous state, a physical phenomenon referred to as sublimation (CHRIST, 2006). The frozen samples are placed in a vacuum drying chamber where both the pressure and temperature is regulated to enable the samples to dry without thawing. The principle is to create an atmospheric pressure in the chamber that is lower than 6.11 mbar, only under such conditions is it possible for ice to be directly converted from a solid phase to a gaseous phase (CHRIST, 2006).

The main advantage of using the freeze drier to remove the water is that the physical structure of the sediment is less altered. As a result, samples containing clay remain friable (Myrbo, 2004).

3.4.9 Water content

The samples were weighed before and after freeze drying, thus, allowing the calculation of the water content using the formula:

$$\frac{Weight\ wet\ sample - Weight\ dry\ sample}{Weight\ wet\ sample} \times 100$$

3.4.10 Grain-size distribution

The grain-size distribution analyses were carried out with a LS 13 320 Laser Diffraction Particle Size Analyzer. This instrument can measure the size distribution of particles, with a range of 0.04 – 2000 µm using the principles of light scattering. The analyser measures the pattern of light scattered by the particles in the sample, where each particle's scattering pattern is characteristic of its size (Beckman Coulter, 2011).

Prior to the analyses, the samples were taken through a stepwise process in order to remove carbonate and organic matter. Approximately one gram of sediment from each sample was extracted and added to a 100-ml plastic container. In the first step, distilled water was added, just so it covered the sediments, and left to react overnight. This was done since the sediments showed a tendency to form aggregates when left to react in an acidic acid solution during a test round. In the following step, the sediments were treated with acidic acid (CH_3COOH), with the purpose of removing the carbonate content. Approximately 10 ml acidic acid was added to each sample and left to react overnight. The samples were then flushed with distilled water two times before hydrogen peroxide (H_2O_2) was added in order to dissolve the organic matter. Approximately 10 ml hydrogen peroxide were added to each sample and left to react overnight. After this treatment the samples were again flushed with distilled water two times. The final step was to treat the sediments with calgon (sodium polyphosphate) and then place the samples in an ultrasonic bath, which both reduces the risk of coagulation of particles. Immediately prior to measuring, the samples were stirred for a couple of minutes using a magnet shaker. In this study the whole of the sample was used in the analysis. For most of the samples the analyzer indicated too high concentrations, which had to be further diluted.

The LS 13 320 Laser Diffraction Particle Size Analyzer only measures grain sizes up to 2000 μm, grains larger than this is therefore not included in the results. However, observed larger grains have been included in the lithological logs. The results are expressed in volume percentages as the laser granulometry measure grain volume. The statistical calculations presented in this thesis have been performed using GRADISTAT v. 8.0, computer program which enables e.g. mean, mode, sorting, skewness and kurtosis to be calculated arithmetically, geometrically and logarithmically using both moment and Folk and Ward graphical methods (Blott & Pye, 2001). In this thesis the statistics will be expressed geometrically (in metric units) using Folk and Ward (1957) graphical measures; a method indicated by the work of Blott and Pye (2001)to provide the most robust basis for routine comparison of compositionally variable sediments. In order to better understand the conditions of the depositional environment the following four grain-size parameters have been included in the results

- **Mean size (M_G)**

  This parameter indicates the average size of the sediment, which reflects the kinetic energy of the processes leading to the deposition. Low velocity of the depositional process will result in an average size of finer fractions, and vice versa for the opposite case (Sahu, 1964). The mean is given by the formula:

$$M_G = exp\frac{lnP_{16} + lnP_{50} + lnP_{84}}{3}$$

  Where P_x = grain diameter in metric units at the cumulative percentile value of x (Folk & Ward, 1957).

- **Sorting (σ_G)**

  The sorting, or standard deviation, is a measure for the spread of the grain sizes around the average and indicates fluctuations in the kinetic energy of depositional process compared to the average. Relatively stable conditions, meaning small variations in the velocity of the sedimentary processes, will give well sorting. Poor sorting often indicate a combination of different processes leading to the deposition (Sahu, 1964). The division of sediments according to sorting is displayed in Table 3.2. The standard deviation is given by the formula:

$$\sigma_G = \exp\left(\frac{lnP_{16} - lnP_{84}}{4} + \frac{lnP_5 - lnP_{95}}{6{\cdot}6}\right)$$

  Where P_x = grain diameter in metric units at the cumulative percentile value of x (Folk & Ward, 1957).

- **Skewness (Sk_G)**

  Skewness is a measure for the shape of the grain-size distribution curve, whether it is symmetrical or if the grain sizes have a preferential spread to one side of the average. If the grain-size distribution curve bends towards the coarser side from the average, the sediments are coarsely-skewed, indicating a lower energy process of deposition than the mean. But if the process of deposition has a higher energy than the average, will the curve bend towards the finer side and the sediments are finely-skewed (Sahu, 1964). The division of sediments according to skewness is displayed in Table 3.2. Skewness is given by the formula:

$$Sk_G = \frac{lnP_{16} + lnP_{84} - 2(lnP_{50})}{2(lnP_{84} - lnP_{16})} + \frac{lnP_5 + lnP_{95} - 2(lnP_{50})}{2(lnP_{25} - lnP_5)},$$

  Where P_x = grain diameter in metric units at the cumulative percentile value of x (Folk & Ward, 1957).

- **Kurtosis (K_G)**

  Kurtosis is the measure of the degree of concentration of the grains relative to the average; it reveals whether the shape of the grain-size distribution curve is peaked or flat. The kurtosis is the ratio of the sorting within the central 90% to the central 50% of the distribution (Sahu, 1964). As a reference is K_G=1.00 for a normal Gaussian curve, meaning that the sorting in the tails of the curve equals that of the central part (Folk & Ward, 1957). The higher the value for the kurtosis is the more likely is it that the distribution is well sorted, while the opposite can be

applied to low values (Cadigan, 1961). The division of sediments according to kurtosis is displayed in Table 3.2. Kurtosis is given by the formula

$$K_G = \frac{lnP_5 - lnP_{95}}{2{\cdot}44(lnP_{25} - lnP_{75})},$$

Where P_x = grain diameter in metric units at the cumulative percentile value of x (Folk & Ward, 1957).

Sorting (σ_G)		Skewness (Sk_G)		Kurtosis (K_G)	
Very well sorted	<1·27	Very fine skewed	⁻0·3 to ⁻1·0	Very platykurtic	<0·67
Well sorted	1·27–1·41	Fine skewed	⁻0·1 to ⁻0·3	Platykurtic	0·67–0·90
Moderately well sorted	1·41–1·62	Symmetrical	⁻0·1 to ⁺0·1	Mesokurtic	0·90–1·11
Moderately sorted	1·62–2·00	Coarse skewed	⁺0·1 to ⁺0·3	Leptokurtic	1·11–1·50
Poorly sorted	2·00–4·00	Very coarse skewed	⁺0·3 to ⁺1·0	Very leptokurtic	1·50–3·00
Very poorly sorted	4·00–16·00			Extremely leptokurtic	>3·00
Extremely poorly sorted	>16·00				

Table 3.2: *The classification of sediments according to sorting (σ_G), skewness (Sk_G) and kurtosis (K_G), a classification after the geometric (modified) Folk and Ward (1957) graphical measures (from Blott & Pye, 2011).*

The divisions of the different grain size fractions have been adopted from the size scale used in the GRADISTAT program (Tab. 3.3). However, subdivisions (e.g. very coarse, coarse, medium etc.) of the grain-sizes were not thought to be necessary for this study, and hence, the text only refers to clay, silt and sand.

Grain size		Descriptive terminology			
phi	mm/μm	Udden (1914) and Wentworth (1922)	Friedman and Sanders (1978)	GRADISTAT program	
			Very large boulders		
−11	2048 mm		Large boulders	Very large	
−10	1024		Medium boulders	Large	
−9	512	Cobbles	Small boulders	Medium	Boulders
−8	256		Large cobbles	Small	
−7	128		Small cobbles	Very small	
−6	64				
−5	32		Very coarse pebbles	Very coarse	
			Coarse pebbles	Coarse	
−4	16	Pebbles	Medium pebbles	Medium	Gravel
−3	8		Fine pebbles	Fine	
−2	4				
		Granules	Very fine pebbles	Very fine	
−1	2				
		Very coarse sand	Very coarse sand	Very coarse	
0	1				
		Coarse sand	Coarse sand	Coarse	
1	500 μm	Medium sand	Medium sand	Medium	Sand
2	250				
		Fine sand	Fine sand	Fine	
3	125				
		Very fine sand	Very fine sand	Very fine	
4	63				
			Very coarse silt	Very coarse	
5	31				
			Coarse silt	Coarse	
6	16	Silt			
			Medium silt	Medium	Silt
7	8				
			Fine silt	Fine	
8	4				
			Very fine silt	Very fine	
9	2	Clay			
			Clay	Clay	

Table 3.3: *The GRADISTAT size scale used in this thesis compared with scales used by Udden (1914), Wentworth (1922) and Friedman and Sanders (1978) (from Blott & Pye, 2011).*

3.4.11 Radiocarbon dating

X-radiographs and observations of the sediment surfaces were used to find undisturbed macrofossils (e.g. paired shells) for radiocarbon dating. However, only a few macrofossils were found, and none of these were located near the deposits of interest for dating. Both core sections were investigated in the hope of finding suitable macrofossils.

As a consequence, benthic foraminifera, shell fragments and wood fragments were used for radiocarbon dating. A total of eight samples with benthic foraminifera was collected from cores HH13-016-GC-MF, HH13-017-GC-MF, HH13-018-PC-MF and HH13-019-PC-MF (Tab. 3.4).
Due to a low content of microfossils in the samples, all benthic foraminifera species, with a few exceptions, were picked. Both the *Miliolida sp.* and the *Cibicides Lobatulus* were excluded during the picking. The *Miliolida sp.* foraminifera have a tendency provide too old ages (Vorren & Plassen, 2002), and the *Cibicides Lobatulus* foraminifera is considered unsuitable in this study due to its vital effects (Zajączkowski *et al.*, 2010). In order to gain the most accurate results from radiocarbon dating, the benthic foraminifera were collected from an interval spanning from 1 cm to 2 cm located as close as possible to selected mass-transport deposits (MTDs) of interest (Tab. 3.4). One sample of wood and one sample of shell fragments were obtained from a larger MTD in core HH13-017-GC-MF (Tab. 3.4). A total of ten samples were collected and dated at the ^{14}CHRONO Centre at Queens University, Belfast, Northern Ireland.

Lab reference	Core	Sampling depth (cm)	Type of material
UBA -26247	HH13-016-GC-MF	364 - 366	Benthic foraminifera
UBA-26248	HH13-017-GC-MF	230 - 231	Benthic foraminifera
UBA-26249	HH13-017-GC-MF	246 - 247	Benthic foraminifera
UBA-26251	HH13-018-PC-MF	368 - 370	Benthic foraminifera
UBA-26252	HH13-018-PC-MF	375,5 – 377,5	Benthic foraminifera
UBA-26250	HH13-018-PC-MF	409,5 – 411,5	Benthic foraminifera
UBA-26253	HH13-019-PC-MF	358,5 – 360,5	Benthic foraminifera
UBA-26254	HH13-019-PC-MF	428 - 430	Benthic foraminifera
UBA-26255	HH13-017-GC-MF	238 - 239	Wood
UBA-26256	HH13-017-GC-MF	238 - 239	Shell fragments

Table 3.4: *Benthic foraminifera, shell fragments and wood collected for radiocarbon dating.*

3.4.11.1 Principle

The radioactive isotope ^{14}C is one of three naturally occurring carbon isotopes. It makes up only about 1 part per trillion of the total amount of carbon in the atmosphere. ^{14}C is continually being formed in the upper atmosphere by the collision of ^{14}N-nitrogene and neutrons, and quickly binds to oxygen creating CO_2. The carbon dioxide containing ^{14}C can be seen as chemically equal as those consisting of any of the other two carbon isotopes, and gets mixed throughout the atmosphere and into the oceans from where it may enter the biosphere. Every living organism will take up CO_2, but as soon as it dies this process ends a closed system is started. Given a constant production rate, there is a dynamic equilibrium between formation and decay. This means that the ^{14}C level in all living organisms can in principle be considered constant. When the organisms die, the ^{14}C level is no longer constant, and the unstable isotopes will decay with a half-life of 5730 years (e.g. Bowman, 1990; Lowe & Walker, 1997).

3.4.11.2 Accelerator Mass Spectrometry (AMS)

The samples were measured at the ^{14}CHRONO Centre at Queens University, Belfast (http://chrono.qub.ac.uk) using Accelerator Mass Spectrometry (AMS) method. This method is based on the differences in atomic weights, and it runs by the principle of charged particle deflection due to the effect of an applied magnetic field. If charged particles of different mass, but same velocity, are subjected to the same magnetic field, the heavier particles will be deflected the least. The AMS is capable to discriminate between elements of similar weight by subjecting the particles to large voltage differences so that they travel at very high speeds (e.g. Bowman, 1990; Vogel *et al.*, 1995; Lowe & Walker, 1997; Vogel & Love, 2005)

3.4.11.3 Calibration

The ^{14}C production is dependent on different time-varying processes, and the ^{14}C level in the atmosphere is therefore not constant. This, together with an uneven distribution of ^{14}C among carbon reservoirs, affect the measured radiocarbon age. The result is a radiocarbon age which may deviate significantly from calendar age and calibration of radiocarbon ages is therefore necessary (Bowman, 1990; Lowe & Walker, 1997; Hughen *et al.*, 2004). In addition to the natural variations, today's atmospheric ^{14}C levels are greatly affected by recent human activity. Both industrial activity and atomic explosions have resulted in an increased release of ^{14}C to the atmosphere, and modern organic samples are therefore unsuitable as they likely show incorrectly young ages. As a consequence, the year AD 1950 is defined as zero age of the radiocarbon time scale for calibrated ages (cal. y. BP) (Bowman, 1990; Lowe & Walker, 1997).

In the case of samples from marine environments is it also necessary to take into account the marine reservoir effect. The water masses of the oceans receive their ^{14}C input at the ocean-atmosphere interface, and here, in the surface waters, the input and decay of ^{14}C will be in equilibrium. However

this does not apply to deeper water masses. While the water sinks ^{14}C continues to decay, but without the same input of isotopes observed at the air-water interface, resulting in apparently older water masses. This effect is referred to as the marine reservoir effect (e.g. Bowman, 1990; Lowe & Walker, 1997; Reimer & Reimer, 2001; Mangerud *et al.,* 2006). The pre-industrial global mean reservoir correction (R(t)) is approximately 400 years, but great local variations exists. The local marine effect (ΔR), which may vary significantly over short distances, could be several hundred years or more (Reimer & Reimer, 2001)

The CALIB 7.0 software (Stuiver & Reimer, 1993; 2014; http://calib.qub.ac.uk/calib/calib.html) was used to calibrate the radiocarbon ages obtained from the AMS dating. The INTCAL13 dataset was used for the wood sampled in core HH13-17-GC-MF. For the marine samples were the MARINE13 dataset used for the calibration. Here, a time-dependent global ocean reservoir correction of about 400 years is used. In order to correct for local effects, were the regional marine effect (ΔR) of the Tromsø region added; $\Delta R = 65 \pm 37$ (Mangerud & Gulliksen, 1975).

4 Swath Bathymetry

4.1 Introduction

The Lyngen- and Storfjorden system is separated into four main basins (Fig. 4.1; *see also Chapter 2.4.2*). The study area is located in the southern parts of Basin 2, south of Kåfjord.

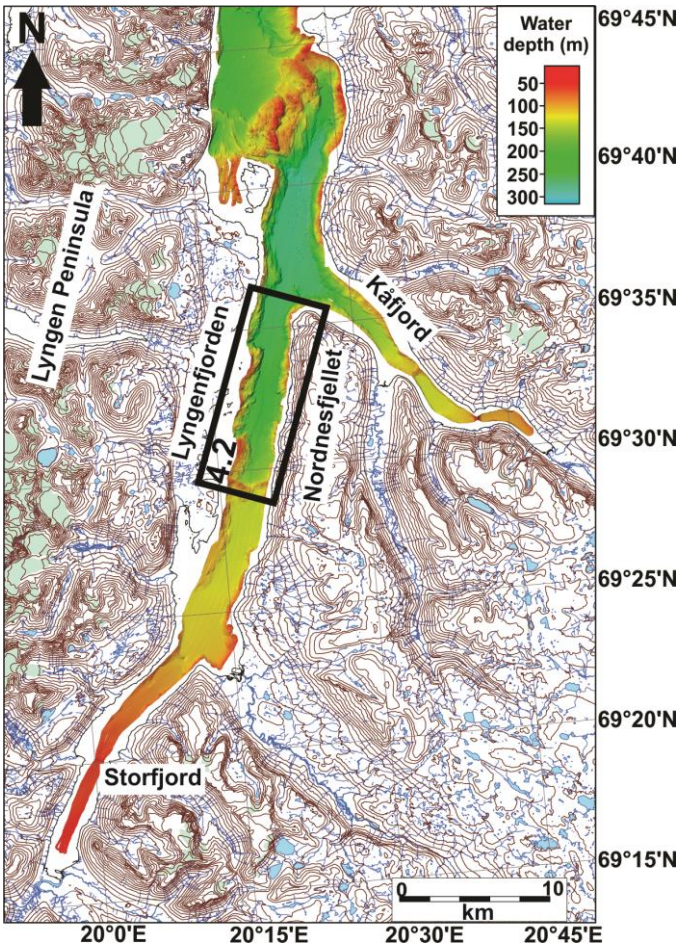

Figure 4.1: *Swath bathymetry data of parts of the Lyngen-and Storfjorden system, as well as Kåfjorden. The study area is indicated by the black box, and is shown in greater detail in Figure 4.2 (after Jenssen, 2006).*

The study area extends from a sill in the inner, southern part of Basin 2 and to the northern tip of Nordnesfjellet (Fig. 4.2). It is ~12 km long and between 1.1 and 2 km wide. Water depth increases northward, from a minimum of 70 m at crest of the sill to maximum 252 m in the north. The sill is a terminal moraine that was deposited at the end of a glacier re-advance during, the so-called Ørnes event 9800 – 9900 ± 150 ^{14}C B.P (Corner, 1980). The gradient of the northern slope (towards the basin) exceeds occasionally 27^{o}. It is cut by several furrows being up to 9 m deep (see also Jenssen, 2006).

The gradients of the eastern and western fjord slope exceed occasionally 30^{o}. They have an irregular morphology with hollows, escarpments and furrows of various size and "freshness" (Fig. 4.2 & 4.3).

The floor of the main basin is mostly smooth. However, several exceptions have been observed. An elevated area with undulating surface occurs in the southernmost part of the study area. It occupies the entire fjord width and is up to >8 m high at its northern margin (*see Chapter 4.4* & Fig. 4.4). An approx. 4 km wide sediment lobe area is identified further north, near the western fjord side (*see Chapter 4.5* & Fig. 4.5 & 4.7). Such undulating lobe areas can also be observed off the eastern fjord flank (*see Chapter 4.6* & Fig. 4.6).

A channel is located north of the sill, terminating downstream into the low-lying area located between the western and eastern sediment lobe areas (*see Chapter 4.3* & Fig. 4.2). Circular depressions of varying sizes and depths (~100-50 m wide and ~7-3 m deep) are scattered over the entire fjord floor (*see Chapter 4.7* & Fig. 4.7).

The entire study area is presented in Figure 4.2, where also the morphological features are illustrated (Fig. 4.2b). The bathymetry data also display areas interpreted to be noise, so called artefacts. The artefacts are observed either as straight lines or areas of hummocky appearance centred along lines, where both run parallel with the longitudinal axis of the fjord (*see Chapter 3.1, Swath bathymetry*).

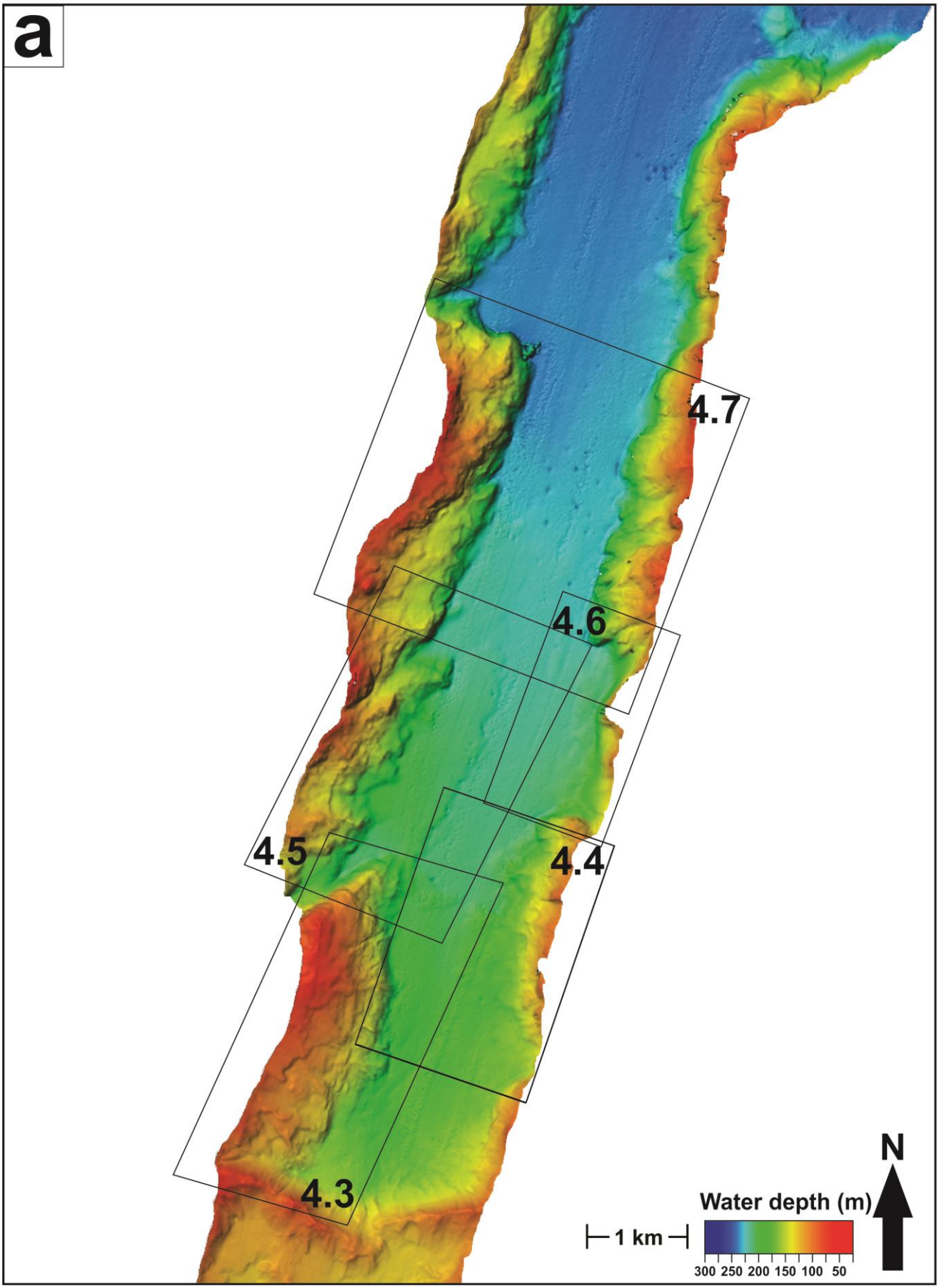

Figure 4.2a: *Swath bathymetry data of the study area (for location see Fig. 4.1). The black boxes indicate the locations of areas shown in Figure 4.3 – 4.7.*

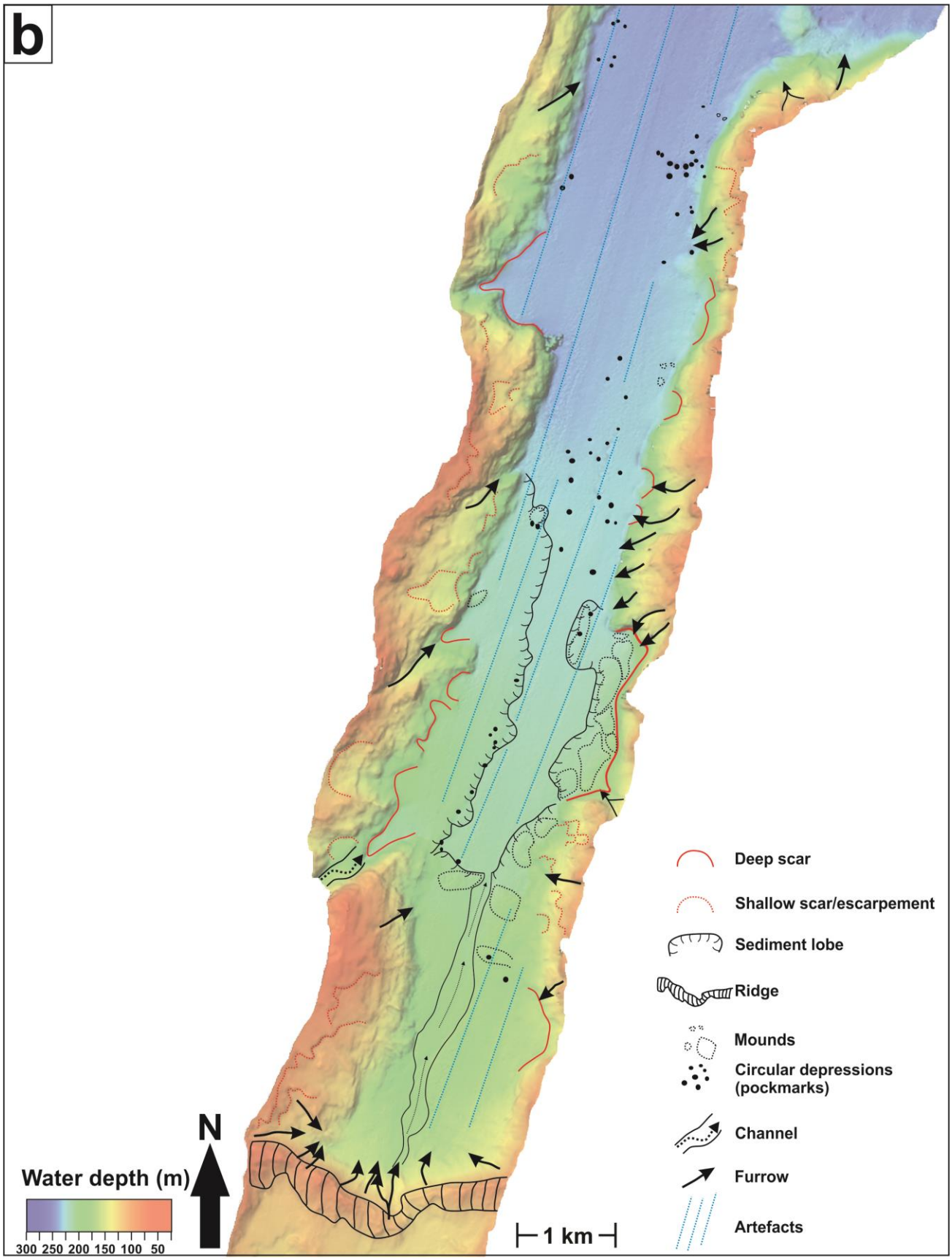

Figure 4.2b: *Interpretation of the main morphology features.*

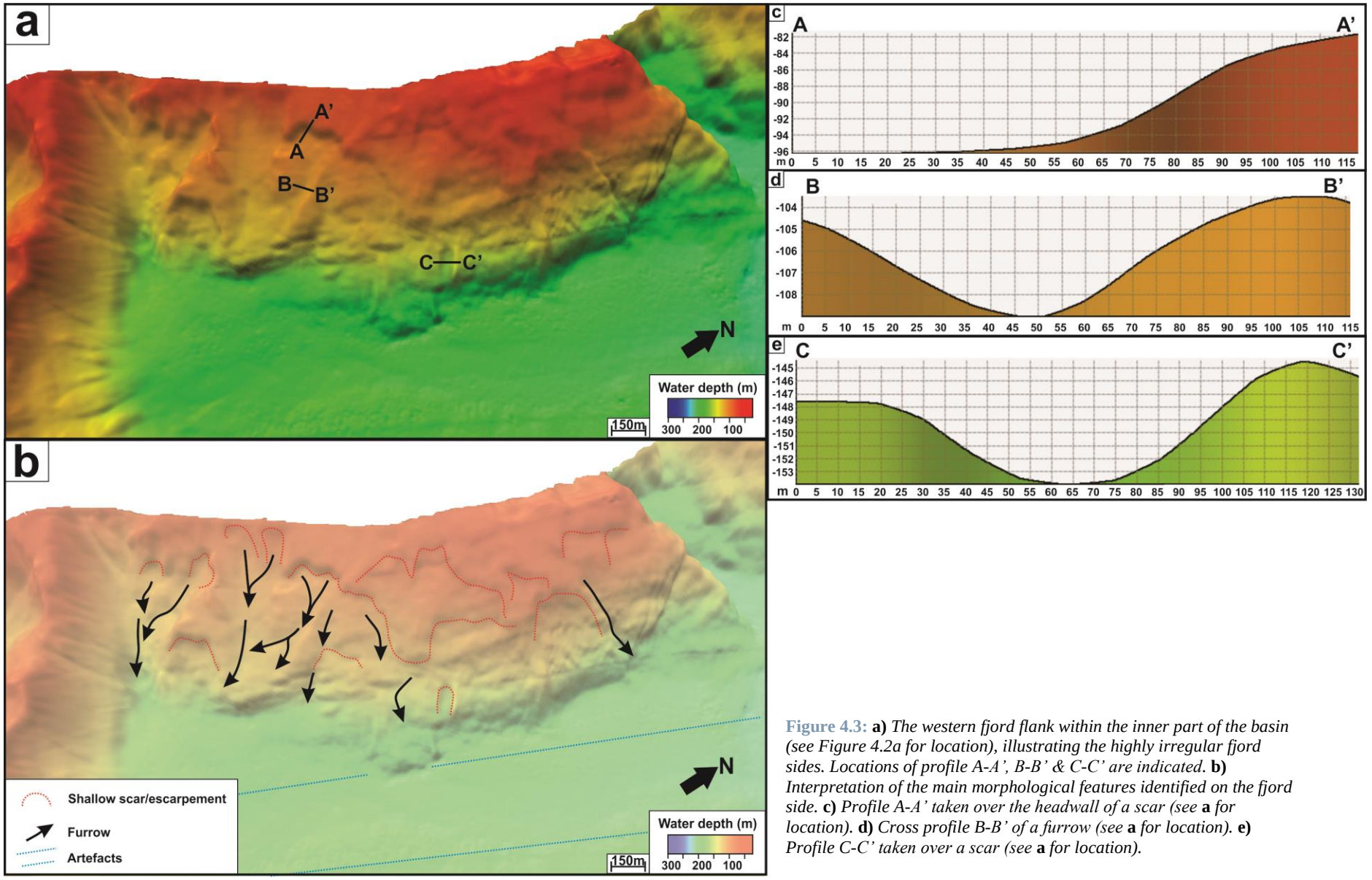

Figure 4.3: **a)** *The western fjord flank within the inner part of the basin (see Figure 4.2a for location), illustrating the highly irregular fjord sides. Locations of profile A-A', B-B' & C-C' are indicated.* **b)** *Interpretation of the main morphological features identified on the fjord side.* **c)** *Profile A-A' taken over the headwall of a scar (see* **a** *for location).* **d)** *Cross profile B-B' of a furrow (see* **a** *for location).* **e)** *Profile C-C' taken over a scar (see* **a** *for location).*

4.2 Fjord sides

Multiple hollows, escarpments and furrows occur on the eastern and western slopes (see Fig. 4.2b for examples). The features are observed at all depths of the sides, i.e. from the basin floor to the shallowest depths within the dataset. The hollows and escarpments, hereafter referred to as scars, vary in shape and size as well as "freshness". Their backscarps are commonly curved, and their profile is concave up. The largest ones are better described as indentations (up to ~1.7 x 0.4 km^2, see Fig. 4.7), which results in a curvy shape of the fjord sides. The smallest scar identified is 7 x 6 x 6 m^3. The backscarps of the scars are often amphitheatre shaped. The smallest vertical offsets are generally located at shallower water depths. Furrows also hold a wide variety of shape and size, where some occur in the vicinity of scars

Fourteen scars are identified within a ~3.5 km long and ~0, 2 km wide area. The amount of furrows exceeds this number (only a few indicated on the figure). The longest, continuous headwall is approx. 1 km long, up to ~14 m high and has a maximum slope angle of about 20^o (Profile A-A', Fig. 4.3c). An approx. 0.5 km furrow is located right below this scar. Profile B-B', crossing the furrow, reveals that the feature is ~5 m deep and ~65 m across in its higher parts and ~10 m at the bottom (Fig. 4.3d). Profile C-C' is taken across a smaller crescentic scar, located within the lowest part of the fjord flank (Fig. 4.3e). The depression is approx. 8 m deep and ~80 m across in its higher parts and ~30 m at the bottom. The length of the scar is approx. 150 m.

The scars are interpreted to be the result of slope failures (e.g. Prior *et al.*, 1982; Syvitski *et al.*, 1987; Aarseth *et al.*, 1989; Bøe *et al.*, 2000; Gardener *et al.*, 2000; Bøe *et al.*, 2003; Longva *et al.*, 2003; Stoker *et al.*, 2010). The step-like morphology with some slide scars is probably the result of multiple slope failures. They might developed from a series of successive slides and slumps; the first failure lead to further instability of the headwall, making each slide a trigger for successive slides in a retrogressive trend (Mulder & Cochonat, 1996; Bøe *et al.*, 2000). The deformation causing the formation of the deep scars may have begun as a creep, but as gravitational stresses increased larger areas were affected and may have ultimately failed as an intact block (Syvitski & Shaw, 1995). The furrows are thought to be gullies or channels, which are indicators of mass movements (e.g. Aarseth *et al.*, 1989; Gales *et al.*, 2013). Gullies in conjunction with slide scars are suggested to have acted as pathways for the failed sediments originating in the slide scars, whereas other gullies could be the result of mass flows e.g. turbidity flows (e.g. Stoker *et al.*, 2010). The interpreted slide paths are observed to be steeper than the main gradient of the fjord sides, indicating erosion (Aarseth *et al.*, 1989). The great dissection within the fjord sides may indicate that erosional processes were active over long time (cf. Gardner *et al.*, 2000). Sediment reworking could have occurred by slides, slumps, debris flows, grain flows and turbidity flows (e.g. Syvitski et al., 1987). Slides and slumps may develop into debris or grain flows, and with further incorporation of water these flows can take the

form of viscous sediment gravity flows. If the viscous flows reach their supercritical point, the continuation may be turbidity flows (Syvitski & Shaw, 1995).

4.3 Channel

In the southern part of the basin a groove is identified. The feature appears to be a prolongation of a system possible to follow from the top of the sill (Fig.4.2); a drain formation extends downslope and merges into the groove at the basin floor. The groove is interpreted to be a gently meandering channel, and terminates into the depression between the western and eastern sediment lobe areas (Fig. 4.2 & 4.4). The channel can be followed for approx. 3 km northwards from the sill, where its width is found to be ~100 – 150 m and its depth is ~2 – 8 m (see also Jenssen, 2006).

Jenssen (2006) suggested various mechanisms leading to the formation of the channel. It could possibly be the result of a subglacial meltwater channel (Benn & Evans, 1998), dating from the Ørnes event, where the channel was formed from underflows deriving from density differences between the glacial meltwater and the water masses in the fjord. Another formation mechanism is erosion by turbidity flows (Carlson, 1989; Syvitski & Shaw, 1995). It can be assumed that the depression today acts like a pathway for water currents flowing over the threshold (Jenssen, 2010).

4.4 Elevated and undulating seafloor in the southern part of the basin

Compared to the general characteristics of the basin floor, the southern part of the study area is shallower and undulating with a clearly outlined northern margin. The latter contains a slight elevation and a relatively steep and up to ~8 m high northern slope (Fig. 4.4).

Five large mounds with volumes between ~200 x 250 x 9 m^3 and ~300 x 300 x 8 m^3 were identified. Additionally, several smaller and larger irregularities, amongst them a depression (~160 x 70 x 7 m^3) located next to the largest mound on the eastern side of the basin, can be observed (Fig. 4.4). Multiple smaller and circular depressions are visible (*see Chapter 4.7* for details). The channel described above (*see Chapter* 4.3), erodes into this elevated area and terminates between two larger mounds (Profile B-B'; Fig. 4.4d).

The fjord sides of this part of the basin, show the same characteristics as described in general terms for the whole study area (*see Chapter 4.2*); steep (up to >28^o), displaying several scars and furrows. A large indentation (~0.8 x 0.4 km^2) within the eastern fjord side is shown in Figure 4.4, together with the most dominant scars. Here as well, the scars are crescentic with concave-up profile of the backscarps. The western fjord side is given a detailed description in chapter 4.2 and Fig. 4.3.

The undulating character of the seafloor is probably the result of multiple mass transport deposits (MTDs) that derived from the fjord sides (Prior *et al.*, 1982; Bøe *et al.*, 2000; Gardner *et al.*, 2000;

Longva *et al.*, 2003; Stoker *et al.*, 2010). The mounds may result from locally enhanced sediment accumulation or they are intact blocks within the sub-seafloor (Gardner *et al.*, 2000). However, they can also be obstacles withstanding erosion.

The depression within the seafloor is suggested to be a plunge pool (Syvitski & Shaw, 1987; Aarseth *et al.*, 1989; Lee *et al.*, 2002; Vergara, 2011). Such features are formed from localized impact of mass removal falls, i.e. as the moving sediments/rocks hit the foot of the slope. As a result, the seafloor might be eroded. The eroded material could be deposited in downslope locations/ in front of the plunge pool, either as a sheet or a constructional rampart (Lee *et al.*, 2002). Its formation can be compared to the process behind subaerial snow avalanches (Aarseth *et al.*, 1989).

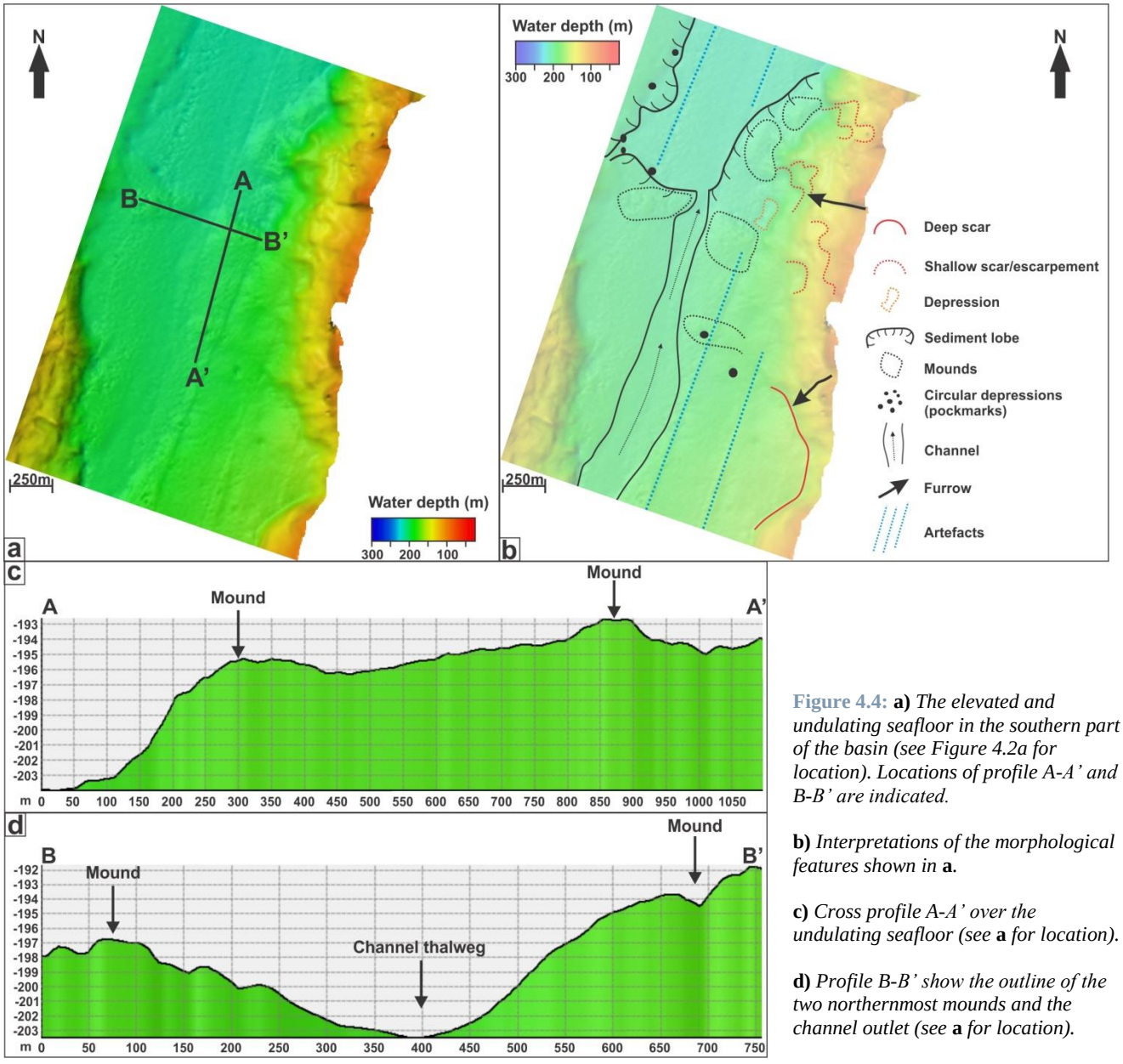

Figure 4.4: **a)** *The elevated and undulating seafloor in the southern part of the basin (see Figure 4.2a for location). Locations of profile A-A' and B-B' are indicated.*

b) *Interpretations of the morphological features shown in* **a**.

c) *Cross profile A-A' over the undulating seafloor (see* **a** *for location).*

d) *Profile B-B' show the outline of the two northernmost mounds and the channel outlet (see* **a** *for location).*

4.5 Sediment lobe area off the western fjord flank

An approx. 4 x 0.7 km^2 large sediment lobe area is located off the western slope of the study area (Fig. 4.2, 4.5, 4.7). The lobe is thickest and widest in the south, and narrows in the northern direction. Profile A-A' (Fig. 4.5) is taken across the eastern limit of the lobe, where the height difference to the adjacent seafloor is ~5 m (Fig. 4.5c). A channel-like feature can be followed down the fjord side, and as it reaches the basin floor it terminates into the south-western corner of the sediment lobe. The channel is u-shaped, however, its base is sinusoidal within its upper part. Profile B – B' is taken across the lower part of the channel, where the erosion appears to have been the greatest. Here, the channel is ~ 60 m wide and ~20 m deep (Fig. 4.5d). The north-western slope of the channel is up to > 43^o steep and displays several furrows, while the southern slope is gentler (< 22^o) and comprises scars. North of the channel, right next to where it terminates into the sediment lobe, an amphitheatre shaped scar is observed to comprise as much as five headwalls/escarpments. The heights of the escarpments decrease with water depth from ~17 m of headwall 1 to ~3 m of headwall 5 (see profile C – C' on Fig. 4.5e). Further north, a wide and deep furrow can be followed downslope into a deep scar located on the seafloor level. From this point a significantly lower elevation/thickness is registered for the sediment lobe in the northern direction. Two mounds can be observed within the sediment lobe (Fig. 4.5 and 4.7), as well as several circular depressions (*see Chapter 4.7*).

The sediment lobe is interpreted to comprise mass flow deposits, partly served by the south-western channel and processes linked to the scar formation within the fjord side. The furrows within the southern slope of the channel might be gullies formed from erosion by e.g. turbidity flows (Stoker *et al.,* 2010), while the arcuate scars along the northern slope probably reflect sliding activity. Both these features are thought to have additionally fed the channel with sediments, which in turn transported and deposited the material within the sediment lobe. The slope failure which developed the scar within the northern slope might have been a direct consequence of the mass flow processes within the channel i.e. triggered by the moving sediment masses.

Since the abruptly thinning of the lobe area coincide with the occurrence of the northern indentation it can be suggested that the slope failure within the indentation occurred later than the sliding and mass-flow processes further south. It is believed that this northern slide eroded the already deposited sediments of the lobe, and that the northern, thinner extension of the lobe was deposited as a result of this event. The two mounds observed within the northern reaches of the lobe can be due to blocks in the sub-seafloor which could have been deposited as a part of a debris flow (Gardner *et al.,* 2000).

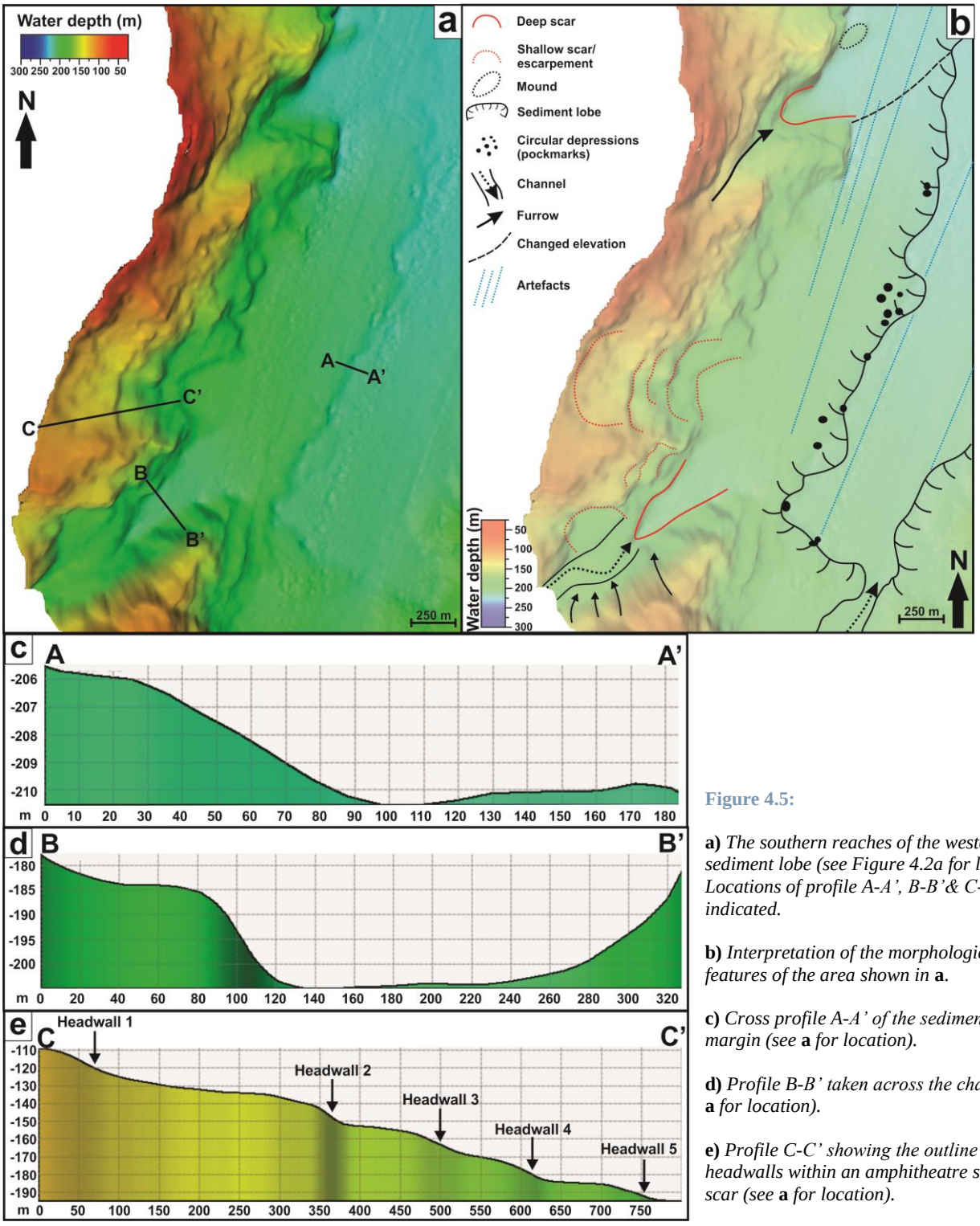

Figure 4.5:

a) *The southern reaches of the western sediment lobe (see Figure 4.2a for location). Locations of profile A-A', B-B'& C-C' are indicated.*

b) *Interpretation of the morphological features of the area shown in* **a**.

c) *Cross profile A-A' of the sediment lobe margin (see* **a** *for location).*

d) *Profile B-B' taken across the channel (see* **a** *for location).*

e) *Profile C-C' showing the outline of 5 headwalls within an amphitheatre shaped scar (see* **a** *for location).*

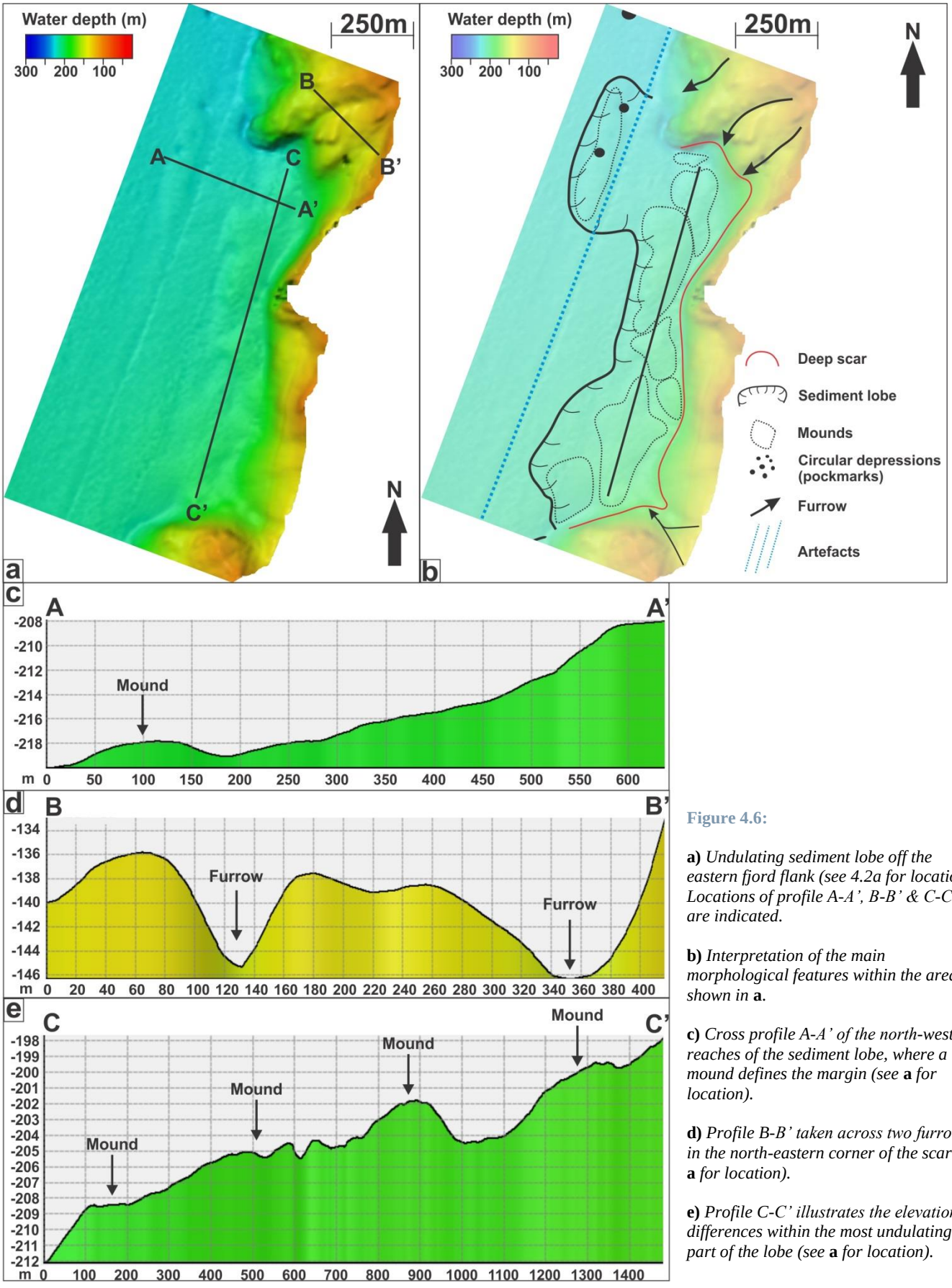

Figure 4.6:

a) *Undulating sediment lobe off the eastern fjord flank (see 4.2a for location). Locations of profile A-A', B-B' & C-C' are indicated.*

b) *Interpretation of the main morphological features within the area shown in* **a**.

c) *Cross profile A-A' of the north-western reaches of the sediment lobe, where a mound defines the margin (see* **a** *for location).*

d) *Profile B-B' taken across two furrows in the north-eastern corner of the scar (see* **a** *for location).*

e) *Profile C-C' illustrates the elevation differences within the most undulating part of the lobe (see* **a** *for location).*

4.6 Undulating sediment lobe area off the eastern fjord flank

Irregular and elevated, lobe-shaped seafloor occurs off the eastern fjord flank between approx. 4 and 6 km north of the sill (Fig. 4.6). The lobe is up to ~8 m high and between ~0.7 and ~0.2 km wide. A 700 x 80 m^2 wide mound occurs close to the northern margin of the lobe. The height difference between the mound and the relatively flat seafloor is ~2 m, while it is ~1 m to the adjacent part of the lobe (see profile A – A', Fig. 4.6c). Seven smaller and larger mounds causing an undulating appearance of the seafloor occur close to the fjord wall (Fig. 4.6b, e). These mounds are up to approx. 650 m long, 400 m wide and 11 m high.

The north-south extent of the lobe coincides with the lateral extent of a deep scar/indentation (1.8 x 0.4 km^2) in the eastern fjord side. The fjord sides within the indentation are steep (some places up to >40^o), and show several furrows which terminate on the lobe. Profile B – B' is taken across two well defined and deep (up to > 9 m) furrows, located in the north-eastern corner of the scar (Fig. 4.6d). Also the south-eastern side is incised with a furrow.

The crescentic indentation and the undulating seafloor below are interpreted to be a slide scar and mass transport deposits (MTDs), respectively (e.g. Prior *et al.*, 1982; Syvitski *et al.*, 1987; Aarseth *et al.*, 1989; Bøe *et al.*, 2000; Gardener *et al.*, 2000; Bøe *et al.*, 2003; Longva *et al.*, 2003; Stoker *et al.*, 2010). The sediment transport has also most probably been through the surrounding gullies (e.g. Stoker *et al.*, 2010).

4.7 Circular depressions

Several circular to elongated depressions, of varying size, are observed within the study area (Fig. 4.2). The depressions occur both as single features or in clusters; an example of the latter is shown in Figure 4.7. The largest depressions are up to approx. 100 m wide and 7 m deep, while the smaller ones are about 50 m wide and 3 m deep (Fig. 4.7c).

The circular to elongated depressions are interpreted to be pockmarks. Pockmarks have earlier been described to occur as both singular and clustered within Lyngenfjorden (Hovland & Judd, 1988; Jensen, 2010). Pockmarks are craters formed from fluid seepage, i.e. upward migration and escape of gas or water, escape through the seafloor (Hovland & Judd, 1988). As the fluids escape through the seafloor they are capable of removing unconsolidated seabed sediments, leading to the formation of depressions (Hovland & Judd, 1988; Judd & Hovland, 1992).

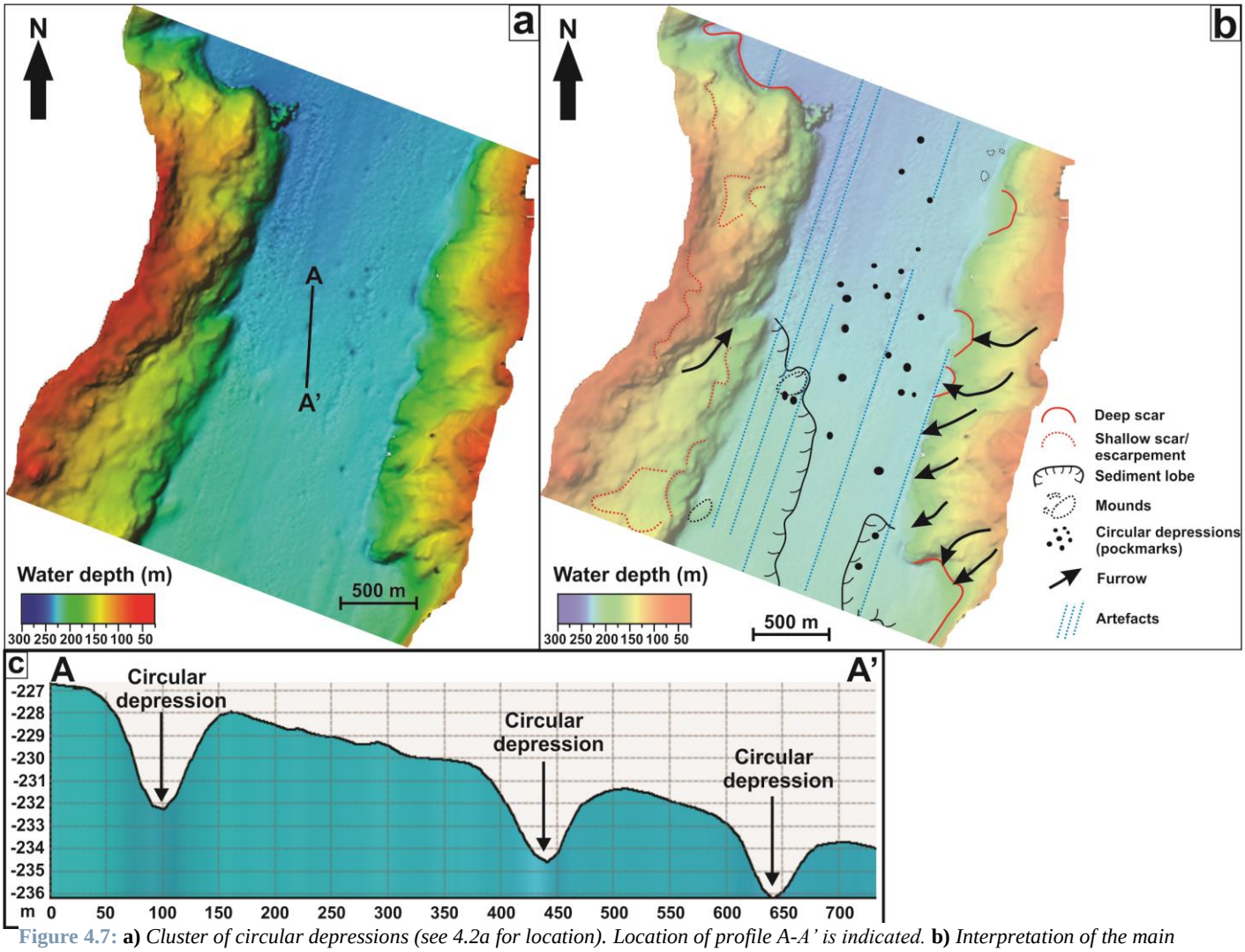

Figure 4.7: **a)** *Cluster of circular depressions (see 4.2a for location). Location of profile A-A' is indicated.* **b)** *Interpretation of the main morphological features within the area shown in* **a**. **c)** *Cross profile A-A' over three of circular depressions (see* **a** *for location).*

5 Seismostratigraphy

5.1 Introduction

In the following chapter the chirp sonar data will be addresses to complement the swath bathymetry data (*Chapter 4*) and the sediment cores (*Chapter 6*). A total of seven lines were selected from the collected data (for location see Fig. 5.1).

Longitudinal lines:
Line 1-1'; Lyngen001
Line 2-2'; Lyngen016
Line 3-3'; Lyngen004

Cross lines:
Line A-A; Lyngen011
Line B-B'; Lyngen010
Line C-C'; Lyngen008
Line D-D'; Lyngen007

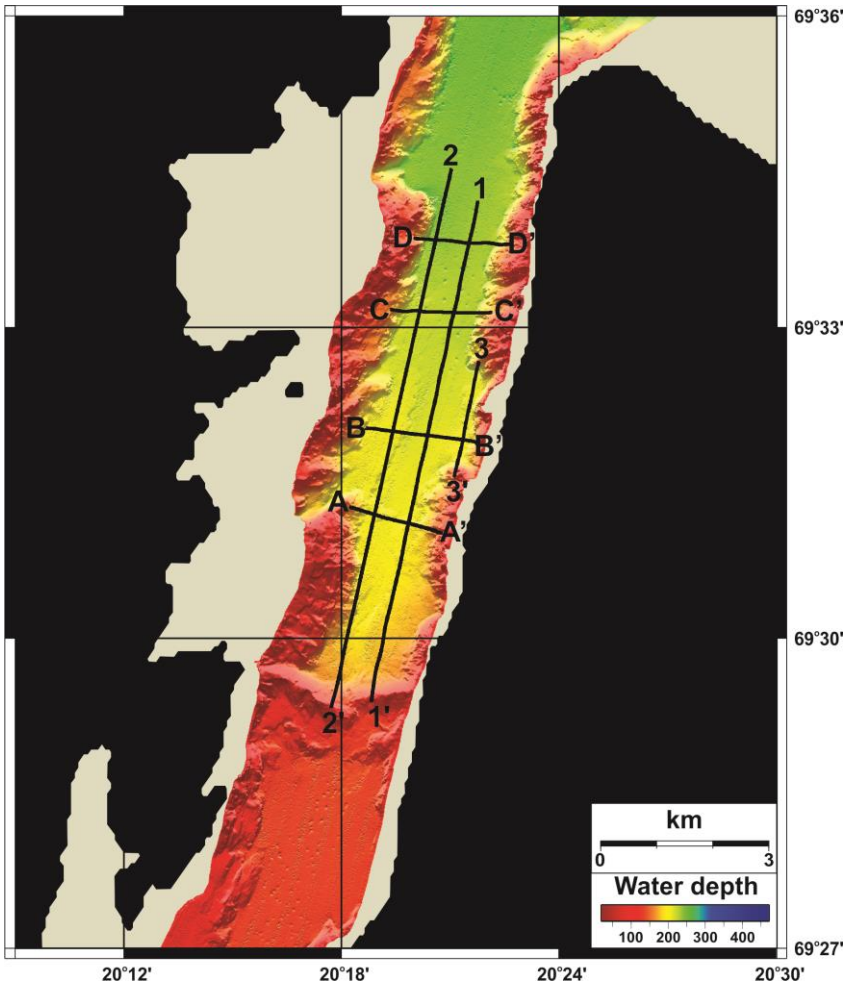

Figure 5.1: Location of the chirp lines selected for this study
(For location of the study area, *see Fig. 4.1; Chapter 4.1)*

The main reflections and units identified in the chirp lines are described and interpreted. However, the main emphasis is given mass transport deposits (MTDs).

In all two-way-travel time (s), twt, to depth (m) conversions a p-wave velocity of 1490 m/s is used, based on average velocities obtained with the MSCL (*see Chapter 3.2.1; Multi-sensor core logger*).

5.2 Seismostratigraphic description and interpretation

The reflection pattern varies from south towards north, as well as between the areas near the western and the eastern fjord flank. However, four regional reflections and two units have been identified within the sub-seafloor together with commonly occurring mass-transport deposits.

5.2.1 Reflection R1 and unit 1

The topmost reflection (R1) is caused by the seafloor. It is the upper boundary (Fig. 5.2, 5.3, 5.4, 5.5, 5.6, 5.7 & 5.8) of the seismostratigraphic unit 1. It is a continuous reflection with varying intensity. The undulating shape of the seabed reflection reflects the morphology of the sub-seafloor generally well. However, local differences occur. E.g. the reflection on-laps both the western end eastern fjord side, as well as the threshold which defines the basin in the southern part (e.g. Fig. 5.2).

Unit 1 is an acoustically semitransparent to transparent package underlying reflections R1. Its thickness is highly depended upon the underlying sub-seafloor, as the lower boundary of the unit is defined by either the regional reflection R3 or occurring MTDs (Fig. 5.2, 5.3, 5.4, 5.5, 5.6, 5.7 & 5.8). Large MTD complexes are observed within the stratigraphy for the entire southernmost part of the basin (*see Chapter 5.2.5, below*), extending approx. 7.25 km from the threshold, and overlying these deposits the thickness of the unit varies the most (~ 1-9 m). Furthermore, in the inner part of the basin the unit appears as a wedge thinning out towards the sill (Fig. 5.2). Within the northern part of the basin, where the unit directly overlies reflection R3 (*see Chapter 5.2.3*), its thickness is more or less uniform (up to ~7.5 m). The unit generally lacks in internal structures. However, a high-amplitude reflection (R2) occurs at depth 2.5-3 m (*see Chapter 5.2.2, below*). Furthermore, few low-amplitude, discontinuous internal reflections are observed.

The acoustically transparent signature of the unit indicates a relatively uniform lithological composition of the sediments. Based on this, together with the position of the unit in the stratigraphy, the unit most probably formed from continuous suspension fallout within an open marine environment.

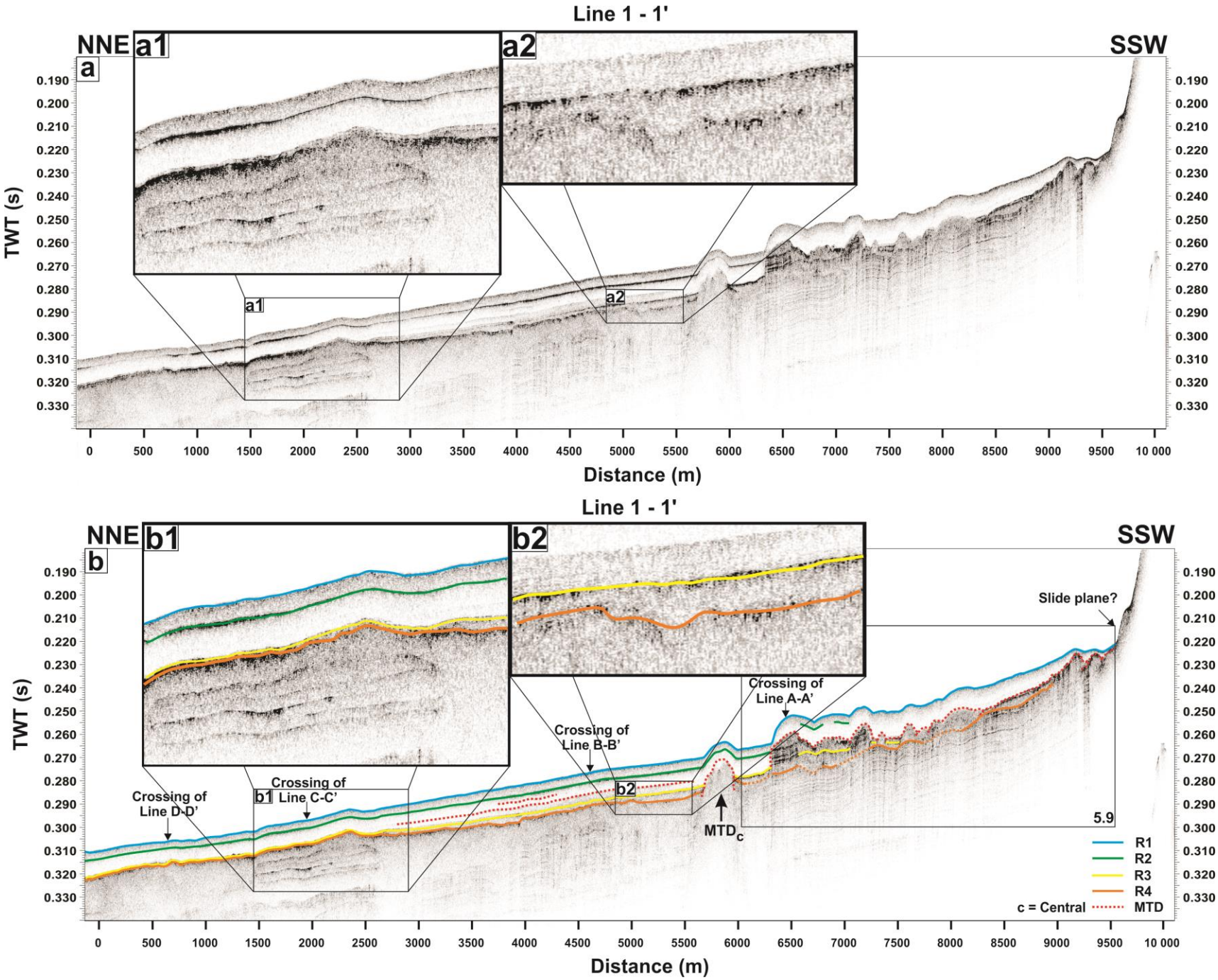

Figure 5.2:

a) *Chirp line 1-1'with close-up in a1 and a2. For location see Fig. 5.1.*

b) *Interpretation of reflections and MTDs, where the latter is provided with a letter indicating the position within the study area. Locations of crossing lines are indicated*

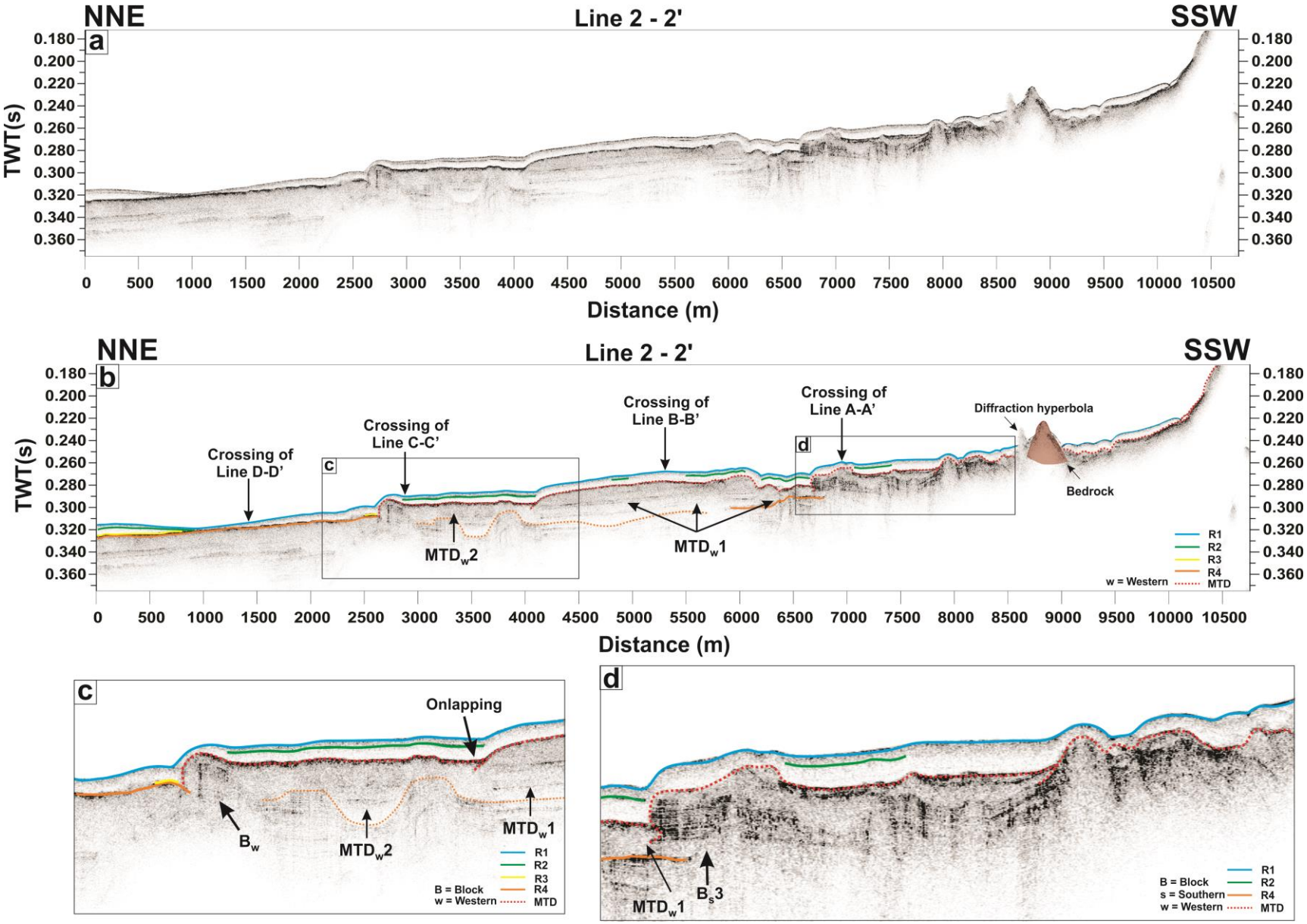

Figure 5.3: **a)** *Chirp line 2-2'. For location see Fig. 5.1.* **b)** *Interpretation of reflections and MTDs, where the latter is provided with a letter and number indicating the position within the study area. Locations of crossing lines are indicated, as well as location of c and d.* **c)** *Close-up of area indicated in b.* **d)** *Close-up of area indicated in b.*

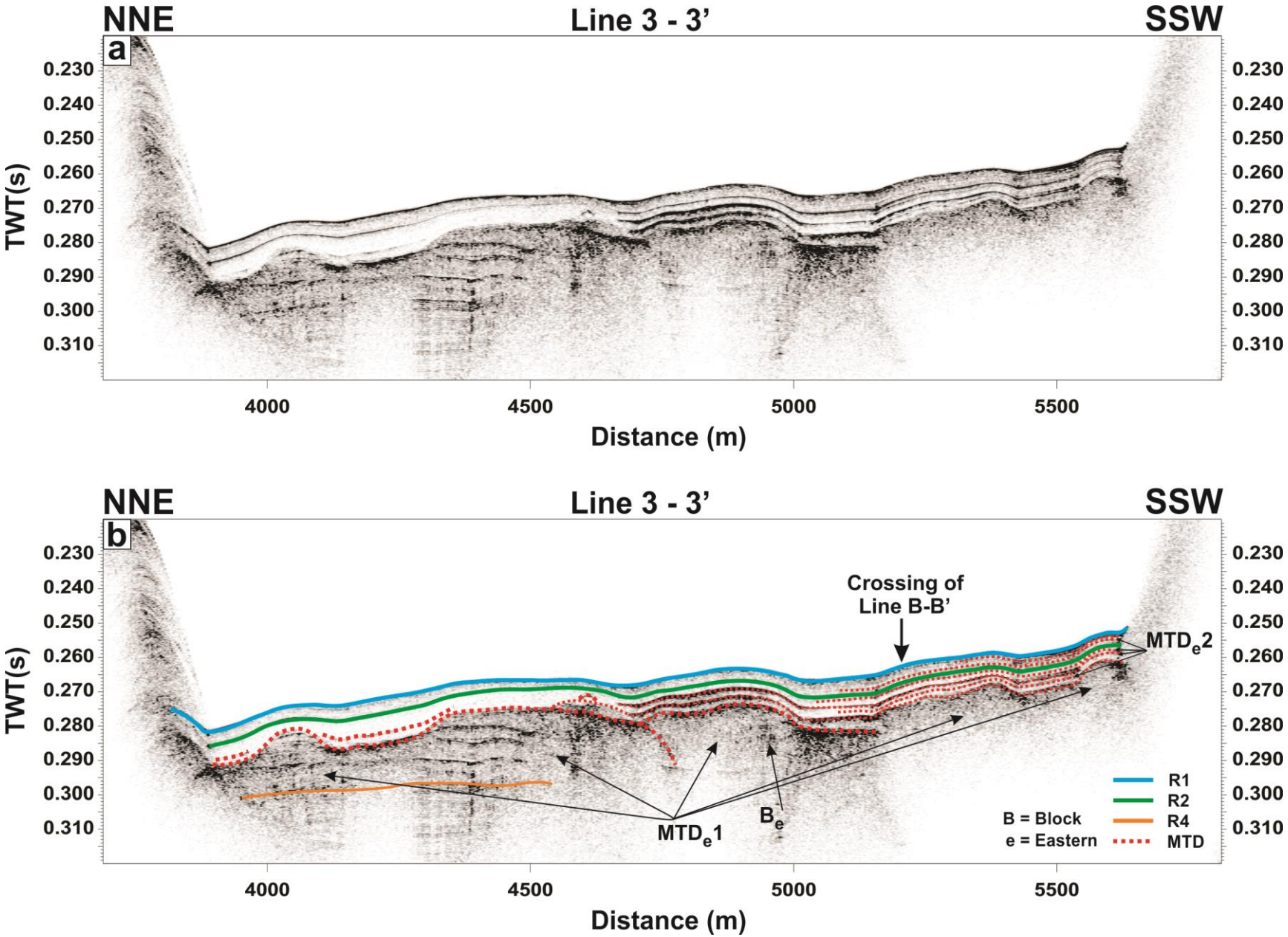

Figure 5.4:

a) *Chirp line 3-3'. For location see Fig. 5.1.*

b) *Interpretation of reflections and MTDs, where the latter is provided with a letter and number indicating the position within the study area. Location of crossing line B-B' is indicated.*

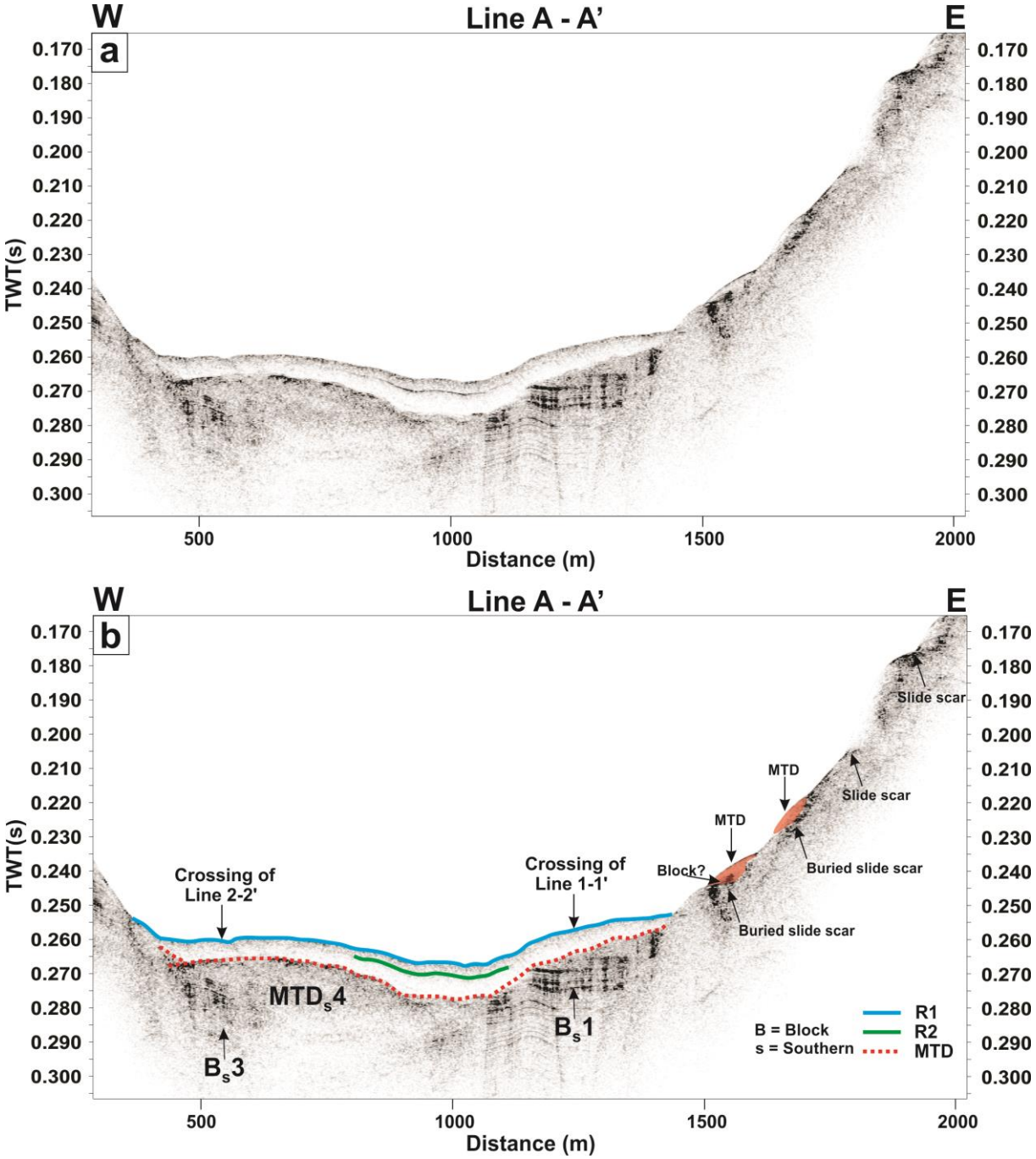

Figure 5.5: **a)** *Chirp line A-A'. For location see Fig. 5.1.* **b)** *Interpretation of reflections and MTDs, where the latter is provided with a letter and number indicating the position within the study area. Locations of the crossing point with line 1-1' and 2-2' are indicated.*

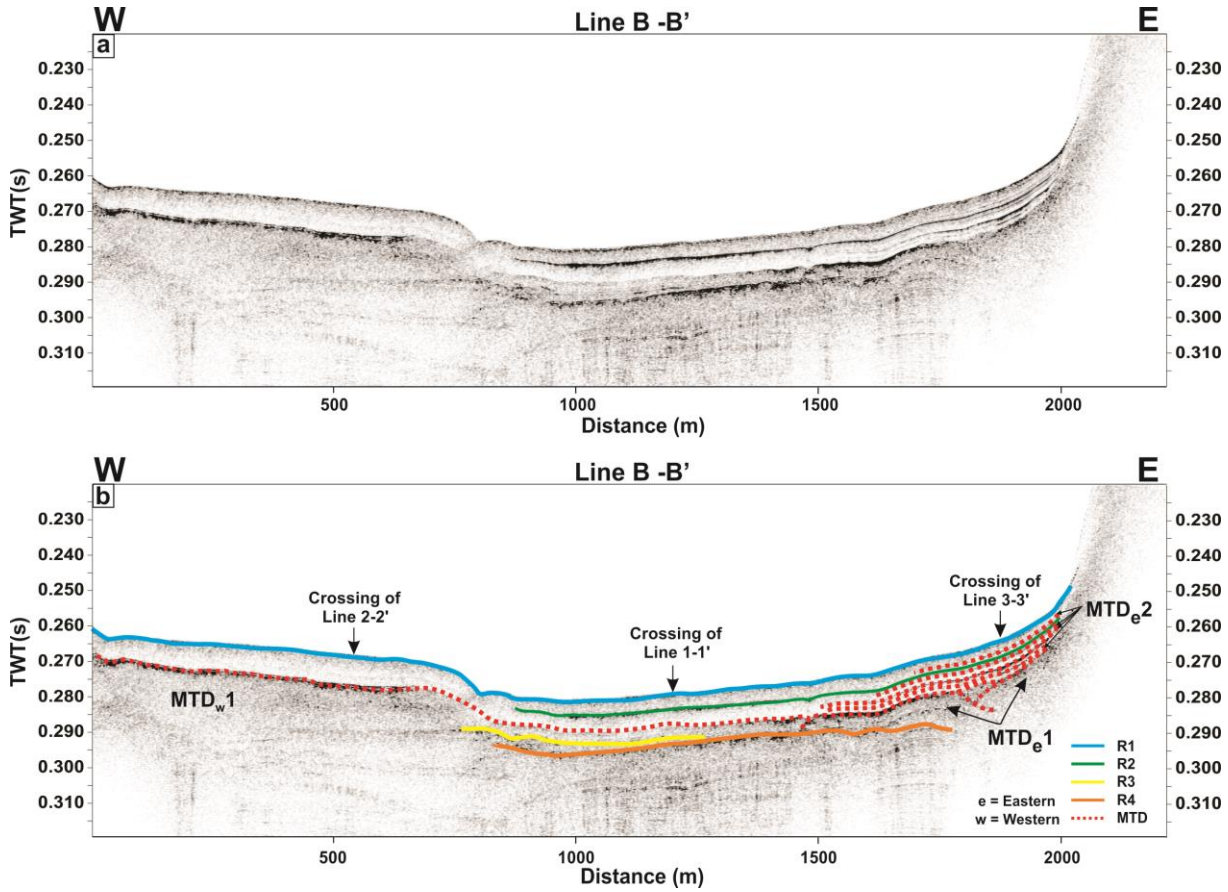

Figure 5.6: **a)** *Chirp line B-B'. For location see Fig. 5.1.* **b)** *Interpretation of reflections and MTDs, where the latter is provided with a letter and number indicating the position within the study area. Locations of the crossing point with line 1-1', 2-2' and 3-3' are indicated.*

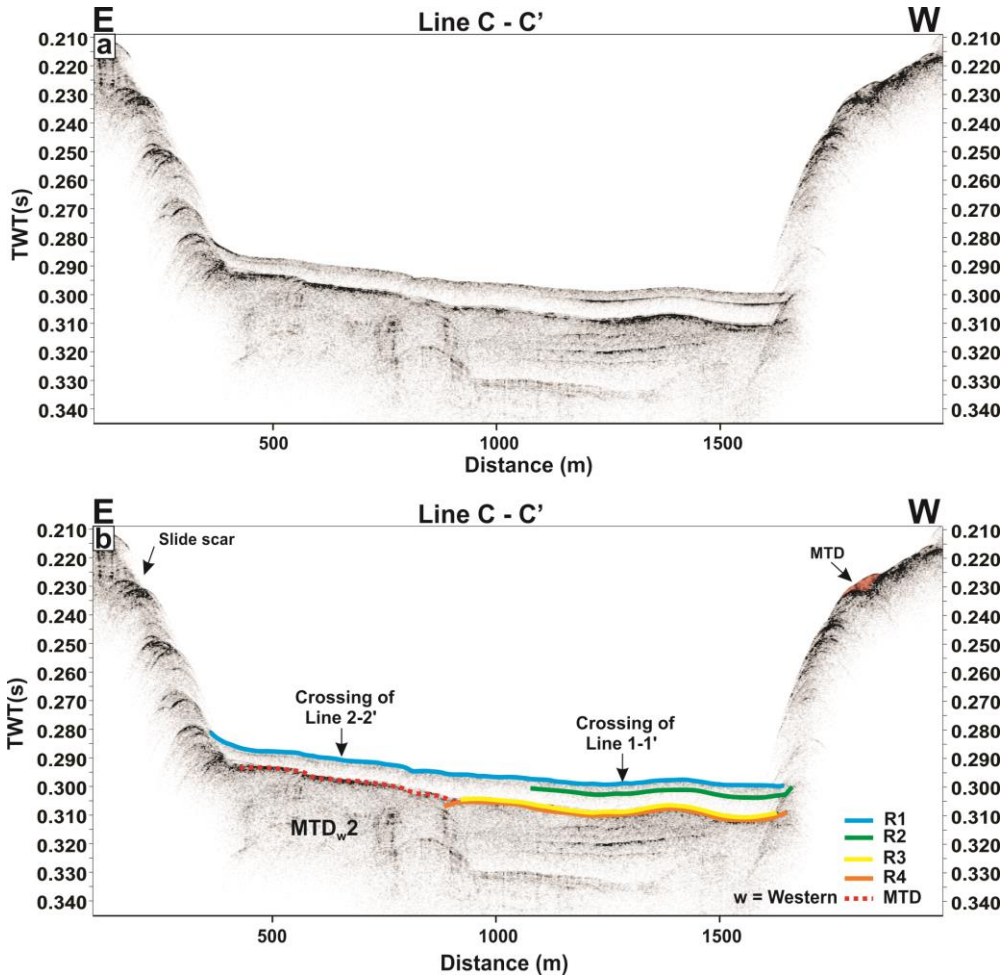

Figure 5.7:

a) *Chirp line C-C'. For location see Fig. 5.1.*

b) *Interpretation of reflections and MTDs, where the latter is provided with a letter and number indicating the position within the study area. Locations of the crossing point with line 1-1' and 2-2' are indicated.*

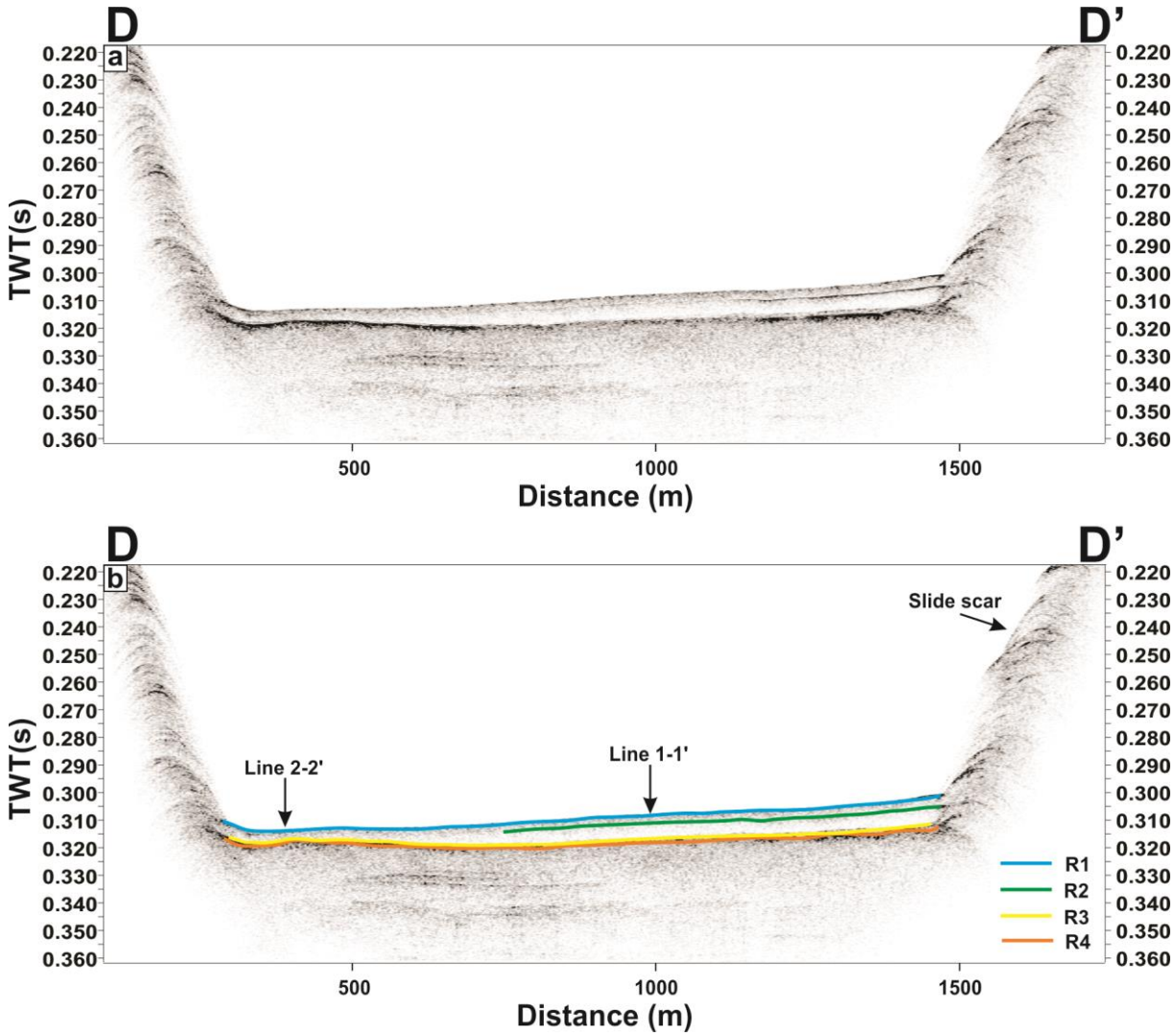

Figure 5.8: **a)** *Chirp line D-D'. For location see Fig. 5.1.* **b)** *Interpretation of reflections. Locations of the crossing point with line 1-1' and 2-2' are indicated.*

5.2.2 Reflection R2

R2 is a high-amplitude and discontinuous reflection (Fig. 5.2, 5.3, 5.4, 5.5, 5.6, 5.7 & 5.8), which underlies reflection R1 with approx. 2.5 – 3 m over an area of minimum 7.4 x 1.3 km^2. It is strongest in the eastern parts of the basin, where it on-laps onto the fjord side. However, it gets weaker and thinner towards west (Fig. 5.6, 5.7 & 5.8). R2 is most dominant within the southern part of chirp line 3-3' (Fig. 5.4) and the eastern part of chirp line B-B' (Fig. 5.6), where it is located slightly deeper in the stratigraphy (depth below R1 is up to ~3.7 m). The reflection is not possible to observe near the western fjord side, nor in the southernmost part of the basin. The southern limit of the reflection is approx. 3.5 km north of the sill, from where the reflection is strongest in the south before getting weaker after ~2.5 km (Fig. 5.2). Reflection R2, as for R1, mirrors the underlying sub-seafloor.

The reflection is interpreted to represent a mass transport deposit. The relatively long run-out distance compared to its length suggests a viscous behavior of the flow (e.g. Vorren & Laberg, 1997). Turbidity

flows are a typical viscous flow/fluid flow (Syvitski *et al.,* 1987), however, a debris flow can also develop a viscous character (Vorren & Laberg, 1997). Since the reflection is strongest and most dominant within the eastern part of the basin, where it additionally on-laps the fjord side, the deposit is suggested to be the result of a mass transport event triggered on the eastern fjord side. Furthermore, the high-amplitude of the reflection in the southern part of chirp line 3-3' correlates well with its strong appearance in the central part of the basin in chirp line 1-1'. Therefore, the initial slide is believed to have occurred within the eastern fjord side within an area approx. 4-5 km north of the threshold. The occurrence of R2 slightly further down in the stratigraphy proximal to the interpreted location of origin (Fig. 5.4), is thought to be caused by a greater erosional effect of the flow here than in its distal reaches.

5.2.3 Reflection R3

R3 is a high- to low- amplitude discontinuous reflection (Fig. 5.2, 5.3, 5.4, 5.5, 5.6, 5.7 & 5.8). The reflection can be traced over an area of at least ~7.25 x 1.5 km^2. However, it cannot be identified in those parts of the basin where MTDs are dominant, i.e. in the southernmost part of the basin, and areas along the western and eastern fjord side (Fig. 5.2, 5.3, 5.4, 5.5, 5.6 & 5.7; *see also Chapter 5.2.5*). Nevertheless, the reflection can be traced underlying parts of the southern MTD complex (Fig. 5.2 & 5.9). It is strongest within an area approx. 3.5 – 7.25 km from the threshold. In this area the reflection is located at depth ~9.5 m below the seafloor and it overlies reflection R4 with approx. 1.5 m, which is highly disturbed within this area (Fig. 5.2b2; *see also Chapter 5.2.4*). The interval separating these two reflections is both semitransparent and partly chaotic. Further north in the basin the reflection is located slightly shallower in the sub-seafloor (~7.5 m), directly overlying reflection R4. The amplitude of the reflection is weaker, and the underlying reflection R4 is not observed to be significantly disturbed (Fig. 5.2b2). Furthermore, within this area the reflection should rather be described as two thinner reflections (too thin to be measured) where a semitransparent wedge (~0.75 m) can be observed between them. Reflection R3 is observed to be stronger in the eastern reaches of the basin compared to the western.

Reflection R3 is suggested to represent a mass-transport deposit that covers an area of at least 7.2 x 1.2 km^2. As for reflection R2, its long lateral extent compared to its thickness suggests a viscous behavior of the flow (e.g. Vorren & Laberg, 1997). This could be obtained by e.g. a turbidity flows (Syvitski *et al.*, 1987) or debris flows (Vorren & Laberg, 1997). The configuration of the reflections (thickest and strongest in the east and the south) indicate that the slope failure occurred within the southeastern parts of the study area. Furthermore, the disturbances of the underlying reflectors also indicate that the flow was initiated in the inner part of the basin since the flow most probably disturbed/eroded the underlying reflectors during its emplacement (cf. Laberg & Vorren, 1995, Vardy *et al.,* 2012, Haussler

et al., 2014). Such an effect indicates a high energy of the flow. As the flow becomes weaker in its distal areas, the impact on the underlying sediments will become smaller.

Since R3 overlies reflection R4, defined as the upper boundary of unit 2 (glacier proximal sediment; *see Chapter 5.2.4*, below), the slope failure most probably occurred shortly after the retreat of the glacier from the sill during the last deglaciation.

5.2.4 Reflection R4 and unit 2

Reflection R4 is a high to low amplitude continuous to discontinuous reflection (Fig. 5.2, 5.3, 5.4, 5.5, 5.6, 5.7 & 5.8), which marks the upper boundary of seismostratigraphic unit 2. The reflection is in many areas difficult to follow, either caused by strong overlying reflections casting acoustic shadows or by disturbance/erosion caused by subsequent mass wasting (*see Chapter 5.2.3 & 5.2.5*). The depth of R4 within the sub-seafloor varies between ~1.5 – 16.5 m.

Unit 2 is the lowermost seismostratigraphic unit. It is generally semitransparent to acoustically stratified. The unit can be recognized underlying R4 in all the chirp lines, however, the lower boundary of unit 2 cannot be identified on the chirp sonar data. Near the threshold the internal reflections of the unit become closer spaced, sub-parallel and more oblique. However, diffraction hyperbolas are also observed (Fig. 5.2).

Based on the semitransparent to acoustically stratified character of the unit, together with its position in the stratigraphy, it is suggested that the unit is composed of glaciomarine proximal sediments (e.g. Cai *et al.*, 1997; Syvitski & Lee, 1997; Forwick & Vorren, 2010; Forwick *et al.*,2010); deposited while the ice front was located at or near the sill. The disturbances near the threshold might reflect unstable sediments and a high energy conditions caused by high sedimentation rates (Jenssen, 2006). Diffraction hyperbolas can represent ice rafted debris (IRD) (cf. Cai *et al.*, 1997; Plassen & Vorren, 2003; Lysså *et al.*, 2004). The discontinuous nature of the upper reflection of the unit, R4, can indicate instability of the sediments caused by e.g. synsedimentary faults and/or mass transport events (Jenssen, 2006).

5.2.5 Mass transport deposits (MTDs)

Different types of mass transport deposits have been identified in addition to R2 and R3. These are commonly found as packages with chaotic acoustic inner structures, defined by a high- to low amplitude, hummocky upper reflection. However, some deposits are also found to be well stratified and some occur as wedges thinning towards the central basin. In the text below are deposits of these characteristics assumed to be MTDs, and their description will be given based upon this assumption.

The MTDs are restricted to the part of the study area/ basin extending 7.25 km in the northern direction from the threshold (Fig. 5.2 & 5.3), where they dominates the sub-seafloor within the southernmost 3.5 km and along (Fig.5.2, 5.3 & 5.9) the western (5.3, 5.6 & 5.7) and eastern fjord side (Fig. 5.4 & 5.6). In the following text the MTDs are described after their location in the basin, which has been separated into four main areas; the southern part, the western side, the eastern side and the central fjord basin.

5.2.5.1 Mass transport deposits in the southern, innermost part of the basin.

The sub-seafloor stratigraphy of the southern, innermost part of the basin, extending ~3.5 km from the threshold, indicate several MTDs at depths between ~5 – 15 m. This area is defined by a hummocky upper reflection with high to low amplitude, and chaotic acoustic internal reflections (MTD_s1, MTD_s2 & MTD_s3 in Fig. 5.9, and MTD_s4 in Fig. 5.5). However, two acoustically well stratified blocks, B_s1 & B_s2, are identified on chirp line 1-1' (Fig. 5.9). The largest and northern block (B_s1) defines the outer margin of this irregular area, hereafter referred to as the southern MTD complex. B_s1 is ~9.7 m high and ~275 m long, and located approx. 3.5 km north of the threshold ~5 m below the seafloor. The block extends ~300 m from the eastern fjord side (Fig. 5.5), suggesting that it was initiated and transported along the eastern side of the fjord. Right across block B_s1, at the same level in the stratigraphy, a great mound can be identified in chirp line A-A' (MTD_s4 in Fig.5.5). The mound reaches ~7 km between the western fjord side and the east lying block (B_s1), and has a high-amplitude discontinues upper reflection and a chaotic inner structure. Near the western fjord side it is observed to be acoustically stratified (B_s3) (Fig. 5.5 & 5.3). The mound could represent a blocky debris flow (cf. Gardner *et al.,* 2000; Vanneste *et al.,* 2012) initiated on the western fjord side. However, the fact that the mound occurs at the same level as B_s1 in the stratigraphy, is measured to have the same height and south-north extent, and is partly acoustically stratified, require a second possible interpretation. The block and the mound can represent the same morphological feature; one block deposited during a single event. The block would in this case be as much as ~1 km from east to west, which demands that a great failure took place. The depression separating the features is the channel described from the bathymetry data (*see Chapter 4.2.2; Channel*), and the depression may therefore be the product os erosion caused by the channel. The chaotic pattern described for the mound can be caused be later disturbances or by noise during data collection. However, transport of one such great block without further deformation is believed to be uncertain, meaning that block B_s1 and B_s3 was deposited during two different events.

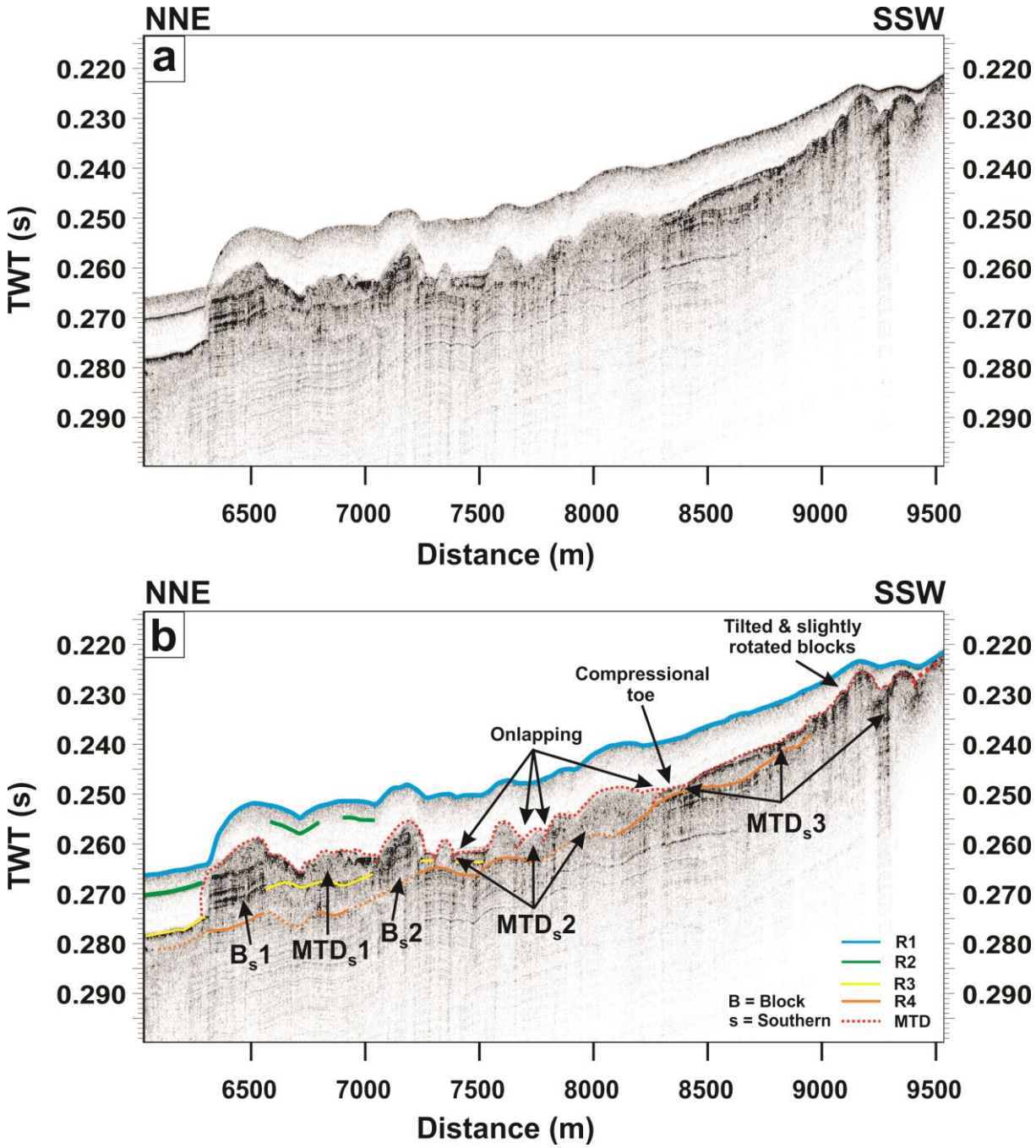

Figure 5.9: **a)** *Close-up of chirp line 1-1'. For location see Fig. 5.2.* **b)** *Interpretation of reflections and MTDs, where the latter is provided with a letter and number indicating their position within the study area.*

The second, and southern block (B_s2) identified in chirp line 1-1' (Fig. 5.9) is located approx. 3 km from the threshold at the same level within the sub-seafloor as the northern block (B_s1) (~5 m below the seabed). The block is ~7.5 m high and ~200 m long.

Below all the identified blocks (B_s1, B_s2 & B_s3), a disturbed reflection overlies the glaciomarine sediments of unit 2. Between this disturbed reflection and the well stratified part of the blocks is a ~3 m thick zone of disturbed reflections (Fig. 5.2, 5.3 & 5.9). The zone of disturbed reflections is assumed to be matrix material of a debris flow, and it is, therefore, suggested that the blocks are rafted

blocks following a debris flow (cf. Gardner *et al.,* 2000; Vanneste *et al.,* 2012). The northern block is overlain by a cover of sediments with disturbed reflections, which is ~0.7 - 3.7 m thick. Following the sediment cover down the southern side of the block it is revealed that this is a part of a larger MTD (MTD_s1 in Fig. 5.9) with chaotic to transparent acoustic internal reflections and a hummocky top reflection located. MTD_s1 is located between the two blocks, B_s1 and B_s2, and is approx. 5 m high and 100 m long in the south-north direction. Since the northern extent of MTD_s2 is observed as a cover over $B_s1$it most represent a later occurring event than the deposition of the block.
Reflection R3 (*see Chapter 5.2.3*) can be identified between block B_s2 and the sill, as well as north of block B_s1. However, the reflection was not possible to trace below the blocks. This indicates that the blocks disturbed/eroded the underlying reflector during emplacement (cf. Laberg & Vorren, 1995, Vardy *et al.,* 2012, Haussler *et al.,* 2014).

South of the block B_s2, a minimum of five mounds/lenses are stacked together (MTD_s2) and extends over ~1 km in the south-northern direction (Fig. 5.9, see also Fig.5.2 & 5.3). They all have a low-amplitude upper reflection and a chaotic to transparent internal structure. The mounds are up to ~6 m high and 400 m long. The deposits are connected with onlapping morphology (Fig. 5.9), indicating different events of deposition. All these mounds/lenses (MTD_s2), together with MTD_s1 located between the two blocks, are probably debris flows (cf. Laberg & Vorren, 1995; Vorren & Laberg, 1997; Bøe *et al.,* 2003; Stoker *et al.,* 2010; Forwick & Vorren, 2012; L'Heureux *et al.,* 2012). The reflection of unit 2 undulates below some of these MTDs, indicating that the debris flow disturbed some of the underlying sediments.

Adjacent to the stacked debris flow mounds (MTD_s2), a feature interpreted to be a sliding complex (MTD_s3) extends 1.5 km from the threshold (Fig. 5.2& 5.9). The slide is thought to be initiated from a slide plane observed on the steep slope of the threshold (Fig. 5.2). The tilted and slightly rotated sediment blocks in the inner part of the complex are thought to represent the initial slide (Fig. 5.9). The sediment blocks have a high amplitude upper reflection and chaotic acoustic internal reflections, however, their upper reaches are partly stratified. Further down the slope a debris flow pile occurs, and further suggests that the slide developed into a debris flow. This deposit has a strong upper reflection and no internal structures, however, chaotic internal structures are observed within what is interpreted to be the compressional toe of the slide (Fig. 5.9) (cf. Syvitski *et al.,* 1987; Aarseth *et al.,* 1988; L'Heureux *et al.,* 2010).

Chirp line A-A' reveals several slide scars and buried slide scars on the eastern slope of the fjord, providing evidence of repeated slope failures (Fig. 5.5).

5.2.5.2 Mass transport deposits along the western fjord side

Located approx. 3.5 km north of the threshold near the western fjord side, a larger MTD (MTD_w1) is observed adjacent to B_s3 described above (*see Chapter 5.2.5.1*) (Fig. 5.3b&d). The MTD_w1 has eroded into the B_s3 (Fig. 5.3d), indicating a later event behind the deposition of this MTD. MTD_w1 extends ~2.6 km in the northerly direction and ~ 1.5 km in the easterly direction (Fig. 5.3 & 5.6). Its thickness varies between ~ 7.5 - 25 m, where its southern reaches (~0.5 km) are much thinner than the rest of the deposit. Within this southern part of MTD_w1 the chirp character is defined by an undulating top reflection and chaotic internal reflections (Fig. 5.3b). The thickness of the rest of MTD_w1 is almost uniform below a relatively straight upper reflection. Some sub-parallel internal reflections are observed in an otherwise acoustically transparent inner reflection (Fig. 5.3b). These properties of the MTD can also be found ~0.8 km in the eastern direction; however, beyond that point the MTD becomes dramatically thinner towards east (< 2.2 m) (Fig. 5.6). MTD_w1 overlies unit 2 (*see Chapter 5.2.4*). However, reflection R4 is difficult to trace (Fig. 5.3) which may indicate that the reflector was disturbed / eroded during mass wasting (cf. Laberg & Vorren, 1995, Vardy *et al.*, 2012, Haussler *et al.*, 2014). The character of the MTD indicates that it was deposited by a debris flow (cf. Laberg & Vorren, 1995; Vorren & Laberg, 1997; Bøe *et al.*, 2003; Stoker *et al.*, 2010; Forwick & Vorren, 2012; L'Heureux *et al.*, 2012), initiated within the western fjord side.

The northern parts of the debris flow deposit (MTD_w1) are onlapped by a later occurring MTD (MTD_w2 in Fig. 5.3b&c) with similar characteristics, including a relative straight high-amplitude upper reflection and an acoustically transparent inner reflection. This feature extends approx. 1.5 km in the northern direction, and ~0.5 km towards the east (Fig. 5.3 & 5.7) where its thickness varies greatly (~3.7 – 22 m). The northern part of the MTD is acoustically stratified (150 x 10 m^2), indicating a sediment block (B_w in Fig.5.3c). MTD_w2 is interpreted to be debris flow initiated within the western fjord side, and where the sediment block represents a slide block embedded in the debris (cf. Gardner *et al.*, 2000; Vanneste *et al.*, 2012). Truncations of reflectors at the base of the unit indicate that it was eroding as it flowed.

MTD_w1 and MTD_w2 will hereafter be referred to as the western MTD complex.

5.2.5.3 Mass transport deposits along the eastern fjord side

Chirp line 3-3' crosses an indentation of the eastern fjord side, and reveals that the sub-seafloor at depths between ~4.5 and 19 m is dominated by MTDs (MTD_e1 in Fig. 5.4). However, in the southern part of the indentation MTDs are observed up to ~0.7 m below the sub-seafloor (MTD_e2). MTD_e1 is composed of minimum 5 mounds/lenses having a high-amplitude upper reflection and a chaotic high- to low-amplitude internal reflection (Fig. 5.4). However, one of these mounds is partly acoustically stratified (B_e in Fig. 5.4). The mounds are up to > 0.5 km long and ~22 m thick. They partly truncate the underlying reflections, indicating erosion. MTD_e2 is composed of several high- to low-amplitude

reflections, which overly the mounds in the southern part of the chirp line 3-3' (Fig. 5.4). Chirp line B-B' (Fig. 5.6) indicate that the MTDs onlaps the eastern fjord side.

The stacked mounds (MTD_e1 in Fig. 5.4) might represent debris flow deposits (cf. Laberg & Vorren, 1995; Vorren & Laberg, 1997; Bøe *et al.*, 2003; Stoker *et al.*, 2010; Forwick & Vorren, 2012; L'Heureux *et al.*, 2012). The stratified internal reflections could represent a slide block incorporated in the debris (B_e in Fig. 5.4) (cf. Gardner *et al.*, 2000; Vanneste *et al.*, 2012). The high- to low-amplitude reflections (MTD_e2) might also be the result of debris flows, but could also be the result e.g. turbidity flows (cf. Syvitski & Schafer, 1994; St.Onge *et al.*, 2012).

5.2.5.4 Mass transport deposits within the central part of the fjord basin

Several transparent wedges thinning towards the fjord axis occur in the central fjord basin between 3.5 and 7.25 km north of the threshold (Fig. 5.2 & 5.6). The lowermost of these wedges is recognized as reflection R3 (*see Chapter 5.2.3*), while the overlying wedges are interpreted to represent the distal parts of the MTDs originating from the western and eastern fjord sides (*see Chapter 5.2.5.2 & 5.2.5.3*). In addition to the wedges, a low-amplitude to acoustically transparent body is located in the southern part of the central fjord basin (~ 4 km from the threshold) (MTD_c in Fig. 5.2). MTD_c is ~300 m long and has a minimum thickness of 11 m and can be followed towards the eastern side of the basin (this chirp data is not displayed in this thesis). The deposit is suggested to be a debris flow (cf. Laberg & Vorren, 1995; Vorren & Laberg, 1997; Bøe *et al.*, 2003; Stoker *et al.*, 2010; Forwick & Vorren, 2012; L'Heureux *et al.*, 2012) originating from the eastern fjord side. MTD_c intersects reflection R3, and is therefore suggested to represent a later mass-transport event than that behind the deposition of R3 (*see Chapter 5.2.3*).

6 Lithostratigraphy

6.1 Introduction

Five sediment cores, three gravity cores and two piston cores were retrieved from the basin described in chapter 4 (Fig. 6.1; Tab. 6.1). They are all located along chirp line 1 – 1' *(see Chapter 5*). The core sites were chosen to penetrate into mass-transport deposits.

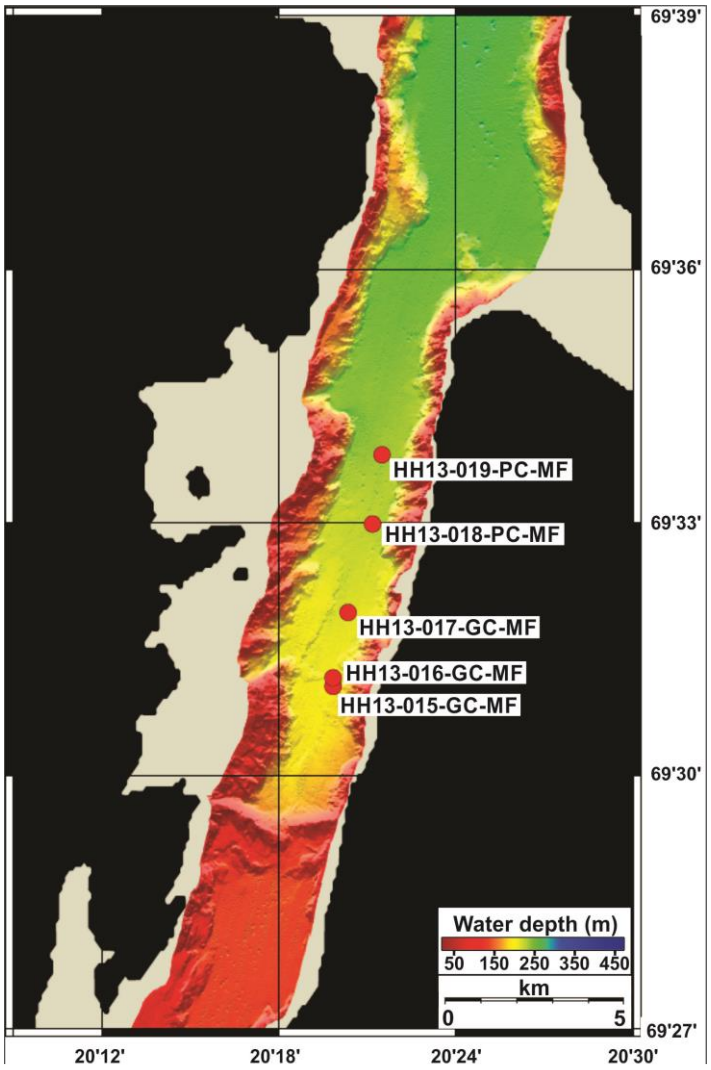

Figure 6.1: *Map of the study area. The core locations are indicated with red circles (see Table 6.1)*

Lithostratigraphic units were defined by visual observations of the sediment surface and of X-ray photographs, complemented by marked changes in physical properties, grain-size and element geochemistry. The units are given numbers, where higher numbers indicate larger depth. In some cases, where the unit appears complex, it was deemed necessary to subdivide into sub-units (a, b, c…etc.). The units are described and interpreted from the lowermost unit to the top of the core.

Core	Lat. (N)	Long. (E)	Water depth (m)	Penetration (m)	Total length (cm)	No. of sections
HH13-015-GC-MF	69° 31.068’	020° 19.829’	195	~6	392	4
HH13-016-GC-MF	69° 31.164’	020° 19.833’	202	~6	374	4
HH13-017-GC-MF	69° 31.943’	020° 20.342’	212	~6	413	5
HH13-018-PC-MF	69° 32.992’	020° 21.174’	225	>8	574	6
HH13-019-PC-MF	69° 33.812’	020° 21.498’	235	~12	474	5

Table 6.1: Core location, water depths, penetrations, total length (total cored interval) and numbers of sections.

6.1.1 Visual description / lithological logs

The lithological logs are based on study of the sediment surface (e.g. colour, lithology, structure) and X-ray images (e.g. structures, bioturbation, lithological changes), supported with results from grain-size analyses. These logs, together with colour pictures of the cores, are presented in figures 6.2, 6.7, 6.13, 6.19 & 6.24. The widths of the logs indicate the composition of the matrix. Clasts are marked as individual features.

Multiple lithofacies are distinguished (*see Chapter 6.1.6, below*). Each lithological unit contains one or more lithofacies. Bioturbation, fossils and fossil fragments are indicated in the logs. Dark spots observed on fresh sediment surfaces are suggested to be sulphide traces caused by a bacterial process of sulphate reduction (e.g. Forwick, 2001). These dark spots disappear after some time.

6.1.2 Grain-size analyses

Volume percentages of clay, silt and sand, together with the grain-size parameters (mean, sorting, skewness and kurtosis) (*see Chapter 3.4.10; Grain-size Distribution*), are presented vs. depth in figures 6.3, 6.8, 6.14, 6.20 & 6.25. The material was generally collected at certain intervals (commonly every 10 cm). Therefore, grain-size distribution results for some units are not provided. Grains larger than 2000 μm are indicated in the lithological logs and noted for in the text.

6.1.3 Physical properties

Water content (%), undrained shear strength (kPa), P-wave amplitude, P-wave velocity (m/s), wet bulk density (g/cm^3), magnetic susceptibility (10^{-8} SI (m^3/kg)), acoustic impedance ($g*m*cm^{-3}*s^{-1}$) and fractional porosity are presented for all the cores (Fig. 6.4, 6.9, 6.15, 6.21 & 6.26). Undrained shear strength (kPa) within hemipelagic sediments generally increases downcore. However, measurements from coarser intervals diverge from this general trend and are, therefore, represented by numbered values next to the plot. Results obtained with the MSCL frequently contained outliers near section boundaries (e.g. related to larger apparent core diameters caused by the end caps). These were in such case removed. P-wave amplitude values below 80 were considered too low and are excluded from the plots. Low P-wave amplitude values indicate poor contact between the core liner and the sediment (*see Chapter 3.4.1; Multi Sensor Core Logger*), and hence, unreliable results for P-wave velocity and acoustic impedance. In consequence, P-wave velocity and acoustic impedance results are left out for these intervals. The MSCL physical properties are generally zigzag-shaped around constant values, while water content and undrained shear strength show a downward decrease and increase, respectively. Changes in physical properties are described relative to the general trend of the cores. Max, min and average values for each unit are found in table 6.3, 6.4, 6.5, 6.6 & 6.7.

6.1.4 Element geochemistry (XRF core scanning)

The element geochemistry is presented by selected element/element ratios and element/sum ratios (*see chapter 3.4.5; Element geochemistry*). This includes: Fe/Ca, Zr/Sr, Zr/Rb, Zr/Sum, Ca/Sum, Fe/Sum, Si/Sum, K/Sum and Ti/Sum (Fig. 6.5, 6.10, 6.16, 6.22 & 6.27). Changes within the element ratios will in the text be described relative to the general trend of the cores. See Chapter 3.4.5 for information about indication properties of the ratios.

6.1.5 Radiocarbon dating

The result from the AMS radiocarbon dating and calibrated ages are presented in Table 6.1, where the calibrated ages are based on the mean of the 1σ range. The sample from 409.5 – 411.5 cm in core HH13-018-PC-MF failed and is, therefore, not taken into account for further discussion.

Corner (1980) established a Preboreal deglaciation chronology for the Lyngen – and Storfjorden area, where dates were established for glacier re-advances and final deglaciation of the fjord valleys (see 2.3.2 *Deglaciation*). Some of the dates, which were presented in ^{14}C age B.P, have been calibrated to easier the correlation between the dated levels of the cores and these events. For the calibration were the same corrections conducted as for the dated material sampled in this study (*see Chapter 3.4.11.3; Calibration*). The radiocarbon dating and the calibrated ages are presented in Table 6.1, where the calibrated ages are based on the mean of the 1σ range.

Lab reference	Core	Sampling depth (cm)	Type of material	^{14}C age BP	Cal.yr BP Calib 7.0.2 1σ range	Cal.yr BP Calib 7.0.2 2 σ range	Cal.yr BP Calib 7.0.2 1 σ mean
UBA-26247	HH13-016-GC-MF	364-366	Benthic foraminifera	7850±46	8188-8315	8129-8375	8252
UBA-26248	HH13-017-GC-MF	230-231	Benthic foraminifera	3217±27	2860-3000	2795-3075	2930
UBA-26256	HH13-017-GC-MF	238-239	Shell fragments	3254±23	2917- 3057	2856-3130	2987
UBA-26255	HH13-017-GC-MF	238-239	Wood	3147±24	3354-3396	3336-3413	3375
UBA-26249	HH13-017-GC-MF	246-247	Benthic foraminifera	3283±29	2951-3101	2877-3165	3026
UBA-26250	HH13-018-PC-MF	409.5-411.5	Benthic foraminifera	Failed			
UBA-26251	HH13-018-PC-MF	368-370	Benthic foraminifera	9648±42	10381-10545	10266-10595	10463
UBA-26252	HH13-018-PC-MF	375.5-377.5	Benthic foraminifera	9780±67	10516-10706	10403-10851	10611
UBA-26253	HH13-019-PC-MF	358.5-360.5	Benthic foraminifera	9210±41	9808-10040	9703-10123	9924
UBA-26254	HH13-019-PC-MF	428-430	Benthic foraminifera	9535±88	10210-10432	10140-10563	10321
Reference	**Event**						
Corner (1980)	Last deglaciation of the fjord-valleys in the area Signaldalen&lower Skibotndalen			9100±150	9526-9943	9438-10167	9735
Corner (1980)	The Ørnes Event			9900±150 9800±150	10583-10984 10436-10858	10400-11155 10253-11047	10784 10647
Corner (1980)	The Skibotn Event			9600±150 9500±150	10217-10569 10126-10506	10001-10810 9847-10675	10393 10316

Table 6.2: *Radiocarbon and calibrated ages from this study and from Corner (1980).*

6.1.6 Lithofacies

Five lithofacies are distinguished: M, Ml, S, Sng and SMi.

6.1.6.1 Massive mud (M)

Massive mud is the most dominant lithofacies in the investigated cores. Its lithology can generally be classified as mud or sandy mud. Clay concentrations vary between 7 % and 20 %, while the content of silt lies between 37 % and 83 %. The percentage of sand range between 1 % and 28 %, however, at certain depths in HH13-018-PC-MF and HH13-019-PC-MF the content reaches a sand concentration of up to 55 %. Sediment colour varies slightly between olive (5Y 4/3 and 5Y 4/4) or olive grey (5Y 4/2). Bioturbation varies from non to intense, generally decreases downcore. Shells and shell fragments occur often in coincidence with bioturbation. Sulphide spots are restricted the uppermost parts of the cores.

6.1.6.2 Laminated mud (Ml)

This lithofacies is only present in the lower parts of cores HH13-018-PC-MF and HH13-019-PC-MF. The sediment colour is either dark grey (5Y 4/1) or olive grey (5Y 4/2). The laminations are determined based on the colour variations and density of the sediment, where the density changes could be related to changes in grain size. The shape of the lamination varies (e.g. planar and convex), and their spacing is not consistent . The sediment can be classified as sandy mud or mud. Silt is the overall main fraction, with concentrations between 7.8 – 80.1%. Clay content varies between 9.4 and 90.2 %, whereas the sand fraction ranges between 0.0 – 50.6 %. Clasts occur within this lithofacies in core HH13-018-PC-MF. Bioturbation is absent, and only a few fossil fragments are observed at one interval.

6.1.6.3 Sandy layer (S)

Coarser sediments that are often darker than the surrounding material characterise this lithofacies. Its thickness varies between 4 and 10 cm. The appearance of coarser material is not consistent; e.g. interval of uniform thickness or lens shaped. Whereas its lower boundary is erosive its upper boundary is sharp. However, more gradual boundaries also occur, both at the top and base of the facies. Sediment colour is olive (5Y 4/3), olive grey (5Y 4/2) or dark olive grey (5Y 3/2). This is often the same colour classification as the surrounding sediment has, but a darker shade. Samples are not always provided, but the existing data indicate either sandy mud or muddy sand texture. Clay concentrations vary between 7.7 and 36 %, silt between 32 and 75.7 %, and the sand content lies within the range 20.7 – 53.6 %. Bioturbation is absent. However the amount of fossils, mainly fragments, varies from absent to abundant.

6.1.6.4 Normally graded sand (Sng)

Normal grading from sand is the major characteristic of this lithofacies. Whereas the lower boundaries of this facies are always erosional, the upper boundaries are gradual. The deposits are typically structureless/massive, but laminations occur occasionally. The thickness of this lithofacies varies

between 4 cm and 13 cm. Sediment colour is olive (5Y 4/3), olive grey (5Y 4/2), dark olive grey (5Y 3/2), dark grey (5Y 4/1) and black (5Y 2.5/2). Bioturbation occurs occasionally, i.e. in the finer, upper parts of the facies. The amount of fossil fragments varies from absent to abundant. Plant fragments were found in core HH13-017-GC-MF. Grain-size distribution analyses of some intervals of this facies were performed. They reveal a muddy sand and sandy mud composition. Clay concentrations varies between 2.9 – 18.4 %, silt between 24.4 – 71.2 % and sand from 10.4 to 72.9 %.

6.1.6.5 Interbedded sand and mud (SMi)

Interbedded sand and mud is only found in cores HH13-018-PC-MF and HH13-019-PC-MF. The thickness of the lithofacies varies between 19 and 43 cm. The sandy layers have thicknesses of 1 mm – 9 cm, while the muddy intervals range between 1 mm and 7 cm. Laminations and normal grading are present. The sandy layers have often an erosional lower boundary. Sediment colour varies between olive grey (5Y 4/3), dark olive grey (5Y 4/2), dark grey (5Y 4/1) and black (5Y 2.5/2). Bioturbation and fossils have only been observed within one interval (HH13-019-PC-MF; *see Chapter 6.6.9*). The lithofacies represents the textural groups: muddy sand, sandy mud and mud, Clay contents lie between 8.0 – 27.2 %, silt between 28.4 – 67.0 %, and sand varies from 5.8 to 65.7 %. Clasts occur.

6.2 Core HH13-015-GC-MF

Core HH13-015-GC-MF was retrieved the southernmost part of the study area (Fig. 6.1; Tab. 6.1). It is divided into 9 units containing the lithofacies M and S (Fig. 6.2). During opening section 1 and 3 smelled H_2S (hydrogen sulphide) – section 3 having had the most intense smell.

Max, min and average values for the grain-size properties and the physical properties is found for each unit in Table 6.3.

6.2.1 Unit 15-9 (392 – 231 cm)

The lowermost unit of the core is composed of lithofacies M. The lower boundary of the unit is not recovered. However, its upper boundary is erosive (Fig. 6.2). The sediment composition is relatively uniform throughout the unit. However, the lowermost part is slightly finer, whereas the uppermost part is slightly coarser. Additionally, the sediments at depths between 384 – 364 cm are also coarser (coarsest between 370 – 375 cm; Fig. 6.2) and have increased Fe, K, Ti contents (Fig. 6.4). The generally uniform granulometric composition of the sediment (Fig. 6.3), together with only negligible changes in the physical properties (Fig. 6.4) and element ratios (Fig. 6.5), indicate a stable sedimentary environment. Whereas water content and fractional porosity decrease downcore, the wet bulk density increases. This is the expected to be a result of compaction due to the weight of the overlying sediments. The fine skewed and leptokurtic grain-size distribution of the sediment suggests low dynamics for the sedimentary environment, however, the poorly sorting indicates that occasional fluctuations occurred. The slightly higher amount of coarser fractions in the uppermost ~70 cm of the unit compared to the more clay enriched underlying sediment, may be caused by turbulence. The appearance of bioturbation is restricted, however, fossils and fossil fragments are observed throughout the whole unit. Due to these observations it is interpreted that the unit was deposited in an open marine environment with stable sedimentary processes.

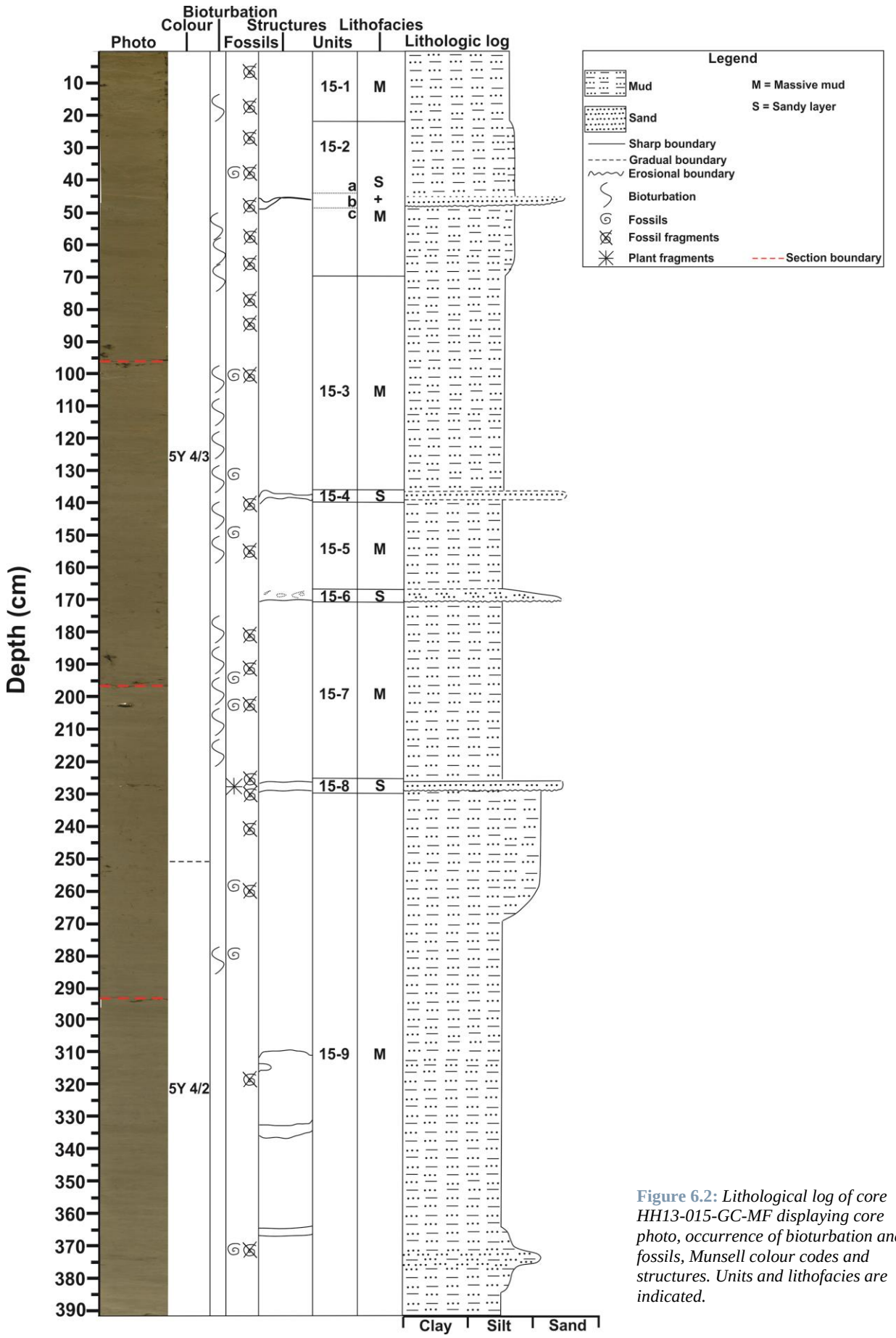

Figure 6.2: *Lithological log of core HH13-015-GC-MF displaying core photo, occurrence of bioturbation and fossils, Munsell colour codes and structures. Units and lithofacies are indicated.*

	15-9 392 - 231 cm		**15-8** 231 - 225 cm		**15-7** 225 - 172 cm		**15-6** 172 -167 cm		**15-5** 167 - 140 cm		**15-4** 140 - 136 cm		**15-3** 136 - 70 cm		**15-2** 70 – 22 cm		**15-1** 22 – 0 cm	
	Average		**Average**		**Average**		**Average**		**Average**		**Average**		**Average**		**Average**		**Average**	
	Max	**Min**	**Max**	**Min**	**Max**	**Min**	**Max**	**Min**	**Max**	**Min**	**Max**	**Min**	**Max**	**Min**	**Max**	**Min**	**Max**	**Min**
Clay content (%)	15.1		X		13.8		1 sample: 11.9		15.0		X		13.7		18.5		15.4	
	17.9	12.1			14.2	13.2			15.2	14.7			15.3	12.1	36.2	13.7	15.4	15.3
Silt content (%)	74.6		X		74.9		1 sample: 64.5		75.7		X		76.9		67.5		77.1	
	77.1	63.0			75.2	74.4			76.5	74.4			83.3	73.4	76.7	32.0	77.1	77.0
Sand content (%)	10.3		X		11.3		1 sample: 22.6		9.3		X		9.4		14.0		7.6	
	24.9	6.3			11.7	10.6			10.3	8.5			13.4	1.4	31.8	9.1	7.6	7.5
Mean (M_G) (µm)	10.54		X		11.51		1 sample: 17.94		10.31		X		11.34		10.53		9.26	
	19.74	8.01			12.03	10.95			10.45	10.07			13.57	8.81	11.12	9.37	9.495	9.031
Sorting (σ_G) (µm)	5.00		X		4.91		1 sample: 6.22		4.83		X		4.62		9.10		4.57	
	7.12	4.62			4.98	4.84			5.03	4.70			5.02	4.02	26.67	4.65	4.60	4.53
Skewness (Sk_G) (µm)	-0.18		X		-0.19		1 sample: -0.07		-0.21		X		-0.22		-0.16		-0.19	
	0.03	-0.2			-0.18	-0.19			-0.19	-0.22			-0.16	-0.3	-0.00	-0.2	-0.18	-0.20
Kurtosis (K_G) (µm)	1.21		X		1.23		1 sample: 1.16		1.18		X		1.19		1.11		1.19	
	1.26	1.09			1.22	1.24			1.19	1.18			1.22	1.15	0.74	1.22	1.20	1.18
Water content (%)	38.6		X		41.5		1 sample: 41.9		41.8		X		42.6		43.8		45.4	
	41.5	35.4			42.2	41.0			42.0	41.5			45.7	41.1	45.1	43.0	46.9	44.0
Undrained shear strength (kPa)	8.2		X		8.2		1 sample: 8.3		7.1		X		6.4		6.1		2.8	
	11.0	5.8			9.2	7.2			8.0	6.4			3.6	9.2	8.0	4.7	3.9	1.7
P-wave amplitude	99.1		85.4		86.9		81.7		89.6		98.5		94.8		99.9		98	
	100	80	100	80	100	80	83	81	81	97	100	95	100	83	100	96	100	81
P-wave velocity (m/s)	1494		1446		1452		1458		1493		1498		1487		1491		1489	
	1509	1416	1498	1410	1494	1323	1489	1400	1497	1488	1502	1494	1503	1486	1498	1487	1495	1478
Wet bulk density (g/cm^3)	1.64		1.59		1.58		1.56		1.57		1.63		1.58		1.55		1.52	
	1.72	1.58	1.6	1.57	1.60	1.54	1.58	1.55	1.60	1.55	1.68	1.59	1.66	1.55	1.59	1.53	1.59	1.40
Magnetic susceptibility (10^{-8} SI (m^3/kg))	10.01		8.04		7.99		8.33		9.17		10.28		14.8		30.06		36.96	
	12.02	7.65	8.08	7.98	9.62	7.12	8.51	8.18	9.93	8.48	10.39	10.14	20.2	10.53	41.57	20.31	40.75	27.74
Acoustic impedance (g*m*cm^{-3}*s^{-1})	2458		2296		2299		2287		2340		2442		2346		2316		2303	
	2575	2362	2384	2219	2376	2112	2349	2167	2385	2308	2522	2368	2478	2240	2368	2274	2383	2224
Fractional porosity	0.643		0.674		0.679		0.687		0.686		0.65		0.681		0.694		0.714	
	0.686	0.597	0.682	0.67	0.703	0.665	0.697	0.679	0.698	0.668	0.675	0.621	0.702	0.635	0.711	0.675	0.780	0.670

Table 6.3: *Max, min and average values for the measured physical and grain-size properties for each unit of the core HH13-015-GC-MF.*

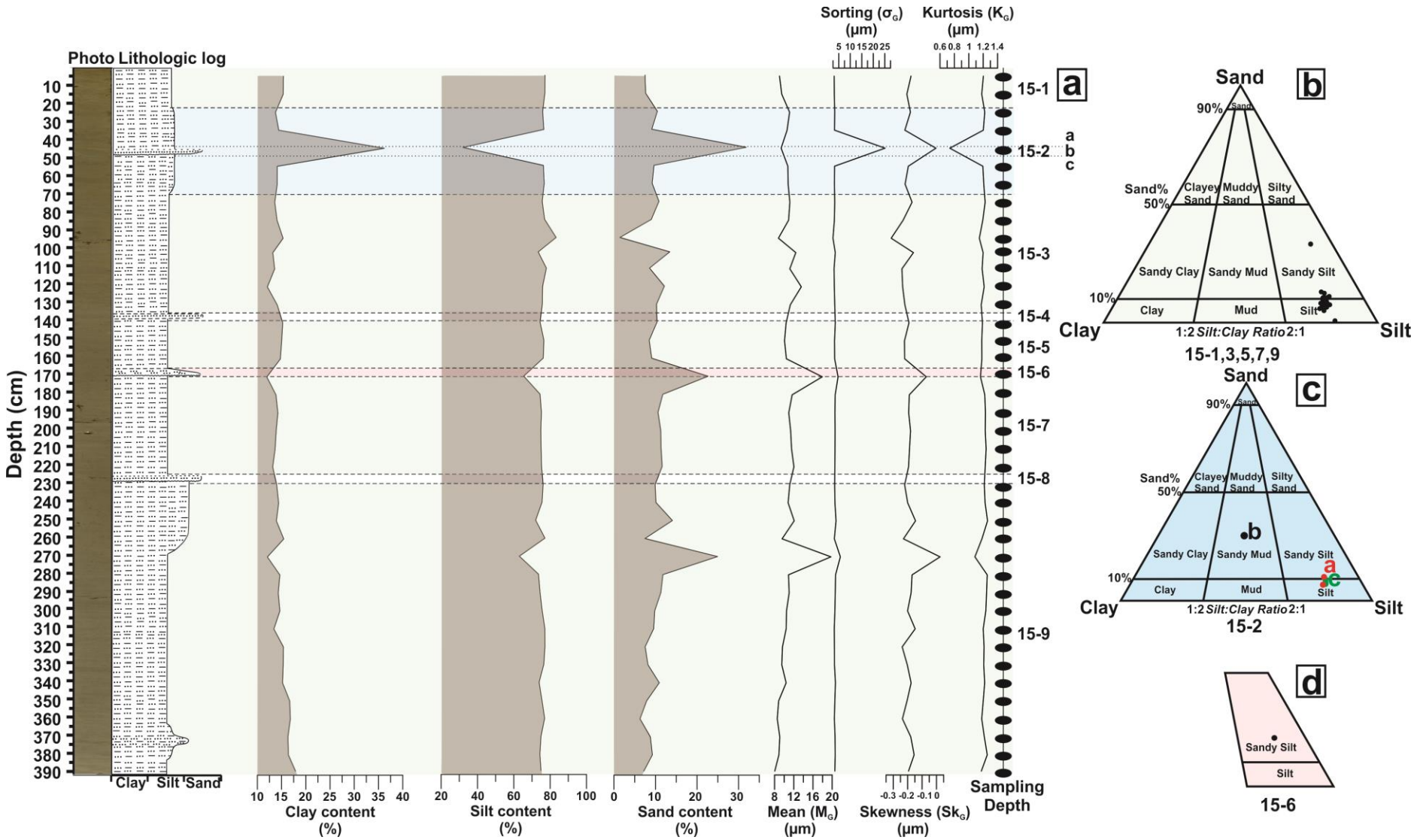

Figure 6.3: **a)** *Clay, silt and sand contents, together with mean, sorting, skewness and kurtosis, of core HH13-015-GC-MF vs. depth. Sampling depths are shown to the right. Colour photo and lithological log are included for reference. Units and sub-units are indicated* **b)** *Sand, silt and clay diagram for unit 15-1, 3, 5, 7, 9*. **c)** *Sand, silt and clay diagram for unit 15-2, where a, b and c refers to the sub-unit a, b and c* **d)** *Relevant sections of the sand, silt and clay diagram for unit 15-6.*

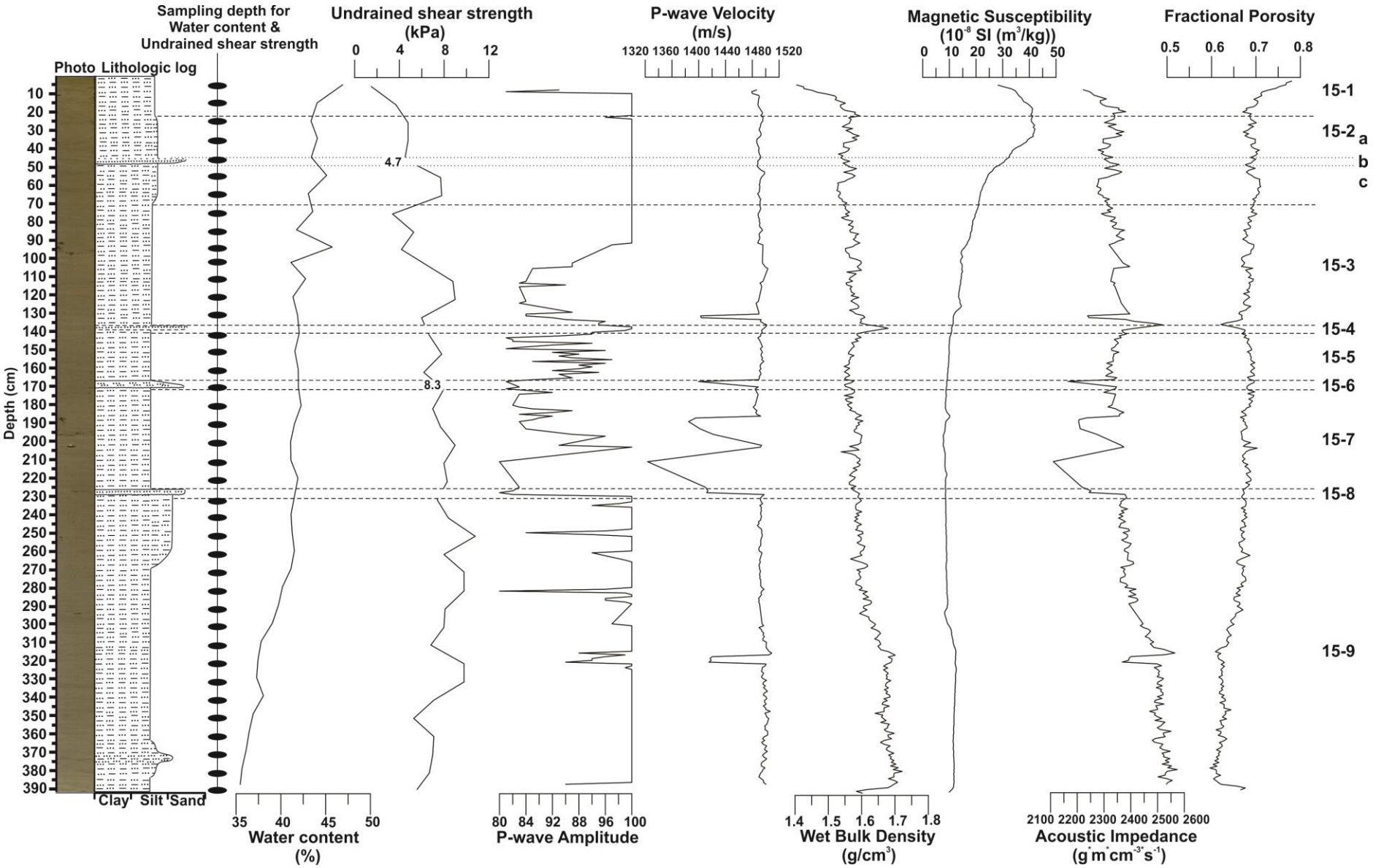

Figure 6.4: *Physical properties of core HH13-015-GC-MF vs. depth, where the sampling depth for water content and undrained shear strength is indicated to the left. Colour photo and lithological log are included for reference. Units and sub-units are indicated.*

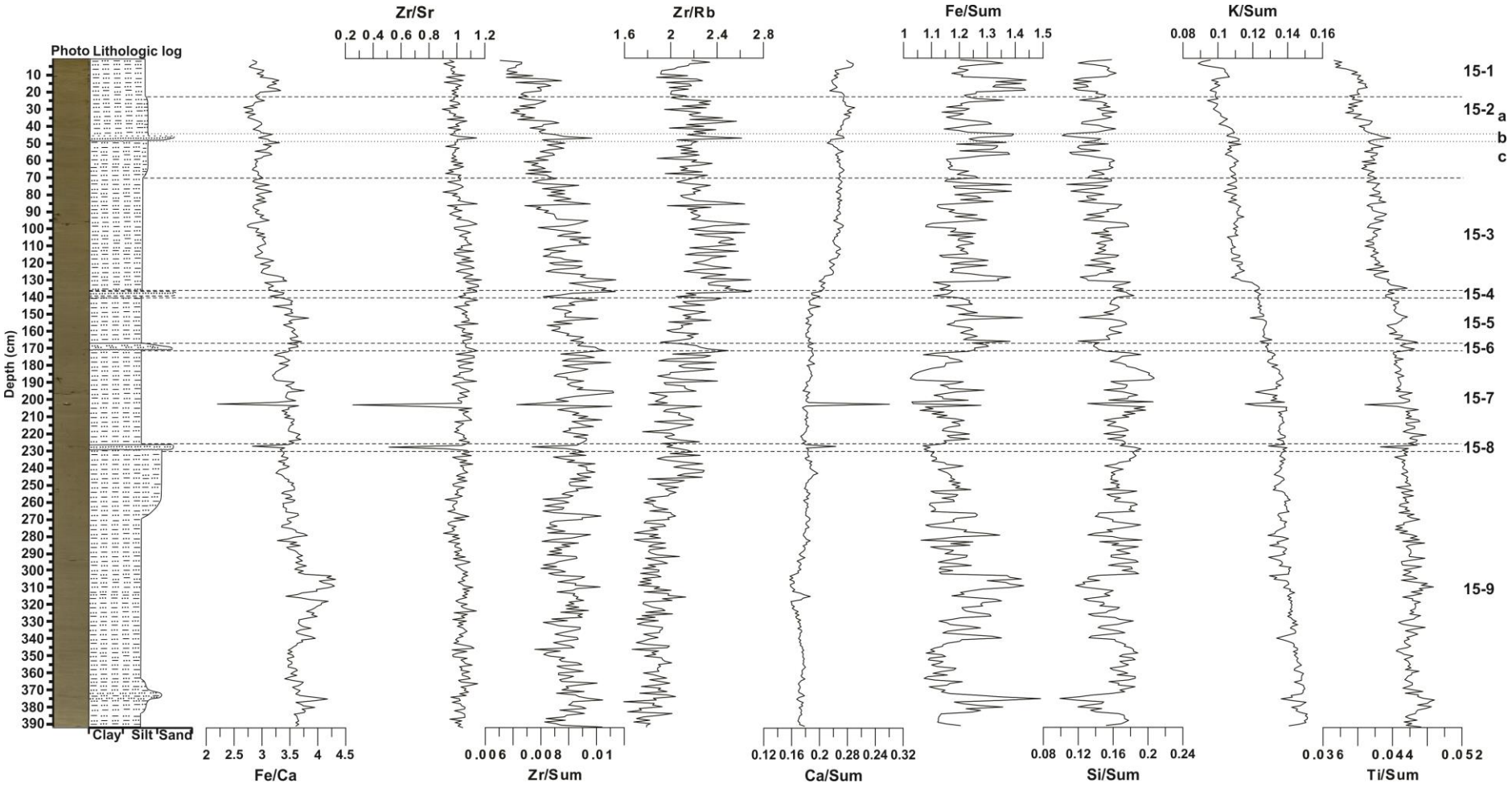

Figure 6.6: *Selected element ratios for core HH13-015-GC-MF vs. depth. Colour photo and lithological log are included for reference. Units and sub-units are*

6.2.2 Unit 15-8 (231 – 225 cm)

The unit contains lithofacies S (Fig. 6.2). Its lower boundary is erosional, while its upper boundary is rather sharp. This unit has a distinct coarser and different character than the surrounding sediment. However, since no material was taken out for analyses, this cannot be further confirmed by grain-size data. Both the P-wave velocity and the acoustic impedance change abruptly at the unit boundary, which most probably indicates changes in lithology. However, the wet bulk density, magnetic susceptibility and fractional porosity are almost constant (Fig. 6.4). The bed comprises a high amount of largely fragmented fossils, together with plant fragments (moss), where the latter is indicative of terrigenous origin. Bioturbation is absent. The Ca, Sr and Si contents increase within the unit, which correlates well with fossil rich sediment (e.g. Dean *et al.*, 1997; Dypvik & Harris, 2001; Heimbürger *et al.*, 2006) (Fig. 6.5). The sharp and erosive contact with the underlying sediments is a common feature of mass transport events (e.g. Forwick and Vorren, 2007, 2011; Benn & Evans, 2010; Forwick *et al.*, 2010). It is therefore, suggested that unit 15-8 is a mass-transport deposit (MTD).

6.2.3 Unit 15-7 (225 – 172 cm)

The unit is composed of lithofacies M (Fig. 6.2). Its lower and upper boundaries are sharp and erosive, respectively. The fine and massive sediment composition suggests a stable sedimentary environment. This is further confirmed by the fine skewed and leptokurtic grain-size distribution, which indicate a low and steady dynamic deposition. However, the poor sorting indicate that the conditions were occasionally more dynamic. P-wave velocity and acoustic impedance are low. However, this can be correlated to low P-wave amplitude and should therefore not be given any further attention. An increased content of shells and shell fragments within the uppermost part of the unit implies improved living conditions for molluscs with time. The intensive bioturbation present for the whole unit suggests ideal circumstances for the benthic organisms to settle, which further implies that the sedimentation rates were relatively low. The occurrence of bioturbation further indicates that the sediments have not been reworked. A peak of calcium between 200 and 205 cm could be correlated to the occurrence of a shell within the XRF scanned surface area, which also explains the excess concentrations of Sr. The unit is interpreted to be deposited by suspension fallout in an open marine environment.

6.2.4 Unit 15-6 (172 – 167 cm)

Unit 15-6 is composed of lithofacies S. Sand appear as a distinct dark line located at the base of the unit (~0.5 cm), whereas above this line the sand appear with a chaotic pattern (Fig. 6.2). The coarser layer has an erosional contact with the unit located below. The upper transition is gradual, where the boundary has been outlined by the occurrence of sandy spots within this unit. The increased sand content of the sediment, its erosional boundary to the underlying sediments, and lack of bioturbation

indicate that this unit is a MTD (*cf. Chapter 6.4.3, below*). The symmetric skewness infers a normal distribution of fine and coarse fractions, and the leptokurtic kurtosis suggests a steady sedimentary process behind the deposition (Fig. 6.3). Changes in P-wave velocity and acoustic impedance coincide with the lithological changes. The unchanged values for the magnetic susceptibility suggest that the re-deposited sediment comes from the same source as the surrounding material (Fig. 6.4).

6.2.5 Unit 15-5 (167 – 140 cm)

Lithofacies M composes unit 15-5, having gradual transition to both the over- and underlying units (Fig. 6.2). The unit contains relatively fine and uniform sediment. However, the grain-size distribution is fine skewed and leptokurtic (Fig. 6.3). Whereas bioturbation is absent in the lower part of the unit, the uppermost ~20 cm are characterized by extensive bioturbation. Fossils and fossil fragments occur in accordance with bioturbation. Based on these observations, together with relatively constant values for the physical properties and the selected element ratios (Fig. 6.4 & 6.5, respectively), is the unit interpreted to be the result of suspension fallout by a steady sedimentary process within an open marine environment.

6.2.6 Unit 15-4 (140 – 136 cm)

The unit is classified as lithofacies S, where both the lower and upper boundary shows a gradual transition to the surrounding sediment (Fig. 6.2). Visual observations reveal that this unit comprises coarser grains than the surrounding units. The X-radiograph reveals that the unit is a high density interval (Fig. 6.6). This is supported by increased wet bulk density and decreased fractional porosity (Fig. 6.4). The unit is suggested to comprise a MTD. However, based on the lack of erosional boundaries, together with bioturbation, it can be assumed that it was deposited by a low-density event e.g. a turbidity or debris flow.

6.2.7 Unit 15-3 (136 – 70 cm)

Lithofacies M composes unit 15-3 (Fig. 6.2). A relatively fine and uniform composition (Fig. 6.3), relatively constant physical properties (Fig. 6.4) and element ratios logs (Fig. 6.5), as well as gradational boundaries characterise this unit. However, sand and water contents are substantially low at ~95 cm. The occurrence of shell and fossil fragments, together with bioturbation, indicate a beneficial environment for living organisms. The unit is interpreted to be deposited from suspension fallout in an open marine environment.

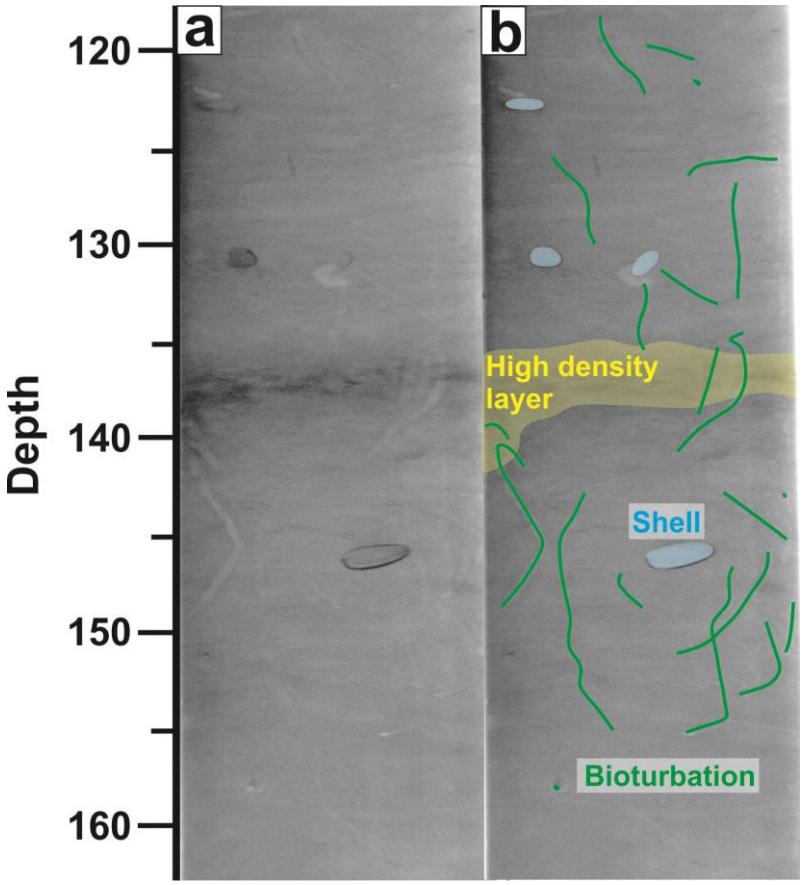

Figure 6.6: **a)** *X-ray photograph of the high density layer comprised in unit 15-4* **b)** *Interpretaions of features observed in a; high denisty layer, shells and bioturbation.*

6.2.8 Unit 15-2 (70 – 22 cm)

Unit 15-2 comprises M and S (Fig. 6.2). Its lower and upper boundaries are gradual, marking a transformation of the sediment appearance, i.e. the unit appears slightly coarser and more compact than the surrounding sediments. It is divided into the three sub-units: *a* = M (uppermost; 46 – 22 cm), *b* = S (48 – 46 cm) and *c* = M (lowermost; 70 – 48 cm). The sandy layer of sub-unit *b* is ~2 cm on its thickest side (left side in Fig. 6.2) and narrows in to be ~2 mm thin on the other side. The layer is tilted and has an erosive contact with sub-unit *c*, while the transition into sub-unit *a* is gradual. Both sub-units *a* and *b* appear greyer than the surrounding sediment, but not sufficiently enough to be classified otherwise. The sediment composition is relatively uniform within *a* and *c*. However, it is markedly different in *b*: Silt content is less than half, clay content is more than doubled and sand content is almost three times as high (Fig. 6.3).

The sharp and erosional lower boundary of sub-unit *b*, and its higher content of coarser fractions with a platykurtic distribution, suggests that it is an MTD. The sediments appear to have another

provenance than the underlying sediments, due to a higher content of Fe, Ti and Si (Fig. 6.5). The higher contents of Zr can be correlated to the coarser-grained material (Dypvik & Harris, 2001; Kylander *et al.*, 2010). The slightly more compact appearance of sub-unit *c* might be due to a compressional effect from the MTD. The fact that the transition from sub-unit *c* to *b* marks a stop in the occurrence of bioturbation also suggests a rapid deposition. The tilted/sigmoidal formation of sub-unit *b* may be the result of deformation caused by the overlying deposit. Sub-unit *a* has a relatively uniform sediment composition, which show a different shade of olive than the above lying unit. This, together with no signs of bioturbation, and the fact that the sediment is overlying the uneven surface of sub-unit *b*, indicates that *a* was deposited from a suspension fallout connected to the MTD (cf. Forwick, 2001).

6.2.9 Unit 15-1 (22 – 0 cm)

The uppermost unit of the core contains lithofacies M (Fig. 6.2). It is bounded by a gradual lower boundary and the top of the core. The sediment composition of the unit is more or less uniform (Fig. 6.3 & 6.5) and it is assumed that it was deposited in an open marine environment with low and steady dynamic depositional processes. The increasing and decreasing trends of the physical properties (Fig. 6.4) and the lack of bioturbation within the uppermost part are thought to be caused by disturbances that occurred during coring.

6.2.10 Summary of core HH13-015-GC-MF

The 392 cm long core was divided into 9 units. The recovered sediments reflect sediment deposition mainly from suspension fallout in an open marine environment with relatively stable conditions (15-9, 15-7, 15-5, 15-3, 15-2c and 15-1). However, slope failures occasionally interrupted these environmental conditions (15-8, 15-6, 15-4 and 15-2b&c).

6.3 HH13-016-GC-MF

Core HH13-016-GC-MF was recovered approx. 220 meters north of core HH13-015-GC-MF (Fig. 6.1; Tab. 6.1). It is divided into 5 lithological units, representing lithofacies M and Sng (Fig. 6.7). Sections 2 and 3 smelled intensely of H_2S (hydrogen sulphide) after opening.

Max, min and average values for the grain-size properties and the physical properties is found for each unit in table 6.4, below.

	16-5 **374-370 cm**		**16-4** **370 - 353 cm**		**16-3** **353 - 184 cm**		**16-2** **184 - 170 cm**		**16-1** **170 – 0 cm**	
	Average		**Average**		**Average**		**Average**		**Average**	
	Max	**Min**	**Max**	**Min**	**Max**	**Min**	**Max**	**Min**	**Max**	**Min**
Clay content (%)	X		1 sample: 13.0		13.7		X		13.6	
					14.7	12.9			15.2	12.8
Silt content (%)	X		1 sample: 66.3		72.1		X		71.9	
					73.9	69.1			75.2	68.7
Sand content (%)	X		1 sample: 20.7		14.3		X		14.5	
					18.5	10.3			18.5	10.8
Mean (M_G) (µm)	X		1 sample: 16.38		12.36		X		12.48	
					13.42	10.38			15.33	11.04
Sorting (σ_G) (µm)	X		1 sample: 6.38		5.35		X		5.39	
					5.75	4.99			6.13	4.84
Skewness (Sk_G) (µm)	X		1 sample: -0.05		-0.14		X		-0.12	
					-0.09	0.17			-0.03	-0.18
Kurtosis (K_G) (µm)	X		1 sample: 1.17		1.26		X		1.25	
					1.28	1.20			1.29	1.22
Water content (%)	X		1 sample: 34.5		40.6		X		43.9	
					42.6	37.1			47.1	40.6
Undrained shear strength (kPa)	X		1 sample: 15.0		10.6		X		4.9	
					13.0	8.2			9.4	2.4
P-wave amplitude	X		97.3		99.6		100		97.2	
			100	81	100	84	100	100	100	80
P-wave velocity (m/s)	X		1499		1487		1516		1486	
			1502	1491	1504	1475	1541	1500	1496	1470
Wet bulk density (g/cm^3)	X		1.66		1.60		1.74		1.54	
			1.68	1.63	1.70	1.49	1.83	1.64	1.64	1.43
Magnetic susceptibility (10^{-8} SI (m^3/kg))	X		7.82		7.88		11.33		20.9	
			8.20	7.43	10.45	6.20	11.86	10.41	38.9	11.4
Acoustic impedance (g*m*cm^{-3}*s^{-1})	X		2492		2391		2609		2301	
			2515	2446	2499	2333	2827	2465	2460	2135
Fractional porosity	X		0.634		0.668		0.584		0.701	
			0.648	0.619	0.732	0.612	0.642	0.531	0.795	0.641

Table 6.4: *Max, min and average values for the measured physical and grain-size properties for each unit of the core HH13-016-GC-MF.*

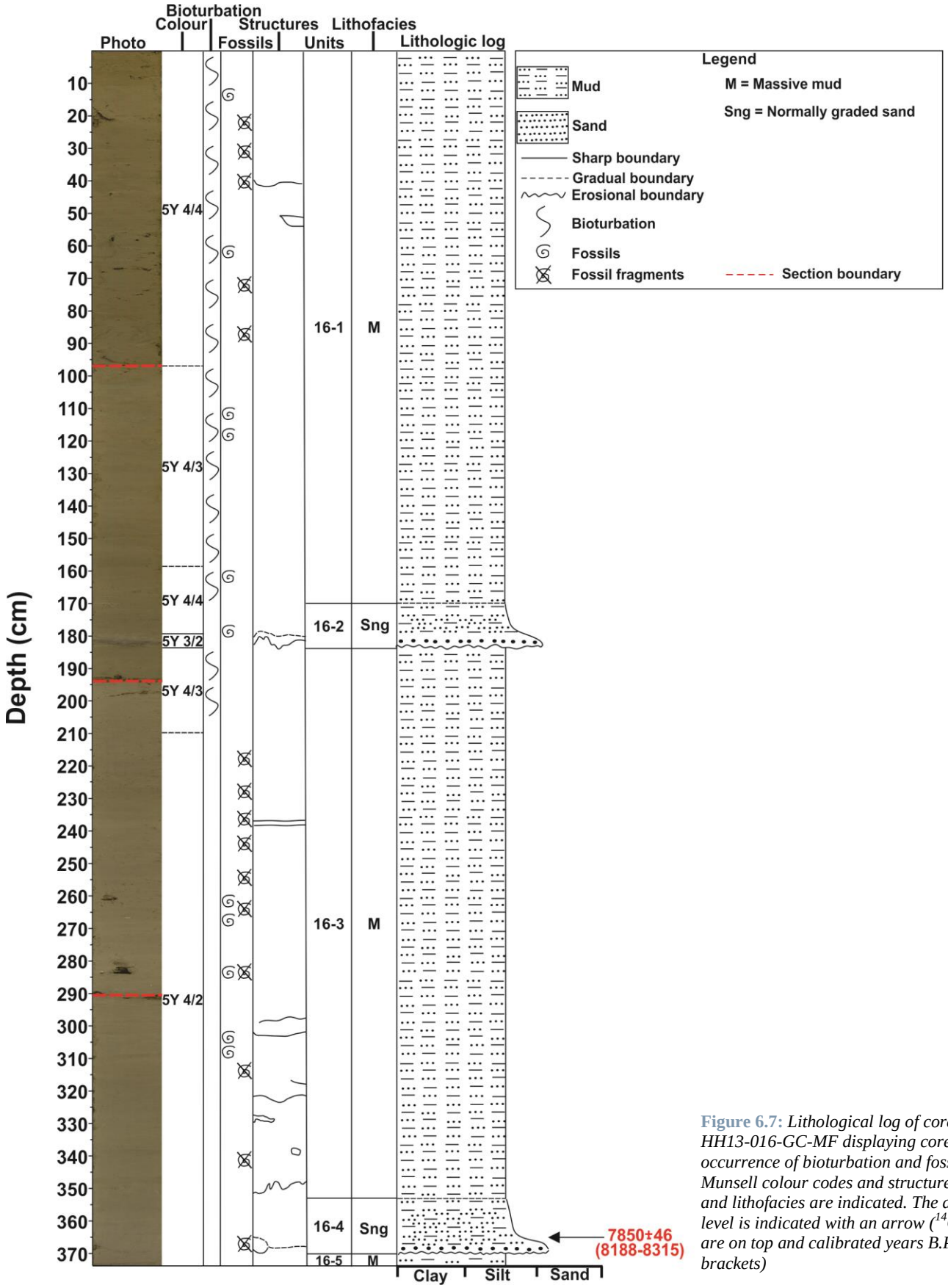

Figure 6.7: *Lithological log of core HH13-016-GC-MF displaying core photo, occurrence of bioturbation and fossils, Munsell colour codes and structures. Units and lithofacies are indicated. The dated level is indicated with an arrow (^{14}C years are on top and calibrated years B.P. in brackets)*

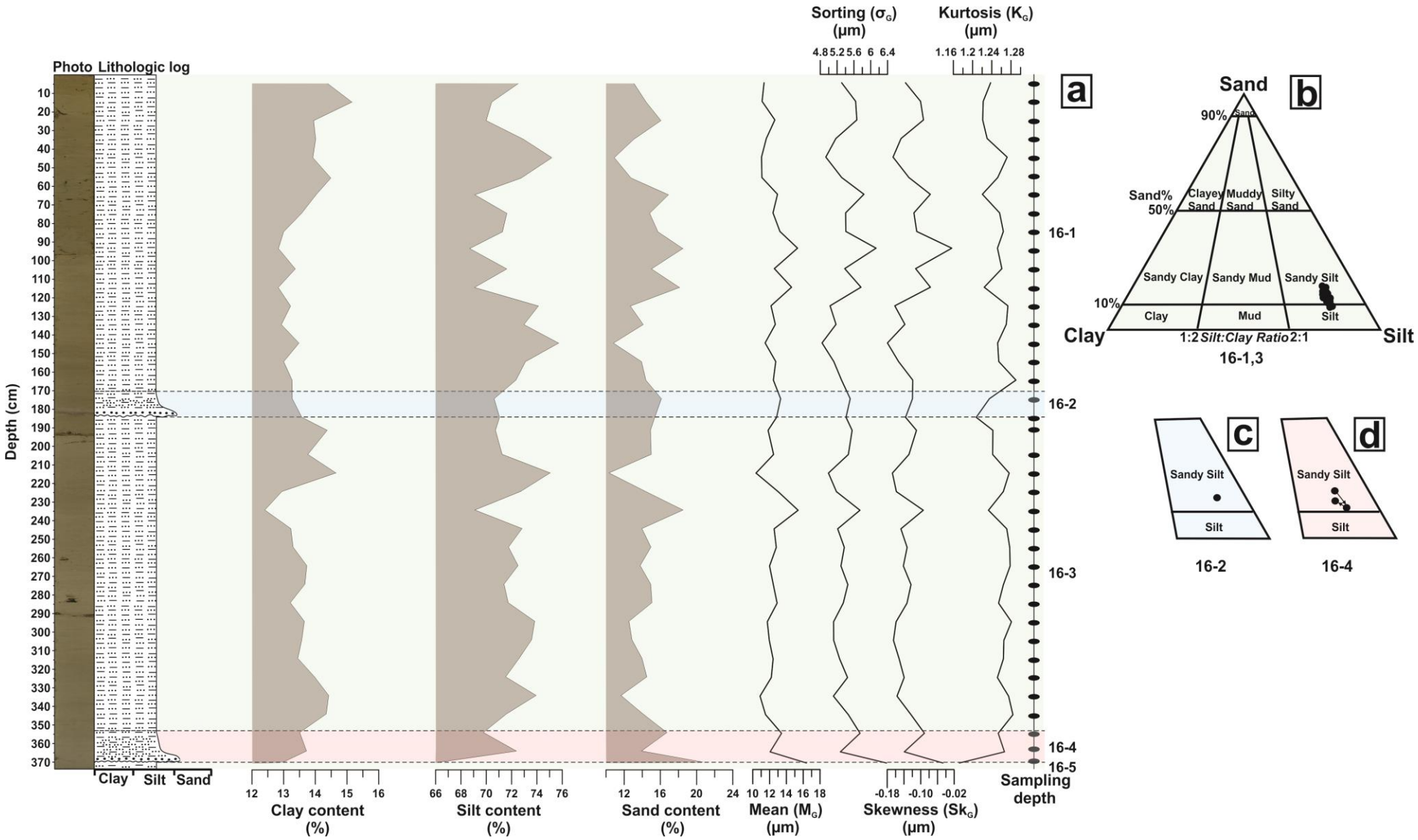

Figure 6.8: **a)** *Clay, silt and sand content, together with mean, sorting, skewness and kurtosis, of core HH13-016-GC-MF vs. depth. Sampling depths are found to the right. Colour photo and lithological log are included for reference. Units are indicated* **b)** *Sand, silt and clay diagram for unit 16-1, 3* **c)** *Relevant sections of the sand, silt and clay diagram for unit 16-2.* **d)** *Relevant sections of the sand, silt and clay diagram for unit 16-4. Arrows indicate decreasing depth.*

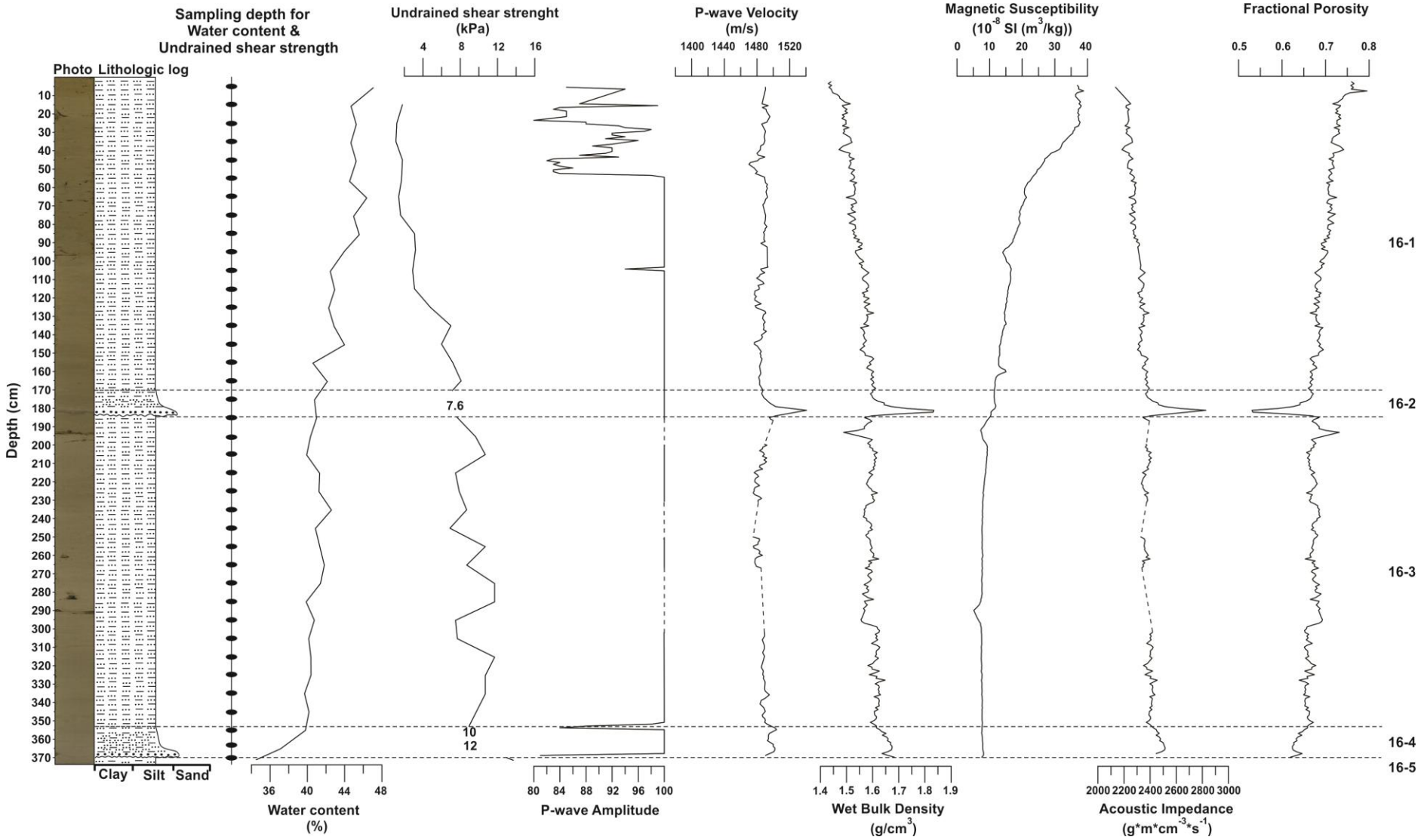

Figure 6.9: *Physical properties of core HH13-016-GC-MF vs. depth, where the sampling depths for water content and undrained shear strength are indicated to the left. Colour photo and lithological log are included for reference. Units are indicated.*

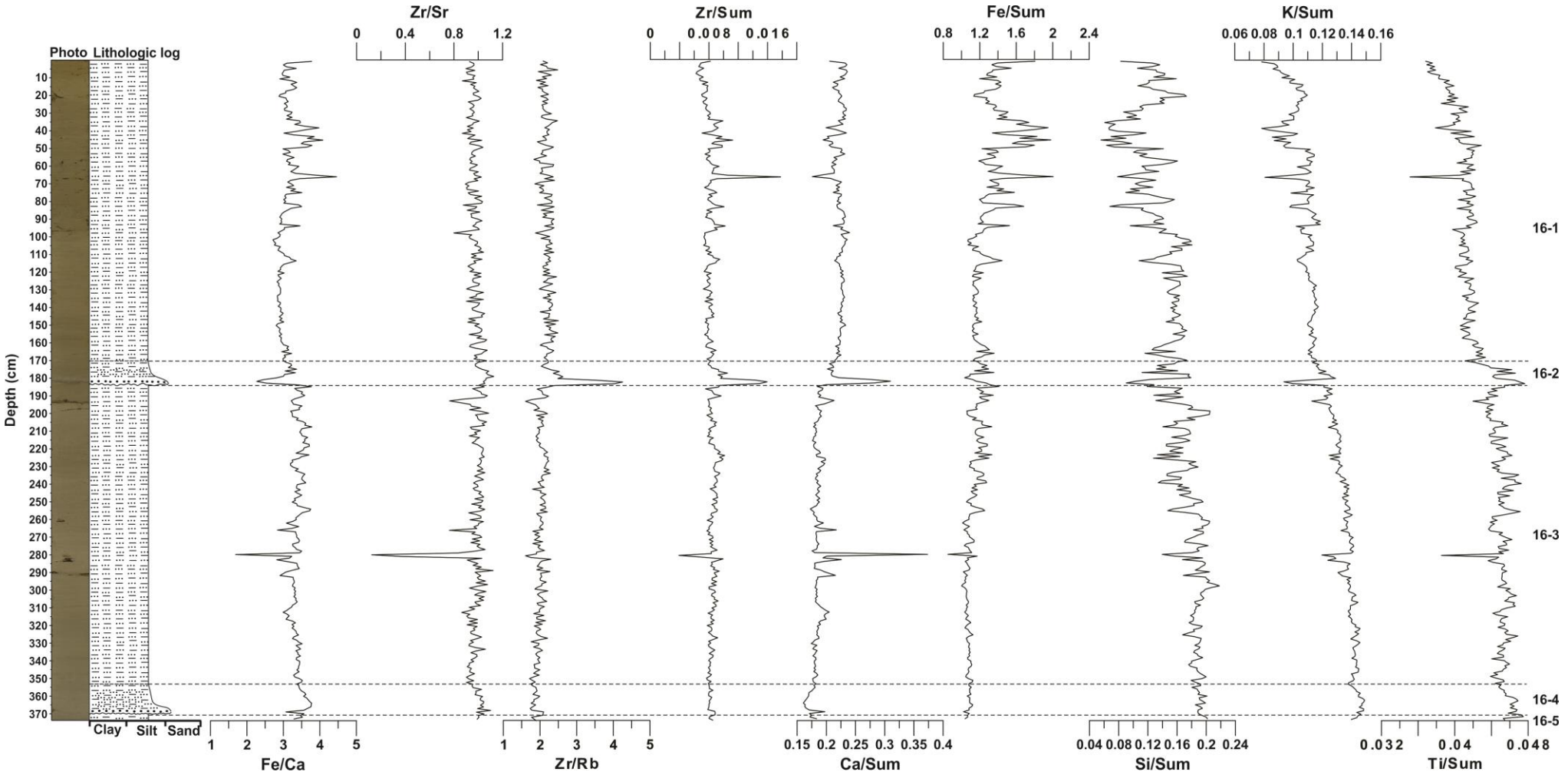

Figure 6.10: *Selected element ratios for core HH13-016-GC-MF vs. depth. Colour photo and lithological log are included for reference. Units are indicated.*

6.3.1 Unit 16-5 (374-370 cm)

The lowermost unit of the core contains the lithofacies M (Fig. 6.7). Whereas its lower boundary is not recovered, its upper boundary is erosional. Based on visual observation is the unit suggested have a similar character as unit 16-3 (*see Chapter 6.3.3*)

6.3.2 Unit 16-4 (370 - 353 cm)

Unit 16-4 comprises the lithofacies Sng (Fig. 6.7). Its lower boundary is erosional, whereas its upper boundary is gradual. The unit is composed of a coarse, dark and eroding bed, with variable thickness and chaotic internal structure. One grain-size distribution sample revealed that this unit has a slightly higher sand content compared to the overlying unit (Fig. 6.8). The chemical elements Fe, K and Ti are increased within the unit (Fig. 6. 10). The distinct and erosive contact between the coarser bed and the underlying sediments, together with lack of bioturbation, higher wet-bulk density, lower fractional porosity, as well as low water content and high shear strength suggests that this is a MTD (compare e.g. with Piper et al., 1997; Flemings et al., 2006; Sawyer et al., 2009). Normal grading indicates that the deposit is a turbidite, which is further implied by the increased Ti content (Rothwell *et al.,* 2006). One radiocarbon date within this unit provide a calibrated age of 8252 cal. years BP (Fig. 6.7; Tab. 6.2).

6.3.3 Unit 16-3 (353 – 184 cm)

Unit 16-3 is composed of lithofacies M. It has a gradual lower boundary and an erosional upper boundary (Fig. 6.7). The X-radiograph reveals sub-horizontal structures of low and high density (Fig. 6.11). These are interpreted to be cracks that could have formed due to the expansion of gas (cf. Forwick & Vorren, 2007). In addition, a high density feature is observed within the X-ray photo at depth ~237 cm. Since no obvious changes in grain-size composition appear to occur at this depth, it is assumed that this feature is the result of enhanced compaction (e.g. Forwick and Vorren, 2007). The high calcium content at ~280 cm (Fig 6.10) is most probably caused by a shell located at the sediment surface (Rothwell *et al.,* 2006). The fine-grained and more or less uniform sediment composition (Fig. 6.8) is inferred to be the result of a stable sedimentary environment. A steady, low dynamic deposition process is suggested by the fine skewed and leptokurtic grain-size distribution. The very poor sorting indicates, however, that the dynamics in the deposition fluctuated occasionally. The sedimentary environment of the unit is interpreted to be open marine.

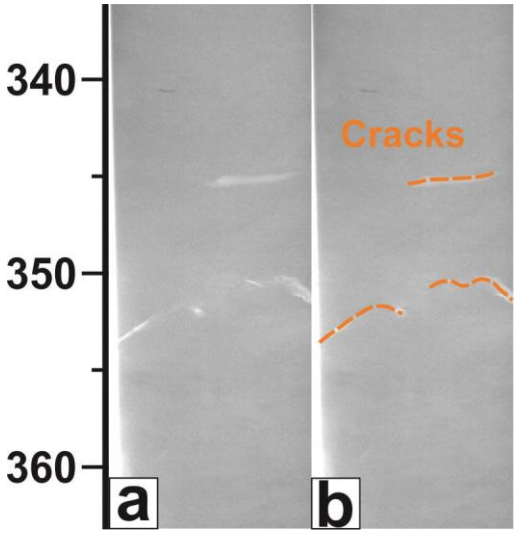

Figure 6.11: **a)** *X-ray photography and* ***b)*** *interpretation of the sub-horizontal structures occurring between ~352-295 cm in core HH13-016-GC-MF***.**

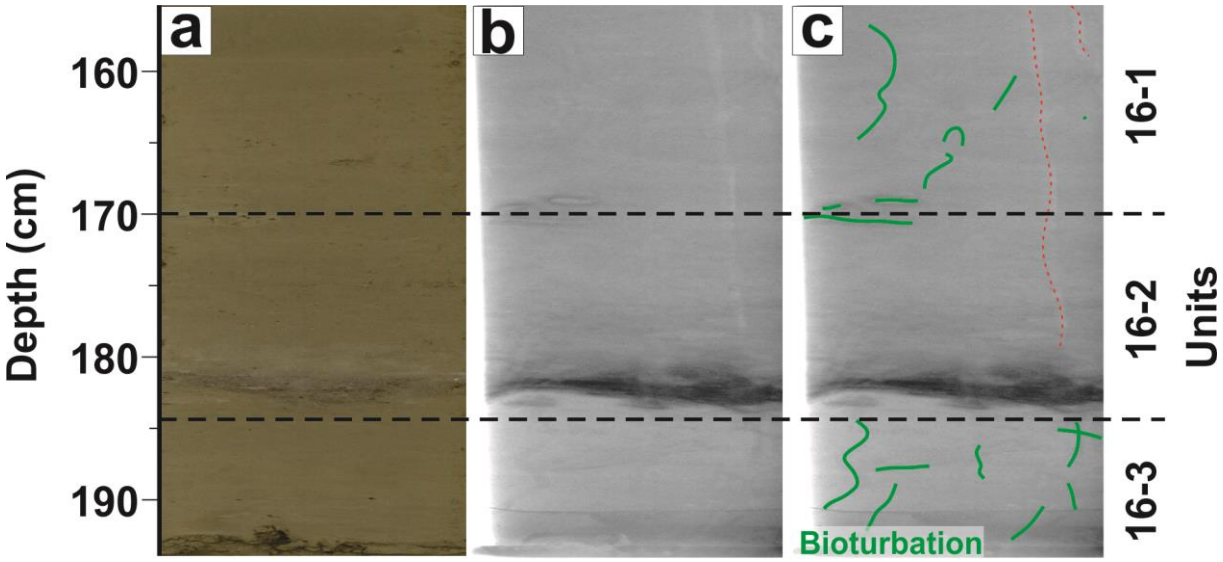

Figure 6.12: *Unit 16-2 (183 -179 cm) with adjacent units* **a)** Colour image **b)** *X-radiograph. Note the density difference (dark interval) between unit 16-2 and units 16-3 and 16-1, respectively* **c)** *Interpretation of X-radiograph. The red stippled line indicates distortion caused by the plastic film overlying the sediment surface during X-ray imaging.*

6.3.4 Unit 16-2 (184 – 170 cm)

The unit is composed of lithofacies Sng (Fig. 6.7) and bounded by an erosional lower boundary and a gradual upper boundary (Fig. 6.9). Sediment colour changes from dark grey at its base to lighter grey towards the top. Grain-size distribution data is absent. However, a different lithology for the unit is defined by visual observations, supported by higher P-wave velocity and acoustic impedance (Fig. 6.9). The enhanced wet bulk density may be correlated to a higher content of coarser fragments (cf. Forwick *et al.,* 2010). This again can be further confirmed by the higher Zr content (Dypvik & Harris, 2001; Kylander *et al.*,2010). Sharp and erosive contacts with the underlying sediments, gradational upper contacts and normal size-grading suggest that unit 16-2 contains a turbidite (Bouma, 1962; Middleton and Hampton, 1973 in McHugh *et al.,* 1996). Furthermore, Ti is typically found increased at the base of turbidites (Rothwell *et al.,* 2006). Increased calcium content is suggested to be an effect of the enrichment of fossil fragments (Rothwell *et al.,* 2006). It is further suggested that the upper, approx. 10 cm of the unit was deposited by suspension fallout following the turbidite.

6.3.5 Unit 16-1 (170 – 0 cm)

The uppermost unit of the core is composed of lithofacies M (Fig. 6.7). The lower boundary of the unit is gradual, while the top of the core defines the upper boundary. The fine, relative uniform sediment composition has been interpreted to reflect a steady, open marine sedimentary environment with low dynamic processes. Bioturbation and fossils/fossil fragments indicate a favourable environment for living organisms.

6.3.6 Summary core HH13-016-GC-MF

Core HH13-016-GC-MF was divided into five lithostratigraphic units. Units 16-5, 16-3 and 16-1 compose the majority of the sediment record, indicating that the deposition mainly occurred from suspension settling in an open marine environment. However, units 16-4 and 16-2 reveal that mass wasting occurred occasionally. The oldest MTD in the core (unit 16-4) was deposited around 8250 cal. years BP.

6.4 HH13-017-GC-MF

Core HH13-017-GC-MF was retrieved from a relatively smooth part of the fjord basin (Fig. 6.1; Tab. 6.1). It is divided into 7 units representing lithofacies M, S and Sng. The smell of hydrogen sulphide (H_2S) could be recognized for section 2, 3, 4 and 5 as they were opened - section 2 the most.

Max, min and average values for the grain-size properties and the physical properties is found for each unit in Table 6.5.

6.4.1 Unit 17-7 (413-306 cm)

The lowermost unit is composed of lithofacies M (Fig. 6.13). The lower boundary of the unit was not recovered, whereas its upper boundary is gradual. Visual observations, together with the X-radiograph, indicate that the lowermost ~30 cm of the sediment was disturbed during coring. These disturbances cause the changes in the physical (Fig. 6.15) and geochemical properties (Fig. 6.16) for this interval of the unit. The fine-grained and relatively uniform granulometric composition of the sediments (Fig. 6. 15), together with only small changes in physical properties above the disturbed sediments; suggests a deposition from suspension fallout in an open marine environment. An increase in calcium content between 340 and 360 cm coincides with the occurrence of fossil fragments on the sediment surface (Rothwell *et al.*, 2006).

6.4.2 Unit 17-6 (306 – 301 cm)

The unit composes lithofacies S (Fig. 6.13). Both its lower and upper boundaries are gradational, and defines an interval of a highly increased sand content (>50 %, Fig. 6.14). The X-radiographs reveal sediments of higher density within this unit. This coincides with increased undrained shear strength (Fig. 6.15). It is suggested that this unit is an MTD; MTDs are often characterised by sharp, lower boundaries (e.g. Forwick & Vorren, 2007, 2011; Benn & Evans, 2010; Forwick *et al.*, 2010). However, the absence of an erosive lower boundary in this case may reflect that sediment transport and deposition occurred from a non-eroding turbidity flow or a hydroplaning debris flow (Elverhøi *et al.*, 2000; Mulder & Alexander, 2001; Forwick & Vorren, 2007; Beaten, 2007).

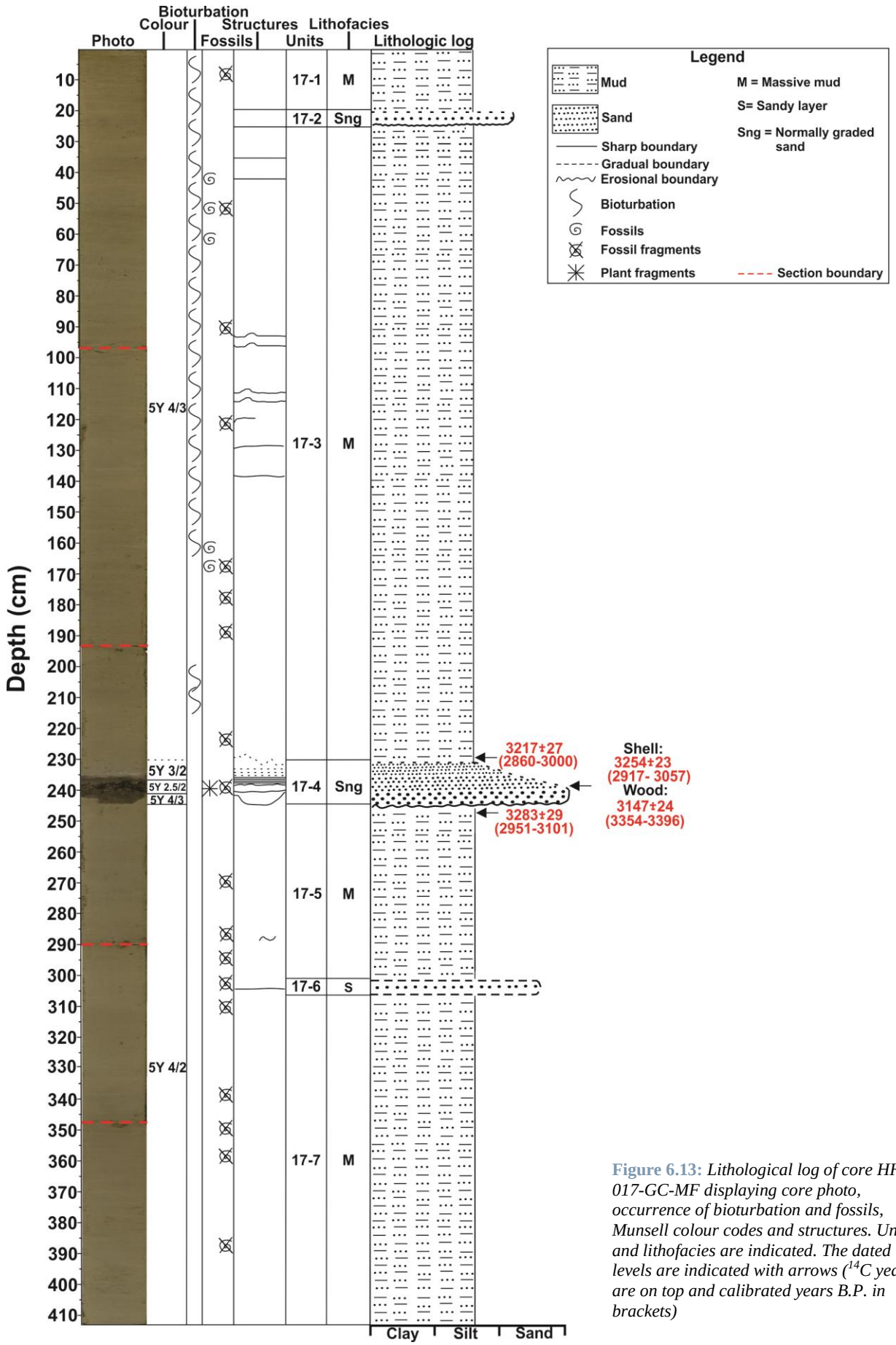

Figure 6.13: *Lithological log of core HH13-017-GC-MF displaying core photo, occurrence of bioturbation and fossils, Munsell colour codes and structures. Units and lithofacies are indicated. The dated levels are indicated with arrows (^{14}C years are on top and calibrated years B.P. in brackets)*

	17-7 **413 – 306 cm**		**17-6** **306 – 301 cm**		**17-5** **301 – 244 cm**		**17-4** **244 – 231 cm**		**17-3** **231 – 24 cm**		**17-2** **24 – 19 cm**		**17-1** **19 – 0 cm**	
	Average		**Average**		**Average**		**Average**		**Average**		**Average**		**Average**	
	Max	**Min**	**Max**	**Min**	**Max**	**Min**	**Max**	**Min**	**Max**	**Min**	**Max**	**Min**	**Max**	**Min**
Clay content (%)	13.1		1 sample: 7.7		13.4		6.6		13.7		X		14.6	
	14.6	11.1			14.7	11.3	10.2	2.9	14.9	12.8			15.6	13.6
Silt content (%)	70.3		1 sample: 38.7		69.8		43.9		72.6		X		70.9	
	75.0	59.6			73.2	63.6	63.6	24.2	78.9	67.8			71.4	70.3
Sand content (%)	16.6		1 sample: 53.6		16.8		49.5		13.7		X		14.5	
	29.1	10.4			25.1	12.5	72.9	26.2	18.7	6.4			16.0	13.0
Mean (M_G) (µm)	14.55		1 sample: 77.42		14.14		60.36		12.04		X		11.57	
	22.89	10.6			21.77	11.1	98	22.7	14.4	9.8			12.9	10.3
Sorting (σ_G) (µm)	5.63		1 sample: 9.32		5.79		4.35		5.29		X		5.52	
	7.35	4.94			7.01	5.22	5.4	3.3	6.33	4.4			5.58	5.47
Skewness (Sk_G) (µm)	-0.12		1 sample: -0.30		-0.09		-0.37		-0.12		X		-0.1	
	-0.01	-0.19			0.01	-0.15	-0.28	-0.46	-0.03	-0.25			-0.1	-0.1
Kurtosis (K_G) (µm)	1.19		1 sample: 0.88		1.24		1.26		1.26		X		1.23	
	1.28	0.94			1.29	1.14	1.35	1.16	1.31	1.14			1.25	1.21
Water content (%)	10.1		1 sample: 9.3		9.9		12.1		10.0		X		7.2	
	11.6	8.8			11.7	8.3	12.6	11.6	15.9	7.7			7.8	6.6
Undrained shear strength (kPa)	14.4		1 sample: 18.0		11.8		10.2		7.0		X		3.2	
	19.0	11.0			15.0	10.0	11.0	9.4	12.0	3.0			3.6	2.8
P-wave amplitude	100		100		99.5		93		98.8		X		X	
	100	99	100	100	80	100	100	81	100	81				
P-wave velocity (m/s)	1479		1480		1476		1524		1482		X		X	
	1492	1471	1486	1477	1484	1471	1596	1479	1504	1399				
Wet bulk density (g/cm^3)	1.60		1.59		1.59		1.78		1.55		1.53		1.45	
	1.63	1.56	1.60	1.57	1.61	1.56	2.03	1.54	1.63	1.50	1.65	1.48	1.47	1.41
Magnetic susceptibility (10^{-8} SI (m^3/kg))	7.70		7.90		8.90		16.21		18.3		32.33		33.94	
	8.08	6.58	7.93	7.86	11.9	6.9	21.81	13.1	33.0	9.9	33.88	29.82	35.26	29.41
Acoustic impedance (g*m*cm^{-3}*s^{-1})	2369		2355		2346		2576		2296		X		X	
	2404	2338	2365	2340	2391	2322	2916	2227	2393	2167				
Fractional porosity	0.666		0.673		0.674		0.566		0.698		0.705		0.756	
	0.688	0.652	0.682	0.667	0.689	0.660	0.672	0.454	0.736	0.653	0.738	0.64	0.778	0.744

Table 6.5: *Max, min and average values for the measured physical and grain-size properties for each unit of the core HH13-017-GC-*

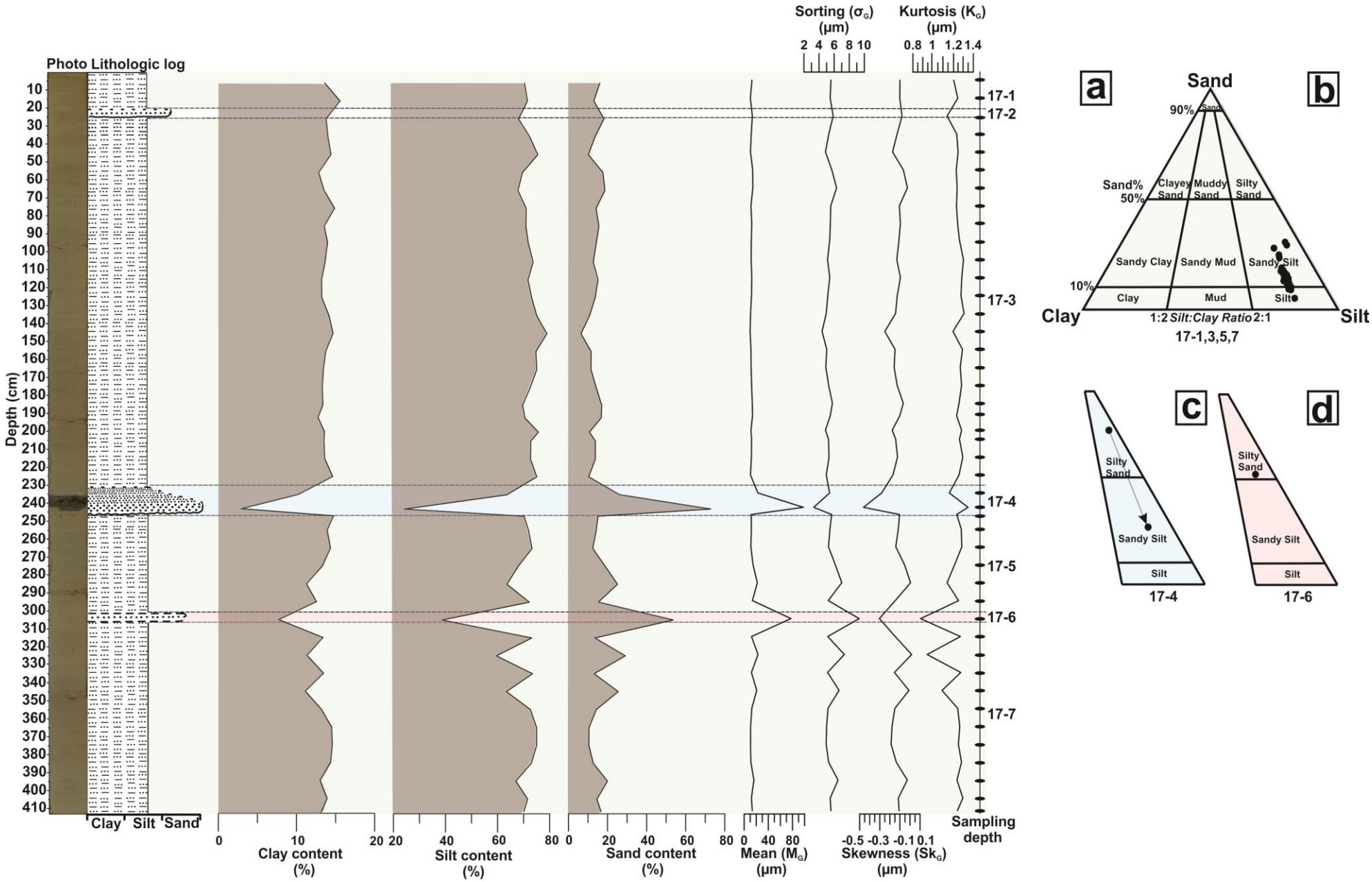

Figure 6.14: **a)** *Clay, silt and sand content, together with mean, sorting, skewness and kurtosis, of core HH13-017-GC-MF vs. depth. Sampling depths are located to the right. Colour photo and lithological log are included for reference. Units are indicated* **b)** *Sand, silt and clay diagram for unit 17-1,3,5,7* **c)** *Relevant sections of the sand, silt and clay diagram for unit 17-4, where the arrow indicates decreasing depth* **d)** *Relevant sections of the sand, silt and clay diagram for unit 17-6.*

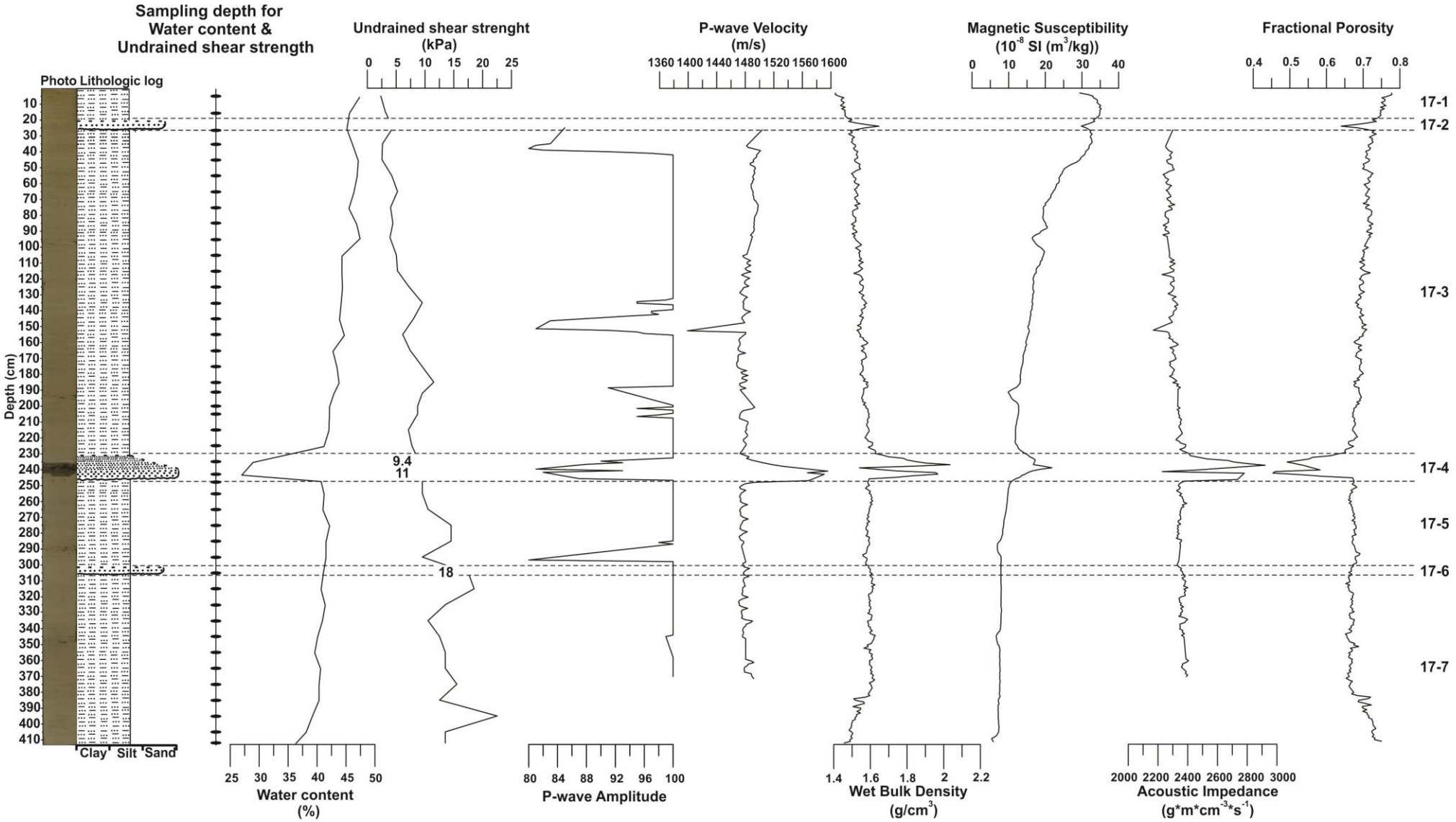

Figure 6.15: *Physical properties of core HH13-017-GC-MF vs. depth, where the sampling depths for water content and undrained shear strength are indicated to the left. Colour photo and lithological log are included for reference. Units are indicated.*

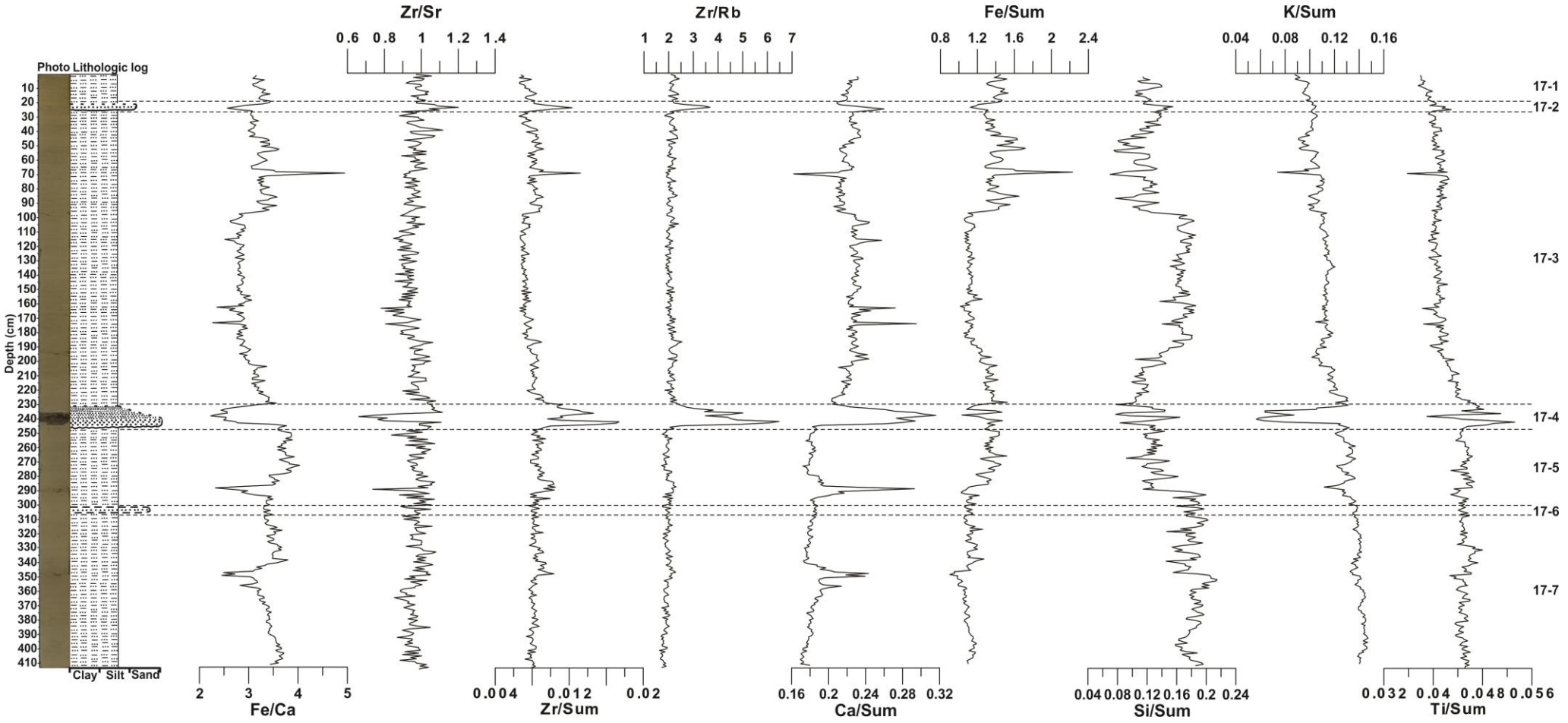

Figure 6.16: *Selected element ratios for core HH13-017-GC-MF vs. depth. Colour photo and lithological log are included for reference. Units are indicated.*

6.4.3 Unit 17-5 (301-244 cm)

The unit comprises lithofacies M (Fig. 6.13), defined between a gradual lower boundary and an erosive upper boundary (Fig. 6.13). The fine-grained and uniform composition of the sediment (Fig. 6.14), together with almost constant physical properties (Fig. 6.15) and element ratios (Fig. 6.16), suggest that the deposition occurred within a stable open marine environment. A steady, low dynamic deposition is also supported by the fine skewed and leptokurtic grain-size distribution. However, the interval between ~295 – 285 cm appears to have a different sediment configuration with a larger abundance of coarse fractions, higher density (darker features on X-radiograph), variations in element ratios, as well as relatively high numbers of fossils and fossil fragments. Increased contents of Ca and Sr are correlated to the fossil fragments at the sediment surface (Dean *et al.,* 1997; Dypvik & Harris, 2001; Rothwell *et al.,* 2006), whereas the increased Zr concentrations most probably reflect larger amounts of coarser material (Dypvik & Harris, 2001; Kylander *et al.,* 2010). This interval of the core has been interpreted to be the result of increased turbulences. One radiocarbon date from 247 -246 cm, i.e. right below the erosional contact with the overlying unit provided a calibrated age of 3026 cal. years BP.

6.4.4 Unit 17-4 (244 – 231 cm)

The unit comprise the most distinct feature of the core (Fig. 6.13), and comprises lithofacies Sng. Whereas its lower boundary is erosional, is upper boundary is gradual. A ~2 mm thick interval at the very base of the unit contains the coarsest grains. The interval at depths ~244 – 237 cm is mostly composed of structureless and massive, normally graded sand. However, an interval mainly composed of shell fragments and plant material (both wood fragments and moss), as well as empty pore space, occurs between ~241 – 237 cm (Fig. 6.18). The lithic grains observed in between the biogenic material are finer than the underlying massive sand. The sand interval between 237 – 235 cm is finer than below 241 cm, and it contains sub-horizontal parallel laminae. A gradual fining of the sediment occurs between 235 and 231 cm. Two samples from the massive sand (243 cm) and the laminated sand (234 cm) reveal fining upward between these depths from very coarse to medium sand (Fig. 6.14). All physical properties (Fig. 6.15) and element ratios (Fig. 6.16) are distinctly different compared to the surrounding units and follow the changes in grain size.

The erosive base, coarse grain-size, graded bedding, absent bioturbation, as well as lamination, indicate that the unit was deposited from a turbidity flow.

Turbidity flows (or currents) are turbulent currents with high velocity and density, driven by autosuspension (turbulent eddies are derived at the base of the current due to the motion of suspended material, which in turn drives additional grains into suspension; e.g. Friedman *et al.,* 1992). A turbidity flow can be divided into three zones; head, body and tail. Coarser grains accumulate in the leading part of the current, the head, causing its erosive character. This further forces sediments into

suspension, which are in turn incorporated into the body and tail of the current. Sediments are deposited by suspension fallouts from the body and the tail as the current fades away (e.g. Boggs, 1995; Stow *et al.*, 1996; Leeder, 2011).

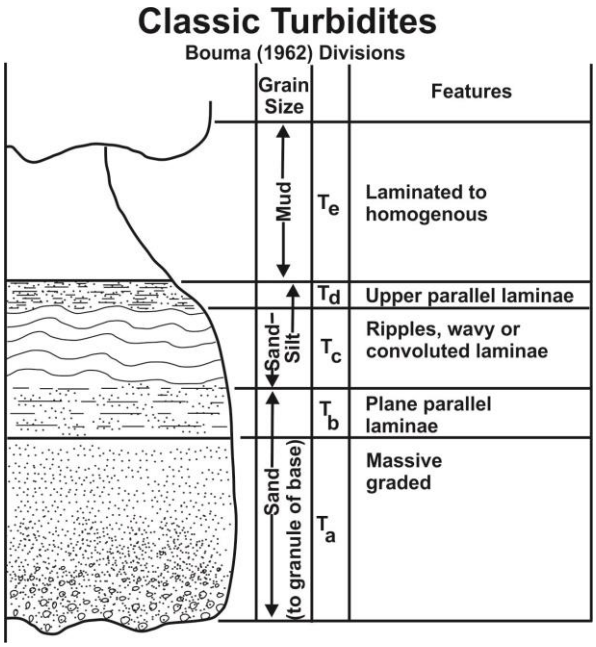

Figure 6.17: *Graphic presentation of the Bouma-sequence showing the characteristics of each unit (Bouma, 1962 in Shanmugam, 2000)*

The Bouma-sequence divides medium-grained turbidites into five intervals (T_a-T_e):

- T_a: The lowermost interval is massive graded with no internal structures, deposited very rapidly.
- T_b: Parallel-laminated interval is deposited by reduced, but still fairly high rates.
- T_c: Interval characterized by cross-laminated fine to very fine sand, often with climbing ripple stratification reflecting high bed aggradation
- T_d: Upper parallel lamination of silts and interlaminated silts and mud.
- T_e: Laminated to massive fine grained interval which reflects low-density current deposition. The uppermost unit represents the transition zone between turbidite and hemipelagic deposition.

(Bouma, 1992; Leeder, 2011)

The massive sand, structureless lowermost interval (~244 – 237 cm) of the unit is interpreted to represent interval T_a, this includes the erosive base, the massive sand and the bed composed of fossil and plant fragments (Fig. 6.18). The sub-horizontal and parallel laminated silt (237 – 235 cm) is suggested to be T_d, while depths between (235 and 231 cm) represents interval T_e of the Bouma-sequence.

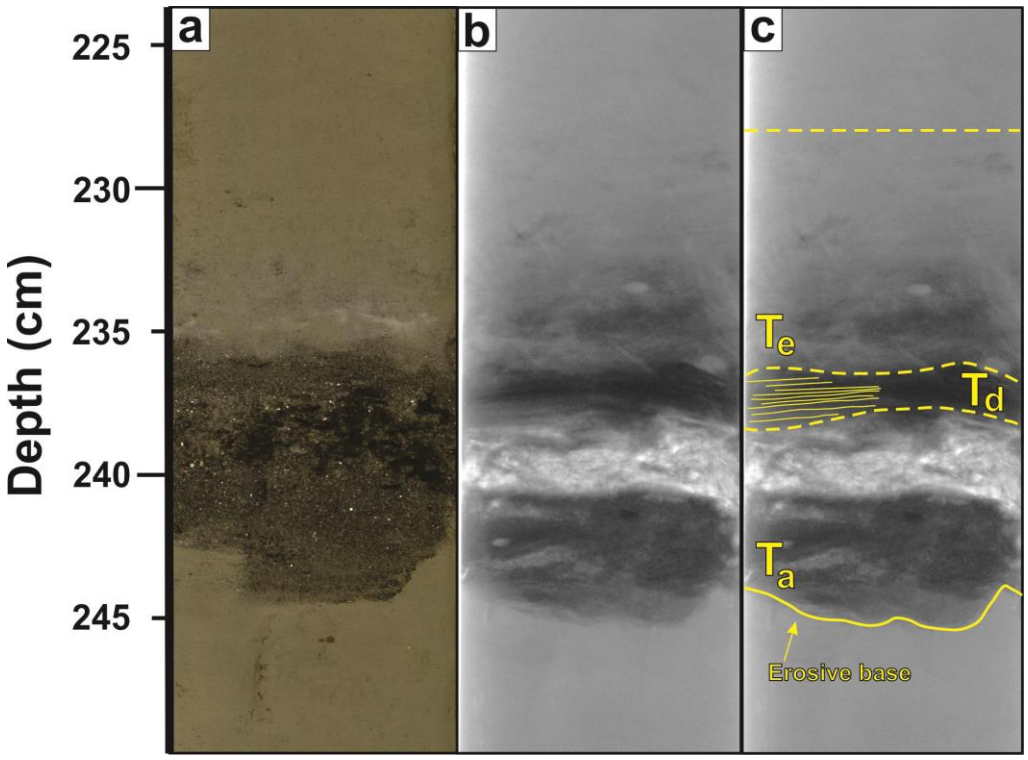

Figure 6.18: *The turbidite composing unit 17-4* **a)** *Colour photography* **b)** *X-radiograph* **b)** *Interpretation and divisions of Bouma sequence.*

The very fine skewed grain-size distribution found of the massive sand reflects the turbidity flow's ability to sort out the coarser fractions (i.e. accumulate the coarser grains at its base/head) (cf. Ananiadis *et al.,* 2004). The distinct differences in magnetic susceptibility and chemical composition indicate a different source for the sediments compared to the overlying and underlying units (Fig. 6.15). The terrigenous material (wood fragments and moss) most probably implies that the mass transport event was originated onshore.

The high Ca, Sr and Si content reflect the enrichment of carbonates (Dean *et al.,* 1997; Dypvik & Harris, 2001; Rothwell *et al.,* 2006; Heimbürger *et al.,* 2012), while higher amounts of Zr correspond well with coarser grain-size (Dypvik & Harris, 2001; Kylander *et al.,* 2010). Ti is often a component in heavy resistant materials which might be the reason why it is enhanced in the lower reaches of the turbidite (Rothwell *et al.,* 2006). Flakes of shining material have been observed and found to be evenly distributed for the whole unit, and are interpreted to be mica and can be correlated to the increased content of Rb (Dypvik & Harris, 2001; Kylander *et al.,* 2010).

Benthic foraminifera were sampled at the upper boundary of the unit, and provide an age of 2930 cal. years BP of these sediments. Together with the age of 3026 cal. years BP of the sediments right below the unit (*see Chapter 6.4.3*), the time of deposition can be interfered to be between 3026 and 2930 cal. years BP. Wood and shell fragments were sampled from the organic rich interval within the deposit

with the purpose of identifying the marine reservoir effect (cf. Bondevik *et al.*, 2000). However, the age obtained from the wood fragments (3375 ca. years BP) was higher than that of the shell fragments (2987 cal. years BP). This indicates that the trees containing the reworked wood fragments died approx. 400 years prior to the slope failure.

6.4.5 Unit 17-3 (231 – 24 cm)

The unit comprises lithofacies M, located between a gradual lower and an erosive upper boundary (Fig. 6.13). The fine-grained and structureless sediment is interpreted to be hemipelagic, deposited from suspension fallout in an open marine environment. Bioturbation varies. The element ratios indicate a slightly different chemical composition of the sediment in the upper part of the unit compared to the lower part (Fig. 6.16). This might be due to a change in the prevailing source area.

6.4.6 Unit 17-2 (24 – 19 cm)

The unit is composed of lithofacies Sng (Fig. 6.13). Its lower boundary is erosional, whereas its upper boundary is gradual. The lowermost ~1 mm can be seen as a coarse, dark, irregular line. The overlying sediments are normally graded. Based on visual observations, the uppermost ~4 cm of the unit appear as a transition zone into the above lying unit. The erosive base and normal grading suggest that unit 17-2 is a MTD. Based on the observed grain-size and the thickness of the bed it is suggested that it may have been deposited a low-density turbidite current. The wet bulk density is increased, while the fractional porosity is decreased (Fig. 6.15). Coarser grain-sizes are also corroborated by the increased content of Zr (Dypvik & Harris, 2001; Kylander *et al.*, 2010). Both magnetic susceptibility (Fig. 6.15) and element ratios (Fig. 6.16) indicate a different source for the sediments within the unit, compared to the surrounding units.

6.4.7 Unit 17-1 (19 – 0 cm)

The uppermost unit of the core comprises lithofacies M (Fig. 6.13). Its lower boundary is gradational; it upper boundary is the top of the core. The fine-grained and massive sediment has been interpreted to be the result of deposition within in a stable open marine environment with low dynamic processes. Bioturbation, fossil fragments and sulphide spots indicate a favourable environment for living organisms. The higher calcium content in the uppermost part of the unit correlates well with observations of fossil fragments at the sediment surface (Rothwell *et al.*, 2006).

6.4.8 Summary core HH13-017-GC-MF

Core HH13-017-GC-MF is divided into 7 lithostratigraphical units. Sedimentation took mainly place from suspension settling in an open marine environment reflected by units 17-7, 17-5, 17-3, 17-1. Here, a massive composition in most of these units reflects relatively stable conditions. Several mass-transport events interrupted the "normal" sedimentation. This includes non-eroding turbidity flows or hydroplaning debris flows (units 17-6), as well as deposition from high-density (17-4) and low-density (17-2) turbidity flows. The largest event (17-4) occurred between 3026 and 2930 cal. years BP. Wood fragments indicate that this event most probably originated onshore.

6.5 HH13-018-PC-MF

Core HH13-018-PC-MF was retrieved from an area with smooth seafloor, close to the eastern slope of Lyngenfjorden (Fig. 6.1; Tab. 6.1). It is divided into 12 units, representing the lithofacies: M, Ml, SMi, S and Sng.

Max, min and average values for the grain-size properties and the physical properties of each unit is listed in Table 6.6.

6.5.1 Unit 18-12 (574 – 531 cm)

The lowermost part of the core comprises lithofacies SMi (Fig. 6.19). Its lower boundary is not recovered; the upper boundary is gradual. The unit is divided into five sub-units; *a*, *b*, *c*, *d* and *e*, respectively. Sub-unit *e* (574 – 565 cm) comprises sandy sediments with a chaotic structure. The overlying sub-unit *d* (565 – 560 cm) comprises convex-down bent coarse and fine strata. Sub-horizontal laminated mud characterise sub-unit *c* (560 – 553 cm). Sub-unit *b* (553 -546cm) is composed of sandy and thin (~3 mm) strata, observed as "lines" of darker material, interlaminated in sub-horizontal laminated mud. Sub-unit *a* (546-531) comprises laminated mud and a half-arc-shaped sand-layer, where the sandy material has an erosive contact with the mud. The muddy laminae tilt downward ending in the erosional contact. Clasts occur throughout the whole unit. Fluctuations in physical properties and element ratios correlate well with the lithological differences of the sub-units (Fig. 6.21). 10784 10647

The unit is suggested to be composed of glacier-proximal glaciomarine sediments, deposited when the glacier front was located at the sill in the southern end of the study area. The glacier re-advanced to this position during the Ørnes event around 10,784 – 10,647 cal. years B.P. (Corner, 1980) (*see Chapter 2.3.2; Deglaciation*). The well-pronounced stratification indicates frequently changing depositional processes, which the platykurtic grain-size distribution further supports. The muddy silt is inferred to be rain-out from suspension, while the clasts are suggested to be ice-rafted debris (IRD) deposited by icebergs or sea ice (e.g. Forwick &Vorren, 2009; Beaten *et al.*, 2010). The coarser layers may reflect periods of enhanced ice rafting, or they could be the result of dumping by overturning icebergs (as described by Vorren *et al.*, 1983). Further, it is implied that sub-unit *a* comprises a MTD because of the truncation of the laminated mud. The magnetic susceptibility (Fig. 6.21) and the element ratios (Fig. 6.22) indicate that the sediment might be derived from a different source than the rest of the core. Higher content of Zr correlates well with coarser intervals of the unit (Dypvik & Harris, 2001; Kylander *et al.*, 2010).

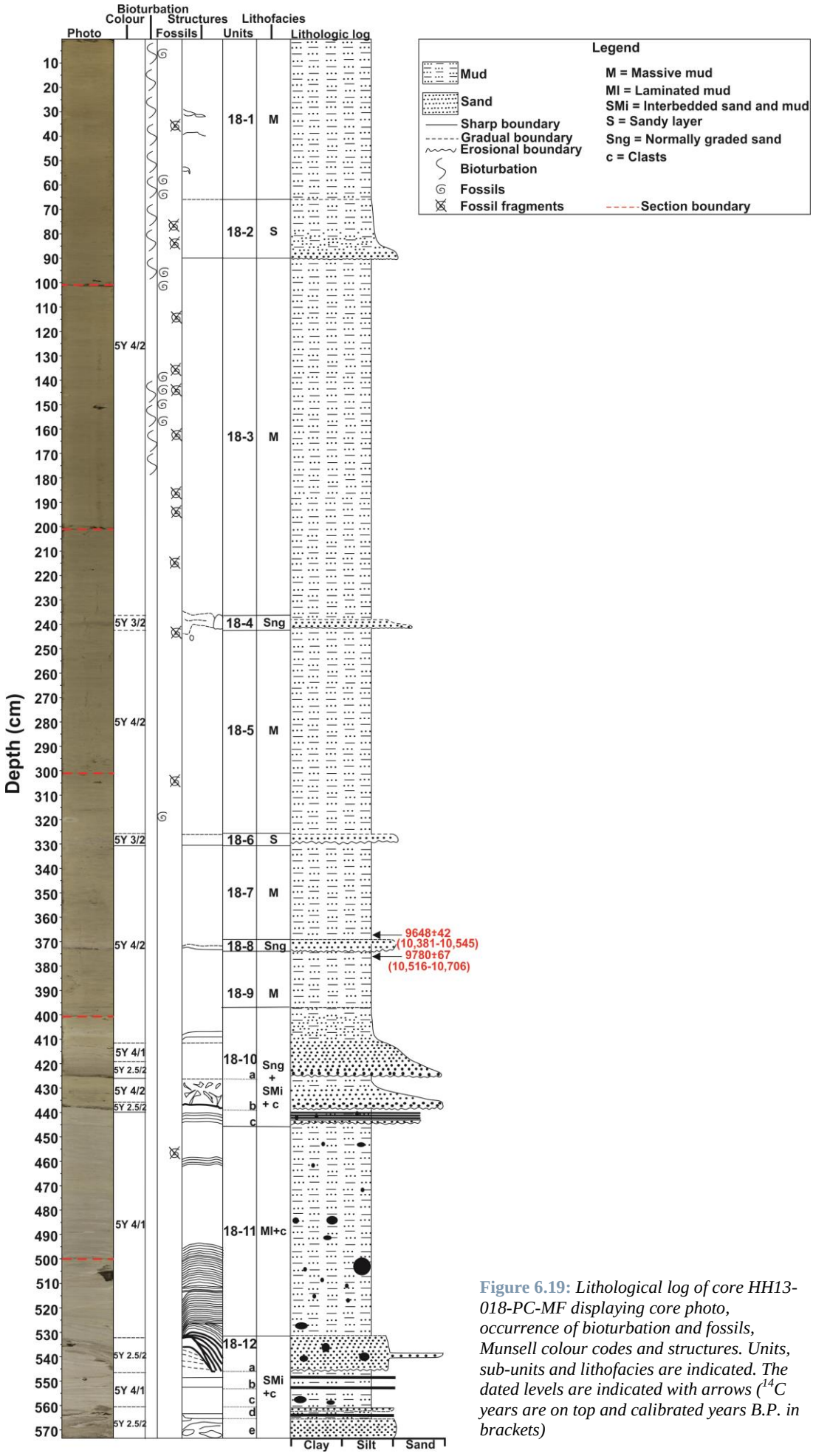

Figure 6.19: *Lithological log of core HH13-018-PC-MF displaying core photo, occurrence of bioturbation and fossils, Munsell colour codes and structures. Units, sub-units and lithofacies are indicated. The dated levels are indicated with arrows (^{14}C years are on top and calibrated years B.P. in brackets)*

	18-12 574 – 531 cm		18-11 531 – 447 cm		18-10 447 – 397 cm		18-9 397 – 375 cm		18-8 375 – 370 cm		18-7 370 -331 cm		18-6 331 – 326 cm		18-5 326 – 242 cm		18-4 242 – 236 cm		18-3 236 – 90 cm		18-2 90 – 66 cm		18-1 66 – 0 cm	
	Average		Average		Average		Average		Average		Average		Average		Average		Average		Average		Average		Average	
	Max	Min	Max	Min	Max	Min	Max	Min	Max	Min	Max	Min	Max	Min	Max	Min	Max	Min	Max	Min	Max	Min	Max	Min
Clay content (%)	15.8		16.7		14.7		17.1		1 sample: 15.7		17.1		1 sample: 9.6		13.5		X		14.3		X		13.9	
	17.6	11.6	21.3	11.5	27.2	6.0	19.7	10.3			17.9	16.3			16.0	8.8			15.2	13.1			15.0	11.2
Silt content (%)	56.8		61.9		56.8		60.1		1 sample: 70.6		70.2		1 sample: 40.7		62.6		X		72.2		X		70.5	
	63.6	40.9	76.4	41.5	67.0	28.4	70.4	36.3			73.9	66.1			72.7	36.4			77.3	64.1			74.7	59.7
Sand content (%)	28.0		21.4		28.5		22.8		1 sample: 13.7		12.7		1 sample: 49.7		24.0		X		13.5		X		15.6	
	47.5	18.8	46.2	2.6	65.7	5.8	53.4	10.7			16.7	8.2			54.8	11.3			22.8	8.1			29.1	11.3
Mean (M_G) (µm)	18.52		14.95		27.57		20.99		1 sample: 11.28		9.67		1 sample: 42.95		21.0		X		11.79		X		12.98	
	37.4	12.1	29.4	6.22	66.2	4.45	58.5	7.72			11.09	8.23			61.5	9.7			17.8	10.2			23.1	10.6
Sorting (σ_G) (µm)	7.3		6.78		5.8		6.9		1 sample: 5.79		5.83		1 sample: 7.79		6.73		X		5.42		X		5.61	
	8.5	6.6	9.29	4.32	9.89	3.33	9.12	5.63			6.64	5.25			7.76	5.38			7.04	4.7			7.12	5.0
Skewness (Sk_G) (µm)	-0.2		-0.09		-0.25		-0.19		1 sample: -0.16		-0.10		1 sample: -0.32		-0.12		X		-0.14		X		-0.1	
	-0.1	-0.3	0.07	-0.3	-0.1	-0.5	0.01	-0.5			-0.03	-0.2			0.03	-0.6			0.00	-0.2			-0.0	-0.2
Kurtosis (K_G) (µm)	0.95		1.02		1.24		1.12		1 sample: 1.89		1.25		1 sample: 0.76		1.11		X		1.24		X		1.21	
	1.04	0.84	1.27	0.73	1.69	0.79	1.27	0.78			1.26	1.22			1.3	0.79			1.29	1.14			1.29	0.9
Water content (%)	23.5		27.4		26.7		36.0		1 sample: 28.3		35.6		1 sample: 34.2		36.8		X		41.8		X		44.7	
	25.7	20.2	30.0	25.7	40.0	17.4	36.6	35.3			36.6	35.1			38.2	35.7			44.2	37.1			46.0	43.6
Undrained shear strength (kPa)	17.8		12.8		33.8		11.3		1 sample: 33.0		11.7		1 sample: 7.7		11.4		X		8.4		X		4.8	
	30(*)	8.2	26	7.7	70.0	6.6	13.0	10.0			14.0	6.8			22.0	8.2			12.0	5.9			6.7	3.3
P-wave amplitude	96.8		99.3		99		100		X		97		100		99.5		X		94.7		X		X	
	100	80	100	84	100	88	100	100			81	100	100	100	100	81			100	80				
P-wave velocity (m/s)	1572		1529		1568		1487		X		1495		1513		1488		X		1483		X		X	
	1635	1540	1544	1501	1730	1372	1491	1482			1525	1478	1524	1507	1506	1479			1525	1397				
Wet bulk density (g/cm^3)	2.0		1.9		1.9		1.7		1.74		1.7		1.8		1.67		1.7		1.6		1.5		1.5	
	2.2	1.9	1.9	1.8	2.2	1.6	1.9	1.7	1.8	1.7	1.8	1.6	1.8	1.7	1.7	1.6	1.7	1.6	1.7	1.5	1.5	1.5	1.5	1.5
Magnetic susceptibility (10^{-8} SI (m^3/kg))	37.0		34.6		41.0		27.9		27.2		20.5		18.9		12.8		12.1		8.7		11.0		18.1	
	42.0	23.2	40.2	25.3	49.0	32.0	31.2	22.6	27.8	26.1	26.0	17.4	20.0	17.5	16.8	10.7	12.6	11.8	11.7	6.5	11.3	10.7	34.6	11.6
Acoustic impedance ($g*m*cm^{-3}*s^{-1}$)	3074		2858		2954		2484		X		2525		2666		2510		X		2348		X		X	
	3352	2862	2977	2706	3692	2416	2512	2454			2719	2436	2763	2607	2614	2390			2643	2158				
Fractional porosity	0.44		0.51		0.51		0.62		0.58		0.62		0.57		0.62		0.63		0.68		0.70		0.71	
	0.52	0.35	0.56	0.49	0.66	0.35	0.64	0.50	0.6	0.6	0.64	0.57	0.59	0.54	0.67	0.59	0.65	0.61	0.72	0.59	0.70	0.70	0.73	0.69

Table 6.6: *Max, min and average values for the measured physical and grain-size properties for each unit of the core HH13-018-PC-MF.* * The undrained shear strength was measured to be 159 kPa at depth 572 cm.

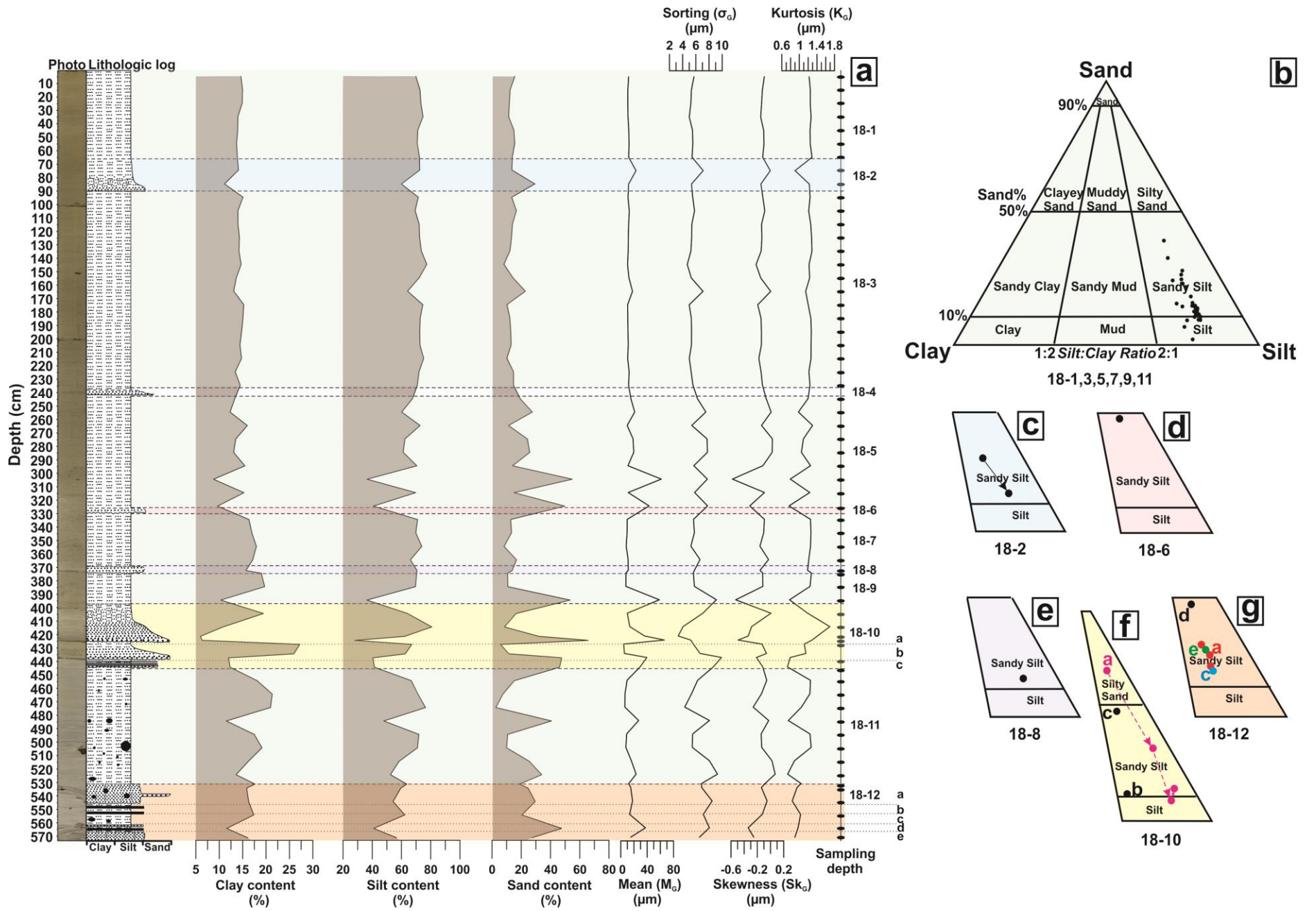

Figure 6.20: **a)** *Clay, silt and sand content, together with mean, sorting, skewness and kurtosis, of core HH13-018-PC-MF vs. depth. Sampling depths are located to the right. Colour photo and lithological log are included for reference. Units and sub-units are indicated* **b)** *Sand, silt and clay diagram for unit 18-1, 3, 5, 7, 9,11* **c)** *Relevant sections of the sand, silt and clay diagram for unit 18-2, where the arrow indicate decreasing depth.* **d)** *Relevant sections of the sand, silt and clay diagram for unit 18-6* **e)** *Relevant sections of the sand, silt and clay diagram for unit 18-8.* **f)** *Relevant sections of the sand, silt and clay diagram for unit 18-10, where a, c and d corresponds to the different sub-units. Arrows indicate decreasing depth.* **g)** *Relevant sections of the sand, silt and clay diagram for unit 18-2, where a, c, e and d corresponds to the different sub-unit.*

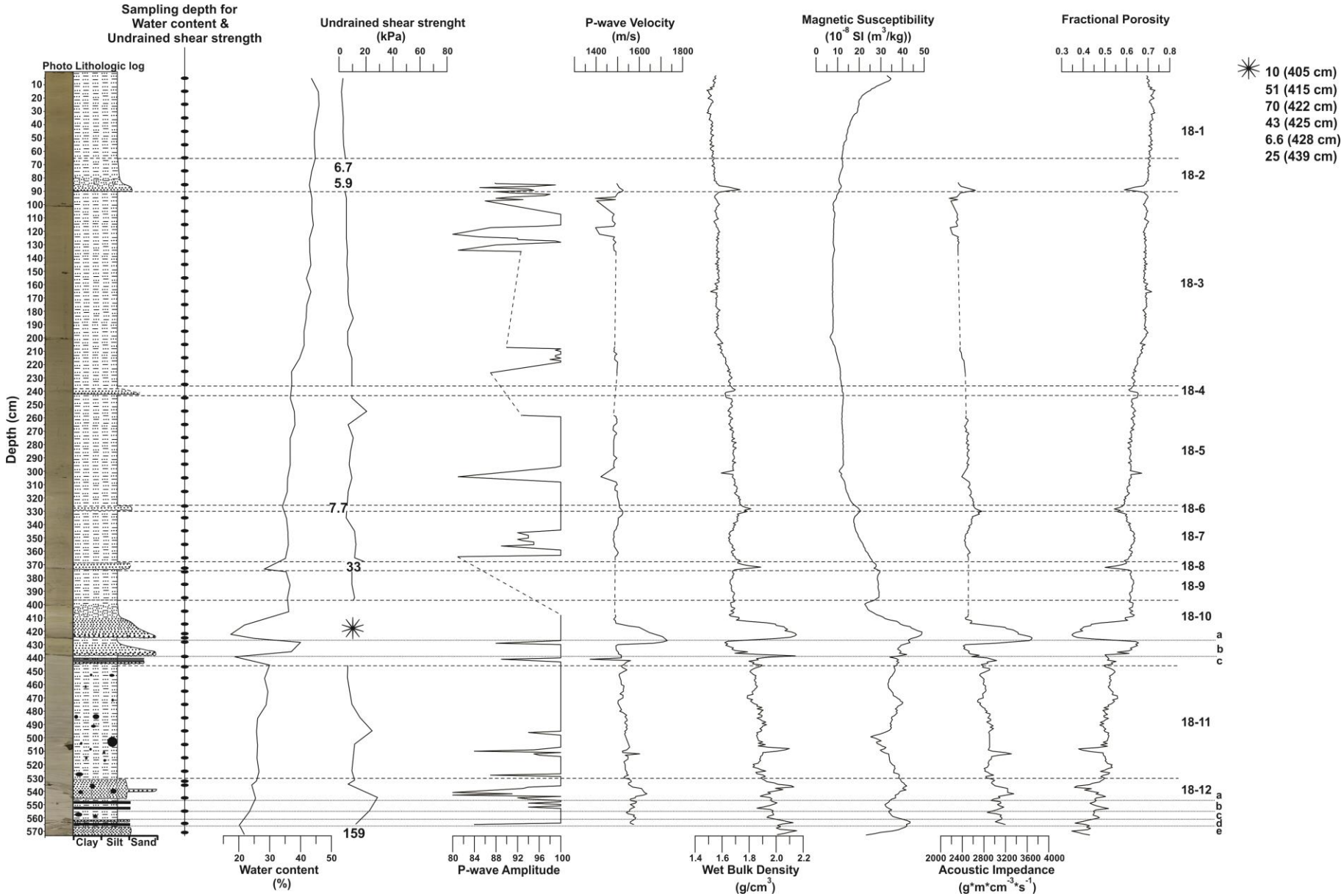

Figure 6.21: *Physical properties of core HH13-018-PC-MF vs. depth, where the sampling depths for water content and undrained shear strength are indicated to the left. Colour photo and lithological log are included for reference. Units and sub-units are indicated.*

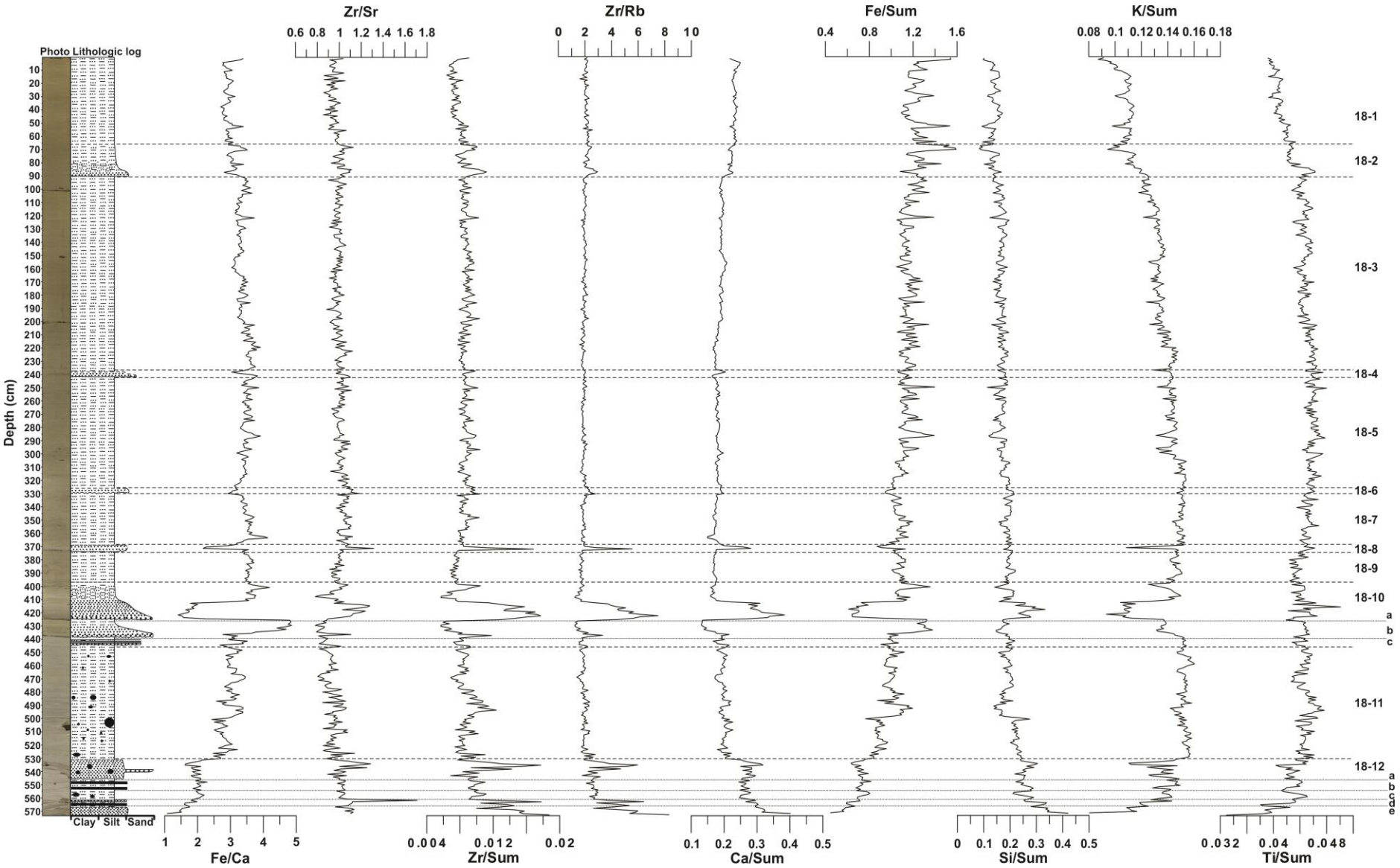

Figure 6.22: *Selected element ratios for core HH13-018-PC-MF vs. depth. Colour photo and lithological log are included for reference. Units and sub-units are indicated.*

6.5.2 Unit 18-11 (531 – 447 cm)

The unit comprises lithofacies M. It is between a gradual lower boundary and an erosional upper boundary (Fig. 6.19). The lowermost laminations (531 -526 cm) appear to be in concordance with the sandy-layering of unit 18-13 (sub-unit *a*). At depth 526, the laminations change and they are now more sub-horizontal with an opposite tilt. These laminations are tightly spaced and are found within the interval 530 – 514 cm. The overlying laminations are almost horizontal (514 – 511 cm) and are successively followed by a down-lapping convex u-shaped lamination (511 – 493 cm). Above this depth, lamination is generally absent, except for some relatively horizontal laminations between 463 – 457 cm (Fig. 6.23). All the laminations are found as weak colour variations on the sediment surface, and with slightly different densities in the X-ray photo, the latter suggesting minor variations in grain size. Clasts have been observed throughout the whole unit, both on the sediment surfaces and in X-radiographs. The unit is suggested to represent sediments deposited in a glacier-proximal glaciomarine environment, where the depositional processes can be correlated to those in the underlying unit (*see Chapter 6.5.1, above*).

6.5.3 Unit 18-10 (447 – 397 cm)

The unit is classified as lithofacies SMi and Sng. The unit is defined between an erosional lower boundary and a sharp upper boundary (Fig. 6.19 & 6.23). The unit is divided into the three sub-units: *a, b* and *c.* Sub-unit *c* (447 –439 cm) forms the erosive base of the unit. It is composed of four thin, coarser and slightly darker beds, where the lowermost is the thickest and most dominant. The X-radiograph reveals that small clasts occur (Fig. 6.23). Sub-unit *b* (439 – 426 cm) has an erosive lower boundary. The lowermost ~3 cm (439-436 cm) are normally grading, while the overlying sediments have a chaotic structure of muddy matrix interspersed with coarser and darker material (436 – 426 cm) (Fig. 6.23). A well-defined bed of distinct dark and coarse sediments characterises the erosional base of sub-unit *a* (426 – 397 cm). This sub-units fines upward. Its upper boundary is defined as the level where the coarse fractions no longer are present in the muddy matrix.

Sub-unit *c* is suggested to represent a minimum of four smaller MTDs (Fig. 6.23). Sub-unit *b* is interpreted to be a turbidite. Based on the characteristics of the lowermost ~4 cm (erosive base, normally graded coarser fractions and lack of structures) it is inferred that this interval represent T_a in the Bouma-sequence (*see Chapter 6.4.4*). The overlying ~10 cm correspond to sequence $T_{e,}$ which reflects the transition between the turbidite and hemipelagic deposition. The massive appearance of coarse and normally graded sediments in sub-unit *a*, as well as the erosive base, suggest that this sub-units contains an additional turbidite. It corresponds most probably to the Bouma-sequence T_a (Fig. 6.23).

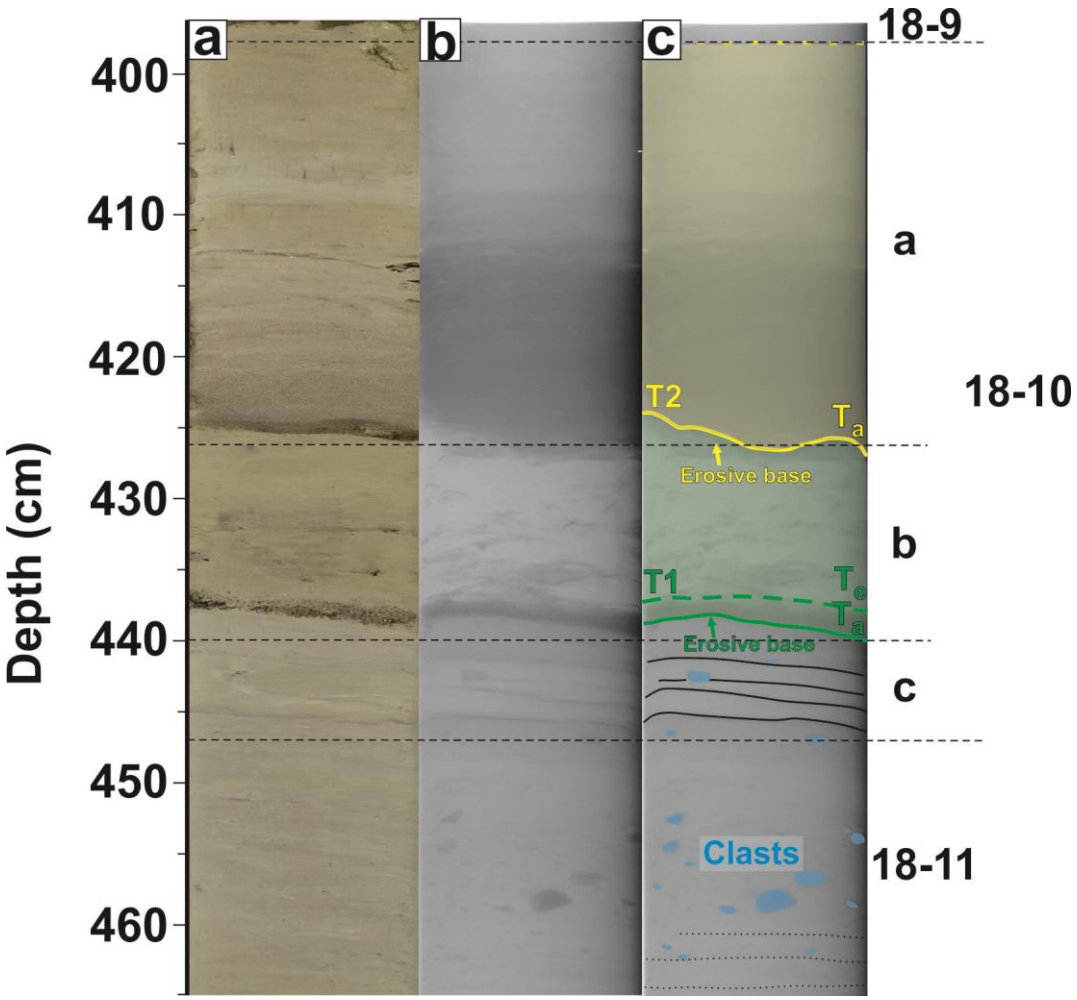

Figure 6.23: **a)** *Colour photo of unit 18-10* **b)** *X-radiograph* **c)** *Interpretations of the observed features in a and b: Clasts (blue), thin & parallel laminae (stippled, black lines), thin coarser layers (black lines). The green area represents the first deposited turbidite,T1, while the yellow area represents the second, T2. Corresponding Bouma-sequence are indicated with Ta and Te. Units and sub-units are indicated on the right side*

The interpretations above are further supported by the lack of bioturbation and changes in the physical properties (Fig. 6.21). Increased undrained shear strength and wet bulk density, with correspondingly low water content and fractional porosity, is consistent with the coarser grain sizes. Changing magnetic susceptibility values (Fig. 6.21) and chemical composition (Fig. 6.22), when entering the unit, suggests a different source for this interval. The increased content of Zr correlates with the coarser fractions of the sediment (Dypvik & Harris, 2001; Kylander *et al.*, 2010). The different Fe/Ca ratios of the two turbidites indicate that they derived from different source areas (Rothwell *et al.*, 2010). The higher content of Ti in sub-unit *a* corresponds well with the fact that turbidite bases often are enriched with Ti (Rothwell *et al.*, 2010).

6.5.4 Unit 18-9 (397 – 375 cm)

The unit is defined by a gradual lower boundary and an erosional upper boundary (Fig. 6.19), and composes lithofacies M. The fine-grained and massive sediment (Fig. 6.20) of the unit is interpreted to be the result of deposition in a stable sedimentary environment. The finer fractions, as well as the absence of clasts and laminations indicate that deposition occurred in an open-marine environment. However, glaciers were still active in the inner parts of the fjord system; depth 375.5 – 377.5 cm is provided by an age of 10.611 cal. years BP (Corner, 1980)

6.5.5 Unit 18-8 (375 – 370 cm)

The unit is mainly composed of one bed, classified as lithofacies Sng (*see Chapter 6.1.6.4*). The unit has an erosional lower and a gradational upper boundary (Fig. 6.19). Visual observations reveal a sharp and erosive contact with the underlying sediments, gradual upper contact and normal size grading. Based on this it is interpreted that the unit was deposited by a turbidity flow (Bouma, 1962; Middleton & Hampton, 1973 in McHugh *et al.*, 1996). The increased undrained shear strength and wet bulk density, together with decreased water content and fractional porosity verifies a coarser grain-size. The increased Zr content correlates to the coarser grains (Dypvik & Harris, 2001; Kylander *et al.*, 2010).

6.5.6 Unit 18-7 (370 – 331 cm)

The unit comprises lithofacies M , and is defined by a gradual lower boundary and an erosional upper boundary (Fig. 6.19). Based on the fine-grained (Fig. 6.20), and massive composition of the sediment, as well as relatively constant physical properties (Fig. 6.21) and element ratios (Fig. 6.22) the unit is interpreted to be deposited from suspension fallout in a stable sedimentary environment. The fine skewed and leptokurtic grain-size distribution further indicates steady sedimentary processes with low dynamics. One radiocarbon date from 368 - 370 cm provided an age of 10,463 cal. years BP.

6.5.7 Unit 18-6 (331 -326 cm)

The unit is classified as lithofacies S, and is located between an erosional lower boundary and a gradual upper boundary (Fig. 6.19). No structures are observed, and the unit is imaged as a chaotic mix of dense and less dense material on the X-radiographs. The physical properties reflect well the coarser granulometric composition of this unit compared to the surrounding units (Fig. 6.21). The platykurtic grain-size distribution indicates a depositional process of variable dynamics. It is suggested that this unit represents a MTD.

6.5.8 Unit 18-5 (326 - 242 cm) (326-242)

The unit comprises lithofacies M. The unit is relatively structureless, except for a higher density lens observed in the X-radiographs at c. 246 cm. The amounts of clay, silt and sand (Fig 6.20), as well as physical properties (Fig. 6.21) and element ratios (Fig. 6.22) are relatively constant throughout the unit, except of ~305 cm, where a coarser interval occurs. The fine-grained and massive sediment composition is assumed to reflect a stable sedimentary environment. However, the coarser interval at ~ 305 cm could be caused by e.g. increased water turbulences or a smaller mass transport event.

6.5.9 Unit 18-4 (242 – 236 cm)

Based on its characteristics, the unit is classified as lithofacies Sng. The layer becomes thinner/more diffuse towards the left side of the core (Fig. 6.19), and has an erosional contact with the underlying unit. No sediments were analysed, nor were the undrained shear strength measured, and the P-wave velocity and the acoustic impedance were found unreliable. The unit comprise a high amount of fossil fragments. Still, based on visual observations, the unit is interpreted to be a MTD. The increased calcium content for the unit can be correlated to the observed fossil fragments (Rothwell *et al.,* 2010). Additionally; Zr, Sr, Si, K and Ti have slightly higher contents within the unit (Fig. 6.22).

6.5.10 Unit 18-3 (236 – 90 cm)

The unit comprises lithofacies M, and is located between a gradual lower boundary and an erosional upper boundary (Fig. 6.19). The grain-size composition is relatively constant throughout the unit, suggesting that the deposition occurred within a stable sedimentary environment. The occurrence of bioturbation, shells, fossil fragments and sulphide spots indicate that the environment was more favourable for living organisms than during the deposition of the underlying units. The physical properties indicate a slightly different sediment composition for the uppermost reaches of the unit (Fig. 6.21), an interval implied to be coarser by the increased zirconium (Dypvik & Harris, 2001; Kylander *et al.,* 2010). This might indicate a period of increased bottom-current velocities.

6.5.11 Unit 18-2 (90 – 66 cm)

The unit is bounded an erosional lower boundary and a gradual upper boundary, and is classified as lithofacies S (Fig. 6.19). The sandy layer has a coarser character (Fig. 6.20) and a significantly higher density according to the X-radiograph. The lower reaches of the unit has an increased wet bulk density, and a decreased fractional porosity (Fig. 6.21). The Fe content is increased for the whole unit, while Zr and Ti have increased contents within the lower parts of the unit (Fig. 6.22). The latter indicates coarser grain sizes (Dypvik & Harris, 2001; Kylander *et al.,* 2010; Rothwell *et al.* 2010). Based on this the unit is suggested to comprise a MTD.

6.5.12 Unit 18-1 (66 – 0 cm)

The unit comprises lithofacies M, and is found between a gradual lower boundary and the top of the core (Fig. 6.19). The sediment composition is relatively constant throughout this interval of the core (Fig. 6.20 & Fig. 6.21). The unit is suggested to be deposited in a steady and low dynamic open marine environment.

6.5.13 Summary core HH13-018-PC-MF

Core HH13-018-PC-MF is divided into 12 lithostratigraphic units. Deposition within a proximal glaciomarine environment is interpreted for the lower reaches of the core; unit 18-12 and 18-11, where sediment reworking is indicated in unit 18-12. A MTD sequence directly follows the proximal glaciomarine sediments (unit 18-10). Sedimentation took mainly place from suspension setting in an open marine environment (unit 18-9, 18-7, 18-5, 18-3 and 18-1), where a massive character of these deposits indicate relatively stable conditions.

Additionally, several mass transport deposits are identified: unit 18-8 comprises a turbidite deposited between 10,611 – 10,463 cal. years BP, furthermore, are three intervals interpreted to represent mass transport events (unit 18-6, 18-4 and 18-2)

6.6 HH13-019-PC-MF

Core HH13-019-PC-MF is the northernmost core in this study. It was retrieved from a flat part of the fjord floor, close to its eastern slope. The core is divided into 11 lithostratigraphic units representing lithofacies M, SMi, S and Sng. During opening of the sections, the smell of hydrogen sulphide (H_2S) could be recognized for section 2 and 3.

Max, min and average values for the grain-size properties and the physical properties is found for each unit in Table 6.7.

6.6.1 Unit 19-11 (474 – 471 cm)

The unit comprises lithofacies M (Fig. 6.24). Its lower boundary was not captured in the core, whereas its upper boundary is erosional. Caused by its limited extent, and its position in the bottom of the core, the unit has not been provided with any data. However, visual observations indicate that it comprise a similar character as unit 19-9 (*see Chapter 6.6.3*).

6.6.2 Unit 19-10 (471 – 452 cm).

The unit is classified as lithofacies Sng, is located between an erosional lower boundary and a gradual upper boundary (Fig 6.24). The lower part of the unit (471 – 454 cm) is normally grading and massive sand (> 50 % sand; Fig. 6.25), whereas the uppermost ~2 cm (454 – 452 cm) show weak laminations. Near the upper boundary of the unit the clay content is > 90 %. A different character between these two intervals is further indicated by the physical properties (Fig. 6.26), where the magnetic susceptibility suggests different provenance between them. The unit has increased contents of Zr indicating coarser grains (Dypvik & Harris, 2001; Kylander *et al.*, 2010), and higher Ca and Sr contents relates to a higher amount of fossil fragments (Dean *et al.*, 1997; Dypvik & Harris, 2001; Rothwell *et al.*,2010). The base of the unit is enriched with Ti which is commonly observed within the base of a turbidite deposit (Rothwell *et al.*, 2010). Based on this the unit is suggested to comprise a turbidite; where the lowermost interval (471 – 454 cm) corresponds with T_a and the upper interval corresponds with T_e of the Bouma-sequence (*see Chapter 6.4.4*).

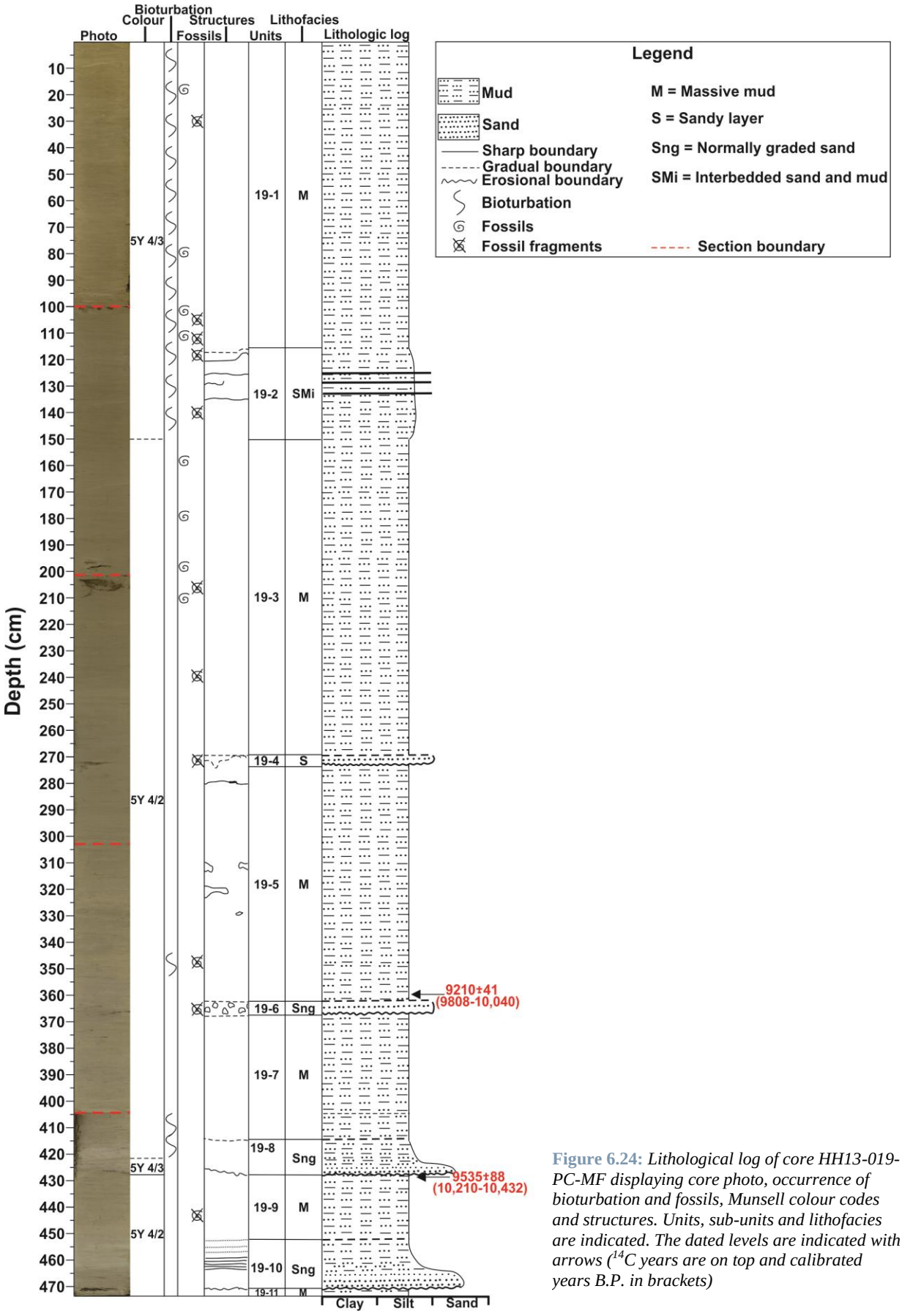

Figure 6.24: *Lithological log of core HH13-019-PC-MF displaying core photo, occurrence of bioturbation and fossils, Munsell colour codes and structures. Units, sub-units and lithofacies are indicated. The dated levels are indicated with arrows (^{14}C years are on top and calibrated years B.P. in brackets)*

	19-11 474 – 471 cm		19-10 471 – 452 cm		19-9 452 – 427.5 cm		19-8 427.5 - 414 cm		19-7 414 - 367 cm		19-6 367 – 362 cm		19-5 362 - 274 cm		19-4 274 - 269 cm		19-3 269 - 150 cm		19-2 150 - 116 cm		19-1 116 – 0 cm	
	Average		Average		Average		Average		Average		Average		Average		Average		Average		Average		Average	
	Max	Min	Max	Min	Max	Min	Max	Min	Max	Min	Max	Min	Max	Min	Max	Min	Max	Min	Max	Min	Max	Min
Clay content (%)	X		37.4		17.6		1 sample:		16.2		1 sample:		16.0		X		14.3		9.5		14.7	
			9.4	92.2	17.7	16.6	18.4		17.4	12.8	16.4		17.6	14.4			16.5	9.7	11.1	8.0	19.0	12.9
Silt content (%)	X		42.6		66.5		1 sample:		64.7		1 sample:		71.9		X		71.5		44.4		70.0	
			80.1	7.8	69.2	64.7	71.2		69.8	49.1	70.6		75.5	67.8			80.1	49.8	51.2	37.7	77.3	64.9
Sand content (%)	X		20.0		15.9		1 sampel:		19.1		1 sample:		12.1		X		14.2		46.0		15.4	
			50.6	0	17.5	14.3	10.4		38.1	13.3	13.0		17.2	7.4			40.5	3.4	54.3	37.8	22.2	5.5
Mean (M_G) (µm)	X		20.36		10.67		1 sample:		13.06		1 sample:		10.31		X		12.91		44.56		12.53	
			47.06	0.47	11.29	9.87	8.37		24.82	9.69	10.16		12.88	8.10			31.90	8.54	61.75	27.38	17.35	8.28
Sorting (σ_G) (µm)	X		4.78		6.51		1 sample:		6.69		1 sample:		5.47		X		5.41		7.55		5.79	
			7.78	2.61	6.97	5.94	5.53		8.92	5.78	5.60		6.16	4.9			7.26	4.34	7.91	7.19	6.78	4.56
Skewness (Sk_G) (µm)	X		-0.07		-0.7		1 sample: -		-0.05		1 sample: -		-0.13		X		5.41		-0.28		-0.09	
			0.4	-0.37	-0.02	-0.14	0.16		0.01	-0.1	1.13		-0.07	-0.2			-0.04	-0.3	-0.03	-0.54	0.003	-0.2
Kurtosis (K_G) (µm)	X		1.28		1.18		1 sample:		1.14		1 sample:		1.23		X		1.18		0.79		1.18	
			1.68	0.77	1.20	1.15	1.26		1.25	0.75	1.18		1.27	1.17			1.25	0.81	0.8	0.78	1.25	1.05
Water content (%)	X		30.9		35		1 sample:		35.1		1 sample:		36.2		X		41.7		43.5		46.2	
			38.1	24.1	38.3	30	30.2		35.4	34.8	29.4		37.3	34.9			44.1	36.9	43.8	43.1	47.4	43.1
Undrained shear strength (kPa)	X		7.8		9.7		1 sample:		12.5		1 sample:		16.2		X		12.9		9.4		4.7	
			10	6.7	12	7	45.0		17.0	6.8	15.0		28.0	10.0			19.0	8.5	12.0	6.7	5.9	3.7
P-wave amplitude	X		100		98.7		100		97.1		96.8		99.9		100		98.4		92.9		94.9	
			100	100	100	81	100	100	100	86	100	90	100	95	100	100	100	80	100	83	100	80
P-wave velocity (m/s)	X		1493		1492		1488		1491		1491		1491		1494		1476		1469		1470	
			1547	1472	1565	1473	1500	1481	1506	1481	1502	1485	1512	1479	1497	1491	1494	1464	1478	1465	1484	1456
Wet bulk density (g/cm^3)	X		1.72		1.73		1.74		1.68		1.74		1.69		1.69		1.59		1.57		1.49	
			1.9	1.63	1.99	1.67	1.77	1.72	1.77	1.60	1.77	1.73	1.84	1.55	1.71	1.67	1.7	1.53	1.65	1.54	1.57	1.27
Magnetic susceptibility	X		28.16		27.58		24.37		16.63		14.4		11.78		12.12		8.74		9.35		17.85	
			32.96	25.98	29.16	25.67	26.7	22.92	22.80	14.99	15.0	13.58	13.36	7.94	12.2	12.03	11.92	7.01	10.4	8.52	36.45	8.19
Acoustic impedance	X		2573		2569		2594		2549		2598		2526		2531		2349		2296		2229	
			2933	2403	3105	2462	2653	2547	2658	2497	2665	2571	2767	2463	2562	2497	2533	2254	2364	2264	2276	2209
Fractional porosity	X		0.596		0.591		0.584		0.623		0.584		0.617		0.612		0.674		0.684		0.731	
			0.649	0.496	0.627	0.438	0.597	0.567	0.691	0.569	0.593	0.566	0.695	0.528	0.624	0.603	0.706	0.61	0.702	0.637	0.861	0.685

Table 6.7: *Max, min and average values for the measured physical and grain-size properties for each unit of the core HH13-019-PC-MF.*

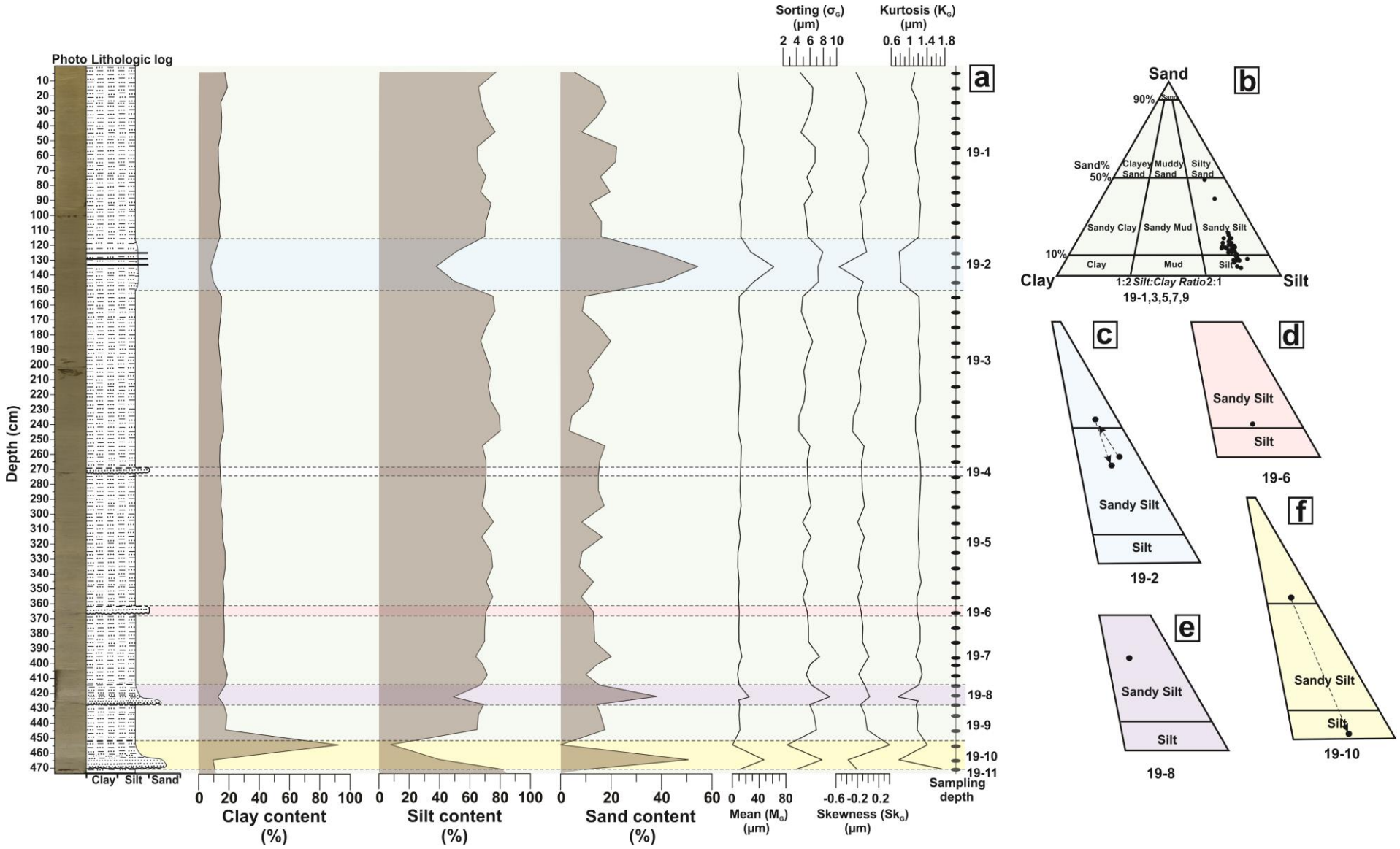

Figure 6.25: **a)** *Clay, silt and sand content, together with mean, sorting, skewness and kurtosis, of core HH13-019-PC-MF vs. depth. Sampling depths are indicated to the right. Colour photo and lithological log are included for reference. Units are indicated.* ***b)*** *Sand, silt and clay diagram for unit 19-1, 3, 5, 7, 9.* **c)** *Relevant sections of the sand, silt and clay diagram for unit 19-2, where the arrow indicates decreasing core depth.* **d)** *Relevant sections of the sand, silt and clay diagram for unit 19-6* **e)** *Relevant sections of the sand, silt and clay diagram for unit 19-8.* **f)** *Relevant sections of the sand, silt and clay diagram for unit 19-10, where the arrow indicates decreasing core depth.*

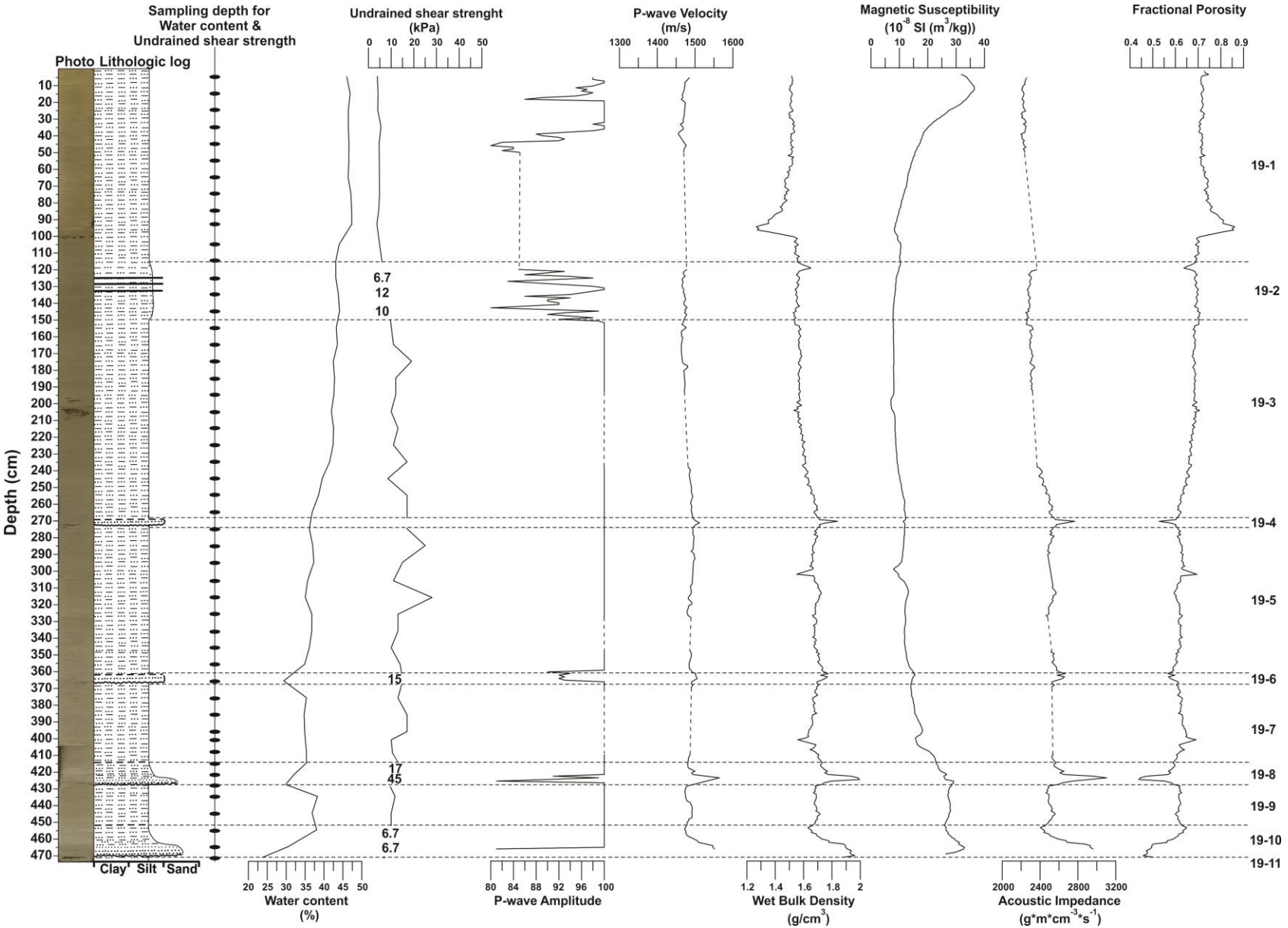

Figure 6.26: *Physical properties of core HH13-019-PC-MF vs. depth, where the sampling depths for water content and undrained shear strength are indicated to the left. Colour photo and lithological log are included for reference. Units are indicated.*

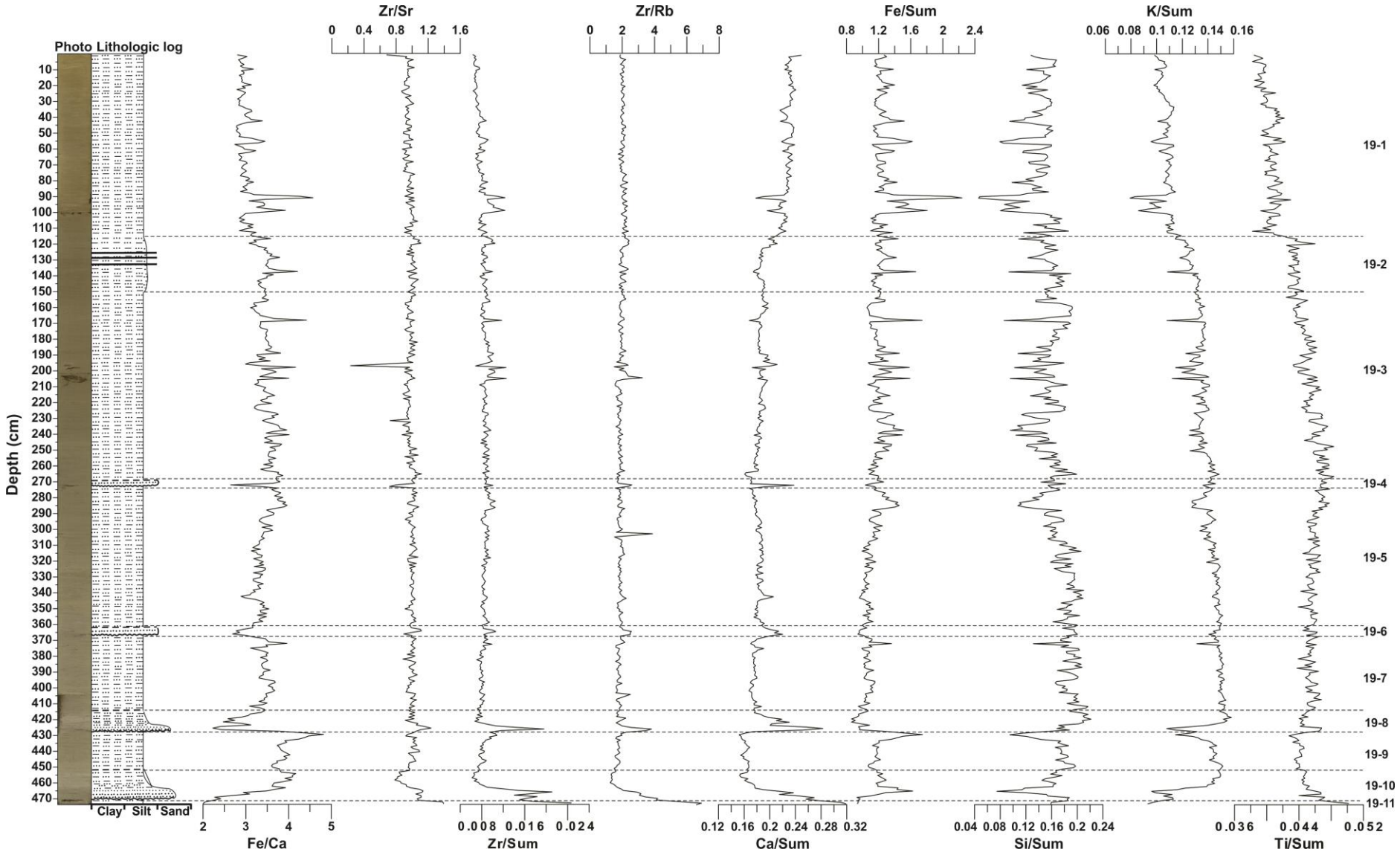

Figure 6.27: *Selected element ratios for core HH13-019-PC-MF vs. depth. Colour photo and lithological log are included for reference. Units are indicated.*

6.6.3 Unit 19-9 (452 – 427.5m)

The unit composes lithofacies M, and is bounded by gradual lower boundary and an erosional upper boundary (Fig. 6.24). The ratio between clay, silt and sand is relatively constant for this unit (6.25), also the physical properties are constant (Fig. 6.26). The fine and relatively structureless sediment is interpreted to indicate a stable depositional process. Benthic foraminifera indicate an age of 10,321 cal. years B.P. for the sediments located just below the upper erosional boundary (428 – 430 cm). This means that the deposition occurred during the Skibotn event, 10393 – 10316 cal. years B.P., when inner parts of the fjord system still was influenced by glaciers (Corner, 1980). However, the coring site would have been in a distal position to the glacier. Furthermore, the threshold located in the inner part of the study area (*see Chapter 4.1*) provide an dampening effect considering the glaciomarine processes further south. Hence, the deposition of the unit occurred within an open marine environment.

6.6.4 Unit 19-8 (427.5 – 414 cm)

The unit comprises lithofacies Sng, and is defined by an erosional lower boundary and a gradual upper boundary (Fig. 6.24). The base of the unit is a well-defined bed (~1 cm thick) comprising distinct darker and coarser material, which has an inclined erosional contact with the underlying sediments. The sediments grade towards a sandy mud at the top of this unit (Fig. 6.25). Bioturbation is absent. Peaks in the physical properties, e.g. low water content and fractional porosity, as well as increased wet bulk density and shear strength correlate with the coarse lithological composition of this unit (Fig. 6. 26). Based on the fining upward trend, the erosive lower boundary, together with changes in physical properties and absence of bioturbation, it is suggested that unit 19-8 contains a turbidite. The increased concentrations of Zr and Ti correlate well with the normal grading (highest at the base of the unit) (Dypvik & Harris, 2001; Rothwell *et al.*, 2006; Kylander *et al.*, 2010), turbidite bases are often enriched in Ti (Rothwell *et al.*, 2006).

6.6.5 Unit 19-7 (414 – 367 cm)

The unit has a gradual lower boundary and an erosional upper boundary (Fig. 6.24), and is classified as lithofacies M. The grain-size composition is relatively constant for this part of the core (Fig. 6.25), as well are the physical properties (Fig. 6.26) and the element ratios (6.27). However, around depth ~410 cm the grain-size and physical properties indicate that the sediments are of a coarser character. The unit is suggested to represent suspension fallout within a stable sedimentary environment, where the change in character at depth ~410 cm reflects might reflect a minor MTD.

6.6.6 Unit 19-6 (367 – 362 cm)

The unit composes lithofacies Sng, and is bounded by an erosional lower boundary and a gradual upper boundary (Fig. 6.24). From observations of the sediment surface, this unit is best described as coarser and darker lenses within a muddy matrix, where each lens is found to have an upward fining from its base which comprises the coarsest material. The X-radiographs reveal a chaotic pattern where higher density areas are dragged/ mixed into the surrounding lower density material (Fig.6.28). Material were only sampled for analysis in the upper reaches of the unit, where its results show a relatively similar composition compared with the sediments collected right above and below this unit (Fig. 6.25). The physical properties, on the other hand, support the coarser composition (Fig. 6.26). The higher amount of Zr correlates to the coarser fractions (Dypvik & Harris, 2001; Kylander *et al.*, 2010), whereas increased Ca concentrations are related to the presence of fossil fragments within the coarser parts of the unit (Rothwell *et al.*, 2006). The unit is suggested to represent a MTD, further, based on the chaotic pattern, the MTD is inferred to be a debris flow.

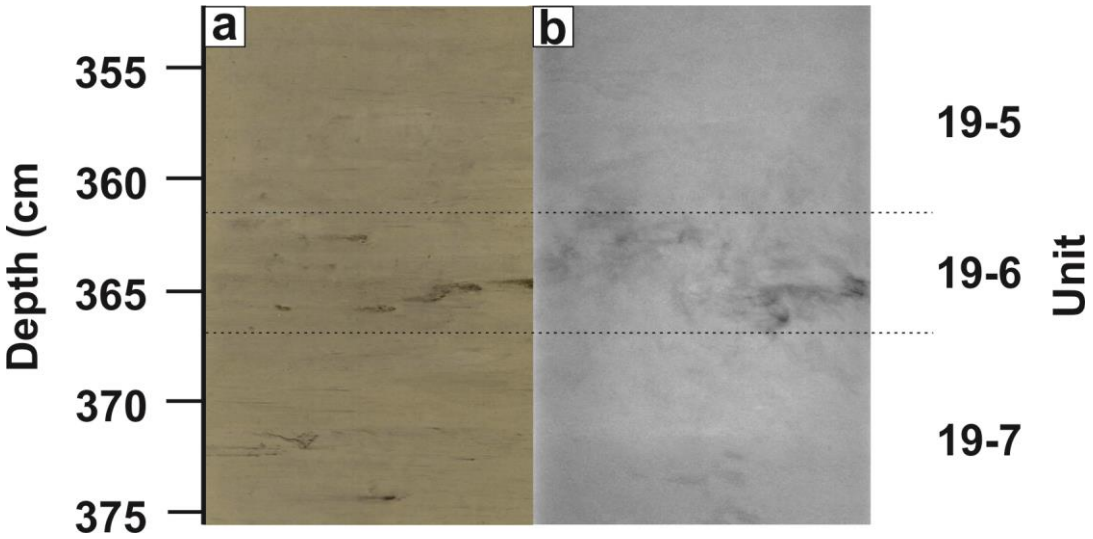

Figure 6.28: **a)** *Colour picture of the debris flow found within unit 19-6. Note how the coarser material is found concentrated in lens shaped areas* **b)** *X-radiograph*

6.6.7 Unit 19-5 (362 – 274 cm)

The unit is classified as lithofacies M, and is located between a gradual lower boundary and an erosional upper boundary. The granulometric compositon (Fig.6.25), physical properties (Fig. 6.26) and element ratios (Fig. 6.27) are relatively constant throughout the unit. It is suggested that the unit was deposited within a stable sedimentary environment, which is further verified by the fine skewed and leptokurtic grain-size distribution. A radiocarbon date from 358.5 – 360.5 cm provided an age of 9924 cal. years B.P.

6.6.8 Unit 19-4 (274 – 269 cm)

The unit comprises lithofacies S, and is located between an erosional lower boundary and a gradual upper boundary (Fig. 6.24). The unit is composed of a wedge-shaped sand layer that thins from ~4 cm on one side of the core to < 0.5 cm on the other side. The sediment is observed to be enriched in fossil fragments. The physical properties obtained by the MSCL change within this unit supporting the different lithology compared to surrounding units (Fig. 6.26). Higher Zr and Ti concentrations correlate well with the observation of coarser fractions (Dypvik & Harris, 2001; Rothwell *et al.*, 2006; Kylander *et al.*, 2010). Increased Ca and Si contents are probably caused by the high content of fossil fragments (Rothwell *et al.*, 2006; Heimbürger *et al.*, 2012). Additionally, K also has an increased content within this unit. It is suggested that this unit is a MTD. The non-uniform thickness is thought to be caused by deformation/compaction from the overlying sediments (cf. Forwick, 2001).

6.6.9 Unit 19-3 (269 – 150 cm)

The unit composes lithofacies M, and is located between a gradual lower boundary and a distinct upper boundary (Fig. 6.24). The grain-size data reveals a slightly changing composition going up the unit, where the kurtosis reflects the changes in dynamics of the depositional process (Fig. 6.25). The physical properties follow their main trend for the core (Fig. 6.26), and changes in element ratios can be correlated to the coarser levels of the unit (Fig. 6.27). It is thought that the sediments were deposited within a open marine environment, where the variations in sediment composition are the weak to be classified any further than normal hemipelagic sediments.

6.6.10 Unit 19-2 (150 – 116 cm)

The unit is classified lithofacies SMi, and is bounded by a distinct lower boundary and a gradual upper boundary (Fig. 6.24). The lowermost part of the unit (150 -134 cm) is massive and slightly coarser than the underlying sediments, whereas the interval 134 – 124 cm comprises three thin (~1 mm) laminae of coarser and darker material. Structureless mud occurs between these laminae. The uppermost part of the unit (124 – 116 cm) is similar with the lowermost; massive and slightly coarser. Grain-size data reveal the changing composition going up the unit; a substantially coarser granulometic composition for interval 134 – 124 cm (Fig. 6.25). Furthermore, the platykurtic grain-size distribution indicates highly dynamic deposition processes. Increased wet bulk density and decreased fractional porosity values correlate well with the coarser parts (Fig. 6.26). Based on this the unit is suggested to comprise a MTD.

6.6.11 Unit 19-1 (116 – 0 cm)

The uppermost unit of the core comprises lithofacies M, and is located between a gradual lower boundary and the top of the core (Fig. 6.24). Grain-size composition (Fig. 6.25), physical properties

(Fig. 6.26) and element ratios (Fig. 6.27) are relatively constant throughout the unit, apart from the magnetic susceptibility that increases towards the core top. Intense bioturbation, together with shells, fossil fragments and sulphide spots occur. Unit 19-1 is suggested to have been deposited in an open marine environment, where the conditions were favourable for living organisms.

6.6.12 Summary core HH13-019-PC-MF

Core HH13-019-PC-MF is divided into 11 lithostratigraphical units. Sedimentation took mainly place from suspension settling in an open marine environment reflected by units 19-11, 19-9, 19-7, 19-5, 19-3 and 19-1.

Several mass-transport events interrupted the "normal" sedimentation. This includes turbidity flow deposits comprised in unit 19-9 and 19-8 and a debris flow in 19-6. Additionally were unit 19-4 and 19-2 deposited by mass-transport processes.

7 Correlation and discussion

In this chapter the results of the previous three chapters will be compiled and compared in order to reconstruct the Holocene mass transport activity within the study area.

The morphological features identified on the swath bathymetry and chirp data are correlated and discussed with regard to classification and development of the different MTDs. Further, the lithostratigraphy of each core will be integrated with the seismostratigraphy in order to correlate the cored MTDs and reflections/features in the sub-seafloor. The MTDs of the different cores are then correlated in order to distinguish regional events from local events. Furthermore, sedimentation rates are estimated in order to determine the age of undated mass transport events, and, subsequently, the frequency of mass wasting.

Possible trigger mechanisms will be addressed and comparison to on-shore mass wasting in the area will be discussed. Finally, the results from the study area will be compared to studies from other fjords.

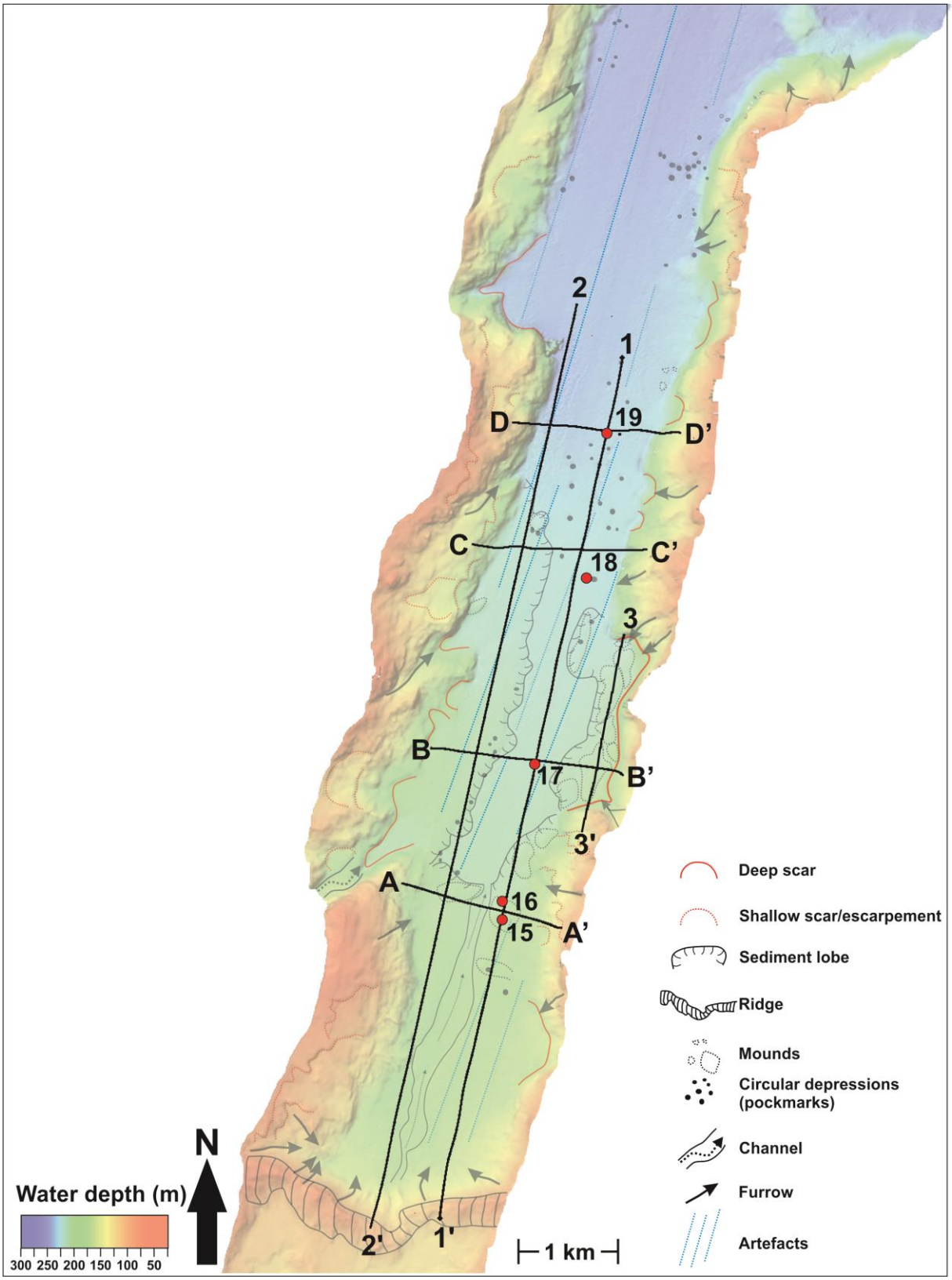

Figure 7.1: *Swath bathymetry map with interpretations, core locations and positions of chirp lines.*

7.1 Correlation of swath bathymetry data and seismic data

Slide scars and mass-transport deposits (e.g. mounds) are the most striking features identified on the swath bathymetry and chirp data.

The bathymetric data reveals that both the western and eastern fjord side have been exposed to frequent slope failures; scars and gullies are described at all depths on the slopes (Fig. 7.1). The scars occur as both single features at one level, as well as with a step-like morphology indicating series of successive slides and slumps (Mulder & Cochonat, 1996; Bøe *et al.*, 2000). This can also be observed on the chirp data, where buried slide scarps indicate successively occurring slides and slumps (Fig.7.2c). Gullies in conjunction with the slide scars (Fig. 7.1) are suggested to have acted as pathways for the failed sediments originating in the slide scars, whereas other gullies could be the result of mass flows such as e.g. turbidity flows (Stoker *et al.*, 2010).

Many of the slope failure features have rounded edges and are associated with smooth seafloor topography, which indicate subsequently erosion or draping of younger sediments, suggesting that they represent old events (cf. Bøe *et al.*, 2000). Most of these features are associated with the shallower seafloor with mounded, lensoid or lobate morphology in the southern part of the basin (extending ~3.5 km north of the threshold, Fig.7.2a), as well as along the western (Fig.7.3a) and eastern fjord sides (Fig.7.4a). Chirp data reveal that the shallower seafloors in these areas are caused by complexes of stacked MTDs (Fig. 7.2b, 7.3b & 7.4b). Most of the MTDs in these complexes have a general lack of internal reflectors, a common characteristic of mass flow-deposits caused by homogenization of the sediments during submarine slope failure (Nardin *et al.*, 1979). However, acoustically stratified composition is also observed for some of these mounds, indicating sediment blocks within the deposits.

Not all the MTDs observed on the chirp data are visible on the bathymetric data. This applies e.g. to deposits from viscous flows including the two mass-flow deposits R3 (*Chapter 5.2.3*) and R2 (*Chapter 5.2.2*).

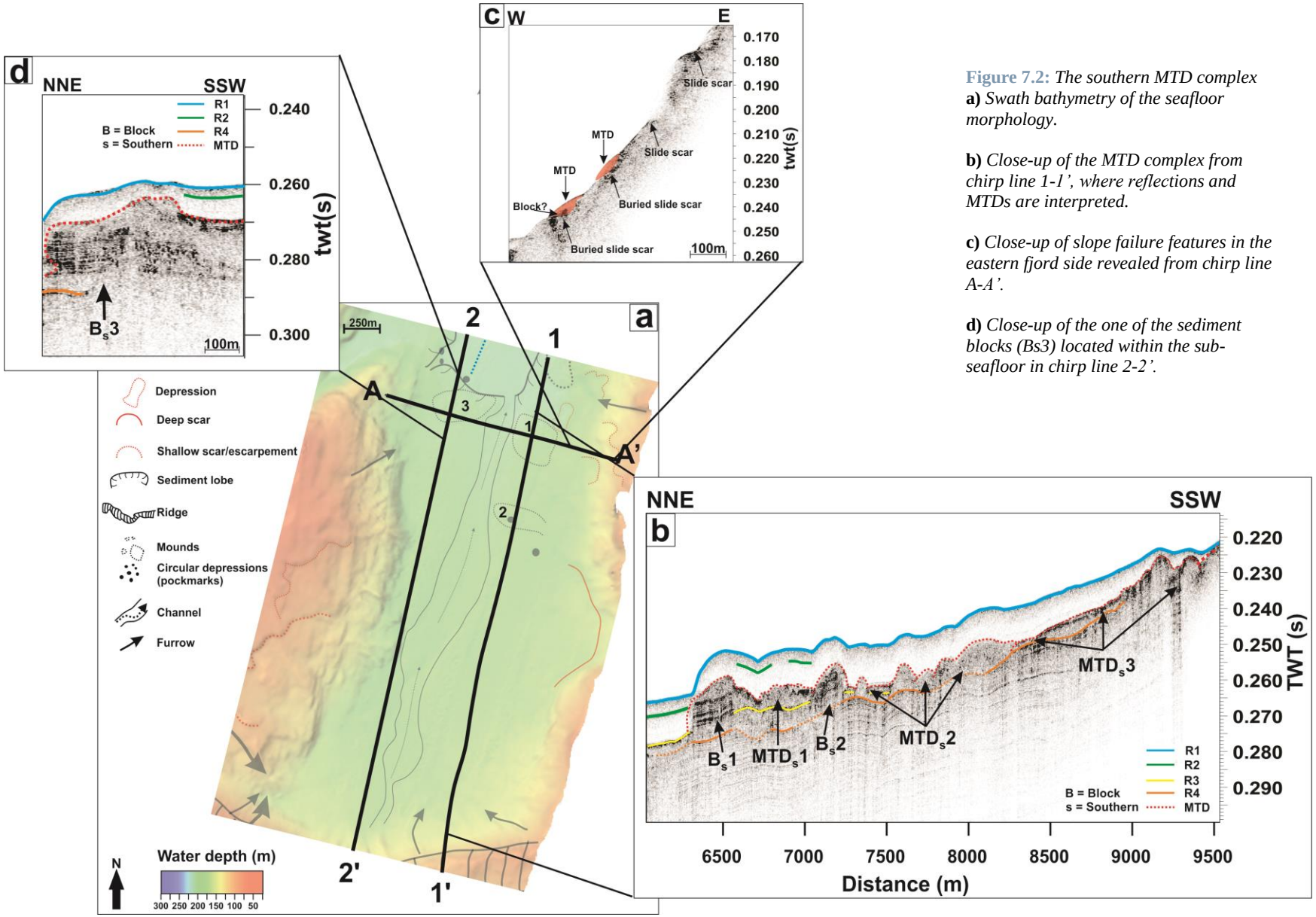

Figure 7.2: *The southern MTD complex*
a) *Swath bathymetry of the seafloor morphology.*

b) *Close-up of the MTD complex from chirp line 1-1', where reflections and MTDs are interpreted.*

c) *Close-up of slope failure features in the eastern fjord side revealed from chirp line A-A'.*

d) *Close-up of the one of the sediment blocks (Bs3) located within the sub-seafloor in chirp line 2-2'.*

The irregular seafloor of the shallow southern part of the basin reflects a larger MTD complex (*the southern MTD complex; see Chapter 5.2.5.1*) covering 1 x 3.5 km^2 of the sub-seafloor at depths between 5 – 15 m. Three of the mounds (1, 2 & 3 in Fig. 7.2a) observed at the seafloor within the northern reaches of the area can be identified on the chirp data. They are composed of hemipelagic sediments draped over underlying sediment blocks (B_s1, B_s2 and B_s3, respectively, in Fig. 7.2b&d). They are all suggested to be rafted blocks embedded in debris flows (cf. Gardner *et al.*, 2000; Vanneste *et al.*, 2012). Since the three blocks occur at the same level within the sub-seafloor they were either deposited during a single event or during a relatively short period of time. The rest of this southern MTD complex is composed of stacked debris flow mounds ($MTD_s1,2$ in Fig.7.2b) (cf. Laberg & Vorren, 1995; Vorren & Laberg, 1997; Bøe *et al.*, 2003; Stoker *et al.*, 2010; Forwick & Vorren, 2011 L'Heureux *et al.*, 2012), except for a sliding complex extending 1.5 km from the threshold (MTD_s3 in Fig.7.2b)

The entire complex directly overlies either the mass flow deposit R3 (*see above*) or the proximal glaciomarine composing unit 2. This indicates that a period of frequent slope failures occurred shortly after the last deglaciation.

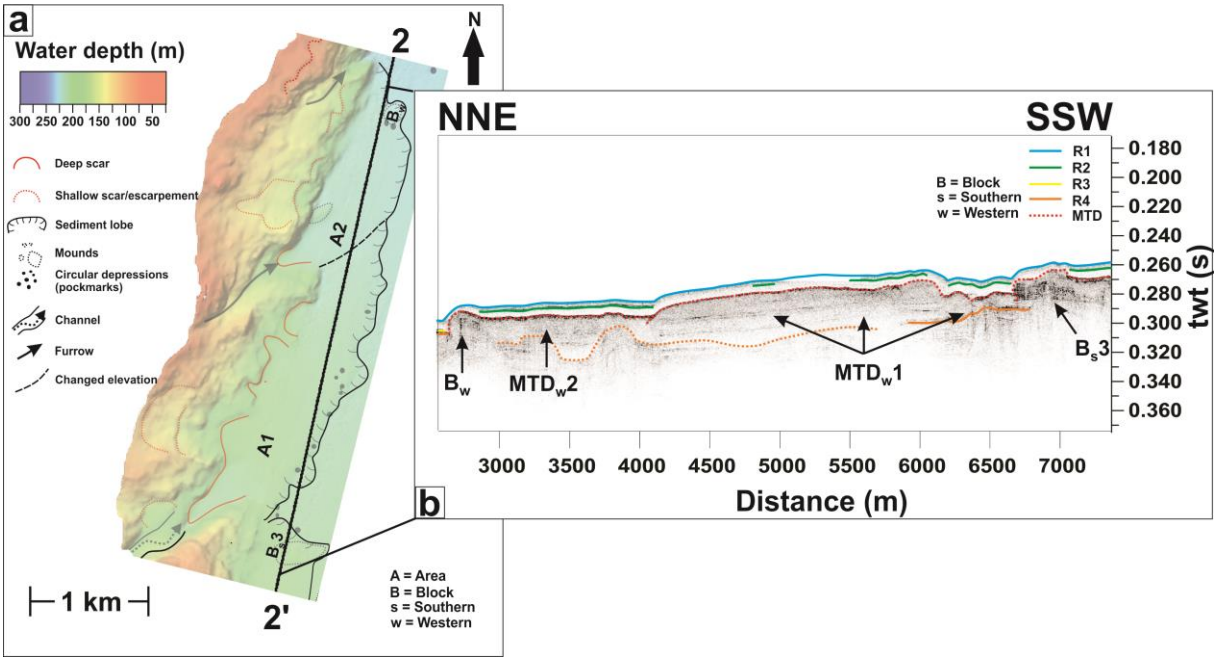

Figure 7.3: *The western MTD complex.* **a)** *Swath bathymetry of the morphology of the seafloor.* **b)** *Close-up from chirp line 2-2' where reflections and MTDs are interpreted.*

The western lobe area (A1, 2 in Fig. 7.3a), covering ~4 x 0.7 km^2 of the seafloor, is located adjacent to the irregular seafloor in the southern part of the basin (Fig. 7.3a). The chirp data reveals that the higher elevation of the seafloor in the southern part of the lobe area (A1 in Fig. 7.3) is caused by a ~7.5 – 25 m thick debris flow mound (MTD_w1 in Fig. 7.3b) located approx. 4 m below the seabed. The debris flow mound erodes parts the southern, adjacent sediment block (B_s3 in Fig. 7.3a&b), indicating that it represents a later event than the one leading to the deposition of the sediment blocks within the

southern area (*see above*). The southern part of the western lobe area (A1 in Fig. 7.3a), as well as MTD_w1, is thickest and has the greatest eastern extent below a part of the seafloor where a channel-like feature terminates from the fjord side (Fig. 7.3a&b). It is assumed that the debris-flow mound (MTD_w1) derived from the channel, which was fed both by mass flowing and sliding processes along its slopes. Additionally, failure leading to the formation of an amphitheatre shaped scar right north of the channel might have contributed to the accumulation of the deposit (*see Chapter 4.5*).

Further north, the lobe area gets abruptly thinner (A2 in Fig. 7.3a). This coincides with the occurrence of an indentation in the fjord side. The chirp data reveals that a second debris flow mound is located within the sub-seafloor in this area (MTD_w2 in Fig 7.3b). This mound is most probably related to the same slope failure which resulted in the adjacent indentation and, since the mound onlaps debris-flow mound MTD_w1, it must be younger. Two mounds are observed at the seafloor within this northern part of the lobe area. Chirp data reveal that at least one of these blocks is a sediment block (B_w in Fig. 7.3a&b) embedded in the MTD_w2 (cf. Gardner *et al.*, 2000; Vanneste *et al.*, 2012).

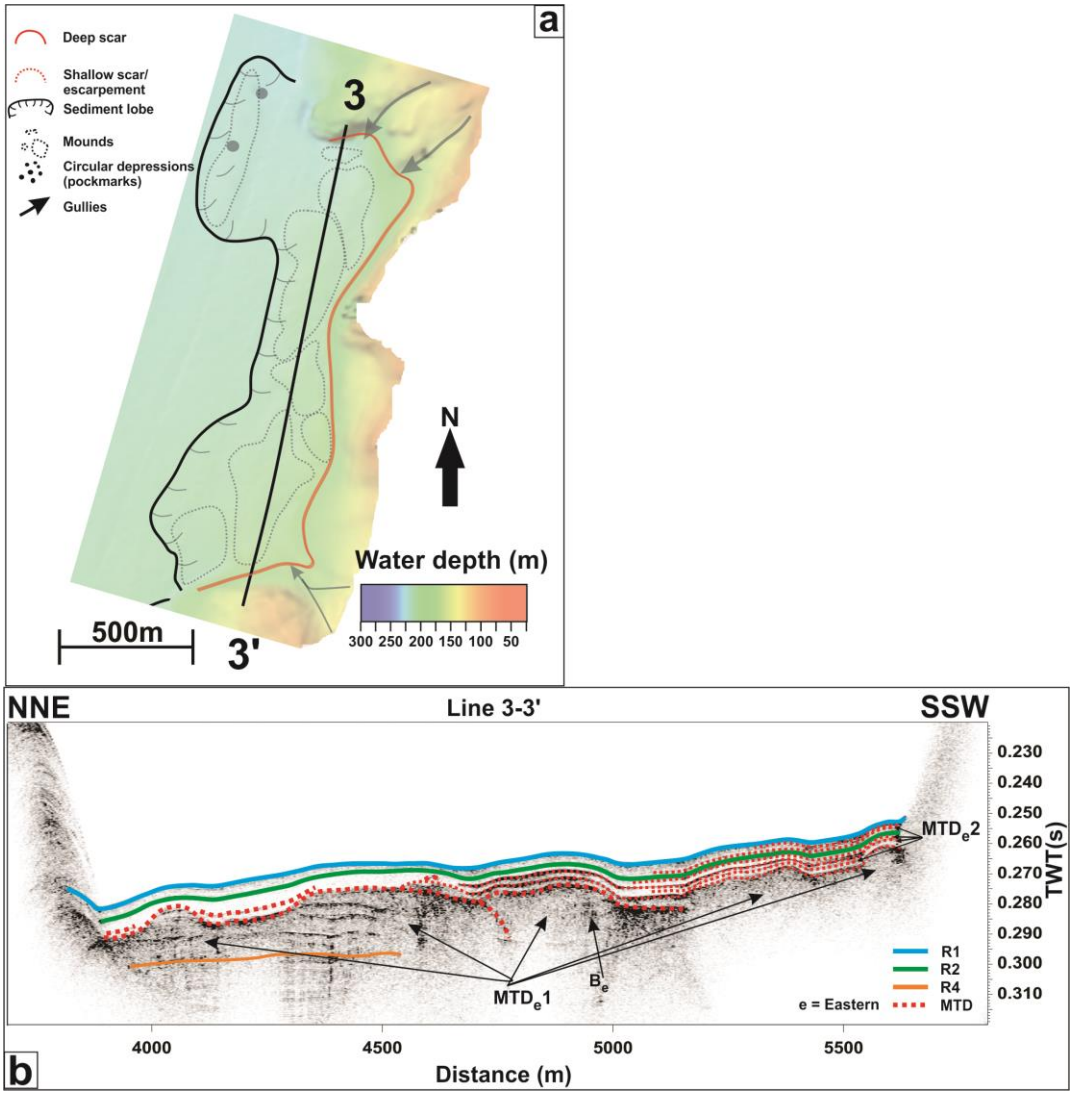

Figure 7.4: *The eastern MTD complex* **a)** *Swath bathymetry of the seafloor morphology.* **b)** *Chirp line 3-3' with interpreted reflections and MTDs*

Stacked debris-flow mounds dominate the chirp stratigraphy at depths between ~4.5 – 19 m below the undulating seafloor of the eastern lobe area, ~4 – 6 km north of the sill (Fig. 7.4). This area is located within a larger indentation in the fjord side, from where, a sequence of slope failures have occurred and resulted in the stacked debris flow mounds (MTD_e1 in Fig. 7.4b). Further, since the mounds directly overlies the proximal glaciomarine unit 2 (*see Chapter 5.2.4*) it can be suggested that their deposition occurred shortly after the last deglaciation.

In the southern part of the indentation several high-and low amplitude reflections overly the mounds (MTD_e2 in Fig. 7.4b), where the uppermost is deposited only ~0.7 m below the seafloor. This set of reflections, which also includes the regional reflection R2 (*see Chapter 5.2.2*), onlaps the eastern fjord side (*see Chapter 5.2.5.3* & Fig. 5.6). The bathymetric data reveals erosional gullies on the adjacent slope terminating this part of the seafloor (Fig. 7.4a). Therefore there is suggested that these reflections are caused by mass-flow deposits sourced from the gullies e.g. by turbidity flows (e.g. Stoker *et al.*, 2010). However, in contrast to the mass flow which resulted in reflection R2, the others had a limited run-out distance. The limited depth of the deposits in the chirp stratigraphy together with a sharp-edged character of the gullies indicates relatively young mass transport events (cf. Bøe *et al.*, 2003).

7.2 Correlation of cores and seismic data

The core data suggests that a variety of mass-transport processes occurred in the study area. The chirp profiles of all the coring sites show predominantly undisturbed, acoustically transparent hemipelagic sediments. However, reflections occur occasionally (Fig. 7.5, 6, 7, 8 & 9). All the coring sites are located along or close to chirp line 1-1' (Figs. 7.1, 7.5). In order to project the cores onto the chirp profiles a P-wave velocity of 1490 m/s, based on the average velocities obtained with the MSCL (*see Chapter 3.2.1, Multi-sensor core logger*), was used.

Core shortening is a common phenomenon observed during marine coring, causing the measured core length to be shorter than the actually cored sediment interval. Core shortening can result from several different processes, i.e. physical compaction, sediment thinning and sediment bypassing (Morten & White, 1997). There is often a combination between several processes causing the observed shortening. However, most common is thinning of the sediment column as the core barrel is pushed into the seafloor. Physical compaction of the sediments involves expulsion of air and water from the pore spaces of the sediments, and possible closer packing of the sediment grains caused by rearrangements (Morten & White, 1997).

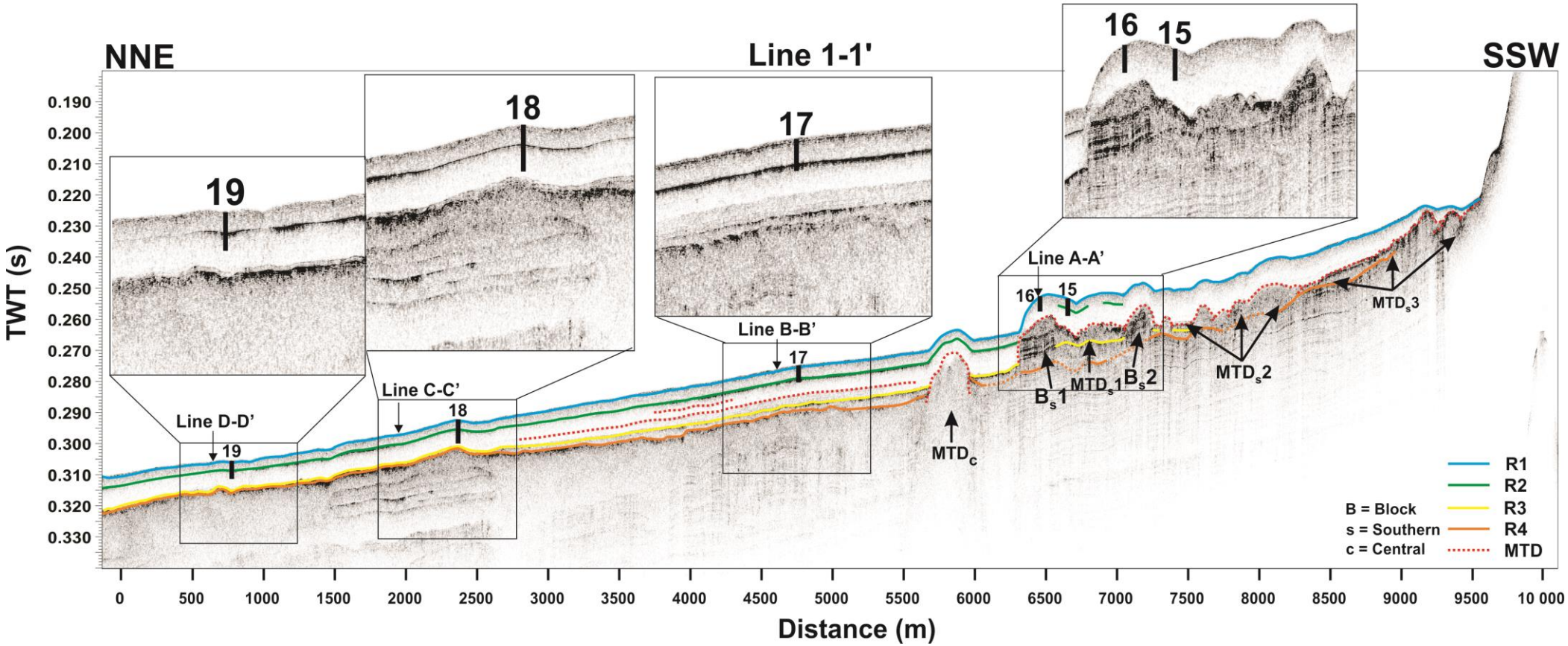

Figure 7.5: *Chirp line 1-1' with approx. core locations, and the approx. cored intervals of the sub-seafloor. Core HH13-018-PC-MF (18 in the figure) was projected onto the profile, see Fig. 7.1 for location*

7.2.1 Core HH13-015-GC-MF

The coring site is located above the southern MTD complex, near sediment block B_s1 (*see Chapter 7.1*). The MTDs are located > 5 m below the seafloor and the core has a total length of only 3.92 m. Hence, it did not penetrate into these deposits. Chirp lines 1-1' (Fig. 7.5) and A-A' (Fig. 7.6), cross the coring site, reveal that the core penetrates mostly through a relatively acoustically transparent package of hemipelagic sediments. The character of the cored sediments is generally massive and structureless, which corresponds well with the chirp stratigraphy. However, at depth of ~2.4 m below the sub-seafloor, the discontinuous and weak southern reaches of reflection R2 are recognised on the chirp data. This coincides well with the occurrence of a MTD in unit 15-8 (2.25 - 2.31 m; *see Chapter 6.2.2*). The cored sediment additionally holds three shallower MTDs which occur in unit 15-6 (*see Chapter 6.2.4*), unit 15-4 (*see Chapter 6.2.6*) and unit 15-2b (*see Chapter 6.2.8*) in the core which are not visible on the chirp data. This can be related to one or several of the following factors: 1) the changes in physical properties of the reworked sediments are too small to cause a reflection on the chirp data; 2) the core was retrieved away from the chirp profile; 3) the event archived in the core reflects a relatively small and local event that did not extent to the chirp profile. Such minor events might be small sub-marine slope failures or sediment supply e.g. related to snow avalanches.

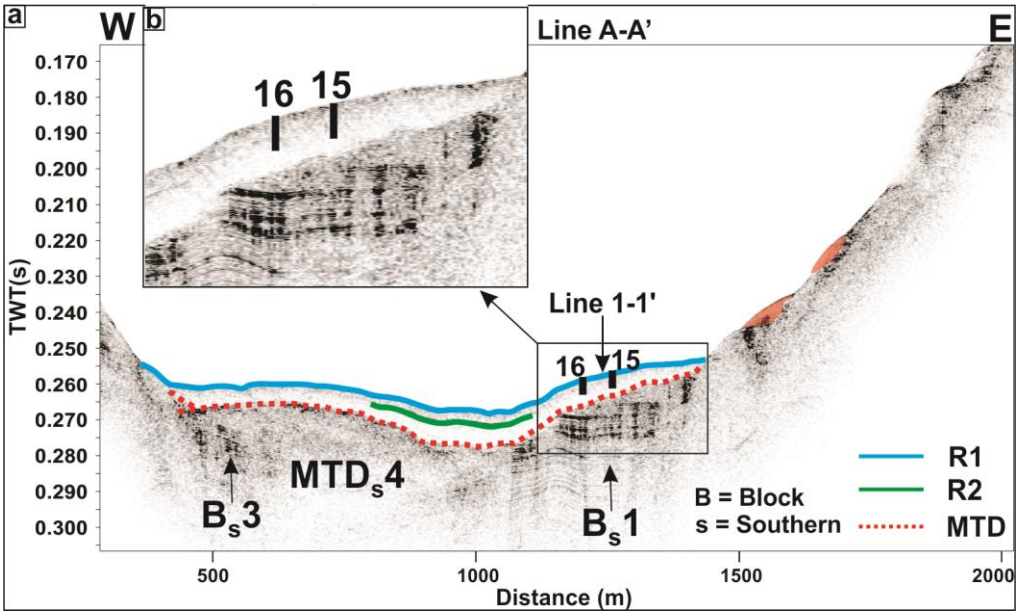

Figure 7.6: **a)** *Approx. location of core HH13-015-GC-MF and HH13-016-GC-MF on chirp line A-A', and their approx. penetration depth. Reflections and MTDs are interpreted.* **b)** *Close-up of the coring sites.*

7.2.2 Core HH13-016-GC-MF

The core was retrieved ~220 m north of core HH13-015-GC-MF, right above the sediment block B_s1 within the southern MTD complex (*see Chapter 7.1*). However, since B_s1 is located at depths greater than 5 m within the sub-seafloor, the 3.74 m long core did not penetrate into these sediments. The

cored interval is on both chirp lines 1-1' (Fig.7.5) and A-A' (Fig. 7.6) acoustically transparent. No internal reflections are possible to observe, neither the regional reflection R2 is recognized. However, as for core HH13-015-GC-MF, the cored sediments contain MTDs not mirrored within the chirp data; a non-classified MTD in unit 16-4 (*see Chapter 6.3.2*) and a turbidite in unit 16-2 (*Chapter 6.3.4*). Possible reasons for the MTDs not to be indicated in the chirp data is proposed in chapter 7.2.1, above.

7.2.3 Core HH13-017-GC-MF

Chirp lines 1-1' (Fig.7.5) and B-B' (Fig.7.7) show the approx. interval of the sub-seafloor covered by core HH13-017-GC-MF. The seismostratigraphy at site HH13-017-GC-MF is mostly acoustically transparent. However, three high-to low-amplitude reflections occur. The lowermost of these reflections occurs > 8 m below the seabed and belongs to the regional reflection R3, which is thought to represent a viscous flow deposit e.g. from a turbidity flow (Syvitski *et al.*, 1987; *see Chapter 5.2.3*). The low-amplitude reflection located at depth ~7 m is identified as the upper reflection of the distal part of a debris flow mound (MTD_w1 in Fig.7.7; *see Chapter 7.1*) in the western sediment lobe area. Since the total length of the core is 4.13 m, none of these deposits are captured within the core. The regional, high-amplitude reflection R2 is located ~2.8 m below the seafloor. It was interpreted to represent a viscous flow e.g. from a turbidity flow (Syvitski *et al.*, 1987; *see Chapter 5.2.2*). This reflection is correlated to the turbidite in unit 17-4 (2.3 – 2.44 m, *see Chapter 6.4.4*), suggesting that the cored sediments experienced a shortening of ~15%. The turbidite was deposited by a high density turbidity flow which occurred between 2930 – 3026 cal. years BP.

The mass flow deposit reflected in R2 was sourced by gullies on the eastern fjord side and having their origin < 100 m below present sea level (*see Chapter 7.1*). This supports the assumption of an onshore development of the cored turbidite (comprises terrigenous material, *see Chapter 6.4.4*). Two additional MTDs are observed within the core. However, these correlate to depths within the stratigraphy were internal reflections are absent. The lowermost MTD is located at core depths between 3.01 – 3.06 m (unit 17-6, *see Chapter 6.4.3*). Assuming a 15% core shortening, it should correlate to the depths ~3.52 - 3.46 m in the undisturbed stratigraphy. A low-amplitude reflection occurs at this depth in the eastern reaches of chirp line B-B' (MTD_e2 in Fig.7.7). It is possible that this viscous mass flow (*see Chapter 7.1*) actually reached further out in the basin than indicated by the chirp data, and that the distal parts of this flow are recovered in the core.

The last MTD identified in core HH13-017-GC-MF is located between 0.19 – 0.24 m (unit 17-2, *see Chapter 6.4.6*) (corresponds to chirp depth ~0.28 m if 15% compaction is assumed). It is inferred to be deposited from a low-density turbidity flow. However, none of the reflections onlapping onto the eastern fjord side (see chirp line B-B'; MTD_e2 in Fig.7.7) occur at such shallow depths (minimum depth is ~0.7 m). Possible reasons for the MTD not to be indicated in the chirp data is proposed in chapter 7.2.1, above.

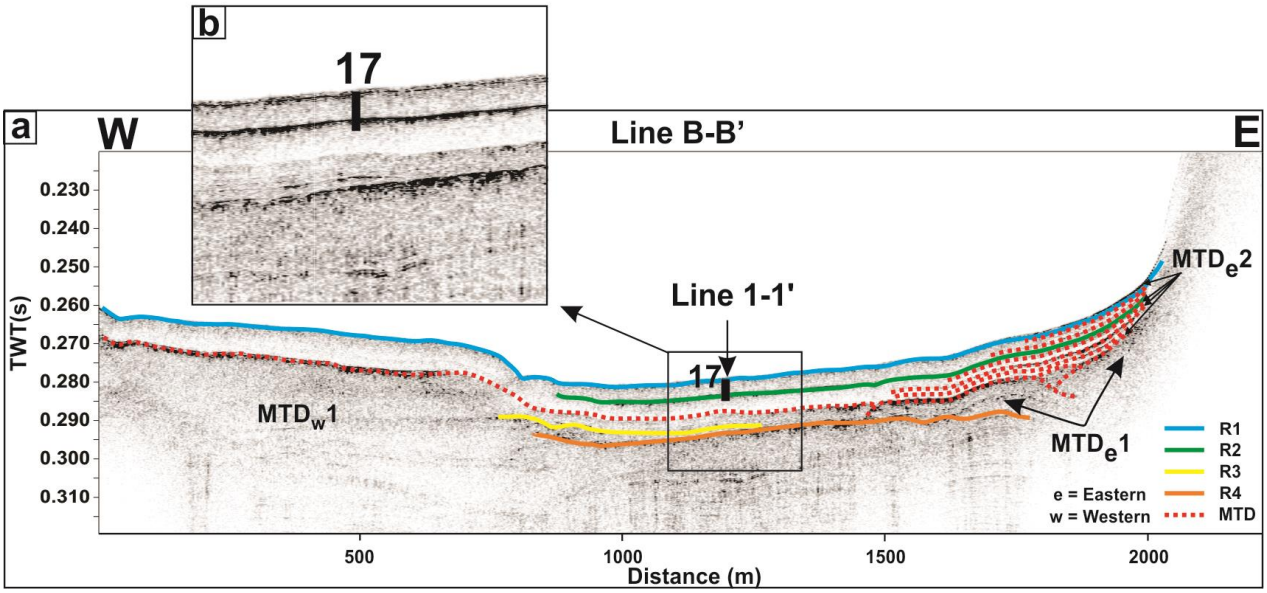

Figure 7.7: a) *The approx. location of core HH13-017-GC-MF on chirp line B-B', and its approx. penetration depth. Reflections and MTDs are interpreted.* **b)** *Close-up of the coring sites.*

7.2.4 Core HH13-018-PC-MF

Core HH13-018-PC-MF is located ~100 m east of chirp line 1-1' (Fig. 7.5) and ~260 m south of chirp profile C-C' (Fig. 7.8), so that only the approx. location of the core is available. The bathymetric data reveals that the core was retrieved within a relatively flat and smooth part of the basin, a little to the east of the fjord central axis. The chirp data indicates that the core contains post-glacial sediment; the upper reflection (R4) of the proximal glaciomarine unit 2 (*see Chapter 5.2.4*) is located at depth ~7.5 m in the stratigraphy at this location and the total core length is 5.74 m. However, the lowermost ~1.35 m of the cored sediment was interpreted to be of proximal glaciomarine origin (*see Chapter 6.5*). This large offset between the chirp data and the core may partly be related to differences within the sub-seafloor between the actual coring site and the projected location, which might also have been amplified by core shortening and incorrect P-wave velocity used for the twt(s) to m conversion (major gaps in the P-wave measurements for the core *see Chapter 6.5 & Fig. 6.22*).

Some reworked sediments have been identified within the proximal glaciomarine deposits (at depths between 5.31 – 5.46 m, unit 18-12, *see Chapter 6.5.1*). The core data reveal, furthermore, that a sequence of MTDs was deposited immediately about the proximal glaciomarine sediments. Four thin MTDs occur in unit 18-10c (4.47 – 4.39 m, *see Chapter 6.5.3*), additional turbidites are located in unit 18-10b (4.39 – 4.26 m) and unit 18-10c (4.26 – 3.97 m). Based on the sequence position relative to the proximal glaciomarine sediments it can be correlated to the regional reflection R3, thought to mirror a

viscous flow (e.g. turbidity flows) shortly after the last deglaciation (*see Chapter 5.2.3*). This implies that R3 most probably results from a sequence of MTDs, rather than from a single deposit. Both chirp lines 1-1' and B-B' suggest that the lithological changes causing reflection R2, should be identified in the core. However, even though the correlation between litho- and seismostratigraphy has been challenging for the lower parts of the core, it is suggested that a MTD at depth 2.36 – 2.42 m (unit 18-4; *see Chapter 6.5.9*) correlates to R2. This is based on the similar depths of occurrence in core HH13-018-PC-MF, as well as in the cores HH13-017-GC-MF and HH13-019-PC-MF. Furthermore, radiocarbon dates and estimated ages obtained close to the remaining three MTDs (18-8, 18-6 and 18-2, *see Chapter 6.5*) provide ages significantly different than the age for the deposit obtained in core HH13-017-GC-MF (*see Chapter 7.3, below*). No indications of these other cored MTDs occur on the chirp data, possible reasons for this are provided in chapter 7.2.1.

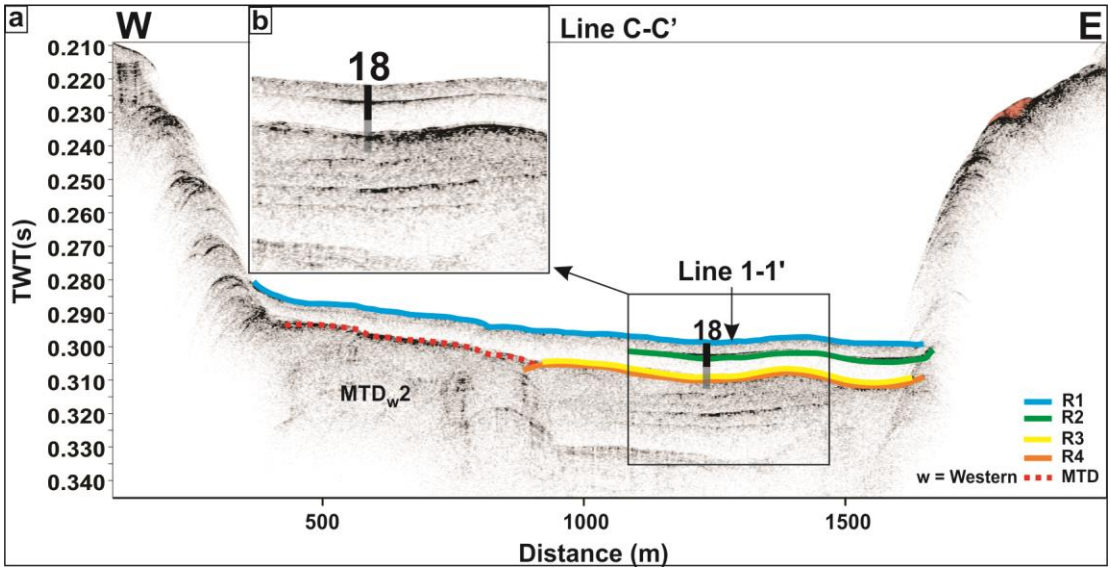

Figure 7.8: **a)** *Approx. location of core HH13-018-PC-MF on chirp line C-C'. The calculated penetration depth is indicated with black, while the estimated depth after correlation is shaded.* **b)** *Close-up of the coring site.*

7.2.5 Core HH13-019-PC-MF

The approx. coring site of core HH13-019-PC-MF is visualised on chirp lines 1-1' (Fig. 7.5) and D-D' (Fig. 7.9), The chirp stratigraphy within the cored interval reveals acoustically transparent hemipelagic sediments where internal reflections are typically absent, except for the regional reflection R2 at ~3 m depth. Five MTDs are identified in the core (unit 19-10, 19-8, 19-6, 19-4 and 19-2, *see Chapter 6.6*). Based on the depth of occurrence is the MTD located in unit 19-4 (2.69 – 2.74 m, *see Chapter 6.6.8*) correlated to reflection R2. No further classification of the MTD exists. None of the other cored MTDs are possible to correlate to the chirp data, possible reasons for this are provided in chapter 7.2.1.

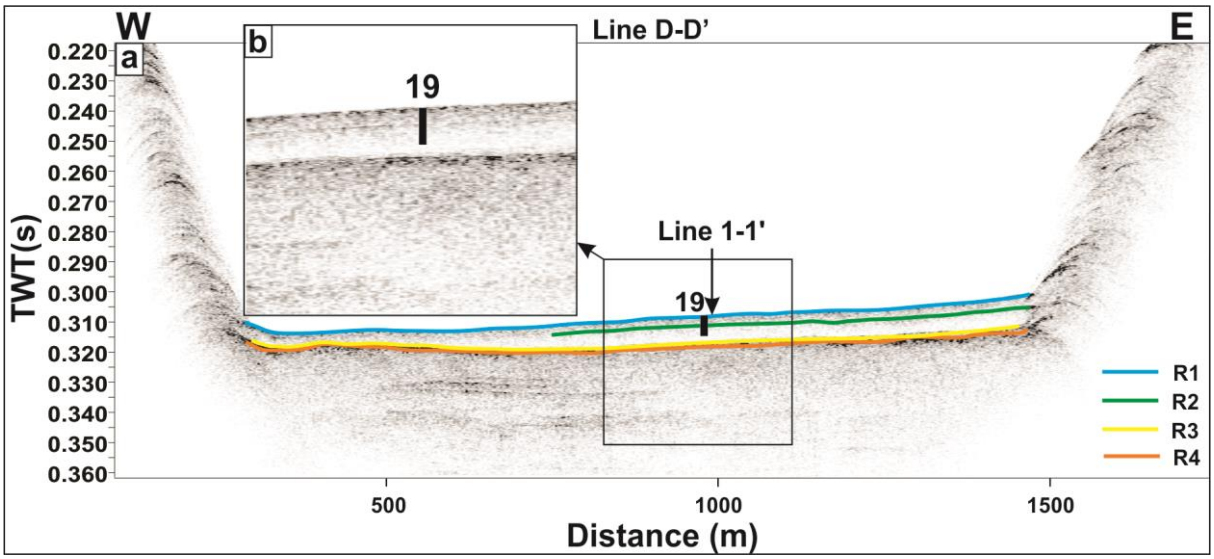

Figure 7.9: **a)** *The approx. location of core HH13-019-PC-MF on chirp line D-D', and its approx. penetration depth. Reflections are interpreted.* **b)** *Close-up of the coring sites.*

7.3 Correlation of the mass transport deposits from the different cores

Depths of occurrence, magnetic susceptibility and chemical composition of the MTDs are used for correlation of the MTDs from the different cores. Correlations performed in Chapter 7.2 will also be included here. The correlated core intervals are presented in Figure 7.10.

The viscous flow mirrored in the regional reflection R2 (Fig. 7.5,6,7,8 & 9) is possible to trace for all the coring sites, except for the cored interval of HH13-016-GC-MF. Correlation between the reflection and core HH13-017-GC-MF indicate that R2 represents the turbidite located in unit 17-4 which occurred between 2930 – 3026 cal. years BP (*see Chapter 7.2.3*). This turbidite is characterised by a high content of fossil and terrigenous fragments (tree and moss), increased magnetic susceptibility and an increased content of Sr, Si and Ti (*see Chapter 6.4.4*). The non-classified MTD located in unit 15-8 in core HH13-015-GC-MF was also correlated to R2 (*see Chapter 7.2.1)*, a correlation which is further verified if comparing the properties of the MTD with the turbidite (Fig.7.10). In addition to occurring within the approx. same core depth, this MTD also contains terrigenous material (moss) and a high content of fossil fragments. Furthermore, Sr and Si are relatively high (*see Chapter 6.2.2*). The MTD in unit 18-4, in core HH13-018-PC-MF, was also correlated to reflection R2 (*see Chapter 7.2.4*), and furthermore, the turbidite in core HH13-017-GC-MF (Fig. 7.10). The MTD is normally graded, has an increased content of Sr, Si and Ti and comprise a greater amount of fossil fragments (*see Chapter 6.5.9*). In core HH13-019-PC-MF the MTD in unit 19-4 is correlated to the mass-flow reflection (R2) (*see Chapter 7.2.5*) (Fig.7.10). Also this MTD is found to comprise a high content of fossil fragments and an increased Si and Ti content (*see Chapter 6.6.7*). Unit 19-4 occurs at a greater depth than the

deposits it has been correlated with. However, this might be explained by less compaction of the sediments in this core (*see Chapter 7.2*).

Slight sediment coarsening and increased Fe, K and Ti contents characterise unit 16-4 (3.53 – 3.7 m, *see Chapter 6.3.2*) and parts of unit 15-9 (3.64 – 3.84 m, *see Chapter 6.2.1*). Since these two core intervals have similar sediment properties and occur at similar depths, they are correlated with each other (Fig. 7.10).The distance between the two cores coring sites is relatively small, and it is likely to believe that even small, local mass-wasting events can have a run-out distance which covers both the areas. However, the other MTDs identified within these two cores are not possible to correlate, indicating greatly limited run-out distances (except for unit 15-8, *see above*)

The MTD sequence in unit 18-10 (*see Chapter 6.5.3*) has been correlated to the regional reflection R3 (*see Chapter 7.2.4*). From comparing core HH13-018-PC-MF with core HH13-019-PC-MF it is possible to correlate the turbidite in unit 19-10 (*see Chapter 6.6.2*) with the MTD sequence in 18-10 (7.10). This correlation is based on their similar chemical composition, e.g. both have increased Sr and Ti contents. Additionally, iron and magnetic susceptibility possess the same pattern within the two cores. Further, material from 429 cm depth (~25 cm above the turbidite) in core HH13-019-PC-MF provided an age of 10,321 cal. years BP, indicating that the turbidite was deposited shortly after the last deglaciation (Corner, 1980). This further verifies the correlation between the two cores (*see Chapter* 7.2.4).
However, correlation of HH13-019-PC-MF and the chirp data indicates that the penetration depth of the core was too shallow to reach R2. Ergo, the correlation between unit 19-10 and R3 means that there is a greater offset between the core and chirp stratigraphy depths (compare with *Chapter 7.2.4*).

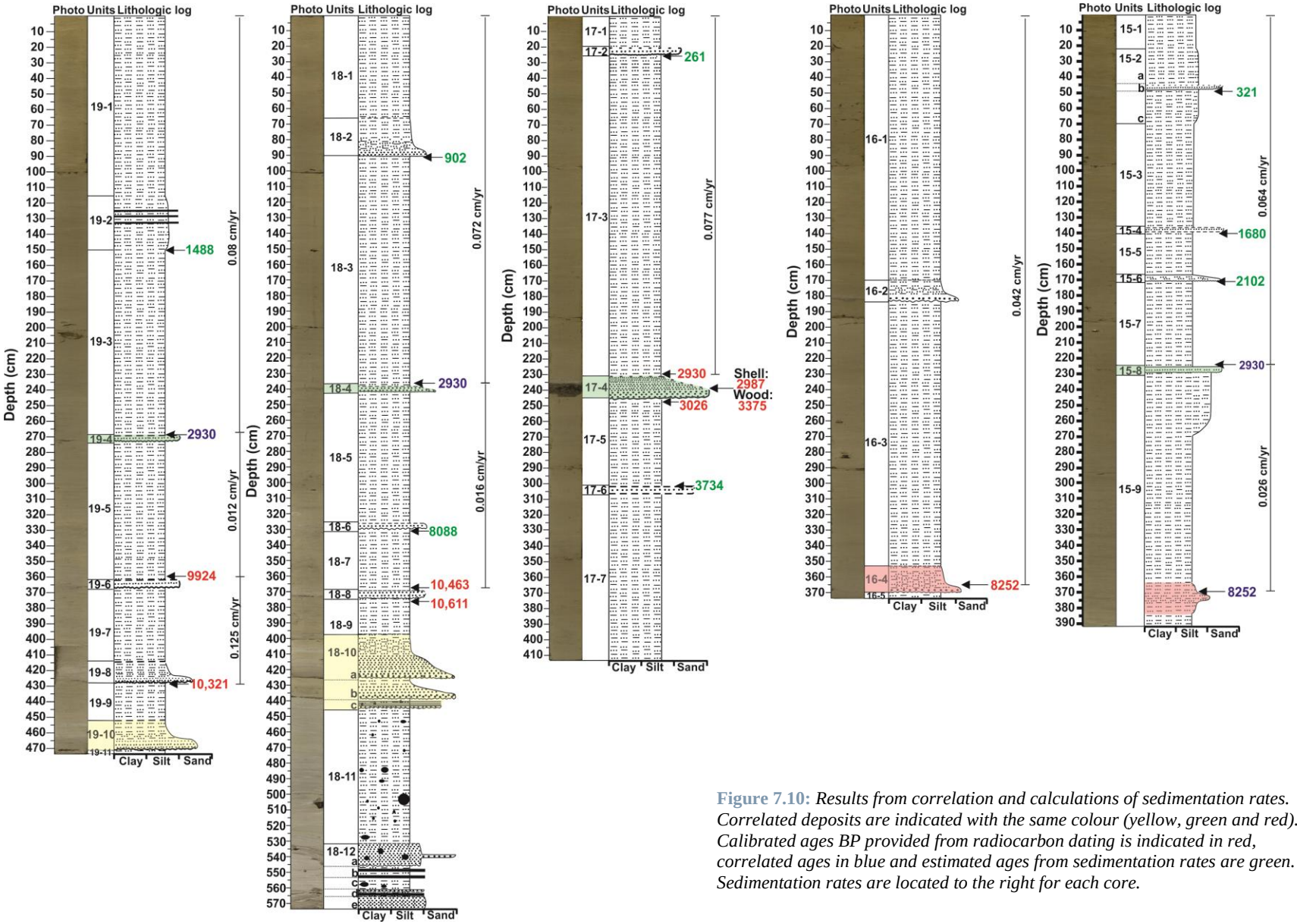

Figure 7.10: *Results from correlation and calculations of sedimentation rates. Correlated deposits are indicated with the same colour (yellow, green and red). Calibrated ages BP provided from radiocarbon dating is indicated in red, correlated ages in blue and estimated ages from sedimentation rates are green. Sedimentation rates are located to the right for each core.*

7.4 Sedimentation rates and estimated ages of the mass transport deposits

For the estimation of linear sedimentation rates, a constant accumulation rate of the sediments was assumed. Sedimentation rates are calculated based on radiocarbon dates (Table 6.1 *Chapter 6.1.5*), as well as litho- and seismostratigraphy. The calculated sedimentation rates are exclusively calculated from deposits that were assumed to be from suspension fallout, i.e. thicknesses for all identified mass transport deposits were excluded. It should be noted that the calculations did not take into account eventual erosion, uncertainties in radiocarbon dating and core shortening (*see Chapter 7.2*). Furthermore, the boundaries between MTDs and hemipelagic deposits were difficult to identify in some cases. Based on these uncertainties, all rates should be regarded minimum rates and the estimated ages should be treated with caution. Hemipelagic sediments (Unit 1, *see Chapter 5.2.1*) have a relatively uniform thickness throughout the study area (average ~8.75 m), except for those areas where MTD complexes occur within the sub-seafloor (varies between ~1 – 9 m). The reason for this is that the pits located between the MTD mounds act like sediment traps, and thus, have higher accumulation rates (e.g. Fig. 7.5).

Core	Depth interval (cm)	Units	Age interval (cal. years BP)	Sedimentation rate (cm/year)
HH13-015-GC-MF	370-225	15-9	8252-2930	0.026
	225-0	15-7,5,3,2c,1	2930-0	0.064
HH13-016-GC-MF	365-0	16-4, 3,1	8252-0	0.042
HH13-017-GC-MF	230.5 - 0	17-3, 1	2930-0	0.077
HH13-018-PC-MF	369-236	18-7,5	10 463-2930	0.016
	236-0	18-3,1	2930-0	0.072
HH13-019-PC-MF	429-359.5	19-7	10 321-9924	0.125
	359.5-269	19-5	9924-2930	0.012
	269-0	19-3,1	2930-0	0.08

Table 7.1: *Calculated sedimentation rates.*

No material was sampled for dating within core HH13-015-GC-MF. Therefore, sedimentation rates have been calculated based on ages provided by the correlation of two MTDs (*see Chapter 7.3*). Core depth 370 cm (unit 15-9) is interpreted to be of age 8252 cal. years BP, while depth 225 cm (right above unit 15-8) is of age 2930 cal. years BP. Based on this, minimum sedimentation rates were 0.026 cm/year for the time interval 8252 – 2930 cal. years BP (370-225 cm) and 0.064 cm/years during the past 2930 years (Fig.7.11). Based on this, the ages of the MTDs comprising units 15-6, 15-4, 15-2b were calculated to be <2102 cal. years BP, <1680 cal. years BP and <321 cal. years BP, respectively.

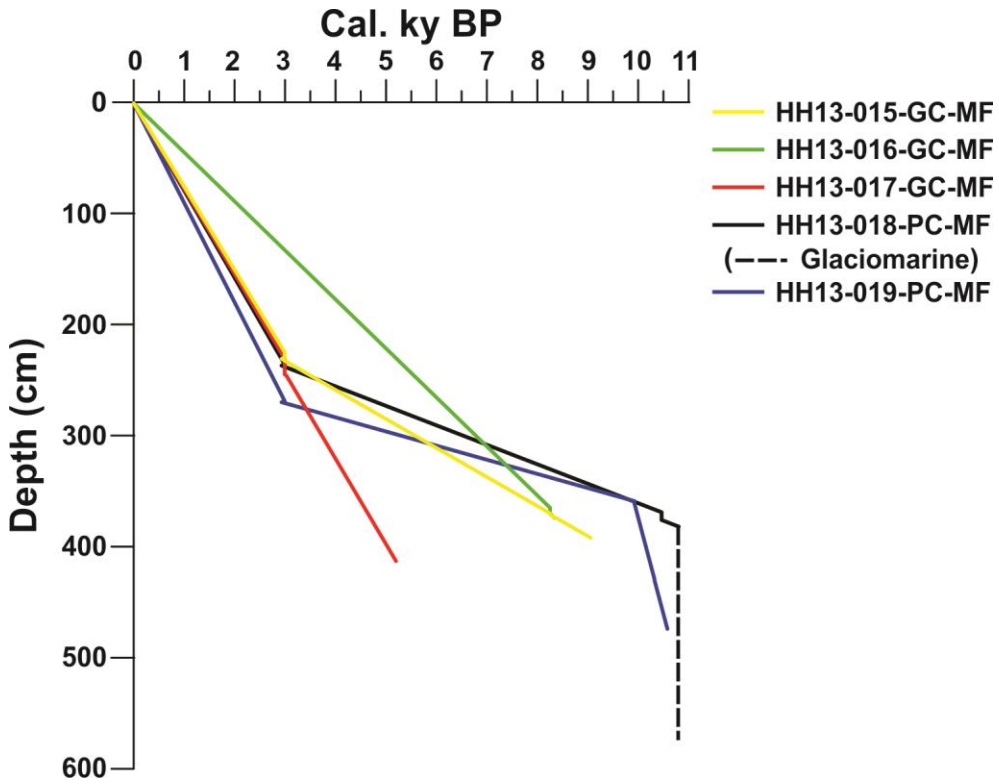

Figure 11: *Sedimentation rates. Since no calculations were performed for the glaciomarine sediments, these are just indicated with a straight, dashed line.*

The age of 8252 cal. years BP from depth 365 cm in core HH13-016-GC-MF reveals that the linear sedimentation rate at this site was 0.042 cm/year (Fig. 7.11). However, the other cores reveals that the sedimentation rate changed around 3000 cal. years BP. Based on this the sedimentation rate of 0.042 cm/year is found unreliable and will therefore not be further addressed.

The date of 2930 cal. years BP from 230.5 cm in core HH13-017-GC-MF suggests a linear sedimentation rate of 0.077 cm/year until the present (Fig. 7.11). The turbidite comprising unit 17-2 was deposited prior to 261 cal. years BP (Fig. 7.10). Assuming the same sedimentation rate beneath unit 17-4, the turbidite composing unit 17-6 was deposited prior to 3734 cal. years BP. (based on the age of 3026 cal. years BP at 246.5 cm).

Two radiocarbon dates suggest that the turbidite composing unit 18-8 was deposited between 10,611 and 10,436 cal. years BP (Fig. 7.10). Based on correlation with other cores (in particular HH13-017-GC-MF) and the seismostratigraphy, the regional turbidite composing unit 18-4 (*see Chapter 7.3*) has a minimum age of 2930 cal. years BP (Fig. 7.10). Two sedimentation rates are calculated based on the two youngest dates. The time interval 10,436 – 2930 cal. years BP (269 – 236 cm) is estimated to have a sedimentation rate of 0.016 cm/year, while the last 2930 cal. years BP (236 – 0 cm) have an rate of 0.072 cm/year (Fig.7.11). Based on the latter rate, the uppermost MTD (unit 18-2) was deposited after

902 cal. years BP, whereas, based on sedimentation rate 0.016 cm/year, the MTD composing unit 18-6 was deposited after 8088 cal. years BP (Fig. 7.10).
Assuming a linear sedimentation rate of 0.016 cm/year during the deposition of unit 18-9, the MTDs comprising unit 18-10 would have been deposited before ~11 900 cal. BP. However, this age is probably too old as it represents a period prior to the deglaciation of the area (Sveian & Corner, 2004). This can be explained based on an assumed higher sedimentation rate shortly after the deglaciation (*see further down*)

Two ages in core HH13-019-PC-MF were obtained from radiocarbon dates, whereas one was inferred from lithological and seismistratigraphic correlation; material from 429 cm is dated to 10,321 cal. year BP, while material from 359.5 cm is dated to 9924 cal. year BP. The MTD composing unit 19-4 is correlated with unit 17-4, thus, suggesting that the MTD was deposited prior to 2930 cal. year BP. Three sedimentation rates are calculated: The rate within the time interval located 10,321-9924 cal. years BP (429 – 359.5 cm) is calculated to be 0.125 cm/year, while the rate within the period 9924 – 2390 cal. years BP (359.5 – 269 cm) is 0.012 cm/year (Fig. 7.11). The sedimentation rate the last 2930 cal. years BP (269 – 0 cm) is calculated to be 0.08 cm/year (Fig. 7.11). Based on this rate, the deposition of unit 19-2 occurred after 1488 cal. years BP (Fig. 7.10).

The results from this study reveal varying sedimentation rates. The highest sedimentation rate of 0.125 cm/year was calculated for the time interval 10,321 – 9924 cal. years BP interval in core HH13-019-PC-MF. At this time, the glaciers draining through the fjord during the last glacial had withdrawn from this part of the basin, and the study area did possess the characteristics of an open marine environment - even though the fjord system still was influenced by glaciers (based on Corner, 1980). High sedimentation rates shortly after deglaciation are common (e.g. Hald, 2009; Forwick & Vorren, 2009). The increased sediment transport was most probably caused by high meltwater discharge, together with rapid isostatic uplift, resulting in high rates of river erosion. Further, the uplift exposed marine, glaciomarine and glaciofluvial ice-front deposits for erosion (e.g. Bøe *et al.*, 2003).

The calculated sedimentation rates are generally low for all the cores. In non-glaciated fjords is the sediment input mainly controlled by river discharge (Howe *et al.*, 2010). The southern (i.e. innermost) parts of the fjord are most probably stronger influenced by the larger sediment sources, the Signaldalen river located at the fjord head and the Skibotn river terminating into basin 3 (*see Chapter 2.7.2.2*). The sedimentation rates within the study area reflect decreasing sedimentation rates with increasing distance to major sediment sources, as well as the influence of sills reducing/preventing sediment transport from one basin to another (e.g. Syvitski et al., 1987). However, comparing the sedimentation rates for the last 2930 cal. years BP between core HH13-015-GC-MF (0.064 cm/year) and core HH13-019-PC-MF (0.08 cm/year), the sedimentation rate is higher in the northern, outermost

part than in the southern, innermost part of the study area. The fjord basin has an increasing depth in the northern direction, i.e. the sediment accumulations have been greatest in the deeper parts of the basin and lower in the shallower areas. The same has been indicated in Isfjorden (Forwick & Vorren, 2005; Forwick *et al.,* 2010).

The sedimentation rates appear to be increased for the upper parts of the cores, i.e. after ~3000 cal. years ago. This period correlates to a climatic deterioration in late Holocene (e.g. Bøe *et al.,* 2002; Sveian & Corner, 2004), which is further discussed in chapter 7.6. Increased sedimentation rates for this period have also been observed by others to occur in e.g. Trondheimsfjorden (Bøe *et al.,* 2003), West Spitsbergen (Hald *et al.,* 2004), Isfjorden (Forwick & Vorren, 2009).

The sedimentation rates for the sediments deposited prior to ~3000 cal.years BP are considered unreliable caused by the large gaps between dated depths and the large variations of the rates from the different cores. These rates are therefore not used for any further calculations i.e. for the mass movement frequencies (*see Chapter 7.5, below)*. However, the upper sedimentation rate, based on the dating of the turbidite, is verified by three radiocarbon dates and regarded relatively certain. The upper sedimentation rate is therefore used in further calculations. The reference point of this sedimentation rate in the sub-seafloor is the regional turbidite (reflection R2), meaning that only the part of the chirp sequence overlying R2 is provided with a sedimentation rate. The average of this accumulation rate is estimated to be 0.073 cm/year.

7.5 Chronology and frequencies of mass movements

The majority of the MTDs observed within the sub-seafloor are the result of frequent mass-wasting within a period shortly after the last deglaciation, i.e. the mass transport sequence mirrored in reflection R3, and the stacked debris flow mounds and sediment blocks in the southern part of the basin (extending ~3.5 km north of the threshold) and along the western and eastern fjord side (*see Chapter 7.1*). All these MTDs directly overlie the proximal glaciomarine sediments of chirp unit 2 (*see Chapter 5.4.2*), indicating that they were deposited after 10,784 cal. years BP which represents the end of the Ørnes Event (Corner, 1980, *see Chapter 2.3.2*).

In core HH13-019-PC-MF depth 428 - 430 cm, located ~24 cm above the MTD sequence/reflection R3, is dated to be 10,321 cal. years BP. Therefore, the MTD sequence/reflection R3 was most probably deposited within the period 10,784 - 10,321 cal. years BP. The southern, western and eastern MTD complexes overlie this deposit, suggesting that they were deposited after 10,321 cal. years BP. The lowermost parts of core HH13-016-GC-MF (depth 364-366 cm) were dated to 8252 cal. years BP. However, this core does not penetrate into the southern MTD complex (Fig.7.5 & 7.6), thus, suggesting that the MTD complex reflects mass-wasting prior to 8252 cal. years BP. More dates are

needed to determine the times of deposition of the southern, western and eastern MTD complexes more exactly.
The swath bathymetry, chirp reflection and core data provide unambiguous evidence for widespread slope instability within the basin. However, more dating results are required to calculate the frequency of mass wasting in the area shortly after the deglaciation.

The chirp data reveals that mass-wasting also has supplied the southern reaches of the eastern lobe area during later events (*see Chapter 7.1*). Here high-to-low amplitude reflections represent mass-flow events, which frequency of occurrence is estimated to be approx. 1 per 1000 years over last 3000 cal. years. These reflections also include the regional turbidite, reflection R2. Additionally, the chirp data reveals several thinner reflections between these deposits as well. They are thought to reflect smaller events, which are not included in the calculated frequency. One of these is correlated to a MTD comprised in unit 17-2 within core HH13-017-GC-MF, thought to have been deposited by a low-density turbidity flow (*see Chapter 7.3*). The turbidite is estimated to have a minimum age of 261 cal. years BP, meaning that mass-wasting has occurred within this area also in modern times.
The high-to low reflections underlying reflection R2 also mirrors mass-flow events, which appear to have occurred frequently following the deposition of the stacked debris flow mounds. Since no certain sedimentation rate is provided for this sequence, it was not possible to estimate any frequency of their occurrence.

MTDs suggested to represent small, local events are found within all the sediment cores. These provide a minimum frequency of such smaller events within the study area, estimated to be 2.3 per 1000 years over the last 3000 cal. years. The frequency can also be estimated for this type of mass transport events within the period ~10,000 – 3000 cal. years, and is then found to be only ~0.6 per 1000 years.

7.6 Post-glacial mass transport history

The most intense phase of mass-wasting within the area occurred immediately after the deposition of the glaciomarine sediments in the basin (*see Chapter 5.2.4*). During this period, mass-transport deposits were deposited in the southern part of the basin (extending ~3.5 km north of the threshold) and along the western and eastern fjord sides (*see Chapter 7.1*).

The data set only allows the determination of their deposition to be distinguished to the period 10,784 - 8252 cal. years BP. Nevertheless, the chirp stratigraphy indicates that the paraglacial mass-flow processes actually ended some time earlier (*see Chapter 7.5*). Based on the lack of hemipelagic intervals between the MTDs, these events most probably occurred during a relatively short time.

Frequent mass-wasting in the period following the last deglaciation is reported from several fjords (e.g. Syvitski *et al.*, 1987; Blikra & Longva, 2000; Forwick & Vorren, 2002; Bøe *et al.*, 2003; Stoker *et al.*, 2010). The landscape exposed after the last glaciation was in an unstable or metastable phase, and thus particularly exposed to modification at high denudation rates (Ballantyne, 2002). This was also the situation in fjords; glaciers deposited subglacial sediments and moraine debris on the commonly very steep sidewalls, and as the glacier retreated, these accumulations of sediments lost support from the ice and became subsequently unstable (Churtch & Ryder, 1972; Ballantyne, 2002; Powell, 2005). Sidewall sediment was therefore prone to failure by gravitational processes soon after the removal of the ice (e.g. Syvitski *et al.*, 1987; Syvitski & Shaw, 1995; Ballantyne, 2002).

Isostatic uplift is typical for coastal areas within the period following deglaciation (Corner, 2006). The isostatic uplift is caused by the response inflicted upon the removed ice load, and commonly resulted in earthquake activity. These earthquakes are the main triggering mechanism for paraglacial mass-wasting activity (e.g. Syvitski & Shaw, 1995).

The period of increased mass wasting within the study area falls into a period of enhanced postglacial uplift with the occurrence of major earthquakes (order of ≥ 6.0). This period lasted from 10,000 to 9500 years BP (Dehls *et al.*, 2000). Therefore, enhanced earthquake activity related to isostatic uplift has most probably been a major trigger for the failures within this area. Studies by Corner and Haugene (1993) indicate a rapid postglacial uplift in the Lyngen area before 8500 BP.

The landscape readjustment following a larger glaciation can occur over timescales of $10 - 10^4$ years, however, the rate of the sediment transfer is greatest right after deglaciation (Ballantyne, 2002). This is in consistence with the aggregated appearance of the larger proportion of the MTDs within this area.

The paraglacial MTDs mostly represent mass-flow deposits, but also sliding blocks occur (*see Chapter 7.1*). It is, therefore, reasonable to assume that both main types of mass-transport processes, i.e. sliding and mass-flow, were active within the basin during the paraglacial period. The initial development of the processes cannot be precisely determined. However, the sediment blocks probably followed weak bedding layers (cf. Stoker *et al.*, 2010, L'Heureux *et al.*, 2012).

Both the bathymetric data and the chirp data indicate that the period which followed the paraglacial mass-wasting is characterized by less active conditions with regard to slope failures. This is inferred from rounded edges of the scars and gullies formed during earlier mass wasting, reflecting long-term sediment deposition and smoothening of irregularities (*see Chapter 7.2*). Furthermore, the chirp stratigraphy reveals an acoustically transparent package of sediments with only few internal reflections (*see Chapter 5.2.1*). The most prominent reflection is the regional reflection R2 formed from a turbidite deposited between 3026 and 2930 cal. years BP (*see Chapter 7.2.3*). The mass-flow is suggested to have originated onshore and has most probably entered the fjord basin along the southern part of the larger indentation on the eastern fjord side (Fig. 7.12). Gullies identified in this indentation are suggested to represent the pathways of the mass-flow into the basin (*see Chapter 7.2.3*).

The mountain section Indre Nordnes (Fig. 7.12), one of the areas along Nordnesfjellet where unstable rock masses have been documented (*see Chapter 1.2*), is located onshore of the indentation, i.e. in an area that could potentially act as a source area for the turbidite. Onshore investigations indicate that avalanches from this part of Nordnessfjellet have taken place earlier; lobes of talus material and fans partially overgrown by vegetation are observed below the mountain, and some places they reach all the way down to the foot of the mountain (Hernes, 2014). Hernes (2014) further suggests that some of the avalanche material might have reached the fjord. Based on this, as well as the coincident location between the avalanche material and the indentation in the fjord side (Fig. 7.12), it is suggested that the turbidity flow might reflect a mass-transport event from Nordnesfjellet.

In addition to the turbidite (reflection R2), several high- to low-amplitude reflections are identified within this part of the sub-seafloor. These are also interpreted to represent viscous flows, most probably sourced by the same gullies as the turbidity flow (*see Chapter 7.2.3*). These mass-flows are estimated to have had a frequency of occurrence of approx. 1 per 1000 years over last 3000 cal. years (*see Chapter 7.5*).

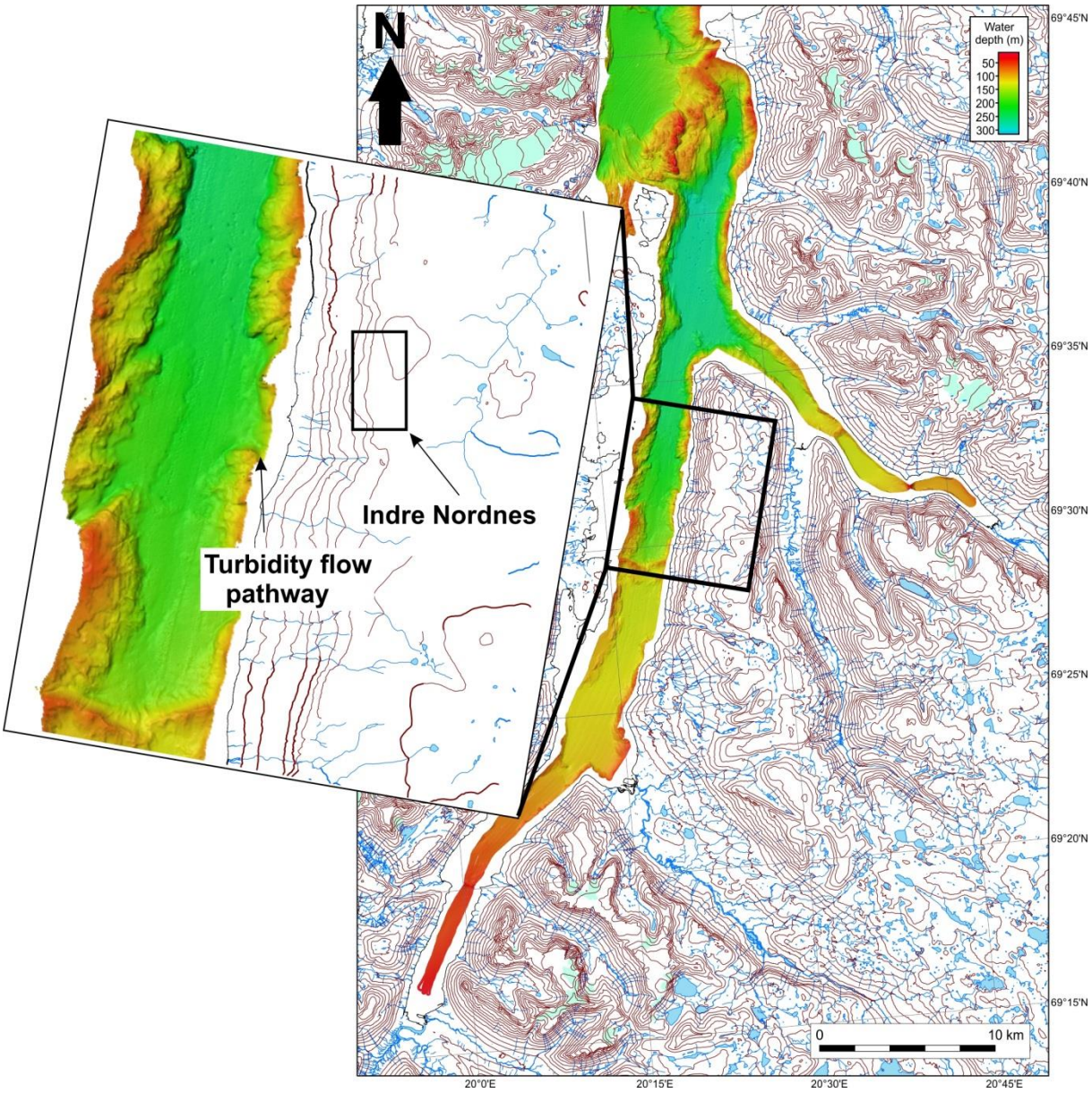

Figure 7.12: Overview map indicating the location of Indre Nordnes relative to the study area, together with the interpreted pathway for the turbidity flow leading to the deposition of the turbidite making up reflection R2.

East of the indentation (onshore), several creeks/rivers drain the area and terminate in the fjord (Fig.7.12). It is possible that the mass-flow deposits represents periods of flooding, which increased the sediment transfer from land to the basin. Sediment transfer from onshore areas to marine basins in form of injection of suspended sediments generally involves turbidity flows and mass-wasting (Mulder *et al.*, 1998).

The minor MTDs observed within the cores are thought represent small, local slope failures or snow avalanches entering the basin. The alpine landscape of the Lyngen Peninsula, located on the western side of the fjord, is prone to snow avalanches (e.g. Corner, 1980; Ballantyne, 1987; Lied *et al.*, 1989), as well is Nordnesfjellet on the eastern side (Hernes, 2014). Snow avalanches are capable of

transporting large amounts of debris (e.g. Blikra & Selvik, 1998), which can be deposited in the fjord basin as the snow avalanche reaches the fjord.

The sediment cores reveal a higher frequency of minor mass-wasting the last 3000 years (2.3 per 1000 years) compared with the period ~10,000 – 3000 cal. years (~0.6 per 1000 years) (*see Chapter 7.5*). The climatic change about 3000 years ago could be a contributor for the increased mass-wasting activity, during this period the climate became colder and local glaciers started to build up again in the highest areas (e.g. Sveian & Corner, 2004). The period between 9000-5000 years BP is characterized by a warmer and more humid climate, which favoured diverse vegetation (Bøe *et al.*, 2002). The prevalence of vegetation in the catchment area will stabilize the sediments and lower the input into the fjord basins (Howe *et al.*, 2010). Then, as the climate became colder, the amount and diversity of the vegetation were reduced and the stabilization of the sediments lowered.

Increased mass-wasting activity has been documented for other Norwegian localities for the same period; Blikra & Nemec (1998) estimated the temporal frequency of Holocene debris flows at 17 localities in western Norway and inferred that debris flow activity increased after ~3200 cal. years BP.

The local glaciers which built up during this colder period reached their maximum extent during the Little Ice Age (1750-1920) (Karlén, 1988; Jørgensen *et al.*, 1997; Bakke *et al.*, 2005; Sveian & Corner, 2004; Vorren *et al.*, 2007; Nesje, 2012). The glacial advance periods during the Holocene represent times of increased glacier erosion, and hence, increased production of debris by mass transport (Grove, 2004). Two minor MTDs were deposited after 321 and 261 cal. years BP, respectively, i.e. during the Little Ice Age when local glaciers reached their maximum late Holocene extents. Therefore, the triggering of these slope failures could be related to climatic cooling. Since no glaciers are located in the vicinity of the study area, glaciers are not thought to have had a direct influence to the fjord basin in this period. However, several processes that could have led to increased sediment transfer are related to climate deterioration, e.g. frost weathering and increased snow accumulation.

7.7 Comparison with other fjords

In order to highlight the diversity of mass-wasting within fjords, as well as providing a perspective for the results of this study, the mass transport history revealed for the central parts of Lyngenfjorden will be compared to that of three other Norwegian fjords: Trondheimsfjorden, Sørfjorden (Finneidfjord) and Fensfjorden.

Trondheimsfjorden in central Norway and Sørfjorden, more precisely Finneidfjord, in northern Norway are both good examples of the important role preconditions of the sediments play upon landslides within certain fjords. Both the fjords are sites of comprehensive investigations caused by their recently incidents of retrogressive landslides. Many slides have occurred in central Trondheimsfjorden during the last 100-200 years, where the three which occurred in 1888, 1955 and 1990 in the bay of Trondheim are the most substantial (e.g. L'Heureux *et al.*, 2010). In Sørfjorden, near Finneidfjord, a landslide occurred in 1996 (e.g Vardy *et al.*, 2012). The stability of the slopes in Trondheimsfjorden and Finneidfjorden are highly influenced by the occurrence of weak beds. Both the areas were, following the deglaciation, subjected to a rapid fall of the relative sea-level caused by the glacio-static rebound (e.g. L'Heureux *et al.*, 2010; Vardy *et al.*, 2012). The consequence was a sub-aerial emergence of marine deposits, which led to the production of quick clays; the marine deposits were exposed to fresh groundwater which leached them in salts (e.g. Vardy *et al.*, 2012). Several larger quick clay landslides were triggered by river erosion on land during Holocene in both the areas, and resulted in the deposition of clay-rich, weak event beds (L'Heureux *et al.*, 2010, 2012). Common for all these landslides are periods of heavy rainfall prior to the sliding, as well as ongoing construction work nearby triggering the slides either by vibrations or overloading. The increased precipitation prior to the sliding caused the ground water to rise leading to excess pore pressure (artesian groundwater pressure), thought to be the fundamental cause for triggering the initial slides (Longva *et al.*, 2003; L'Heureux *et al.*, 2010, 2012; Vardy *et al.*, 2012). Swath bathymetry data from Sørfjorden indicate that mass-wasting occurred at several locations in the fjord (L'Heureux *et al.*, 2012). Weak event beds are a common feature for uplifted valleys in Scandinavia (L'Heureux *et al.*, 2012), and also in Lyngen sensitive clays occur; in 2010 a larger quick-clay landslide occurred near Lyngseidet (e.g. L'Heureux *et al.*, 2013; NGU).

A study by Bøe *et al.* in 2003 presents data of Holocene mass movement in Trondheimsfjorden, and suggests that both the sedimentation rates and the frequency of mass movements have changed during the Holocene. The results from this study have some similarities with the results presented by Bøe et al. (2003). Also in Trondheimsfjorden, the sedimentation rates and mass-transport frequencies were highest around 9000 cal. years BP. Furthermore, late Holocene climatic deterioration may have led to increased sedimentation rates and mass-transport frequency in Trondheimsfjorden.

In Fensfjorden, western Norway, a larger sequence of mass-transport deposits is assumed to relate to the rapid isostatic adjustments immediately after the last deglaciation. These MTDs are found as stacked slide debrites observed above acoustically well-laminated glaciomarine sediments (Hjelstuen *et al.*, 2013). However, as for the study area in Lyngenfjorden, mass-wasting occurred at later stages as well; two well-defined upward-fining units are inferred to represent turbidite layers (Hjelstuen *et al.*, 2013). In similarity with the turbidites in Lyngenfjorden, these turbidites can be identified as thin bands of high-amplitude reflections. The reflections can be traced across the entire fjord basin, indicating a run out distance of ~2 km for the turbidity flows (Hjelstuen *et al.* 2013). The oldest turbidity flow has a minimum age of 2040 cal. years BP, while the youngest occurred between 1860 and 1190 cal. years BP. Different triggering mechanisms are suggested for the two events: the oldest may be time synchronous with a regional 2100 cal. years BP event triggered by an earthquake, whereas the youngest turbidite event is rather suggested to relate to trigger mechanisms such as local climatic changes or rock avalanches along the fjord sides (Hjelstuen *et al.*, 2013).

8 Summary and conclusions

Swath bathymetry, high-resolution seismic data and five sediment cores were analysed in order to reconstruct the post-glacial mass-transport history within the central parts of Lyngenfjorden.

- Slide scars and mass-transport deposits, e.g. sediment lobes, mounds and blocks, are the most striking features identified on the swath bathymetry and chirp data.
- The seafloor is generally relatively smooth and flat, however, three shallower areas stand out with a mounded, lensoid or lobate morphology i.e. the southernmost ~3.5 km of the basin, as well as along the western fjord and eastern fjord sides. Chirp data reveal that the shallow and undulating character of the seafloors in these areas is caused by complexes of stacked MTDs.
- The MTD complexes are mainly composed of acoustically transparent to chaotic deposits, e.g. debris flows or turbidites. However, acoustically stratified sediment blocks occur occasionally; either transported as run-out blocks embedded in the debris flow or as single slide blocks. It is suggested that the complexes formed during a relatively short period of frequent mass-wasting following directly after the last deglaciation (~10,800 cal. years BP).
- The MTD complexes overlie either glaciomarine sediments or a discontinuous high-amplitude reflection covering an area of at least 7.2 x 1.2 km^2. The reflection represents a MTD sequence, including two turbidites, deposited within the period 10,784 – 10,321 cal. years BP.
- The period which followed the paraglacial mass-wasting is characterized by less active conditions with regard to slope failures. This is inferred from rounded edges of the scars and gullies formed during earlier mass wasting, reflecting long-term sediment deposition and smoothening of irregularities. Furthermore, the chirp stratigraphy reveals an acoustically transparent package of sediments with only few internal reflections, suggested to reflect relatively stable depositional conditions.
- The post-glacial hemipelagic package of sediments in the stratigraphy is interrupted by a regional high-amplitude reflection covering an area of at least 7.4 x 1.3 km^2. The reflection is formed from a turbidite deposited between 3026 and 2930 cal. years BP. The mass-flow is suggested to have originated onshore, and might have followed a rock avalanche from the mountain section Indre Nordnes; one of several areas along Nordnesfjellet where unstable rock masses have been documented.
- Several high-to low-amplitude reflections interpreted to represent viscous flows, e.g. debris flows or turbidites, onlap the eastern fjord side together with the onshore originated turbidite. The occurrence of these mass-flows coincides with the onshore location of several creeks/rivers, and it is possible that they were deposited as a consequence of periods of flooding.

- The high- to low-amplitude mass-flow deposits, together with the turbidite, have had a frequency of occurrence of approx. 1 per 1000 years over the last 3000 cal. years BP.
- Several minor MTDs are observed within the five sediment cores. They were probably deposited from small, local slope failures or snow avalanches entering the basin from the steep mountains surrounding the fjord.
- The sediment cores reveal a higher frequency of minor mass-wasting the last 3000 cal. years BP (~2.3 per 1000 years), compared with the period ~10,000 – 3000 cal. years BP (~0.6 per 1000 years).
- It is inferred that a climatic change about 3000 years ago could be a contributor for the increased mass wasting activity the last 3000 cal. years BP. During this period the climate became colder and local glaciers started to build up again in the highest areas. However, no glaciers were located in the vicinity to the study area and could not have influenced the basin directly. The main contributors to the increased mass wasting are thought to be e.g. frost weathering and increased snow accumulations.
- The low mass-wasting frequency indicated for the earlier period can be correlated to a warmer and humid period (9000 – 5000 years BP).
- Two minor MTDs were deposited after 321 and 261 cal. years BP, respectively, i.e. during the Little Ice Age when local glaciers reached their maximum late Holocene extents. Therefore, the triggering of these slope failures could be related to climatic cooling.

9 Recommended future work

The results from this study provided new information about the history of mass wasting in Lyngenfjorden. However, several uncertainties about the lateral extent and source areas of mass-transport deposits remain. These uncertainties could be addressed through the following actions:

- More detailed mapping of the sub-seafloor would contribute to a better understanding of the lateral extent of the mass-transport deposits. This could be achieved through the acquisition of additional, i.e. more closely-spaced, chirp lines.
- Recovery of additional sediment cores:
    - Longer sediment cores would allow to identify the sedimentary processes leading to the deposition of the MTD complexes (*see Chapter 7.1*), as well as to date the periods of their formations.
    - Cores from the eastern sediment lobe area would provide information about the composition of the deposits leading to the high- to low-amplitude reflections (MTD_e2 in Fig. 7.4, *see Chapter 7.1*).
- The descriptions of several MTDs in this study are mainly based upon visual observations, i.e. that grain-size analyses were not performed. Furthermore, it was occasionally difficult to distinguish the exact boundary between the MTDs and the hemipelagic sediments. Additional samples (closer sampling intervals) would improve the understanding of the sedimentary processes leading to the deposition of these MTDs.
- Additional radiocarbon dates would provide a better chronology for the mass-transport events and, in consequence, improve the estimated mass-movement frequencies. More exact chronologies would also be useful for improved correlations with mass-wasting activities in other areas, with the purpose of 1) distinguishing local from regional events and 2) to infer the influence of climate change on slope stability.

10 References

Aarseth, I., 1997, Western Norwegian fjord sediments: age, volume, stratigraphy, and role as temporary depository during glacial cycles: Marine Geology, v. 143, p. 39-53.

Aarseth, I., Lønne, Ø., and Giskeødegaard, O., 1989, Submarine slides in glaciomarine sediments in some western norwegian fjords: Marine Geology, 88, 1-21.

Ananiadis, G., I., V., N., K., and A, Z., 2004, Grain size statistical parameters and palaeoflow velocity measurments of the tertiary Pindos foreland basin turbidites: Bulletin of the Geological Society of Greece vol. XXXV.

Andersen, B. G., 1968, Glacial geology of western Troms, North Norway: Norges geologiske undersøkelse 256, p. 1-160.

Andersen, B. G., Manglerud, J., Sørensen, R., Reite, A., Sveian, H., Thoresen, M., and Bergstrøm, B., 1995, Younger Dryas ice-marginal deposits in Norway: Quaternary International, v. 28, p. 147-169.

Andresen, A., 1988, Caledonian Terranes of Northern Norway and their characteristics: Trabajos de Geologia, Univ. de Oviedo, v. 17, p. 103-117.

Aure, J., 1983, Akvakultur i Troms. Kartlegging av høvelige lokaliteter for fiskeoppdrett: Fisken og havet; serie B, nr.1. Rapporter og meldinger fra Fiskeridirektoratets havforskningsinstitutt - Bergen., p. 92.

Avaatech, 2014, www.avaatech.com.

Baeten, N. J., 2007, Late Weichselian and Holocene sedimentary processes and environments in Billefjorden, Svalbard: Master's thesis at the Faculty of Science, Department of Geology, University of Tromsø, November 2007.

Baeten, N. J., Forwick, M., Vogt, C., and Vorren, T. O., 2010, Late Weichselian and Holocene environments and glacial activity in Billefjorden, Svalbard.: In: Howe, J.A., Austin, W.E.N., Forwick, M. & Paetzel, M. (eds) Fjord systems and archives. Geological Society, London, Special Publications, 344, pp. 207-223.

Bakke, J., Dahl, O. D., Paaske, Ø., Løvlie, R., and Nesje, A., 2005, Glacier fluctuations, equilibrium-line, altitudes and palaeoclimate in Lyngen, northern Norway during the Lateglacial and Holocene: The Holocene, v. 15, p. 518-540.

Ballantyne, C. K., 1987, Some Observations on the Morphology and Sedimentology of Two Active Protalus Ramparts, Lyngen, Northern Norway: Arctic and Alpine Research, v. 19, no. 2, p. 167-174.

Ballantyne, C. K., 2002, Paraglacial geomorphology: Quaternary Science Reviews, v. 21, no. 8, p. 1935-2017.

BeckmanCoulter, 2011, Instruction For Use: LS 13 320 Laser Diffraction Particle Size Analyzer.

Benn, D. I., and Evans, D. J. A., 1998, Glaciers & Glaciation: Arnold, London. 733 pp.

-, 2010, Glaciers and glaciation: Second edition. London: Hodder Education.

Bergh, S. G., Eig, K., Kløvjan, O. S., Henningsen, T., Olesen, O., and Hansen, J., 2007, The Lofoten-Vesterålen continental margin: a multiphase Mesozoic-Palaeogene rifted shelf by offshore-onshore brittle fault-fracture analysis: Norwegian Journal of Geology, v. 87, no. 1&2, p. 29-58.

Bergstrøm, B., Olsen, L., and Sveian, H., 2005, The Tromsø-Lyngen glacier readvance (early Younger Dryas) at Hinnøya-Ofotfjorden, northern Norway: a reassessment: NGU Bulletin 445, p. 73-88.

Blikra, L. H., and Bunkholt, H., 2012, Tunnel gjennom Nordnesfjellet i Kåfjord, Troms: Oversikt over nærliggende ustabile fjellparti og påvirkning på stabilitet: Åkenes rapport 02 2012.

Blikra, L. H., Eiken, T., Henderson, I., and Venvik-Ganerød, G., 2006b, Forprosjekt fjellskred i Troms – Status 2005: NGU Rapport 2006.040, p. 37.

Blikra, L. H., Henderson, I., and Nordvik, T., 2009, Faren for fjellskred fra Nordnesfjellet i Lyngenfjorden, Troms: NGU Rapport 2009.026, p. 29.

Blikra, L. H., and Longva, O., 2000, Gravitational-slope failures in Troms: Indications of palaeoseismic activity?: In: Dehls, J & Olesen, O. (Red): Neotectonics in Norway: Annual Technical Report. NGU Report, p. 31-40.
Blikra, L. H., Longva, O., Braathen, A., Anda, E., Dehls, J. F., and Stalsberg, K., 2006a, Rock slope failures in Norwegian fjord areas: Examples, spatial distribution and temporal pattern *in* Evans, S., Mugnozza, G., Strom, A., and Hermanns, R., eds., Landslides from Massive Rock Slope Failure, Volume 49, Springer Netherlands, p. 475-496.
Blikra, L. H., and Nemec, W., 1998, Postglacial colluvium in western Norway: depositional processes, facies and palaeoclimatic record: Blackwell Scientific Publishers [etc.] Oxford, Boston [etc.]
Blikra, L. H., and Selvik, S. F., 1998, Climatic signals recorded in snow avalanche-dominated colluvium in western Norway: depositional facies successions and pollen records: The Holocene, v. 8, no. 6, p. 631-658.
Blott, S. J., and Pye, K., 2001, GRADISTAT: a grain size distribution and statistics package for the analysis of unconsolidated sediments: Earth Surface Processes and Landforms, v. 26, no. 11, p. 1237-1248.
Boggs, S. J., 1995, Principles of Sedimentology and Stratigraphy: Prentice Hall, New Jersey, 774 pp.
Bondevik, S., Mangerud, J., and Gulliksen, S., 2001, The marine 14C age of the Vedde Ash Bed along the west coast of Norway: Journal of Quaternary Science, Vol. 16 (1), 3-7.
Bouma, A. H., 1962, Sedimentology of Some Flysch Deposits: Elsevier, Amsterdam, 168 pp.
Bowman, S., 1990, Radiocarbon Dating, University of California Press.
Bøe, R., Bellec, V. K., Dolan, M. F. J., Buhl-Mortensen, P., Buhl-Mortensen, L., Slagstad, D., and Rise, L., 2009, Giant sandwaves in the Hola glacial trough off Vesterålen, North Norway: Marine Geology, v. 267, no. 1–2, p. 36-54.
Bøe, R., Hovland, M., Instanes, A., Rise, L., and Vasshus, S., 2000, Submarine slide scars and mass movements in Karmsundet and Skudenesfjorden, southwestern Norway: morphology and evolution: Marine Geology; 167; p.147-165.
Bøe, R., Lepland, A., Blikra, L. H., Longva, O., and Sønstegaard, E., 2002, Postglacial mass movements in western Norway with special emphasis on the 2000-2200 BP and 2800-3200 BP periods - final report NOrges Geologiske Undersøkelse, rapport no.: 2002.020.
Bøe, R., Rise, L., Blikra, L. H., Longva, O., and Eide, A., 2003, Holocene mass-movement process in Trondheimsfjorden, Central Norway: Norwegian Journal of Geology, Vol.83, pp.3-22.
Cadigan, R. A., 1961, Geologic Interpretation of Grain-Size Distribution Measurements of Colorado Plateau Sedimentary Rocks: The Journal of Geology, v. 69, no. 2, p. 121-144.
Cai, J., Powell, R. D., Cowman, E. A., and Carlson, P. R., 1997, Lithofacies and seismic-reflection interpretation of temperate glacimarine sedimentation in Tarr Inlet, Glacier Bay, Alaska.: Marine Geology, Vol. 143, pp. 5-37.
Carlson, P. R., 1989, Seismic reflection characteristics of glacial and glacimarine sediment in the Gulf of Alaska and adjacent fjords.: Marine Geology 85, 391-416.
Carter, L., 2009, Charting the seafloor: Multibeam echo sounding, *Te Ara - the Encyclopedia of New Zealand.* URL: http://www.TeAra.govt.nz/en/charting-the-sea-floor/page-4 (Updated 13 July 2012).
CHRIST, 2006, Operating manual, ALPHA 1-4 LSC / ALPHA 2-4 LSC; Version 09.2006.
Christiansen, H. H., and Blikra, L. H., 2010, Thermal regimes in bedrock and open fractures in the Nordnes rockslide, Norway: Geophysical Research Abstracts, v. 12, EGU2010-8969-1.
Church, M., and Ryder, J. M., 1972, Paraglacial sedimentation: consideration of fluvial processes conditioned by glaciation: Geological Society of America Bulletin 83, 3059-3072.
Corner, G., 2006a, A transgressive-regressive model of fjord-valley fill: stratigraphy, facies and depositional controls: Society of Sedimentary Geology, Vol. 85.
-, 2006b, A transgressive-regressive model of fjord-valley fill: stratigraphy, facies and depositional controls: Society of Sedimentary Geology, v. 85.
Corner, G. D., 1980, Preboreal deglaciation chronology and marine limits of the Lyngen-Storfjord area, Troms, North Norway: Boreas, v. 9, no. 4, p. 239-249.
-, 2005a, Atlantic Coast and Fjords; Geography of Fennoscandia: Oxford University Press, 432pp, ISBN 0-19-924590-8.

-, 2005b, Scandes Mountains; Geography of Fennoscandia: Oxford University Press, 432pp, ISBN 0-19-924590-8.
Corner, G. D., and Haugane, E., 1993, Marine-lacustrine stratigraphy of raised coastal basins and postglacial seal-level change at Lyngen and Vanna, Troms, northern Norway: Norsk Geologisk Tidsskrift, Vol. 73, pp. 175-197.
Croudace, I. W., Rindby, A., and Rothwell, R. G., 2006, ITRAX: description and evaluation of a new multi-function X-ray core scanner: Geological Society, London, Special Publications, v. 267, no. 1, p. 51-63.
Dahl, R., 1989, Kvartærtiden og dens avsetninger i Norge: Kompendium i emne TBA4100 geoteknikk-geologi. Institutt for geoteknikk, NTNU. *Revidert i 1995 og 2005 av Bjørge Brattli*.
Dannevig, P., 2009, Troms:klima: http://snl.no/Troms/klima. Retrieved 2014.
Dean, W. E., Gardner, J. V., and Piper, D. Z., 1997, Inorganic geochemical indicators of glacial-interglacial changes in productivity and anoxia on the California continental margin: Geochimica et Cosmochimica Acta, v. 61, no. 21, p. 4507-4518.
Dehls, J. F., Olesen, O., Olsen, L., and Harald Blikra, L., 2000, Neotectonic faulting in northern Norway; the Stuoragurra and Nordmannvikdalen postglacial faults: Quaternary Science Reviews, v. 19, no. 14, p. 1447-1460.
Donner, J., 1995, The Quaternary History of Scandinavia: Cambridge University Press, 200 pp.
Dypvik, H., and Harris, N. B., 2001, Geochemical facies analysis of fine-grained siliciclastics using Th/U, Zr/Rb and Zr+Rb/Sr ratios: Chemical Geology, v. 181, p. 131-146.
Elverhøi, A., Harbitz, C. B., Dimakis, P., Mohrig, D., Marr, J., and Parker, G., 2000, On the dynamics of subaqueous debris flows: Oceanography, Vol. 13(3), pp. 109-117.
Ersdal, G., 2001, An overview of ocean currents with emphasis on currents on the Norwegian continental shelf: NPD(preliminary version), p. 40.
Fjeldskaar, W., Lindholm, C., Dehls, J. F., and Fjeldskaar, I., 2000, Postglacial uplift, neotectonics and seismicity in Fennoscandia: Quaternary Science Reviews, v. 19, no. 14, p. 1413-1422.
Flemings, P. B., Behrmann, J. H., John, C. M., and Scientists, E., 2006, Gulf of Mexico Hydrogeology: Integrated Ocean Drilling Program Management International, Inc., College Station, Tex.
Folk, R. L., and Ward, W. C., 1957, Brazos River bar; a study in the significance of grain size parameters: Journal of Sedimentary Petrology, 27(1):3-26.
Forwick, M., 2001, Development of the sedimentary environment in Balsfjord (northern Norway): CAND. SCIENT. THESIS IN GEOLOGY, University of Tromsø.
-, 2010, Educational crusie to the Lyngen area, Troms County, northern Norway: Unpublished crusie report, University of Tromsø, p. 16.
Forwick, M., Dijkstra, N., Fabian, C., Faust, J., Franek, P., Iversen, S., Jernas, P., Kneis, K., O'Regan, M., Preto, P., Sauer, S., and Velle, J., 2013, CRUISE REPORT; Marine-geological cruise to north Norwegian fjords and the continental shelf off northern Norway on R/V Helmer Hanssen, April 15th - 24th 2013; Department of Geology, University of Tromsø.
Forwick, M., and Rasmussen, T., 2012, CRUISE REPORT about joint educational cruises in the courses; GEO-3111 Reconstructing Marine Climate and Environments, GEO-3121 Marine Geology and GEO-3122 Micropaleontology. Department of Geology, University of Tromsø, Norway.
Forwick, M., and Vorren, T., 2012, Submarine Mass Wasting in Isfjorden, Spitsbergen, *in* Yamada, Y., Kawamura, K., Ikehara, K., Ogawa, Y., Urgeles, R., Mosher, D., Chaytor, J., and Strasser, M., eds., Submarine Mass Movements and Their Consequences, Volume 31, Springer Netherlands, p. 711-722.
Forwick, M., and Vorren, T. O., 2002, Deglaciation History and Postglacial Sedimentation in Balsfjord (North Norway): Polar Research 2002, Vol. 21, pp. 259 - 266.
-, 2005, Late Weichselian and Holocene sedimentation and environments in the Isfjorden area: *In:* Forwick, M. (ed.) Sedimentary processes and palaeoenvironments in Spitsbergen Fjords. A dissertation for the degree of Doctor Scientiarum, University of Tromsø.
-, 2007, Holocene mass-transport activity and climate in outer Isfjorden, Spitsbergen: marine and subsurface evidence: The Holocene, 17(6), pp. 707-716.

-, 2009, Late Weichselian and Holocene sedimentary environments and ice rafting in Isfjorden, Spitsbergen: Palaeogeography, Palaeoclimatology, Palaeoecology, 280, pp. 258-274.
-, 2011, Mass wasting in Isfjorden, Spitsbergen: In Y.Yamada,K. Kawamura, K. Ikehara, Y. Ogawa, R. Urgeles, D. Mosher, J. Chaytor & M. Strasser (Eds.), Submarine mass movements and their consequences. Advances in Natural and Technological Hazards Research (Vol. 31, pp. 711-722). Netherland: Springer-Verlag, New York.
Forwick, M., Vorren, T. O., Hald, M., Korsun, S., Roh, Y., Vogt, C., and Yoo, K. C., 2010, Spatial and temporal influence of glaciers and rivers on the sedimentary environment in Sassenfjorden and Tempelfjorden: In: Howe, J.A., Austin, W.E.N., Forwick, M. & Paetzel, M. (eds.) Fjord systems and archives. Geological Society, London, Special Publications, 344, pp. 163-193.
Fossen, H., Pedersen, R. B., Bergh, S., and Andresen, A., 2007, En fjellkjede blir til. Oppbygningen av Kaledonidene; ca. 500 - 450 millioner år: In: Ramberg, I.B., Bryhni, I., Nøttvedt, A. & Rangsnes, K. (Eds.) Landet blir til. Norges Geologi. Chapter 6, p. 178-229.
Friedman, G. M., Sanders, J. E., and Kopaska-Merkel, D. C., 1992, Principles of sedimentary deposits - stratigraphy and sedimentology: Maximillan Publishing Company, New York, 717 pp.
Gade, H. G., 1986, Features of fjords and ocean interaction: In: B.G. Hurdle (Editor), The Nordic Seas. Springer Verlag, New York, p. 183-189.
Gales, J. A., Larter, R. D., Mitchell, N. C., and Dowdeswell, J. A., 2013, Geomorphic signature of Antarctic submarine gullies: Implications for continental slope processes: Marine Geology, v. 337, no. 0, p. 112-124.
Gardner, J. V., Mayer, L., and Hughs Clarke, J. E., 2000, Morphology and processes in Lake Tahoe (California-Nevada): Geological Society of America Bulletin, 112, no.5; 736 - 746.
GEONOR, 2014, www.geonor.no.
GEOTEK, 2000, Geotek Multi-Sensor Core Logger (MSCL) Manual; version November 2000.
-, 2014, Geotek Multi-Sensor Core Logger (MSCL) Manual; version 17-02-14: http://www.geotek.co.uk/.
Glimsdal, S., and Harbitz, C. B., 2008, Flodbølger etter mulig fjellskred, Nordnes, Lyngen kommune NGI-rapport 20071677-1: Norges geotekniske insititutt.
Grove, J. M., 2004, Little Ice Ages: ancient and modern: Routledge, London.
Haeussler, P., Parsons, T., Finlayson, D., Hart, P., Chaytor, J., Ryan, H., Lee, H., Labay, K., Peterson, A., and Liberty, L., 2014, New Imaging of Submarine Landslides from the 1964 Earthquake Near Whittier, Alaska, and a Comparison to Failures in Other Alaskan Fjords, *in* Krastel, S., Behrmann, J.-H., Völker, D., Stipp, M., Berndt, C., Urgeles, R., Chaytor, J., Huhn, K., Strasser, M., and Harbitz, C. B., eds., Submarine Mass Movements and Their Consequences, Volume 37, Springer International Publishing, p. 361-370.
Hald, M., 2009, Past Climate Change and Perspectives for Archaeological Research: Examples from Norway, Svalbard, and Adjoining Seas: Arctic Anthropology; Volum 46 (1-2).
Hald, M., Ebbesen, H., Forwick, M., Godtliebsen, F., Khomenko, L., Korsun, S., L., R. O., and Vorren, T. O., 2004, Holocene paleoceanography and glacial history of the West Spitzbergen area, Euro-Arctic margin: Quaternary Science Reviews, 23(20-21), 2075-2088.
Hansbo, S., 1957, A new approach to the determination of the shear strength of clay by the fall-cone test: Proc. Royal Swedish Geotechnical Institute, 14:7–47.
Hansen, J. A., 2009, Onshore-offshore tectonic relations on the Lofoten and Vesterålen Margin : Mesozoic to early Cenozoic structural evolution and morphological implications: University of Tromsø, Faculty of Science, Department of Geology, p. 229.
Heimbürger, L.-E., Cossa, D., Thibodeau, B., Khripounoff, A., Mas, V., Chiffoleau, J.-F., Schmidt, S., and Migon, C., 2012, Natural and anthropogenic trace metals in sediments of the Ligurian Sea (Northwestern Mediterranean): Chemical Geology, v. 291, no. 0, p. 141-151.
Hermanns, R., Oppikofer, T., Anda, E., Blikra, L., Böhme, M., Bunkholt, H., Crosta, G., Dahle, H., Devoli, G., Fischer, L., Jaboyedoff, M., Loew, S., Sætre, S., and Yugsi Molina, F., 2013, Hazard and Risk Classification for Large Unstable Rock Slopes in Norway: Italian journal of engineering geology and environment, p. 245-254.
Hernes, I., 2004, Fjellskred ved Indre Nordnes, Nordnesfjellet, Lyngen, Troms: GEO-3900 Masteroppgåve i Geologi, UiT-Norges Arktiske Universitet.

Hjelstuen, B. O., Kjennbakken, H., Bleikli, V., Ersland, R. A., Kvilhaug, S., Euler, C., and Alvheim, S., 2013, Fjord stratigraphy and processes – evidence from the NE Atlantic Fensfjorden system: Journal of Quaternary Science, v. 28, no. 4, p. 421-432.

Hopkins, T. S., 1991, The GIN Sea - A synthesis of its physical oceanography and literature review 1972-1985: Earth-Science Reviews, v. 30, p. 175-318.

Hovland, M., and Judd, A. G., 1988, Seabed Pockmarks and Seepages: Graham & Trotman, London. 293 pp.

Howe, J. A., Austin, W. E. N., Forwick, M., Paetzel, M., Harland, R., and Cage, A. G., 2010, Fjord systems and archives: a review: Geological Society, London, Special Publications, v. 344, no. 1, p. 5-15.

Hughen, K., Lehman, S., Southon, J., Overpeck, J., Marchal, O., Herring, C., and Turnbull, J., 2004, 14C Activity and Global Carbon Cycle Changes over the Past 50,000 Years: Science, v. 303, no. 5655, p. 202-207.

Jenssen, O. A., 2006, Deglasiasjon og sedimentasjonsmiljø i Lyngen og Storfjorden, Troms: Mastergradsoppgave i arktisk marin geologi og geofysikk, Universitetet i Tromsø, p. 149.

Johannessen, M. O., 1986, Brief overview of the physical oceanography: In: Hurdle, B. G. (ed(s).): The Nordic Seas. Springer Verlage, New York, p. 103-127.

Judd, A. G., and Hovland, M., 1992, The evidence of shallow gas in marine sediments: Continental Shelf Research, v. 12, no. 10, p. 1081-1095.

Jørgensen, P., Sørensen, R., and Haldorsen, S., 1997, Kvartærgeologi: Book. Landbruksforlaget.

Kammerer, E. L. L. M., 2000, A new method for the removal of refraction artifacts in multibeam echosounder systems: ProQuest Dissertations And Theses; Thesis (Ph.D.)--University of New Brunswick (Canada), 2000.; Publication Number: AAINQ65461; ISBN: 9780612654617; Source: Dissertation Abstracts International, Volume: 62-12, Section: B, page: 5941.; 191 p.

Karlèn, W., 1988, Scandinavian glacial and climatic fluctuations during the Holocene: In: Thompson, D. P. & Gerald, O. (ed(s).): Holocene glacier fluctuations. Pergamon, Oxford., p. 199-209.

Koinig, K. A., Shotyk, W., Lotter, A. F., Ohlendorf, C., and Sturm, M., 2003, 9000 years of geochemical evolution of lithogenic major and trace elements in the sediment of an alpine lake - the role of climate, vegetation, and land-use history: Journal of Paleolimnology, volume: 30, pp. 307 - 320.

KongsbergMaritime, 2003, EM 300 30 kHz multibeam echo sounder product specifics.

Kylander, M. E., Ampel, L., Wohlfarth, B., and Veres, D., 2010, High-resolution X-ray fluorescence core scanning analysis of Les Echets (France) sedimentary sequence: new insights from chemical proxies: Journal of Quaternary Science, v. 26, no. 1, p. 109-117.

L'Heureux, J.-S., Hansen, L., Longva, O., Emdal, A., and Grande, L. O., 2010, A multidisciplinary study of submarine landslides at the Nidelva fjord delta, Central Norway, - Implications for the assessment of geohazards: Norwegian Journal of Geology, Vol 90, pp. 1-20.

L'Heureux, J.-S., Longva, O., Steiner, A., Hansen, L., Vardy, M., Vanneste, M., Haflidason, H., Brendryen, J., Kvalstad, T., Forsberg, C., Chand, S., and Kopf, A., 2012, Identification of Weak Layers and Their Role for the Stability of Slopes at Finneidfjord, Northern Norway, *in* Yamada, Y., Kawamura, K., Ikehara, K., Ogawa, Y., Urgeles, R., Mosher, D., Chaytor, J., and Strasser, M., eds., Submarine Mass Movements and Their Consequences, Volume 31, Springer Netherlands, p. 321-330.

Laberg, J. S., and Vorren, T. O., 1995, Late Weichselian submarine debris flow deposits on the Bear Island Trough Mouth Fan: Marine Geology 127; 45-72.

Lee, S., Talling, P. J., Ernst, G. J. G., and Hogg, A. J., 2002, Occurrence and origin of submarine plunge pools at the base of the US continental slope: Marine Geology; 185; p.363-377.

Leeder, M., 2011, Sedimentology and Sedimentary Basins. From Turbulence to Tectonics: Second edition, Willey-Blackwell,179-180, pp. 203-204.

Lied, K., Sandersen, F., and Toppe, R., 1989, Snow-avalanche maps for use by the Norwegian army: International Glaciological Society.

Longva, O., Janbu, N., Blikra, L., and Boe, R., 2003, The 1996 Finneidfjord slide: seafloor failure and slide dynamics.: In: Locat J, Mienert J (eds) Submarine mass movements and their consequences, 531 - 538.

Lowe, J. J., and Walker, M. J. C., 1997, Reconstructing Quarternary Environments: Book. Longman Group Ltd.
Lyså, A., and Aarseth, I., 2004, The late glacial-Holocene seismic stratigraphy and sedimentary environment in Ranafjorden, northern Norway: Marine Geology, Vol. 211, pp. 45-78.
Lyså, A., and Vorren, T. O., 1997, Seismic facies and architecture of ice-contact submarine fans in high-relief fjords, Troms, northern Norway: Boreas, v. 26, p. 309-328.
Mangerud, J., Bondevik, S., Gulliksen, S., Karin Hufthammer, A., and Høisæter, T., 2006, Marine 14C reservoir ages for 19th century whales and molluscs from the North Atlantic: Quaternary Science Reviews, v. 25, no. 23–24, p. 3228-3245.
Mangerud, J., and Gulliksen, S., 1975, Apparent radiocarbon ages of Recent marine shells from Norway, Spitsbergen, and Arctic Canada. Quaternary Research 5:236-237.
Mareano, 2014, http://www.mareano.no/.
McHugh, C. M. G., Damuth, J. E., Gartner, S., Katz, M. E., and Mountain, G. S., 1996, Oligocene to Holocene mass-transport deposits of the New Jersey continental margin and their correlation to sequence boundaries Proceedings of the Ocean Drilling Program, Scientific Results, Vol. 150.
Mellem, G. B., 1991, Seismisk stratigrafi og sedimentasjonsmiljø i Ullsfjord og Lyngen, Troms. Upublisert hovedfagsoppgave, Universitetet i Tromsø, p. 153.
Mork, M., 1981, Circulation Phenomena and Frontal Dynamics of the Norwegian Coastal Current: Philosophical Transactions of the Royal Society of London. Series A, Mathematical and Physical Sciences, v. 302, no. 1472, p. 635-647.
Morton, R. A., and White, W. A., 1997, Characteristics of and Corrections for Core Shortening in Unconsolidated Sediments: Coastal Education & Research Foundation, Inc.
Mulder, T., and Alexander, J., 2001, The physical character of subaqueous sedimentary density flows and their deposits: Sedimentology, Vol. 48(2), pp. 269-299.
Mulder, T., and Cochonat, P., 1996, Classification of Offshore Mass Movements: Journal of Sedimentary Research, Section A: Sedimentary Petrology and Processes; Vol. 66, No. 1, p.43-57.
Mulder, T., Syvitski, J. P. M., and Skene, K. I., 1998, Modelling of erosion and deposition by turbidity currents generated at river mouths: Journal of sedimentary Research, Vol. 68, pp. 124-137.
Myrbo, A., 2004, Freeze drying: Limnological Research Center Core Facility; SOP series.
Nardin, T. R., Hein, H. J., Gorsline, D. S., and Edwards, B. D., 1979, A review of massmovement processes, sediment and acoustic characteristics, and contrasts in slope and base-of-slope systems v. Canyon-fan-basin floor systems: Society of Economic Palaeontologists and Mineralogists Special Publication, Vol. 27, pp. 61-73.
Nesje, A., 2012, Brelære: Book: Kristiansand: Høyskoleforlaget AS - Norwegian Academic Press, v. 2.ed.
NGU, 2014, www.ngu.no.
NNFO, 2014, www.nnfo.no.
NOC, 2014, www.noc.ac.uk.
Nordvik, T., Blikra, L. H., Nyrnes, E., and Derron, M. H., 2010, Statistical analysis of seasonal displacements at the Nordnes rockslide, northern Norway: Engineering geology, v. 114(3), p. 228-237.
NVE, 2014, atlas.nve.no.
Olesen, O., Blikra, L. H., Braathen, A., Dehls, J., Olsen, L., Rise, L., Roberts, D., Riis, F., Faleide, J. I., and Anda, E., 2004, Neotectonic deformation in Norway and its implications: a review: Norwegian Journal of Geology, v. 84, p. 3-34.
Osmundsen, P. T., Henderson, I., Lauknes, T. R., Larsen, Y., Redfield, T. F., and Dehls, J., 2009, Active normal fault control on landscape and rock-slope failure in northern Norway: Geology, v. 37, no. 2, p. 135-138.
Piper, D. J. W., Pirmez, C., Manley, P. L., Long, D., Flood, R. D., Normark, W. R., and Showers, W., 1997, Mass-transport deposits of the Amazon Fan: In: Flood, R. D., Piper, D. J. W, Klaus, A. and Peterson, L. C., eds., Proceedings of the Ocean Drilling Program, Scientific Results, Leg 155: College Station, Texas, Ocean Drilling Program, p. 109 - 145.

Plassen, L. I. V., and Vorren, T. O., 2003, Sedimentary processes and the environment during deglaciation of a fjord basin in Ullsfjorden, north Norway: Norsk Geologisk Tidsskrift, Vol. 83, pp. 23-36.
Powell, R. D., 2005, Subaquatic landsystems: fjord: In: Evans, D. J. A. (ed.) Glacial Landsystems. Hodder Arnold, London, 313-347.
Prior, D. B., Bornhold, B. D., Coleman, J. M., and Bryant, W. R., 1982, Morphology of a submarine slide, Kitimat Arm, British Columbia: Geology; 10; p.588 - 592.
QueensUniversityBelfast[14]CHRONO, 2014, Centre for Climate, the Environment, and Chronology (http://chrono.qub.ac.uk)
Quinn, R., Bull, J. M., and Dix, J. K., 1998, Optimal Processing of Marine High-Resolution Seismic Reflection (Chirp) Data: Marine Geophysical Researches, v. 20, no. 1, p. 13-20.
Randall, B. A. O., 1961, On the relationship of valley and fjord directions to the fracture pattern of Lyngen, Troms, N. Norway: Geografiska Annaler, v. 43, p. 336-338.
Reimer, P. J., and Reimer, R. W., 2006, A marine reservoir correction database and on-line interface, 2006.
Rey, P., Burg, J.-P., and Casey, M., 1997, The Scandinavian Caledonides and their relationship to the Variscan belt: Geological Society, London, Special Publications, v. 121, no. 1, p. 179-200.
Richter, T. O., van der Gaast, S., Koster, B., Vaars, A., Gieles, R., de Stigter, H. C., De Haas, H., and van Weering, T. C. E., 2006, The Avaatech XRF Core Scanner: technical description and applications to NE Atlantic sediments: Geological Society, London, Special Publications, v. 267, no. 1, p. 39-50.
Roberts, D., 2002, The Scandinavian Caledonides: event chronology, palaeogeographic settings and likely modern analogues: Tectonophysics, v. 365, no. 1-4.
Roberts, D., and Gee, D., 1985, An introduction to the structure of the Scandinavian Caledonides: In: Gee, D. G. & Sturt, B. A. (ed(s).): The Caledonide Orogen - Scandinavia and Related Areas.John Wiley & Sons Ltd, Chichester, p. 55-68.
Rothwell, R. G., Hoogakker, B., Thomson, J., Croudace, I. W., and Frenz, M., 2006, Turbidite emplacement on the southern Balearic Abyssal Plain (western Mediterranean Sea) during Marine Isotope Stages 1–3: an application of ITRAX XRF scanning of sediment cores to lithostratigraphic analysis: Geological Society, London, Special Publications, v. 267, no. 1, p. 79-98.
Sahu, B. K., 1964, Depositional mechanisms from the size analysis of clastic sediments: Journal of Sedimentary Petrology, 34(1):73-83.
Sawyer, D. E., Flemings, P. B., Dugan, B., and Germaine, J. T., 2009, Retrogressive failures recorded in mass transport deposits in the Ursa Basin, Northern Gulf of Mexico: JOURNAL OF GEOPHYSICAL RESEARCH, VOL. 114.
Schock, S., LeBlanc, L., and Mayer, L., 1989, Chirp subbottom profiler for quantitative sediment analysis: GEOPHYSICS, v. 54, no. 4, p. 445-450.
Skei, J., 1983, Why sedimentologists are interested in Fjords: Sedimentary Geology, v. 36, no. 2, p. 75-80.
St-Onge, G., Chapron, E., Mulsow, S., Salas, M., Viel, M., Debret, M., Foucher, A., Mulder, T., Winiarski, T., Desmet, M., Costa, P. J. M., Ghaleb, B., Jaouen, A., and Locat, J., 2012, Comparison of earthquake-triggered turbidites from the Saguenay (Eastern Canada) and Reloncavi (Chilean margin) Fjords: Implications for paleoseismicity and sedimentology: Sedimentary Geology, v. 243–244, no. 0, p. 89-107.
Stoker, M. S., Wilson, C. R., Howe, J. A., Bradwell, T., and Long, D., 2010, Paraglacial slope instability in Scottish fjords : examples from Little Loch Broom, NW Scotland: In: Howe, J.A.; Austin, W.E.N.; Forwick, M.; Paetzel, M., (eds.) Fjord systems and archives. London, UK, Geological Society of London. (Geological Society Special Publication, 344), p. 225-242.
Stow, D. A. V., Reading, H. G., and Collinson, J. D., 1996, Deep Seas: In: H.G. Reading (Editor), Sedimentary Environments - Processes, Facies and Stratigraphy. Blackwell Science, pp. 395-453.
Stuiver, M., and Reimer, P. J., 1986-2013, 03/10/2014, CALIB Radiocarbon Calibration; http://calib.qub.ac.uk/calib/.

Sundby, S., 1976, Oseanografiske forhold i området Malangsgrunnen-Fugløybanken-Tromsøflaket. En oversikt: Fisken og havet; serie B, nr.1. Rapporter og meldinger fra Fiskeridirektoratets havforskningsinstitutt - Bergen., p. 53.

Sundby, S., 1984, Influence of bottom topography on the circulation at the continental shelf off northern Norway: Fiskeridirektoratets Skrifter Serie Havforskningsundersøkelser, v. 17, p. 501-519.

Sveian, H., 2004, Isen kom - og forsvant: IN: Ka dokker mein førr stein! (R.Dahl & H. Sveian Eds.): Norges geologiske undersøkelse.

Sveian, H., Bergstrøm, B., Blikra, L. H., and Dahl, R., 2004, Og landet steg..... In: Ka dokker mein førr stein! (R.Dahl & H. Sveian Eds.): Norges geologiske undersøkelse.

Sveian, H., and Corner, G., 2004, Lyngens isbreer før og nå: IN: Ka dokker mein førr stein! (R.Dahl & H. Sveian Eds.): Norges geologiske undersøkelse.

Svendsen, H., 1995, Physical oceanography of coupled fjord-coast systems in northern Norway with special focus on frontal dynamics and tides: In: Skjoldal, H. R., Hopkins, C., Erikstad, K. E. & Leinaas, H. P. (ed(s).): Ecology of Fjords and Costal Waters - Proseedings of the Mar Nor Symposium on the Ecology of Fjords and Costal Waters. Elsevier, Amsterdam, p. 149-153.

Syvitski, J. M. P., Burrel, D. C., and Skei, J. M., 1987, Fjords: processes and products: Springer-Verlag, New York, p. 379.

Syvitski, J. P. M., and Lee, H. J., 1997, Postglacial sequence stratigraphy of Lake Melville, Labrador: Marine Geology, Vol. 143, pp. 55-79.

Syvitski, J. P. M., and Schafer, C. T., 1996, Evidence for an earthquake-triggered basin collapse in Saguenay Fjord, Canada: Sedimentary Geology, v. 104, no. 1–4, p. 127-153.

Syvitski, J. P. M., and Shaw, J., 1995, Sedimentology and Geomorphology of Fjords: In G. M. E. Perillo (Ed.), Developments in Sedimentology: Elsevier. Chapter 5, v. 53, p. 113-178.

Sætre, R., Aure, J., and Ljøen, R., 1988, Wind effects on the lateral extension of the Norwegian Coastal Water: Continental Shelf Research, v. 8, no. 3, p. 239-253.

Tjallingii, R., Röhl, U., Kölling, M., and Bickert, T., 2007, Influence of the water content on X-ray fluorescence core-scanning measurements in soft marine sediments: Geochemistry, Geophysics, Geosystems, v. 8, no. 2, p. Q02004.

Vanneste, M., L'Heureux, J.-S., Baeten, N., Brendryen, J., Vardy, M., Steiner, A., Forsberg, C., Kvalstad, T., Laberg, J., Chand, S., Longva, O., Rise, L., Haflidason, H., Hjelstuen, B., Forwick, M., Morgan, E., Lecomte, I., Kopf, A., Vorren, T., and Reichel, T., 2012, Shallow Landslides and Their Dynamics in Coastal and Deepwater Environments, Norway, *in* Yamada, Y., Kawamura, K., Ikehara, K., Ogawa, Y., Urgeles, R., Mosher, D., Chaytor, J., and Strasser, M., eds., Submarine Mass Movements and Their Consequences, Volume 31, Springer Netherlands, p. 29-41.

Vardy, M. E., L'Heureux, J. S., and Vannete, M., 2012, Multidisciplinary investigation of a shallow near–shore landslide, Finneidfjord, Norway: Near Surface Geophysics, 10, (4), 267-277.

Vergara, J. F. A., 2011, Submarine failures in the bottom of the Aysén fjord, Northern Patagonia, Chile: Investig. Geogr. - Santiago, Chile, 43: 17-34.

Vogel, J. S., and Love, A. H., 2005, Quantitating Isotopic Molecular Labels with Accelerator Mass Spectrometry, *in* Burlingame, A. L., ed., Methods in Enzymology, Volume Volume 402, Academic Press, p. 402-422.

Vogel, J. S., Turteltaub, K. W., Finkel, R., and Nelson, D. E., 1995, Accelerator mass spectrometry: Analytical Chemistry, v. 67, no. 11, p. 353A-359A.

Vorren, T. O., Hald, M., Edvardsen, M., and Lind-Hansen, O.-W., 1983, Glacigenic sediments and sedimentary environments on continental shelves: General principles with a case study from the Norwegian shelf.: In: Ehlers, J. (ed.): Glacial Deposits in North-West Europe. Balkema, Rotterdam, pp. 61-73.

Vorren, T. O., and Laberg, J. S., 1997, Trough mouth fans - Paleoclimate and ice-sheet monitors: Quaternary Science Reviews, Vol.16, pp.865-881.

Vorren, T. O., and Mangerud, J., 2007, Istider kommer og går: In: Ramberg, I.B., Bryhni, I., Nøttvedt, A. & Rangsnes, K. (Eds.) Landet blir til Trondheim, Norsk geologisk forening, Chapter. 15, p. 478-531.

Vorren, T. O., Mangerud, J., Blikra, L. H., and Torsvik, T. H., 2007, Norge trer fram: In: Ramberg, I.B., Bryhni, I., Nøttvedt, A. & Rangsnes, K. (Eds.) Landet blir til Trondheim, Norsk geologisk forening. Chapter 16, p. 532-555.

Vorren, T. O., and Plassen, L. I. V., 2002, Deglaciation and palaeoclimate of the Andfjord-Vågsfjord area, North Norway: Boreas, v. 31, no. 2, p. 97-125.

Wassmann, P., Svendsen, H., Keck, A., and Reigstad, M., 1996, Selected aspects of the physical oceanography and particle fluxes in fjords of northern Norway: Jornal of Marine Systems, v. 8, p. 53-71.

Weber, M. E., Niessen, F., Kuhn, G., and Wiedicke, M., 1997, Calibration and application of marine sedimentary physical properties using a multi-sensor core logger: Marine Geology, v. 136, no. 3–4, p. 151-172.

Weltje, G. J., and Tjallingii, R., 2008, Calibration of XRF core scanners for quantitative geochemical logging of sediment cores: Theory and application: Earth and Planetary Science Letters, v. 274, no. 3–4, p. 423-438.

Yang, F., Li, J., Wu, Z., Jin, X., Chu, F., and Kang, Z., 2007, A Post-Processing Method for the Removal of Refraction Artifacts in Multibeam Bathymetry Data: Marine Geodesy, v. 30, no. 3, p. 235-247.

Zajączkowski, M., Szczuciński, W., Plessen, B., and Jernas, P., 2010, Benthic foraminifera in Hornsund, Svalbard: Implications for paleoenvironmental reconstructions: Polish Polar Research, v. 31, no. 4, p. 349-375.

Zwaan, K. B., 1988, Geologisk kart over Norge. Berggrunnskart Nordreisa - M 1:250 000: Norges Geologiske Undersøkelse.